# Study of Novel Electron Injection Mechanisms for Laser-Wakefield Accelerators




Marko W. von der Leyen

University College

University of Oxford

A thesis submitted for the degree of

*Doctor of Philosophy*

Trinity 2021

For you, dear reader.

Wenn Du vor mir stehst und mich ansiehst, was weißt Du von den Schmerzen, die in mir sind und was weiß ich von den Deinen. Und wenn ich mich vor Dir niederwerfen würde und weinen und erzählen, was wüßtest Du von mir mehr als von der Hölle, wenn Dir jemand erzählt, sie ist heiß und fürchterlich. Schon darum sollten wir Menschen vor einander so ehrfürchtig, so nachdenklich, so liebend stehn wie vor dem Eingang zur Hölle.

Franz Kafka

# Abstract

Laser-driven plasma wakefields are structures that can sustain large electric fields and offer a promising route to reducing the size and cost of electron (or positron) accelerators with applications in areas such as fundamental research, (biomedical) imaging or radiotherapy. In this thesis, I discuss novel mechanisms through which electrons are injected into the accelerating structure and methods used to achieve better control over experimental conditions. Experimental and numerical results are presented for injection of electrons into a wakefield driven by a short relativistic laser pulse propagating through a plasma of overcritical nanometre-sized clusters. The wakefield structure is found to be modified by the clusters and the creation of high-charge large energy spread electron beams is discussed. Furthermore, experimental and numerical results are presented for externally induced ionisation injection using two pulses of equal wavelength decoupling the processes of driving the accelerating structure from the injection into the structure finding quasi-monoenergetic electron beams. Finally, a reinforcement learning based algorithm for laser beam alignment is introduced and training results of alignment performance for an interferometer set-up as well as an off-axis parabolic mirror are presented.

# Acknowledgements

It would be an unfeasible undertaking to acknowledge the support of all the people that helped me on my journey which led to this thesis. Nevertheless, I want to highlight some people who had a great impact on me.

First, I want to thank my family. Thank you, Mama, for enabling me to pursue my dreams and being there for me. Thank you, Papa, for giving me perspective on what is important in life and teaching me critical thinking. Thank you, Florian, Chrystyna, Anna-Lena, and Sarah for great memories growing up and for loving me as a brother. Thank you, Victoria, for accepting me the way I am while enabling me to become a better person in every aspect and for making me smile in happy and difficult times.

Next, I wish to thank my supervisor Peter for allowing me to explore fascinating topics and for providing the framework, tools and guidance necessary for me to complete the degree. My time in Oxford was also enriched by many other people: Bernd, who went through many minor and major crises with me that come with a doctoral degree and who has been a good friend and companion ever since I met him at the Oktoberfest Formal Hall; Ramy, both friend and colleague with whom I have shared an incredible journey leading to us being able to communicate entirely in catchphrases; and Ben, who has always been very patient with me while I was asking him countless questions about science, software, hardware, or the United Kingdom. Thanks, Joey, Tom, Marcel, Leonardo and Oliver for good memories and for making Oxford a fun experience and Benjamin, Clemens, Florian, and Lukas for remote support. Thanks, James, for introducing me to the topic of PIC simulations and helping me in my first weeks at Oxford. Thanks, Jimmy, for always having an open door when it comes to discussing results. I also want to acknowledge all other past and present members in the research group who have helped me with useful discussions. Many thanks also to the high-power laser research group at the University of Michigan who warmly welcomed me at their laboratory and gave invaluable help during the experiment.

Finally, I want to acknowledge funding from the *Konrad-Adenauer-Stiftung* which supported me through awarding me their doctoral scholarship and thank the people of Austria for deciding to offer a decent, well-rounded and debt-free education to children irrespective of their financial background.

# Contents


**1 Introduction** **1**

1.1 Particle accelerators . . . . . 1
1.2 Laser-wakefield accelerators . . . . . 4
1.3 Thesis outline . . . . . 10
1.4 Contributions of the author . . . . . 10
1.5 List of peer-reviewed publications . . . . . 12

**2 Theoretical background of relevant topics** **14**

2.1 Electromagnetic wave propagation in vacuum . . . . . 14
2.1.1 Gaussian beam solution . . . . . 15
2.1.2 Beam at focus . . . . . 16
2.2 Single electron behaviour in electromagnetic fields . . . . . 17
2.2.1 Nonrelativistic motion . . . . . 18
2.2.2 Relativistic treatment . . . . . 18
2.3 Ponderomotive force . . . . . 21
2.4 Plasma . . . . . 23
2.4.1 Debye length . . . . . 23
2.4.2 Plasma oscillation . . . . . 24
2.4.3 Ionisation . . . . . 26
2.4.4 Dispersion relation of light in plasma . . . . . 28
2.4.5 Plasma optics . . . . . 29
2.4.5.1 Self-focusing . . . . . 29
2.4.5.2 Pulse compression . . . . . 30
2.5 Laser-wakefield acceleration . . . . . 31
2.5.1 Wakefield regimes . . . . . 31
2.5.2 Wave breaking . . . . . 33
2.5.3 Energy gain . . . . . 33
2.5.4 Electron trapping and injection mechanisms . . . . . 35

2.5.4.1 External injection . . . 36
2.5.4.2 Self-injection . . . 36
2.5.4.3 Ionisation injection . . . 37
2.5.4.4 Injection through tailored density profile . . . 38
2.5.4.5 Injection using multiple pulses . . . 39
2.6 Computational methods for simulating laser-plasma interactions . . . 40
2.6.1 Fundamentals of the PIC method . . . 41
2.6.2 Moving window frame . . . 43

**3 Wakefields in a cluster plasma 44**
3.1 Wakefield structure in the weakly non-linear acceleration regime . . . 51
3.1.1 Experimental data . . . 51
3.1.2 Two-dimensional particle-in-cell simulations . . . 60
3.1.2.1 Modifications to OSIRIS code . . . 60
3.1.2.2 Results of simulations . . . 63
3.1.3 Quasi-analytic one-dimensional model . . . 72
3.1.4 Discussion . . . 77
3.2 Cluster electron self-injection and acceleration in the non-linear wakefield regime . . . 79
3.2.1 Numerical challenges . . . 80
3.2.2 Simulation parameters . . . 81
3.2.3 Wakefield behaviour . . . 84
3.2.4 Electron trapping and acceleration . . . 89
3.2.4.1 Electron beam charge calculation . . . 96
3.2.4.2 Quantitative comparison . . . 99
3.2.5 Analysis of laser pulse properties . . . 100
3.3 Summary and conclusion . . . 104

**4 Experimental study of electron injection using a two-pulse ionisation injection scheme 106**
4.1 Experimental investigation of the 2PII mechanism . . . 108
4.1.1 Experimental considerations and restrictions . . . 108
4.1.2 The HERCULES high-power laser facility . . . 110
4.1.3 Generating two collinear pulses . . . 110
4.1.4 Target chamber layout . . . 113
4.1.5 Gas selection . . . 116
4.1.6 Gas cell design . . . 116

4.1.7 Diagnostics . . . 117
4.1.7.1 Measuring electron density . . . 117
4.1.7.2 Measuring wavefront for adaptive optics optimisation 119
4.1.7.3 Measuring focal spot properties . . . 122
4.1.7.4 Measuring spatial jitter . . . 130
4.1.7.5 Measuring temporal pulse delay . . . 130
4.1.7.6 Measuring accelerated electron bunch energy . . . 134
4.1.7.7 Measuring properties related to electron bunch charge 135
4.1.8 Results . . . 135
4.1.8.1 Run I . . . 137
4.1.8.2 Run II . . . 155
4.1.8.3 Run III . . . 156
4.1.8.4 Run IV . . . 161
4.2 Simulations . . . 164
4.3 Conclusion . . . 171

**5 Reinforcement learning-based laser alignment system 173**
5.1 Introduction to reinforcement learning . . . 174
5.2 Alignment of Mach-Zehnder interferometer arms . . . 178
5.2.1 Experimental implementation . . . 178
5.2.1.1 Reward . . . 179
5.2.1.2 Image processing using computer vision . . . 180
5.2.1.3 Equipment . . . 180
5.2.2 Training the model . . . 181
5.2.2.1 Simulation environment . . . 181
5.2.2.2 Deep Q-Network (DQN) . . . 183
5.2.2.3 Training from experiment . . . 185
5.2.3 Testing agent performance . . . 185
5.2.3.1 Probability distribution and limits of beam initialisation 186
5.2.3.2 Results . . . 188
5.3 Alignment of off-axis parabolic mirror . . . 190
5.3.1 Experimental implementation . . . 190
5.3.1.1 Equipment . . . 191
5.3.2 Training the model . . . 191
5.3.2.1 Reward calculation . . . 193
5.3.2.2 Simulation environment . . . 195

5.3.2.3 Training from experiment . . . . . 196
5.3.3 Testing agent performance . . . . . 200
5.4 Conclusion . . . . . 203

**6 Summary and outlook** **204**
6.1 Summary . . . . . 204
6.2 Future work . . . . . 206

**A Detailed derivations** **207**
A.1 Solution to Maxwell equations . . . . . 207
A.2 Frequency of electron oscillations in a cold plasma . . . . . 208
A.3 Redundancy of Maxwell equations for subsequent iterations in the particle-in-cell method . . . . . 209
A.4 Calculation of pre-factor for density reconstruction . . . . . 209
A.5 Cluster initialisation factor for linear ramp . . . . . 210
A.6 Equation of motion in co-moving frame . . . . . 211
A.7 Error Factor for Overlapping Beams . . . . . 213
A.8 Probability distribution function for beam initialisation position . . . 213
A.9 Fit of the annular injector beam profile . . . . . 214
A.10 Airy disk spot size . . . . . 215

**B Code** **216**
B.1 Modifications to OSIRIS 4 . . . . . 216

**C Further simulation results** **220**
C.1 Error of phase shift measurement using oblique angle probe pulse . . 220
C.2 Impact of ionisation on cluster wakefield behaviour . . . . . 223

**D Photograph of laboratory setup** **228**

**Bibliography** **230**

# List of Figures


2.1 Gaussian laser beam parameters . . . . . 17
2.2 Modification of binding potential by external electric field. . . . . 28
2.3 Separatrix for electron trapping. . . . . 36

3.1 Schematic of the cluster expansion process . . . . . 48
3.2 Schematic of FDH set up . . . . . 52
3.3 Steps of phase reconstruction algorithm. . . . . 54
3.4 Schematic of variables involved in Abel transform . . . . . 54
3.5 Interferometry data for electron density analysis . . . . . 55
3.6 Spectrogram for FDH analysis . . . . . 56
3.7 Experimental results from FDH experiment . . . . . 59
3.8 Diagram of phase distortion . . . . . 60
3.9 Simulation of phase blur . . . . . 61
3.10 Results of 2D moving window particle-in-cell simulations . . . . . 65
3.11 Close-up of cluster expansion . . . . . 66
3.12 Longitudinal electric field for various laser pulse amplitudes . . . . . 69
3.13 Comparison of cluster expansion for varying initial electron density . 71
3.14 Comparison of model to cluster expansion data. . . . . 75
3.15 Results of numerical WENO integration . . . . . 76
3.16 Impact of grid resolution on injection properties . . . . . 82
3.17 Wakefield structure for different plasma structures . . . . . 85
3.18 Comparison of the wakefield evolution in a uniform and a cluster plasma 87
3.19 Longitudinal electric fields in uniform and cluster plasma . . . . . 88
3.20 Electron and ion density in cluster plasma wakefield bubble . . . . . 90
3.21 Trapped particle trajectories for cluster and uniform plasma . . . . . 91
3.22 Analysis of the electron injection behaviour . . . . . 94
3.23 Longitudinal and transverse particle momentum for different cluster parameters . . . . . 96
3.24 Spectrum of electrons in cluster plasma with different cluster parameters. 97

3.25 Plot of distribution functions for charge calculation . . . . . 99
3.26 Fourier transform of laser electric field . . . . . 103
3.27 Laser energy depletion for different scenarios . . . . . 104

4.1 Schematic of the beam splitting process. . . . . 111
4.2 Layout of the target chamber . . . . . 115
4.3 CAD drawings of gas cell. . . . . 117
4.4 Raw interferometry image. . . . . 118
4.5 Image of reconstructed electron density from phase modulations. . . . 120
4.6 Schematic of imaging system for wavefront optimisation. . . . . 121
4.7 Wavefront after being corrected for refractive errors as seen by the *Wavetune* software. . . . . 121
4.8 Focal spot images for drive and injector pulse. . . . . 123
4.9 Study of focusing of various beam shapes. . . . . 127
4.10 Focal spot image of annular injector pulse away from focus. . . . . 128
4.11 Fit of beam divergence measurement. . . . . 129
4.12 Correlation measurement for jitter determination. . . . . 131
4.13 Gas cell interferograms and shadowgrams for timing measurements. . 132
4.14 Focal spot images for delay scan. . . . . 133
4.15 Lanex screen calibration curve. . . . . 134
4.16 Data analysis routine for measuring electron bunch properties. . . . . 138
4.17 Intensity correction on Lanex screens. . . . . 139
4.18 Raw images from Lanex screens showing single electron bunches. . . . 140
4.19 Raw images from Lanex screens showing double electron bunches. . . 140
4.20 Pulse delay and energy versus shot number for run I. . . . . 142
4.21 Pulse delay versus energy properties for run I. . . . . 143
4.22 Divergence measurement. . . . . 144
4.23 Energy error on Lanex screen. . . . . 145
4.24 Jitter measurement for Run I. . . . . 147
4.25 Oscilloscope reading for two different shots in run I. . . . . 148
4.26 Maximum Energy, PMT, and EMP signals in run I. . . . . 149
4.27 Correlation of PMT signals for Run I. . . . . 150
4.28 Correlation of PMT signals with charge and electron energy for Run I. 151
4.29 Results of density measurement for run I. . . . . 152
4.30 Analysis of uncertainty for electron density measurement. . . . . 153
4.31 Energy versus density plot for run I. . . . . 155

4.32 Oscilloscope readings for run II. . . . . 157
4.33 Pulse delay versus energy plot for run III. . . . . 158
4.34 Oscilloscope readings for run III. . . . . 159
4.35 Jitter measurement for run III. . . . . 160
4.36 Observed electron bunch shapes in run IV. . . . . 161
4.37 Oscilloscope readings for run IV. . . . . 162
4.38 Jitter measurement for run IV. . . . . 163
4.39 Longitudinal electric field and injected number density in simulations. 167
4.40 Kinetic energy of tracked particles in PIC simulation. . . . . 168
4.41 Temporal evolution of off-axis injection. . . . . 169
4.42 Maximum kinetic energy and trapped particle density from PIC simulations. . . . . 170

5.1 Reinforcement learning flowchart. . . . . 176
5.2 Schematic of two mirror set-up. . . . . 179
5.3 Illustration of a possible observation on near field camera (A) and far field camera (B). . . . . 182
5.4 Training data for DQN2M. . . . . 184
5.5 Probability density function of random initialisation. . . . . 187
5.6 Schematic of initialisation limits in two mirror set-up. . . . . 187
5.7 Results of DQN2M test run. . . . . 189
5.8 Schematic of OAP alignment set-up. . . . . 191
5.9 Beam post-processing for observation preparation. . . . . 194
5.10 Reward functions for the RL OAP training. . . . . 196
5.11 Results of training for DQNOAP1 agent. . . . . 197
5.12 Results of the training of the *NACOAP1* agent. . . . . 199
5.13 Results of training for DQNOAP2 agent. . . . . 201
5.14 Results of training for NACOAP2 agent. . . . . 202

C.1 Temporal evolution of probe pulse phase shift. . . . . 222
C.2 Electron density for ionisation comparison. . . . . 223
C.3 Longitudinal momentum for ionisation comparison. . . . . 224
C.4 Ionisation states of argon clusters . . . . . 224
C.5 Temporal evolution of ionisation states of single cluster. . . . . 226

D.1 Photograph of reinforcement learning alignment setup. . . . . 229

# List of Tables


2.1 Parameters from independent experiments showing quasi-monoenergetic electron beams. . . . . 32

3.1 List of first and second wakefield wavelengths for different laser amplitudes. . . . . 69
3.2 List of cluster parameters for the study of cluster expansion. . . . . 70
3.3 PIC simulation parameters for the study of high-power laser-cluster interactions. . . . . 83
3.4 List of accelerated electron bunch charge. . . . . 99

4.1 Atom and electron ratios obtained from three different He-$N_2$ mixtures. 116
4.2 Table of distance measurements for imaging system. . . . . 119
4.3 Experimental parameters for runs I to IV. . . . . 136
4.4 Results of error approximation for the electron density reconstruction. 154
4.5 Simulation parameters. . . . . 165

5.1 List of constants used for training the 2-mirror setup. . . . . 185
5.2 Step sizes measurements for picomotors. . . . . 188
5.3 Observation values for OAP set-up for two cases. . . . . 193
5.4 List of constants used for training *DQNOAP1*. . . . . 198

# Chapter 1

# Introduction

## 1.1 Particle accelerators

Broadly speaking, a particle accelerator is an object which takes particles and increases their velocity through the use of elementary forces. By this definition, many naturally occurring objects are particle accelerators, for example, the sun which erupts particles in solar flares. In the context of this thesis, I will focus on human-made objects which have specific applications to satisfy a purpose. This limits the elementary forces used to the class of electromagnetic forces which are (at practical magnitudes) more easily controllable than others. We encounter various manifestations of these electromagnetic fields every day, for example as photons or as static electric or magnetic fields. Electromagnetic forces only affect charged particles which is why they are "used" in particle accelerators.

When conducting research, a useful question to ask before "how?" is "why?". Other than arguing that research can be a personally satisfying and fun task (which might be a satisfactory answer to many), one should also have a compelling reason for why investing one's limited time and resources is beneficial to humankind. As a matter of fact, this plays an important role in how public funding for research projects is typically awarded. Concerning particle accelerators (as is the case for many other areas of research) answers to why one should pursue research in this area might be two-fold.

Firstly, applied and fundamental accelerator research is closely linked to other disciplines and findings in one can benefit the other. Curiosity, wanting to understand how processes work, how to describe and predict events is a human trait that has driven us for as long as we exist. CERN's Large Hadron Collider (LHC), a multinational scientific experiment that is used for elementary particle research, is probably the world's most famous particle accelerator known for discoveries such as the Higgs

Boson [1, 2]. Today's increased life expectancy, for example, is a result of countless discoveries based on research which, at the time the discoveries were made, did not have an application in mind. Electricity, radio waves or even lasers[1] are among many of those discoveries. In the short term, however, accelerators used for fundamental research might not have an immediate impact on the lives of the people who finance these endeavours.

Secondly, accelerators have "real-life" applications in medicine, imaging, security, and other fields. For example, precise treatment of tumours using radiotherapy and hadrontherapy [4] is only possible because of the existence of particle accelerators. To this end, electrons, protons, ions, and X-rays can be used to treat affected regions in the body noninvasively and with high precision. X-rays, which are also used for biomedical imaging (e.g. tomography) are also often produced from accelerated electron beams. Further areas in which accelerators are used include industrial radiography, isotope production, nuclear forensics, or cargo scans at airports and other facilities [5].

This great range of applications suggests that, in order to satisfy each application's needs, different mechanisms of accelerating particles could be favourable. Indeed, historically, different approaches were developed to target this problem. The first particle accelerators used static electric potentials. The one built by Cockcroft and Walton in 1932 used capacitor banks and created large electric fields in which protons were accelerated to energy levels of 710 kiloelectronvolt which is the energy that one proton gains by being accelerated across an electric potential difference of 710,000 volt [6]. Another approach, the Van de Graaff generator, used a fabric or rubber belt to transport charges to an insulated electrode. In comparison, 80 years later the Large Hadron Collider accelerated proton beams to 6.5 teraelectronvolt which is almost a factor of 10 million higher. It should be noted, however, that the construction of LHC took a decade and had a rather high price tag of 4.3 billion CHF [7]. Another caveat is that the ring in which superconducting magnets accelerate protons has a circumference of 27 kilometres. The LHC belongs to the class of synchrotrons which use magnetic fields to keep particles on a circular path during the acceleration process to reuse the path many times. Synchrotron radiation, which is the tangential emission of radiation from charged particles that are accelerated towards the centre of a circular path, scales inversely to the particle's mass as $\propto m^{-4}$. While this emission can be

[1] "Laser" is an acronym for the process of "light amplification by stimulated emission of radiation" but has also become the name for machines producing coherent beams (or pulses) of light. A detailed introduction to lasers can be found in [3].

purposefully used in synchrotron light sources, it puts a limit on the maximum energy that can be gained which favours the use of heavier particles with this method such as protons. This explains why another approach has to be found to accelerate lighter particles such as electrons and positrons to high energies.

Linear accelerators (or "linacs") are, as the name suggests, straight tubes that use alternating current (AC) radio frequency (RF) high voltage electrodes of increasing length to accelerate charged particles. These reverse their polarity in a synchronised manner with the passing electron bunch. The RF cavities can only withstand an electric field of $< 100\,\mathrm{MV\,m^{-1}}$ before vacuum breakdown occurs [8] which is why it is necessary to build long accelerators to reach electron energies in excess of several GeV.

The question now is: what is there to improve? From an economical perspective, the cost and size of accelerators are the most pressing issues that need addressing. Furthermore, improvements in beam quality (smaller emittance and increased phase space density), maximum charge, maximum energy, reproducibility and tunability are currently in the focus of research.

Some of these issues such as the cost, size, and phase space density can be addressed with plasma[2]-based electron acceleration. The first work towards this concept was proposed by Veksler in 1956 [9]. His paradigm-shifting idea was to use microscopic accelerating structures that moved with the particles to be accelerated (seemingly) removing the need for synchronisation (of acceleration stages). The locality of the process allowed for strong fields while avoiding breakdown due to field emission from the accelerator wall (which is non-existent with his approach). This idea to use a plasma that can withstand much larger potential differences (because it is already in an ionised and moving state) was far from developed and it took many years to be refined and extended on by Faĭnberg [10]. A breakthrough came when Tajima and Dawson presented a physical proposal including simulation results for achieving plasma-based acceleration using laser pulses of high intensity [11]. They showed that it can be possible to accelerate electrons to 1 GeV over a distance of 1 cm. The laser-wakefield accelerator was born.

[2]A plasma is a medium consisting of ionised particles of positive and negative charge which show collective behaviour mediated through electromagnetic forces. A more detailed description will be given in the next chapter.

## 1.2 Laser-wakefield accelerators

When a laser pulse of finite duration propagates through a plasma it gives electrons a push, broadly speaking due to its radiation pressure. The ions in the plasma have higher inertia and—on the time-scale of this effect—remain stationary. This builds up a strong electrostatic force proportional to the number of particles displaced and the distance from their origin. The electrons are pulled back, overshoot and set up an oscillation at the plasma frequency which scales as the square root of the electron density. The accelerating field caused by the density perturbation (the wakefield) propagates at the speed of the laser group velocity (which, in a plasma, is smaller than the speed of light in vacuum) and can accelerate particles until they outrun the accelerating part of the field.

Over the years, many proposals which built on Tajima and Dawson's idea were published, some of them acknowledging the fact that particle beam-driven wakefield accelerators may have practical advantages over laser-driven accelerators due to their lower energy loss (limited diffraction, higher phase velocity, etc.). Both approaches to plasma-wakefield acceleration have coexisted successfully next to each other with impactful results on both sides. As in other fields, it has proven to be wise not to bet only on one horse.

The caveat with both is that they need highly specialised apparatuses to create the beam which drives the wakefield in the plasma. Neither (proton or electron) particle beams of sufficiently high energy and quality nor ultra-short high power laser pulses are easy to come by outside of dedicated research facilities. The large footprint of these facilities currently outweighs the advantage of being able to miniaturise the accelerator to a centimetre-sized plasma column. However, as is the case with many technologies, lasers have evolved at a rapid pace from its first footsteps in the late 1950s [12] and its functional realisation in 1960 [13] to cheap mass-products seen in everyday life as well as high-performance equipment in research. Lasers in the latter category can deliver 30 J in 30 fs (1 PW) pulses at a repetition rate of 10 Hz, 1.5 kJ in 150 fs (10 PW) pulses at a repetition rate of 1/60 Hz (both at the pan-European Extreme Light Infrastructure Beamlines [14]), or can be combined on target to deliver 1.8 MJ in $\sim$ 3 ns (0.6 PW) as seen in the National Ignition Facility [15]. Among the most important inventions leading to these great successes were the chirped pulse amplification (CPA) by Strickland and Mourou [16] and, building on this technology, optical parametric chirped pulse amplification (OPCPA) [17, 18].

Advances in laser-wakefield acceleration (LWFA) have been (and will be) closely coupled to advances in laser science. When Tajima and Dawson started their work, high-power laser systems could not deliver pulses with less than 100 fs duration. Therefore, they proposed to use the beatwave of two co-propagating laser pulses which could be tuned through a mismatch in laser wavelength. The first experiment successfully implementing this scheme managed to accelerate externally injected electron beams from 2.1 MeV to 9.1 MeV [19]. The concept was evolved to a self-modulated regime that used the plasma's response instead of a resonance beat to shape the laser pulse [20, 21]. Here, a laser pulse sufficiently powerful to undergo relativistic self-focusing[3] sets up a wakefield, defocuses in high-density regions and interacts with forward-scattered Raman photons. These photons have a frequency which is shifted by the plasma frequency. Later, with the discovery of CPA, pulses with shorter duration than the plasma wavelength[4] and intensities in excess of $1 \times 10^{18}\,\mathrm{W\,cm^{-2}}$ were available to drive wakefields directly, for example in the bubble regime [22–25]. In 2004, three experiments simultaneously reported accelerated electron beams of high charge and mono-energetic spectrum [26–28] using this scheme.

After reaching this milestone, some obstacles remained concerning the further increase of beam energy. These are linked to the achievable potential gradient (increasing with electron density) and the achievable acceleration path length (decreasing with electron density). It will be shown in the following chapter that acceleration at lower density is favourable to reach higher energies. However, as is the case with many other problems in plasma physics, optimising one quantity creates numerous new difficulties that have to be mitigated carefully (for example, the laser spot size has to be roughly matched to the plasma wavelength to achieve efficient acceleration which puts a lower limit on density values).

Going towards lower density plasmas meant that the focus of research had to shift to tackling problems linked to increasing the maximum path length in the accelerating region of the wakefield. This length depends on

- the length of the plasma (independent of density),
- the wakefield's phase velocity (increases with lower density),
- the time within which the laser pulse is depleted in the plasma (increases with lower density),

[3] This effect will be explained in more detail in chapter 2.

[4] In this thesis, duration - especially in the context of laser pulses - will sometimes be compared to quantities of unit length. In these cases, the time can be converted to length using the speed of light.

- the time within which the laser pulse is diffracted in the plasma (decreases with lower density above a density threshold but independent below this threshold), and
- the amplitude of the laser pulse (dependent on diffraction length).

Because low density implies low field strength of the wakefield, the length of the plasma has to increase to gain higher total energy in the electron bunch. This promotes laser diffraction of tightly focused beams to a serious obstacle. There are two "obvious" solutions to this problem. The first is laser "self-guiding"[5] which is caused by the "self-focusing" effect. In this process, the electron plasma response conveniently acts as a focusing lens for laser pulses of critical power (a value that is inversely proportional to the plasma density) which helps to guide the pulse over long distances. The second solution is the use of externally induced plasma channels which can guide beams below the critical density. Long guiding channels of several Rayleigh lengths (see Eq. 2.11) have been produced successfully [29, 30] and were recently shown to be operable at kHz repetition rates [31]. Both mechanisms have been experimentally verified and have shown to create beams on the GeV level in the 2000s [32–34]. The peak energy limit was shown to be pushed to 2 GeV (2013) [35], 4.2 GeV (2014) [36], and 8 GeV (2019) [37]. As will be discussed in Section 2.5.3, a particular parameter called "dephasing length" (related to the difference between electron bunch velocity and velocity of the accelerating field structure) limits the maximum reachable electron energy in laser-driven wakefield accelerators. Recently, researchers have tried to work on concepts which remove the limitations imposed by dephasing. One proposed method [38] considers the use of quasi-Bessel beams [39] generated from an axiparabola [40] in addition to spatio-temporal couplings (see "flying focus" method in [41]) to achieve phase-locked acceleration (electrons stay within the accelerating phase of the wakefield and maximum energy is limited by focal depth of the quasi-Bessel beam). Using this method, the authors estimate the generation of 1 GeV electron beams at a repetition rate of 1 kHz from a laser pulse with power of 12 TW and duration of 5 fs. A similar concept of dephasingless acceleration suggests it is possible to accelerate electrons to TeV energies in a single plasma stage using an echelon optic [42].

Another possibility to increase the peak energy of the electron beam is to utilise a mechanism that is used in linacs—building stages. This task is challenging due to the necessity of extremely precise temporal and spatial control of the electron

[5] A detailed description of this process is given in chapter 2.

bunch in the coupling process between subsequent stages (in both extraction and injection). The technology is far from being mature but first steps have been made experimentally in [43] where an energy gain of $\sim 100\,\mathrm{MeV}$ in a second quasi-linear stage was achieved. This method seems to be a promising route to exceed the barrier of 10s of GeV potentially reachable with single-stage devices but great effort will have to be undertaken to reach this goal.

Further to advancing the maximum reachable energy in LWFA devices, reaching better beam quality is a topic the LWFA community is currently researching. Decreasing an electron beam's transverse emittance leads to high luminosity in high energy physics applications [44] due to a tighter electron beam focus and smaller interaction area. In the context of free electron lasers (FEL), high beam brightness and operation at smaller wavelengths can be achieved when low emittance electron beams are generated [45]. Nowadays, laser-driven wakefield accelerators typically claim to achieve normalised emittance values of $\epsilon_n \simeq 1\mathrm{mm\,mrad}$ [46, 47]—a value which understandably depends on the specifics of the LWFA scheme and parameters [48]. Although these values are already comparable to "conventional" X-ray FELs, better and more reliable emittance characterisation is necessary to make further improvements to quality and repeatability which requires future work on building improved LWFA beam diagnostics [44]. Increasing the electron current while keeping the emittance low leads to higher peak brightness which is, again, required for good FEL performance, especially for low wavelength operation [49]. High electron currents of up to $\sim 0.5\,\mathrm{nC}$ with monoenergetic beam profile have been demonstrated in [50] using a $2.5\,\mathrm{J}$ laser pulse at $30\,\mathrm{fs}$.

To be competitive with other (non-LWFA) systems, a high repetition rate (in the kHz regime) of beams at high brightness is necessary. To operate at this rate, stable laser systems and environmental conditions (such as constant gas density) are required. Therefore, high-power laser development for LWFA applications, for example through replacing flash lamps through diodes, is a very active area of research. Another approach to reach these high repetition rates is using low-power laser technology (which already allows for high repetition rates) to resonantly excite wakefields in the plasma [51]. An ultrashort mJ pulse might be able—in combination with a Joule-level ps pulse—to generate GeV electron beams [52]. These low-cost low-power laser systems also have the advantage of having a high wall-plug efficiency making LWFA more accessible to research labs around the world.

Another important parameter which has to be accounted for in LWFA optimisation is the energy spread, which is desired to be small. This is because electrons of

same energy are easier to control. For example, the aforementioned staging process requires precise control which favours beams of narrow energy spread. Especially for applications in devices such as X-ray FELs, sub-percent spreads are necessary [44]; this is a difficult task for state-of-the-art laser-wakefield accelerators which typically and consistently achieve energy spreads of more than a few percent [53, 54].

For the use in high-energy physics facilities, requirements such as a centre-of-mass energy of over 1 TeV and a luminosity of over $1 \times 10^{34}\,\mathrm{cm}^{-2}\,\mathrm{s}^{-1}$ have to be met [55]. To facilitate the transport of electron beams between stages such that luminosity can be kept high, low energy spread ($< 1\%$) and low normalised transverse emittance ($< 0.1\,\mu\mathrm{m}$) are required [55]. While many of the currently achieved values above are already sufficient for LWFA to be useful in FELs and other applications, their simultaneous reproduction and experimental stability remains an obstacle [56].

So far, I have not mentioned one crucial part of LWFA which is important for all points raised before—the question of how an electron bunch ends up in a wakefield which can then be accelerated. This process of electron injection (see Section 2.5.4) into the wakefield is important when it comes to overcoming remaining challenges in LWFA such as shot-to-shot stability and phase-space control. Concerning advanced injection mechanisms, Hidding *et al.* believe that "This area of research will become increasingly important as applications of plasma accelerators are developed [...]" [44]. It is possible to inject electrons from an external source such as a linac where timing problems as those mentioned above play a significant role. Another approach is to trap electrons in the wakefield which originate in the plasma—a method which will be discussed in detail in the following chapter. In the bubble regime, self-injection occurs directly through a process called wave breaking. This method is difficult to control and, therefore, may cause large energy spreads. Other schemes use the collision of two laser pulses or locally confined density gradients (ramps) to create short trapping events, or use dopants in the gas target which can lead to narrow energy spreads.

Electron injection is the topic towards which I hope to contribute a small part with this thesis. In particular, through experiments, simulations and theoretical analysis, I will explore how different targets and laser pulse arrangements may be used to modify the injection process and to improve specific aspects of the accelerated electron beams from LWFA. First, I will explore how particular deviations from uniform plasma targets—so-called clusters which may occur in set-ups using high-pressure gas jets—affect the electron trapping condition and, therefore, influence the electron charge, maximum energy and energy spread of accelerated beams. These clusters have been observed in various wakefield experiments but up to this point there does not exist a

thorough analysis of their influence on the electron injection process. The research in this thesis seeks to explain the impacts of cluster media on both the acceleration and injection processes in different intensity regimes to better understand the generation of high-charge beams with broad energy spectrum. Next, I will explore a particular injection method utilising two separate laser pulses with the goal of experimentally showing that a second, co-propagating laser pulse can act as an injector. Using this method, a low-amplitude drive laser pulse can be used which may be guided over long distances. Injection of a high-quality electron beam into a low-amplitude wakefield has been an obstacle for the community and with this research I want to show that the route via a two-pulse ionisation injection scheme [57] is a promising contender for its realisation. Lastly, this thesis will show the first reinforcement learning based laser beam alignment system for two types of optical set-ups. The goal of this work is to show that particular aspects of laser-wakefield experiments[6] can be made more easily controllable through artificial intelligence. This could be a small step towards removing the human error component from experimental set-ups.

Finally, I want to mention some current and future applications of LWFA (for a review on this interesting topic see [58]). Just like conventional accelerators, laser-wakefield accelerators may be used for imaging purposes or medical treatment. Electrons accelerated in a wakefield bubble undulate due to the perpendicular forces and generate betatron (hard X-ray) radiation. This radiation can be used for high-resolution imaging since they are emitted from a small source in a short amount of time and have been successfully used for phase-contrast imaging [59] or micro-computed tomography [60, 61]. Using external undulators, electron beams can also be used to create soft X-rays [62]. Furthermore, LWFA is a promising contender for radiotherapeutic treatment [63, 64]. Lastly, electron beams from LWFA can be used as a source to generate beam-driven wakefields which have the potential to create high-quality electron beams for free electron lasers at a compact footprint. A proof of principle experiment of this combined scheme is presented in [65] where two separate stages (gas jets) were used to achieve an unprecedented energy transfer from the driver beam to the witness beam.

[6]The method aims to be as universal as possible and should not be limited to a particular branch of laser experiments.

## 1.3 Thesis outline

- Chapter 2 covers some of the theory behind the concepts and mechanisms used and described in chapters 3, 4, and 5.
- Chapter 3 introduces the topic of LWFA in non-uniform clustered media. I will show analysis done on data from an experiment conducted at the ASTRA laser facility (before I was part of the group) studying modifications to the wakefield shape. I will then present work on changes to a particle-in-cell code to incorporate clusters and compare the results of these simulations to the experimental data and to the numerical solution of an analytic model. Furthermore, I will introduce data suggesting the existence of a new injection mechanism in cluster plasmas. Using simulations I will then give an explanation for observations presented in articles by other research groups.
- Chapter 4 presents data from an experiment conducted at the HERCULES laser facility to study a two-pulse ionisation injection mechanism. I will introduce the set-up of the experiment, its results and will use particle-in-cell simulations to illuminate the observations made.
- Chapter 5 introduces a new reinforcement learning aided laser beam alignment system. I will show results from training an agent in laboratory and simulation environments that tries to solve the problem of aligning the near and far-field of an interferometer as well as an off-axis parabolic mirror.
- Chapter 6 gives a conclusion of this thesis and discusses further work.

## 1.4 Contributions of the author

This thesis is based on work to which several people have contributed – as is the case with many projects in the field of laser-plasma physics. As chapters 3, 4, and 5 involve experiments, I will give an account of others' contributions below.

The experiment on which the first part of Chapter 3 is based was conducted in my absence before I was part of the research group. I was given the data by Prof. P. Norreys and M. Kasim who have kindly introduced me to the workings behind the experiment at the ASTRA laser facility. It was also M. Kasim who shared his analysis scripts for the FDH reconstruction which I modified and used in this thesis. I conducted all simulations in this chapter myself and wrote the new modules of the

code mentioned in the appendix. In numerous meetings, B. Spiers kindly supported me with coding and compiling issues and it was he who pointed out the WENO scheme to me and supported me in its implementation. The second half of chapter three is solely my work. It has to be pointed out that I had many useful discussions with A. Helm and C. Sillett who, respectively, wrote and modified the file conversion script for macro-particle trajectories.

Several people contributed to Chapter 4. My supervisor, Prof. P. Norreys asked me to write a proposal for a wakefield experiment at the HERCULES laser facility. I was helped in this process through contributions from J. Holloway, R. Aboushelbaya, and Prof. P. Norreys who have been very supportive over the entire project with comments and guidance throughout the planning and subsequent data analysis. Prof. K. Krushelnick's team at the University of Michigan was involved in the planning of the experiment. I was the only person from Oxford allowed to travel to the US to conduct the experiment due to the travel restrictions associated with the COVID-19 pandemic but several people from the University of Michigan operated the laser and supported me in building the beam line and diagnostics and helped with setting up the data acquisition system. These were T. Campbell and Y. Ma who were Target Area Officers along with Q. Qian, J. Nees, A. Maksimchuk, A. Antoine, M. Balcazar, J. Cardarelli, R. Fitzgarrald, B. Hou, G. Kalinchenko, J. Latham, A. McKelvey, K. Krushelnick, and A. Thomas. I was involved in every aspect of the experiment other than the operation of the laser back-end. The simulations and data analysis were done by myself and R. Shalloo and A. Picksley contributed with helpful discussions about density measurements.

The experiments in Chapter 5 were done by myself. I provided the training data and framework for the machine learning algorithm and undertook the analysis of the data. Unless stated differently, the code was written by myself. I was inspired to use reinforcement learning by R. Aboushelbaya with whom I had many discussion about the feasibility of its implementation. The first prototype of the two-mirror set-up (with communication to the PC) was built in the lab by H. Davies. My work partially used his adaptation of the picomotor control code which he received from A. Alejo. S. Jordan wrote a function for simplified use of his rllib natural actor-critic code which I used for training. N. Bourgeois and the Central Laser Facility loaned the first components to realise the initial experimental tests.

The thesis was written by myself and all parts which are taken from somewhere else are indicated as such.

## 1.5 List of peer-reviewed publications

There are two articles in preparation for submission the results of which are presented in Chapter 4 and Chapter 5.

1. **MW Mayr**, B Spiers, R Aboushelbaya, RW Paddock, JD Sadler, C Sillett, K Krushelnick, PA Norreys. Nonlinear wakefields and electron injection in cluster plasma. Physical Review Accelerators and Beams. 23(9):093501, 2020

2. **MW Mayr**, L Ceurvorst, MF Kasim, JD Sadler, B Spiers, K Glize, AF Savin, N Bourgeois, F Keeble, AJ Ross, DR Symes, R Aboushelbaya, RA Fonseca, J Holloway, N Ratan, RMGM Trines, RHW Wang, R Bingham, LO Silva, PN Burrows, M Wing, PP Rajeev, PA Norreys. Wakefields in a cluster plasma. Physical Review Accelerators and Beams. 22(11):113501, 2019

3. RW Paddock, H Martin, RT Ruskov, RHH Scott, W Garbett, Brian Michael Haines, AB Zylstra, R Aboushelbaya, **MW Mayr**, BT Spiers, RHW Wang, PA Norreys. One-dimensional hydrodynamic simulations of low convergence ratio direct-drive inertial confinement fusion implosions. Philosophical Transactions of the Royal Society A. 379(2189):20200224, 2021

4. BT Spiers, MP Hill, C Brown, L Ceurvorst, N Ratan, AF Savin, P Allan, E Floyd, J Fyrth, L Hobbs, S James, J Luis, M Ramsay, N Sircombe, J Skidmore, R Aboushelbaya, **MW Mayr**, R Paddock, RHW Wang, PA Norreys. Whole-beam self-focusing in fusion-relevant plasma. Philosophical Transactions of the Royal Society A. 379(2189):20200159, 2021

5. R Aboushelbaya, K Glize, AF Savin, **MW Mayr**, B Spiers, R Wang, N Bourgeois, C Spindloe, R Bingham, PA Norreys. Measuring the orbital angular momentum of high-power laser pulses. Physics of Plasmas. 27(5):053107, 2020

6. R Aboushelbaya, K Glize, A F Savin, **MW Mayr**, B Spiers, R Wang, J Collier, M Marklund, RMGM Trines, R Bingham, PA Norreys. Physical Review Letters. 123(11):113604, 2019

7. JD Sadler, Y Lu, B Spiers, **MW Mayr**, A Savin, RHW Wang, R Aboushelbaya, K Glize, R Bingham, H Li, K Flippo, PA Norreys. Kinetic simulations of fusion ignition with hot-spot ablator mix. Physical Review E. 100(3):033206, 2019

8. Alex F Savin, Aimee J Ross, Ramy Aboushelbaya, **MW Mayr**, Ben Spiers, Robin H-W Wang, Peter A Norreys. Energy absorption in the laser-QED regime. Scientific Reports. 9(1):1-8, 2019

9. JD Sadler, LO Silva, RA Fonseca, K Glize, MF Kasim, A Savin, R Aboushelbaya, **MW Mayr**, B Spiers, RHW Wang, R Bingham, RMGM Trines, PA Norreys. Advantages to a diverging Raman amplifier. Communications Physics. 1(1):1-7, 2018

# Chapter 2

# Theoretical background of relevant topics

This chapter will review the theory of physical concepts necessary to describe the generation of laser-driven wakefields in plasma and the behaviour of accelerated electrons in such accelerators. First, I will discuss how electromagnetic waves propagate in vacuum and how single electrons interact with them. Next, I will introduce the fundamental properties of a plasma – the medium allowing for wakefield acceleration to exist – and its generation. Then, I will review how Gaussian laser pulses behave while propagating through a plasma and how they drive wakefields. After discussing different aspects of wakefield acceleration such as maximum energy gain and particle injection this chapter ends with a brief overview of relevant computational methods for studying laser-plasma interactions.

## 2.1 Electromagnetic wave propagation in vacuum

The propagation of electromagnetic waves and, therefore, photons can be described by Maxwell's equations. The set of (microscopic) Maxwell equations[1] in differential form consist of Gauss's law

$$\nabla \cdot \mathbf{E} = \frac{\rho}{\epsilon_0} \ , \tag{2.1}$$

Ampere's law

$$\frac{\partial \boldsymbol{E}}{\partial t} = c^2(\nabla \times \boldsymbol{B}) - \frac{\boldsymbol{j}}{\epsilon_0} \ , \tag{2.2}$$

Gauss's law for magnetism

$$\nabla \cdot \mathbf{B} = 0 \ , \tag{2.3}$$

[1] SI units are used throughout this chapter unless otherwise stated.

and Faraday's law

$$\frac{\partial \boldsymbol{B}}{\partial t} = -\nabla \times \boldsymbol{E} \ . \tag{2.4}$$

In vacuum, these equations can be solved (see Appendix A.1) by a vector potential

$$\mathbf{A}(\mathbf{z}, t) = \tilde{\mathbf{A}}(\mathbf{z}, t) \cos\left(\omega_0 t - \mathbf{k_z} \cdot \mathbf{z} + \phi_0\right) \ , \tag{2.5}$$

which describes a plane wave if $\tilde{A}(\mathbf{z}, t)$ is constant. Here, $\mathbf{z}$ is the spatial coordinate, $t$ is the time, $\tilde{A}$ is an envelope function, $\omega_0 = 2\pi c/\lambda_0$ is the angular frequency of the oscillation associated with the light's wavelength $\lambda_0$, $\mathbf{k_z}$ is the wave vector, and $\phi_0$ is a constant phase. The electric field can be expressed using potentials

$$\mathbf{E}(\mathbf{z}, t) \equiv -\frac{\partial \mathbf{A}(\mathbf{z}, t)}{\partial t} - \nabla\Phi = \tilde{\mathbf{E}}(\mathbf{z}, t) \sin\left(\omega_0 t - \mathbf{k_z} \cdot \mathbf{z} + \phi_0\right) \ , \tag{2.6}$$

where the tilde indicates an envelope function describing the pulse shape and where $\nabla\Phi = 0$ in vacuum. An analogous solution can be found for the magnetic field ($\mathbf{B} \equiv \nabla \times \mathbf{A}$). The cycle averaged intensity of the light propagating along $\mathbf{k_z}$ can be found from the energy flux density which is given by the Poynting vector $\mathbf{S} = (\mathbf{E} \times \mathbf{B})/\mu_0$ and the intensity is the cycle averaged Poynting vector which reads $I = \langle|\mathbf{E} \times \mathbf{B}|\rangle/\mu_0 = \epsilon_0 c E_0^2/2$.

### 2.1.1 Gaussian beam solution

By combining equations 2.2 and 2.4 in vacuo, one obtains two partial differential equations for the electric and the magnetic fields which read

$$\left(\frac{1}{c^2}\frac{\partial^2}{\partial t^2} - \nabla^2\right)\mathbf{E} = 0 \tag{2.7}$$

and

$$\left(\frac{1}{c^2}\frac{\partial^2}{\partial t^2} - \nabla^2\right)\mathbf{B} = 0 \ . \tag{2.8}$$

These equations are wave equations and are solved using an *ansatz* which is confined in all spatial directions. Both, $\mathbf{E}$ and $\mathbf{B}$ can be written as

$$u = \Psi(x, y, z) e^{-i(\omega t - k_0 z + \phi_0)} \ , \tag{2.9}$$

where $|k_0| = \omega/c$, $\Psi$ is an envelope function, $\phi_0$ is a phase term, and the propagation direction is assumed to be $\hat{z}$.

The paraxial wave approximation assumes that the complex envelope of a carrier wave changes its magnitude slowly with position (compared to the wavelength). One

form of expressing this condition is $|\partial^2\Psi/\partial z^2| \ll |k_0\partial\Psi/\partial z|$, where $k_0 = 2\pi/\lambda_0$. In the paraxial approximation, a Gaussian wave solution of form

$$\Psi(x,y,z) = \frac{w_0}{w(z)}\exp\left\{-(x^2+y^2)\left(\frac{1}{w(z)^2} - \frac{ik_0}{2R(z)}\right) - i\psi(z)\right\} \tag{2.10}$$

is found [66, 67] which satisfies the wave equations for $\mathbf{E}$ and $\mathbf{B}$. The right-hand side phase term in the exponent of equation 2.10 is called the Gouy phase shift originating from transverse spatial confinement [67, 68] and reads $\psi(z) = \arctan(z/z_R)$, where

$$z_R = \pi\frac{w_0^2}{\lambda_0} \tag{2.11}$$

is the Rayleigh length which gives the distance from the focal position at which the beam radius $w(z)$ has increased from it's focal spot value $w_0$ to $\sqrt{2}w_0$. $R(z) = z\left[1 + (z_R/z)^2\right]$ is the radius of wavefront curvature and $w(z) = w_0\sqrt{1+(z_R/z)^2}$ is the beam radius in the x-y-plane where the field strength drops to $1/e$ of its peak value. $\Psi(x,y,z)$ is the fundamental lowest order solution to the transverse electromagnetic modes (TEM) which describe field patterns in the plane perpendicular to the propagation direction of the electromagnetic radiation. Fig. 2.1 shows how the beam intensity evolves close to focus and shows how the values of spot size radius $w_0$ and full width at half-maximum FWHM are obtained.

### 2.1.2 Beam at focus

In order to achieve the high intensities necessary for several applications within the field of laser-plasma interaction, one has to focus the beam, typically using reflective optics (to avoid spherical aberrations and damage from energy deposition). This is often done using a parabolic mirror. The smallest possible focal spot area depends on the diffraction limited radius $w_0$ and reads $A = w_0^2\pi$. 90% of a perfect Gaussian beam's energy will flow through an area given by radius $r_{90} = 1.07w_0$.

However, in real laser experiments it is difficult to reach the minimum focal spot area due to imperfections of optical components in the laser chain that affect the laser beam properties. Various (monochromatic) wavefront aberrations can occur which diminish the spot size quality.

Optimal focusing of a beam using parabolic mirrors typically suffers from

1. Astigmatism: This is caused by collimated light incident at the wrong angle. The parabolic structure of the optic then causes a separation of the horizontal and vertical focal planes which results in an elliptical beam going through a

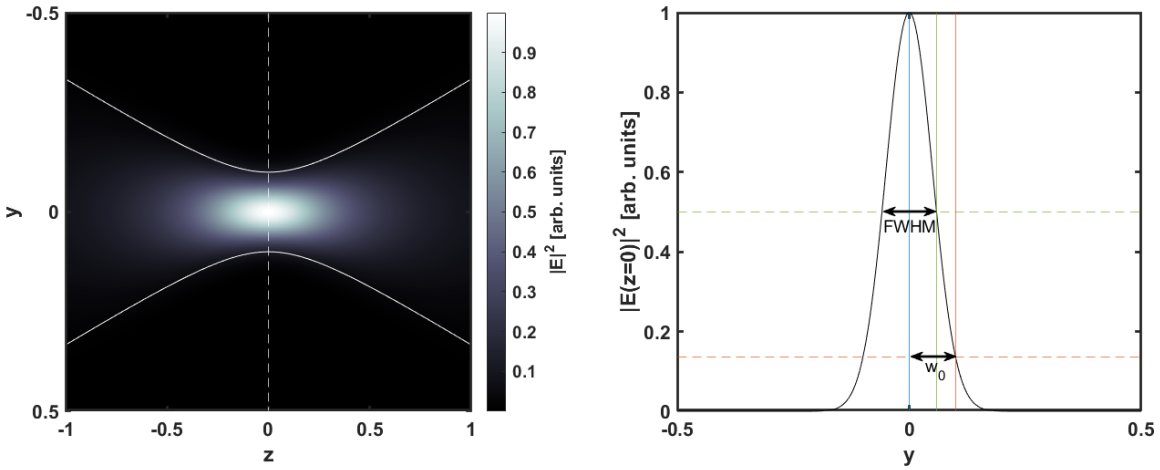



Figure 2.1: Intensity of Gaussian laser beam close to focus propagating along the z-axis (left) and perpendicular intensity profile at focus (right). The continuous white lines in the left panel give the position y(z) at which the intensity value falls to $I(y,z) = I(0,z)/e^2$ and therefore correspond to the z-evolution of the orange vertical line in the right panel. The dashed white line in the left panel shows the focal position at which the intensity slice in the right plot is taken (z=0). The full width at half-maximum (FWHM) of the intensity and $w_0$ are shown in the right panel.

"circle of least confusion" (which is still larger than the optimal focal spot) and then changing its orientation so that major and minor axes are exchanged. In an extreme case this produces two separated line foci perpendicular to another.

2. Coma: This also results from a non-optimal angle of incidence but is caused by a small displacement of the focal spot depending on the radial position on which the optic is hit. The effect is a comet-shaped focal spot.

Chapter 5 of this thesis explores to which extent a specific type of machine learning algorithm is able to maximise the spot size quality through control of the positioning of a motorised focusing optic, thus making experimental set up easier and countering unwanted shifts from optimal settings.

## 2.2 Single electron behaviour in electromagnetic fields

Electron behaviour in electromagnetic fields is governed by the relativistic equation of motion including the Lorentz force acting on the electron:

$$\frac{d\mathbf{p}}{dt} = \frac{d\gamma m_e \mathbf{v}}{dt} = -e(\mathbf{E} + \mathbf{v} \times \mathbf{B}) \tag{2.12}$$

where it is assumed that radiation emitted from the electron has negligible impact on its momentum $\mathbf{p}$. $\gamma = (1 - v^2/c^2)^{-1/2}$ is the relativistic Lorentz factor, $m_e$ is the electron mass and $\mathbf{v}$ is the velocity of the particle.

### 2.2.1 Nonrelativistic motion

Considering the case of small electromagnetic potential (non-relativistic electron motion; $\gamma \approx 1$) the magnetic field amplitude in a plane wave is $|\mathbf{B}| = |\mathbf{E}|/c$ which is why its impact on the electron can be neglected. This assumption simplifies equation 2.12 to

$$\frac{d(m_e\mathbf{v})}{dt} = -eE_0 \sin(\omega t - \mathbf{k}\cdot\mathbf{z})\hat{\mathbf{x}} \ , \tag{2.13}$$

where the electric field was assumed to be linearly polarised (in x-direction) and to propagate in the z-direction. Integrating and rearranging of equation 2.13 yields

$$\beta = \frac{\mathbf{v}}{c} = \frac{e}{m_e\omega_0 c}E_0 \cos(\omega_0 t - \mathbf{k}\cdot\mathbf{z})\hat{\mathbf{x}} \tag{2.14}$$

from which the maximum value for the normalised electron velocity can be found to be $\beta_{\max} = eE_0/m_e\omega_0 c \equiv a_0$. Here, $a_0$ is the dimensionless normalised laser amplitude and can be written in terms of the laser intensity as $a_0 \equiv 8.55\times10^{-10}(I\lambda^2[\mathrm{W\,cm^{-2}}\mu\mathrm{m}^2])^{1/2}$ ($I$ is the intensity in $\mathrm{W\,cm^{-2}}$ and $\lambda$ is the laser wavelength in µm). As can be seen from equation 2.14 the electron oscillates at the frequency of the electric field oscillation.

### 2.2.2 Relativistic treatment

The energy equation of the electron can be obtained when multiplying equation 2.12 with the electron momentum $\mathbf{p}$:

$$\mathbf{p}\cdot\frac{d\mathbf{p}}{dt} = -e\mathbf{p}\cdot\mathbf{E} \tag{2.15}$$

where the magnetic field term was omitted since the particle momentum has to be perpendicular to the cross product of the particle's velocity and the magnetic field. The temporal derivative of the kinetic energy can be obtained from taking the temporal derivative of the Lorentz factor (which are linked through $E_{\mathrm{kin}} = (\gamma - 1)m_e c^2$) giving

$$\frac{dE_{\mathrm{kin}}}{dt} = m_e c^2\frac{d\gamma}{dt} = m_e c^2\frac{d}{dt}\sqrt{1 + \frac{\mathbf{p}^2}{m_e^2 c^2}} = \frac{1}{\gamma m_e}\mathbf{p}\cdot\frac{d\mathbf{p}}{dt} = -e\mathbf{v}\cdot\mathbf{E} \tag{2.16}$$

where equation 2.15 was used in the last step.

For convenience, equations 2.12 and 2.16 can be written in index notation (in this section, I use the Einstein convention of summing over double indices):

$$\frac{dp_i}{dt} = -e(E_i + \varepsilon_{ijk} v_j B_k) \ , \tag{2.17}$$

$$\frac{dE_{\text{kin}}}{dt} = -e v_i E_i \ , \tag{2.18}$$

where $\varepsilon$ is the Levi-Civita symbol with values $\varepsilon_{ijk} \in \{-1, 0, +1\}$ depending on index order. In the absence of an electrostatic potential the electric and magnetic fields can be rewritten using the vector potential A as $E_i = -\partial_t A_i$ and $B_k = \varepsilon_{klm} \partial_l A_m$. Here, I used the convention that $\partial_\varrho$ is the partial derivative with respect to variable $\varrho$. Using the vector potential, equations 2.17 and 2.18 are

$$\frac{dp_i}{dt} = e(\partial_t A_i - \varepsilon_{ijk} v_j \varepsilon_{klm} \partial_l A_m) \ , \tag{2.19}$$

$$\frac{dE_{\text{kin}}}{dt} = e v_i \partial_t A_i \ . \tag{2.20}$$

The Kronecker symbol $\delta_{ij}$ which is 0 if $i \neq j$ or 1 if $i = j$ can be used to further simplify the equation of motion with the identity $\varepsilon_{ijk}\varepsilon_{klm} = \delta_{il}\delta_{jm} - \delta_{im}\delta_{jl}$:

$$\frac{dp_i}{dt} = e(\partial_t A_i - v_m \partial_i A_m + v_l \partial_l A_i) = e\left(\frac{dA_i}{dt} - v_m \partial_i A_m\right) \ . \tag{2.21}$$

In the last step I used the total derivative $dA_i/dt = \partial_t A_i + v_l \partial_l A_i$. The vector potential of the plane wave lies in the same plane as the electric field. This means that (since $\mathbf{E} = E_0 \sin(\omega t - k_z z)\hat{x}$) the term $v_m \partial_i A_m$ only has a component $v_x \partial_i A_0 \cos(\omega t - k_z z)$. In a plane wave $v_x$ and $A_x$ have no x or y-dependence. Writing the spatial components of equation 2.21 gives

$$\frac{dp_x}{dt} = e\frac{dA_x}{dt} \ , \tag{2.22}$$

$$\frac{dp_y}{dt} = 0 \ , \tag{2.23}$$

$$\frac{dp_z}{dt} = -e v_x \frac{\partial}{\partial z} A_x \ . \tag{2.24}$$

Integrating 2.22 with respect to time and setting the integration constant equal to zero as an initial condition yields

$$p_x = e A_x \ . \tag{2.25}$$

The value for the z-component of the electron momentum is found by verifying that $dp_z/dt = c^{-1} dE_{\text{kin}}/dt$, which when substituted using equations 2.20 and 2.24 reads

$-ev_x\partial_z A_x = ev_x\partial_t A_x/c$. The last statement is true for any $A_x \propto \cos(\omega t - k_z z) = \cos(\omega t - (\omega/c)z)$ where the expression for the phase velocity of light propagating along the z-direction in vacuum $c = \omega/k_z$ has been used. Again, integration with respect to time gives

$$p_z - \frac{E_{\text{kin}}}{c} + K = 0 \tag{2.26}$$

with an integration constant $K$. Setting the initial condition ($t = 0$) for the longitudinal momentum to $p_z = 0$ yields $K = 0$ since $\gamma(p_x = 0) = 1$. Therefore,

$$p_z = (\gamma - 1)mc \ . \tag{2.27}$$

In terms of the laser vector potential $\mathbf{A}$, $p_z$ can be expressed after arranging and squaring equation 2.26 which gives

$$\begin{aligned} p_z^2 &= ([\gamma - 1]mc)^2 \\ p_z^2 + 2p_z mc + m^2c^2 &= \gamma^2 m^2 c^2 \\ p_z &= \frac{p_x^2}{2mc} \\ p_z &= \frac{(eA_x)^2}{2mc} \ . \end{aligned} \tag{2.28}$$

In the third line of equation 2.28 $\gamma^2$ was replaced by squaring the identity $\gamma \equiv (1 - \beta^2)^{-1/2}$ which gives $\gamma^2 = (1 - \beta^2)^{-1} = 1 + \gamma^2 v^2 c^{-2} = 1 + \mathbf{p}^2 (mc)^{-2}$.

Therefore, the electron motion for a linearly polarised plane laser wave is described by

$$p_x = eA_x = amc \ , \tag{2.29}$$

$$p_y = 0, \tag{2.30}$$

$$p_z = \frac{e^2 A_x^2}{2mc} = \frac{1}{2} a^2 mc \ , \tag{2.31}$$

where I used the identity $a \equiv eA/(mc)$ and the initial condition $p_{y,0} = 0$.

A co-moving frame of reference ($t = \tau - z(t)/c$) allows for convenient integration. Using $d/d\tau = \gamma(d/dt)$ gives

$$\frac{dx}{d\tau} = ac \ , \tag{2.32}$$

$$\frac{dy}{d\tau} = 0 \ , \tag{2.33}$$

$$\frac{dz}{d\tau} = \frac{a^2}{2} c \ , \tag{2.34}$$

which, acknowledging that $\omega t - k_z z = \omega t - (\omega/c)z = \omega\tau + \omega z/c - (\omega/c)z = \omega\tau$ and $a(\tau) = a_0 \cos(\omega\tau)$, is integrated to give

$$x(\tau) = \int a(\tau) c \, d\tau = \frac{a_0 c}{\omega} \sin(\omega\tau) + x_0 \tag{2.35}$$

$$y(\tau) = \int d\tau = y_0 \ , \tag{2.36}$$

$$z(\tau) = \int \frac{1}{2} a^2(\tau) c d\tau = \frac{a_0^2 c}{2} \left( \frac{2\omega\tau + \sin(2\omega\tau)}{4\omega} \right) \ . \tag{2.37}$$

This shows that the electron will oscillate in the polarisation direction and will have a constant drift in the longitudinal (z) direction overlaid with a second harmonic oscillatory motion. After re-substitution of $\tau = t + z/c$, the time-averaged drift is

$$\bar{v}_z = \frac{c a_0^2}{a_0^2 + 4} \ . \tag{2.38}$$

If the laser is pulsed the longitudinal position of the electron will have changed after the interaction due to the drift motion [69]. The energy gained by the electron will again be lost to the electromagnetic field such that there is no net gain in energy. Here, the assumptions of the Lawson-Woodward theorem [70–72] are met. These are an infinite interaction region, vacuum without boundaries, relativistic particle motion, absence of static EM fields, and disregarding non-linear effects [73]. In order to accelerate charged particles to relativistic energies using laser pulses, the theorem has to be violated which is indeed the case in LWFA for all criteria.

## 2.3 Ponderomotive force

Due to the finite extent of ultrashort laser pulses both radially and longitudinally a non-linear force arises from the interaction with an electron. Qualitatively, due to the (typically) Gaussian field strength distribution the electron's quiver motion will push the electron into regions of different (time averaged) field strength. This means that the electron experiences different field strengths, for example, at each turning point in its oscillatory motion (of course, this argument can be applied to infinitesimal increments in time).

To illustrate a quantitative approach, I consider the case in which the magnetic field's impact on electron motion is, again, negligible. The motion in the polarisation direction $\hat{x}$ is then split into components arising from the oscillatory motion $v_{\mathrm{osc}}$ and

from drift motion $v_\mathrm{d}$. Therefore, the (non-relativistic) equation of motion is written as

$$m\frac{d}{dt}(\mathbf{v}_\mathrm{osc}+\mathbf{v}_\mathrm{d}) = -eE(x)\sin(\omega t - k_z z)\ . \tag{2.39}$$

As shown in [74], the drift motion is assumed to be small in lowest order which results in a dominating oscillatory motion with velocity

$$v_\mathrm{osc} = \frac{eE(x)\cos(\omega t - k_z z)}{m\omega}\ . \tag{2.40}$$

The impact of the drift motion becomes more relevant when looking at the next order where the temporal average $\langle\rangle_t$ is taken:

$$\begin{aligned}
m\left\langle\left(\frac{\partial}{\partial t}+\mathbf{v}\cdot\nabla\right)(\mathbf{v}_\mathrm{osc}+\mathbf{v}_\mathrm{d})\right\rangle_t &= -e\langle E(x)\rangle_t \\
m\frac{\partial\langle\mathbf{v}_\mathrm{osc}+\mathbf{v}_\mathrm{d}\rangle_t}{\partial t} &= -e\langle E(x)\rangle_t - m\langle([\mathbf{v}_\mathrm{osc}+\mathbf{v}_\mathrm{d}]\cdot\nabla)(\mathbf{v}_\mathrm{osc}+\mathbf{v}_\mathrm{d})\rangle_t \\
m\frac{\partial\mathbf{v}_\mathrm{d}}{\partial t} &= -e\langle E(x)\rangle_t - m\langle(\mathbf{v}_\mathrm{osc}\cdot\nabla)\mathbf{v}_\mathrm{osc}\rangle_t \\
m\frac{\partial\mathbf{v}_\mathrm{d}}{\partial t} &= -e\langle E(x)\rangle_t - \frac{e^2}{4m\omega^2}\nabla E^2(x)
\end{aligned} \tag{2.41}$$

The oscillatory velocity $v_\mathrm{osc}$ in the third line of equation 2.41 was replaced with the result of equation 2.40. The second term on the right-hand side of equation 2.41 is called the ponderomotive force, which acts in the opposite direction as the gradient of the square of the electric field. For non-relativistic amplitudes and a Gaussian pulse shape, it can be written in terms of the normalised laser potential as

$$\mathbf{F}_p = -\frac{m_e c^2}{2}\nabla a^2\ . \tag{2.42}$$

The result is that electrons are pushed out of regions of high intensity (the same holds for positively charged ions even though the effect is smaller due to their larger mass).

For relativistic amplitudes, a more involved derivation is necessary (see [73]) in which the force is expressed using $\gamma = (1+\mathbf{p}^2/(m_e c)^2)^{1/2}$ as

$$\mathbf{F}_p = -mc^2\nabla\gamma\ . \tag{2.43}$$

## 2.4 Plasma

A plasma is a medium consisting of partially or fully ionised atoms (how these atoms are ionised by a laser pulse will be discussed in Section 2.4.3). The plasma's charged constituents interact with each other through electric and magnetic forces and exhibit collective behaviour (external fields impact plasma on a large scale as individual particles behave similarly). However, a plasma is quasi-neutral meaning that even though there can be microscopic areas of high charge the resulting fields will be shielded by mobile plasma constituents on a characteristic length scale much smaller than the plasma dimension. The wakefield acceleration mechanisms described in this and the following chapters rely on the fact that plasmas can sustain large electric fields.

### 2.4.1 Debye length

A test charge can be placed in a neutral plasma which leads to a rearrangement of particle locations. The Poisson equation

$$\nabla \cdot \mathbf{E} = -\nabla^2 \Phi = \frac{\rho}{\epsilon_0} = \frac{q(n_i + n_e)}{\epsilon_0} = \frac{e(Zn_i - n_e)}{\epsilon_0} \tag{2.44}$$

links the electric potential $\Phi$ to the charge density $\rho$. The Coulomb potential of a test charge is $\Phi(q_t, \mathbf{r}) = q_t/(4\pi\epsilon_0|\mathbf{r}|)$ where $q_t$ is the magnitude of the electric test charge and $\mathbf{r}$ is the distance from the charge. Following Kruer [74] the electron number density follows the Boltzmann relation

$$n(\mathbf{r}) = n_\infty \exp\left\{-\frac{q\Phi(q_t, \mathbf{r})}{k_B T}\right\} \tag{2.45}$$

with $n_\infty$ being the unperturbed number density. The term $k_B T$ gives the thermal energy of the species where $k_B = 1.38 \times 10^{-23}\,\mathrm{m^2\,kg\,s^{-2}\,K^{-1}}$ is the Boltzmann constant and $T$ is the temperature. The mean kinetic energy of a particle species with Maxwell-Boltzmann velocity distribution $f_v$ is [75]

$$\bar{E}_k = \frac{1}{2} m \frac{\iiint (\mathbf{v} \cdot \mathbf{v}) f_v d^3 v}{\iiint f_v d^3 v} = \frac{3}{2} k_B T \ . \tag{2.46}$$

In the case of electrons, the energy of 1 eV corresponds to a temperature of $T_e \approx 11\,600\,\mathrm{K}$.

The density distribution can be used in equation 2.44 to substitute $n_i$ and $n_e$:

$$\begin{aligned} -\nabla^2 \Phi &= \frac{e n_\infty}{\epsilon_0} \left( Z \exp\left\{\frac{-e\Phi}{k_B T_i}\right\} - \exp\left\{\frac{e\Phi}{k_B T_e}\right\} \right) \\ &\simeq \frac{e n_\infty}{\epsilon_0} \left( Z \left\{1 - \frac{e\Phi}{k_B T_i} + \dots\right\} - \left\{1 + \frac{e\Phi}{k_B T_e} + \dots\right\} \right) \ , \end{aligned} \tag{2.47}$$

where the Taylor expansion used to simplify the exponential function is valid in a region not too close to the test charge. For an isothermic ($T_i = T_e$) hydrogen plasma ($Z = 1$) the equation simplifies to

$$\nabla^2\Phi \simeq \frac{2n_\infty e^2}{\epsilon_0 k_B T_e}\Phi \equiv \frac{2}{\lambda_D^2}\Phi \ . \tag{2.48}$$

The Debye length $\lambda_D = \sqrt{\epsilon_0 k_B T/(n_0 e^2)}$ corresponds to the distance over which a test charge is shielded through the rearrangement of local density distributions. A solution for the potential is

$$\Phi = \Phi_0 \exp\left\{-\frac{\sqrt{2}|r|}{\lambda_D}\right\} \tag{2.49}$$

with $\Phi_0 = Q/(4\pi\epsilon_0 r)$. If the plasma density is high, charges are shielded more strongly whereas if the plasma's thermal energy is high (corresponding to increased particle velocity) charges are shielded more weakly. This concept of a Debye length is only valid for a sufficient number density. This leads to a condition defining whether the material probed is indeed a plasma:

$$\frac{4}{3}\pi\lambda_D^3 n = N_D \gg 1 \ . \tag{2.50}$$

$N_D$ gives the number of particles in a sphere of radius $\lambda_D$.

Plasma currents cause long-range forces which can be described using a magneto-hydrodynamic "fluid" approach. All particle behaviour on scales smaller than the Debye length cannot be described through this approximation.

### 2.4.2 Plasma oscillation

Due to the Coulomb forces between charged particles in a plasma, oscillations occur when restoring forces act on electrons that have been displaced to cause any deviation from uniform charge density. The waves caused by this oscillation are called Langmuir waves and have a temperature-dependent dispersion relation. In a cold plasma without external fields and assuming that the ions are immobile on the timescales of electron oscillation due to their comparatively large mass, the frequency of the electron oscillations (plasma frequency) can be derived from the (one-dimensional) equation of motion

$$m_e\left(\frac{\partial v_x}{\partial t} + v_x\frac{\partial v_x}{\partial x}\right) = -eE(x) \ , \tag{2.51}$$

continuity equation

$$\frac{\partial n_e}{\partial t} = -\frac{\partial}{\partial x}(n_e v_x) \ , \tag{2.52}$$

and Poisson equation

$$\frac{\partial E}{\partial x} = \frac{e(n_i - n_e)}{\epsilon_0} \ . \tag{2.53}$$

Combining equations 2.51, 2.52, and 2.53, expanding the electron variables into terms of different order (i.e. $n_e = n_{e,0} + n_{e,1} + \dots$), neglecting products of higher-order terms which imposes the condition of small perturbations, and taking a plane wave *ansatz* for these perturbations results in a oscillation frequency of

$$\omega_p = \sqrt{\frac{n_{e,0}e^2}{\epsilon_0 m_e}} \tag{2.54}$$

which is called the plasma frequency. The derivation is shown in Appendix A.2.

When considering a plasma with $T_e \neq 0$ a kinetic pressure term (as opposed to magnetic pressure in magnetised plasmas) has to be added to the equation of motion. From the equation of state $pn^{-\gamma} = K = \text{const.}$, where $\gamma = C_p/C_v$ is the ratio of specific heats (at constant pressure $p$ and constant volume $v$, respectively), one obtains a relation between the pressure and density gradients

$$\frac{\nabla p}{p} = \frac{K\gamma n^{\gamma-1}\nabla \mathbf{n}}{p} = \gamma \frac{\nabla n}{n} \ . \tag{2.55}$$

For adiabatic compression, $\gamma$ is written in terms of the degrees of freedom $\gamma = (f + 2)/f$ and equals three in one dimension. Adding the (force density) pressure term $\nabla p = 3k_B T_e \nabla \mathbf{n}$ to the equation of motion then changes the dispersion relation to

$$\omega^2 = \omega_p^2 + \frac{3k_B T_e}{m_e}k^2 = \omega_p^2 + \frac{3}{2}k^2 v_{th}^2 \ , \tag{2.56}$$

which is called the Bohm-Gross dispersion relation. The thermal velocity is defined as $v_{\text{th}} = \sqrt{(2k_B T)/m_e}$. The associated group and phase velocities are

$$v_{\text{gr}} = \frac{\partial \omega}{\partial k} = \frac{3k}{2\omega} v_{\text{th}}^2 \ , \tag{2.57}$$

$$v_{\text{ph}} = \frac{\omega}{k} = \frac{3}{2} v_{\text{th}} \ . \tag{2.58}$$

Ion modes can also exist in a plasma with the ion acoustic wave dispersion relation being

$$\frac{\omega}{k} = \sqrt{\frac{(k_B T_e + \gamma_i k_B T_i)}{m_i}} \ . \tag{2.59}$$

These modes are less relevant for the work presented in this thesis due to the short time-scales associated with the processes studied and the comparably slow ion motion.

### 2.4.3 Ionisation

Ionisation is the process of removing electrons from the electric potential of the atomic nucleus. Therefore, in order to understand how a plasma is formed from the interaction of a laser pulse with atoms, it is important to understand how the ionisation process works.

There are different mechanisms by which a laser pulse can ionise atoms depending on the intensity and wavelength of the pulse. For single photons, the angular frequency $\omega$ (which is directly related to the energy $E = \hbar\omega = h\omega/(2\pi)$, where $h$ is Planck's constant) has to be high enough to overcome an electron's binding energy for it to be removed (photoelectric effect). At a wavelength of $\lambda = 800\,\mathrm{nm}$, the photon energy is $E \simeq 1.6\,\mathrm{eV}$. The binding energy depends on the size and composition of the atomic nucleus (element) and the associated electron configuration (including current ionisation state and number of electron shells). For the simplest case of a hydrogen atom in its ground state, the ionisation energy is $E_{ion} \simeq 13.6\,\mathrm{eV}$. Hence, if the photon's frequency is insufficient, multiple photons are needed to ionise an atom. This process, which can be described using a perturbation theory approach [76], is called multi-photon ionisation (MPI) or above-threshold ionisation (ATI) if the electron has excess kinetic energy after it is released from the atom's electric potential. This process increases in likelihood with increasing intensity $I$ as $P \sim I^n$, where $n$ is the number of photons which are needed to ionise the electron. Experimentally, this has been verified at intensity values of $I \sim 1 \times 10^{11}\,\mathrm{W\,cm^{-2}}$ using Xenon atoms [77]. ATI was first observed at intensities around $I \geq 8 \times 10^{12}\,\mathrm{W\,cm^{-2}}$ [78].

If the Keldysh parameter

$$\gamma = \sqrt{\frac{E_{ion}}{2\Phi_{pond}}} \tag{2.60}$$

is much larger than one, MPI and ATI dominate the ionisation process. Here, $E_{ion}$ is the ionisation potential for the respective electron and $\Phi_{pond} \simeq (eE_L)^2/(4m\omega_0^2)$ is the ponderomotive potential of the laser pulse.

When the laser electric field increases and becomes comparable to the field associated with the Coulomb potential, the Keldysh parameter approaches one. If $\gamma \ll 1$, a process called tunneling ionisation becomes more important than MPI[2]. Here, the atomic potential

$$V(\mathbf{x}) = -\frac{Ze^2}{4\pi\epsilon_0|x|} - e\mathbf{x}\mathbf{E} \tag{2.61}$$

[2]A sharp transition between these mechanisms is not given by the Keldysh parameter as the ionisation process depends on other parameters such as the pulse length or polarisation, too [79].

is modified by the laser pulse's electric field **E** to such a great extent that the electron can tunnel through the barrier. The electric field is taken to be constant over the relevant distance.

The task of numerically computing the time-dependent Schrödinger equation

$$i\hbar\frac{\partial\Psi(\mathbf{x},t)}{\partial t} = H\Psi(\mathbf{x},t) \ , \tag{2.62}$$

where $H$ is the Hamiltonian including the interaction between the field and atom and $\Psi$ is the wave function, to get the ionisation probability, is complex and depends on the assumptions made about the physical system. The tunneling probability can be found from the (quasi-static) ADK model (named after Ammosov, Delone, and Krainov)—even for nontrivial atoms [80]. Here, the laser contribution to the potential is taken to be linear because it is assumed that the laser wavelength is much larger than the dimensions of the atom which results in small deviations from the local electric laser field at any given time. To include both MPI and tunneling ionisation rates, one can resort to the YI model (named after Yudin and Ivanov) [81] the necessity for which depending on the intensity and wavelength of the laser used (typically, when $\gamma \sim 1$).

For very high laser intensities such as those used throughout this thesis ($I \sim 1 \times 10^{18}\,\mathrm{W\,cm^{-2}}$) and a typical wavelength of 800 nm (Ti:Sapphire laser) Barrier Suppression Ionisation (BSI), where the potential is modified so strongly that the electron does not have to tunnel to escape the potential, becomes dominant. The modification of the potential in Eq. 2.61 through an external electric field is shown in Fig. 2.2. The stronger the electric field, the stronger the modification of the potential energy leading to higher ionisation probability. Even before the laser reaches its peak intensity many gases will be fully ionised, depending on their respective $Z$ number. Good agreements have been found between experiments and a simple BSI model for a range of atoms [79]. The intensity for ionising the $Z$ state was approximated [79] to be

$$I_{BSI}(\mathrm{W\,cm^{-2}}) = 4.00 \times 10^{9} \left[\frac{E_{ion}^{4}(\mathrm{eV})}{Z^{2}}\right] \ , \tag{2.63}$$

which for atomic hydrogen is $I_{BSI} \sim 1 \times 10^{14}\,\mathrm{W\,cm^{-2}}$ – orders of magnitude lower than the peak intensities used in this thesis. Similar to the tunnel ionisation mechanism, the polarisation of the laser pulse plays an important role in BSI as for linear polarisation the ionised electron's oscillatory motion depends on the point at which it has been ionised while for circular polarisation the amplitude of the electric field is constant during the ionisation process. Therefore, electrons ionised in a circularly polarised laser pulse are more likely to be detected at higher kinetic energies [82].

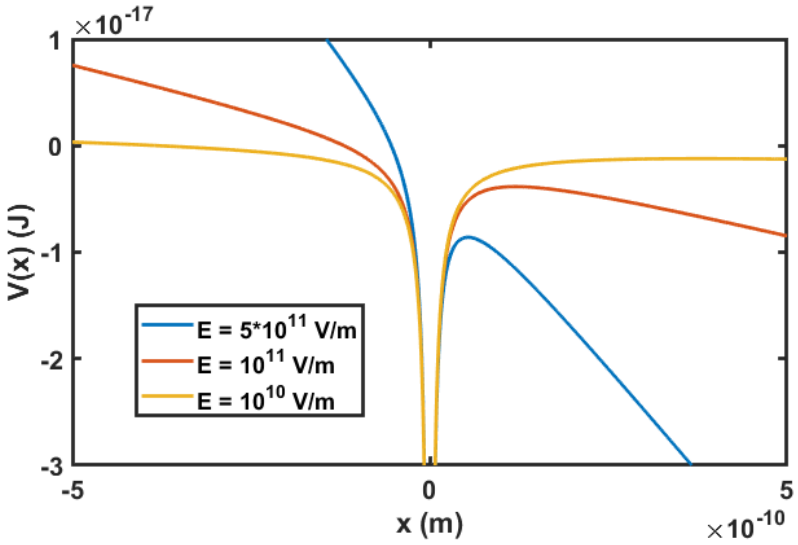



Figure 2.2: The electron binding potential (as a function of space $x$) is modified by a constant electric field $E$. Shown is the impact of three different field strengths.

### 2.4.4 Dispersion relation of light in plasma

In order to describe how light propagates in a plasma one has to find the dispersion relation from which the phase and group velocities can be obtained. Combining Ampere's law and Faraday's law gives

$$-\nabla\times(\nabla\times\mathbf{E}) = -\nabla(\nabla\cdot\mathbf{E}) + \nabla^2\mathbf{E} = \frac{1}{c^2}\left(\frac{1}{\epsilon_0}\frac{\partial\mathbf{j}}{\partial t} + \frac{\partial^2\mathbf{E}}{\partial t^2}\right) \ . \tag{2.64}$$

Here, $\mathbf{j} = -en_e\mathbf{v}$. Using, again, a plane wave *ansatz* $\mathbf{E} = E_0\exp\{i(\mathbf{k_0}\mathbf{z} - \omega_0 t)\}$ and the transversality condition for vectors $\mathbf{k_0}\cdot\mathbf{E} = 0$, equation 2.64 simplifies to

$$-k_0^2\mathbf{E} = \frac{1}{c^2}\left(-\frac{en_e}{\epsilon_0}\frac{\partial\mathbf{v}}{\partial t} - \omega_0^2\mathbf{E}\right) \ . \tag{2.65}$$

The electron velocity can be found by integrating the linearised equation of motion to give $\mathbf{v} = e\mathbf{E}/(im_e\omega_0)$. This result is then used to give the dispersion relation

$$\omega_0^2 = k_0^2c^2 + \omega_p^2 \ , \tag{2.66}$$

which shows that light of frequency $\omega_0 < \omega_p$ cannot propagate in plasma as there would not exist a real solution for the wave vector. Whenever this condition is fulfilled, plasma is referred to as over-dense. Otherwise, it is referred to as under-dense. In other words, for light to be able to propagate in a plasma, the electron density has to be lower than the critical density $n_{cr} = \omega_0^2 m_e\epsilon_0/e^2$.

The phase velocity is

$$v_{ph} = \frac{\omega_0}{k_0} = \sqrt{c^2 + \frac{\omega_p^2}{k_0^2}} = \sqrt{c^2 + \frac{\omega_p^2 c^2}{\omega_0^2 - \omega_p^2}} = \frac{c}{\sqrt{1 - \omega_p^2/\omega_0^2}} \ . \tag{2.67}$$

The group velocity is

$$v_{gr} = \frac{d\omega_0}{dk_0} = \frac{1}{2} \frac{2k_0 c^2}{\sqrt{k_0^2 c^2 + \omega_p^2}} = \frac{k_0 c^2}{\omega_0} = \frac{c^2}{v_{ph}} \ . \tag{2.68}$$

Both group velocity and phase velocity are important concepts when dealing with laser-driven wakefield acceleration and will be used in the following chapters.

### 2.4.5 Plasma optics

A high-intensity laser pulse propagating through plasma will modify the refractive index of the medium itself. This induces a feedback loop in which the laser pulse is modified leading to effects such as self-focusing or pulse compression.

#### 2.4.5.1 Self-focusing

There are two physical processes that can cause a laser pulse to be self-focused within an underdense plasma. These are related to a radial change of the refractive index due to

1. a density inhomogeneity caused by the radial change in ponderomotive force acting on the electrons,

2. the intensity-dependent relativistic mass increase of electrons.

Under the assumption that the ionisation rate is constant over the region in which a Gaussian laser pulse's intensity has a large gradient (region relevant in wakefield acceleration where $r \sim w_0$), the refractive index in plasma is

$$\eta(r) = \sqrt{1 - \frac{n(r)}{n_{cr}}} = \sqrt{1 - \frac{\omega_p(r)^2}{\omega_0^2}} \ . \tag{2.69}$$

In case 1 the electron density increases with radial position (and with decreasing ponderomotive potential) which results in a decreasing refractive index. In case 2 the increase in plasma frequency with decreasing laser intensity (and, therefore, decreasing average Lorentz factor $\langle\gamma\rangle = 1 + a^2/4$ of electrons in a sinusoidal field)

$$\omega_p = \sqrt{\frac{n_e e^2}{\langle\gamma\rangle m_e \epsilon_0}} = \frac{\omega_p'}{\sqrt{\langle\gamma\rangle}} = \frac{\omega_p'}{\sqrt{1 + \frac{a^2}{4}}} \tag{2.70}$$

causes a decrease of the refractive index at large radii. Here, $\omega_p'$ is the non-relativistic plasma frequency. Hence, for both cases $d\eta/dr < 0$ holds. The focusing effect can be illustrated when looking at the dependence of the wavefront curvature on $d\eta/dr$. The local phase velocity at each radial position is obtained using equations 2.69 and 2.70. It is given by

$$v_{ph} = \frac{c}{\eta} = \frac{c}{\sqrt{1 - \frac{\omega_p'^2}{(1+\frac{a^2}{4})\omega_0^2}}} \ . \tag{2.71}$$

If the effect of focusing due to the radial change in the refractive index of the plasma is larger than the diffraction of the beam, the term self-focusing is used. It was found [83] that for a Gaussian laser beam this effect occurs at a power threshold of

$$P_c \simeq 17.4 \frac{n_{cr}}{n_e} [\mathrm{GW}] \ . \tag{2.72}$$

Self-focusing was experimentally observed for a 400 fs pulse (3 J) in the self-modulated regime [84] and a 50 fs pulse (700 mJ) [85], both experiments showing that it is possible to drive wakefields over several Rayleigh lengths. The former experiment showed at a maximum electron density of $3.6 \times 10^{19}\,\mathrm{cm}^{-3}$ how the intensity increases when the beam is refocused and guided for various power values larger than the critical power. The latter experiment showed differences in self-focusing (via electron generation) at electron densities between $1 \times 10^{18}\,\mathrm{cm}^{-3}$ and $3 \times 10^{19}\,\mathrm{cm}^{-3}$ using two different focal lengths (f/3 and f/12 leading to $a_0$ between 1 and 5) to focus the laser pulse. This showed that for self-focusing to occur, the vacuum focal spot size needs to be larger than the plasma wavelength $w_0 > \lambda_p$.

#### 2.4.5.2 Pulse compression

The ponderomotive force also acts on the longitudinal electron density profile causing an electron bunching in front of the short ($c\tau < \lambda_p$) laser pulse's peak and a decrease of electron density towards to back of the laser pulse. This density gradient (or gradient in refractive index) co-propagates with the laser pulse causing variations in local group velocity. The effect that can be observed is spectral broadening (and temporal pulse compression). A red-shift is caused at the front of the laser pulse and a blue-shift at the back. A theoretical analysis of the process can be found in [86]. The compression of a 38 fs pulse by a factor of three was observed in experiment and simulations in [87]. The experiment used electron densities between $n_e = 5 \times 10^{18}\,\mathrm{cm}^{-3}$ and $1 \times 10^{19}\,\mathrm{cm}^{-3}$ and a laser amplitude of $a_0 = 1.26$. The pulse shortening was measured using an intensity autocorrelation method as well as inferred through the spectral

broadening of the pulse using a spectrometer. Particle-in-cell simulations confirm the pulse shortening and spectral broadening through time-dependent spectral analysis which shows both a blueshift (frequency increase) and redshift (frequency decrease) on the opposite ends of the laser pulse caused by the propagation in a non-uniform electron density profile.

## 2.5 Laser-wakefield acceleration

A laser pulse propagating through an underdense plasma causes a longitudinal electron wave due to the ponderomotive force associated with the pulse's field gradient (see equation 2.42). Electrons are pushed towards regions of lower intensity while ions are not affected as strongly due to their comparably large mass. This charge separation causes a restoring Coulomb force which pulls the electrons back towards the region of low electron density. Due to the momentum gained, electrons overshoot their original position setting up an oscillation. This oscillatory motion is governed by the plasma frequency $\omega_p$ and has a wavelength $\lambda_p = 2\pi c/\omega_p$ (valid in the case of linear density perturbation driven by laser amplitudes $a_0 < 1$). If the laser pulse's duration is $d \simeq \omega_p^{-1}$ the ponderomotive push is resonant with the electron oscillation reinforcing the effect. The electric field set up in the longitudinal electron plasma wave is called a wakefield and propagates at the laser group velocity $v_g$.

### 2.5.1 Wakefield regimes

Depending on the magnitude of the laser intensity, one can distinguish between different regimes in which the plasma responses to the driver of the wakefield and the acceleration properties differ. A detailed derivation of the equations involved will be given in Section 3.1.3 and Appendix A.6 but for the benefit of the reader I want to give a short overview here.

I have shown in Section 2.4.2 that a plasma oscillation can be derived from the fluid equations including the Poisson equation, the continuity equation, and the equation of motion which give a relation between the electrostatic potential, electric field, electron density and its evolution given a current and a driving force.

If a laser pulse (of arbitrary field strength) is present, it drives a plasma perturbation and an equation is found for the one-dimensional description of the problem [69, 73]. This equation relates the electrostatic potential to the laser vector potential. In the case in which the the Lorentz factor of the wake's phase velocity satisfies

| | Mangles *et al.* [26] | Geddes *et al.* [27] | Faure *et al.* [28] |
|---|---|---|---|
| $n_e(\mathrm{cm}^{-3})$ | $2 \times 10^{19}$ | $2 \times 10^{19}$ | $6 \times 10^{18}$ |
| $d(\mathrm{fs})$ | 40 | 55 | 33 |
| $I_{peak}(\mathrm{W\,cm}^{-2})$ | $3 \times 10^{18}$ | $7 \times 10^{18}$ | $3 \times 10^{18}$ |
| $E_{peak}(\mathrm{MeV})$ | $\sim 70(\pm 3\%)$ | $\sim 170(\pm 24\%)$ | $\sim 86(\pm 2\%)$ |

Table 2.1: Parameters from independent experiments showing quasi-monoenergetic electron beams. $n_e$ is the plasma electron density, $d$ is the pulse duration, $I_{peak}$ is the peak laser pulse intensity, and $E_{peak}$ is the electron beam's peak energy with the energy spread shown in brackets.

$\gamma_p \gg 1$ this equation is given by [88]

$$k_p^{-2}\frac{\partial^2\Phi}{\partial\xi^2} = \frac{1+a^2}{2(1+\Phi)^2} - \frac{1}{2}\,. \tag{2.73}$$

Here, $k_p$ is the plasma wave vector, $\Phi$ is the electrostatic potential, $\xi = x - v_g t$ is the spatial coordinate of a co-moving frame, and $a = eE/m_e\omega c$ is the normalised laser potential. The equation has used the quasi-static approximation which says that the temporal derivative in the co-moving frame applied to quantities such as $\Phi$ is negligible ($\partial\tau(\cdot) = 0$, where $\tau = t$).

In the limit of small perturbations for $\Phi$, equation 2.73 becomes $\left(\partial_\xi^2 + k_p^2\right)\Phi = k_p^2 a^2/2$ which is the equation of a driven oscillator. The solution for $\Phi$ is $\propto \sin k_p\xi$ and holds for cases of small laser amplitude $a_0 \ll 1$.

When the laser amplitude is increased, the approximation made is no longer valid and a solution can be found numerically for arbitrary pulse shapes. In this non-linear regime the density is spiked rather than sinusoidal and the electric field becomes sawtooth shaped.

The "blowout" or "bubble" regime[3] is a three-dimensional manifestation of the non-linear regime at highly relativistic laser amplitudes and ultrashort durations ($d_{\mathrm{FWHM}} < \lambda_p/(2c)$). It is named after the feature that the wakefield behind the laser pulse is shaped like a bubble caused by the complete expulsion of electrons to form a symmetric cavity. It was experimentally exploited to generate the first quasi-monoenergetic electron beams from LWFA in independent experiments [26–28] whose parameters are given in the table below (Tab. 2.1). Note, that higher energies were achieved in [27] due to a preformed plasma channel which guided the driving laser pulse rather than utilising self-focusing. This regime has also been theoretically studied in [22–25] showing how the bubble is formed and how it evolves, as well as

[3]Most authors use these terms interchangeably when a distinct spherical electron cavity is formed in the plasma.

how electrons can be trapped and accelerated to form monoenergetic beams within it. A phenomenological characterisation of physical parameters such as wake amplitude, laser depletion length, and beam loading was derived in [89]. It was shown that for $a_0 \geq 2$ and pulse lengths $d < w_0/c \simeq 2\sqrt{a_0}/\omega_p$, the laser spot-size $w_0$, bubble radius $R$, and normalised laser amplitude $a_0$ are related through $k_p R \simeq k_p w_0 = 2\sqrt{a_0}$.

In this thesis, different regimes are probed with laser amplitudes reaching from as low as $a_0 = 0.63$ up to fully relativistic levels of $a_0 = 5.0$.

### 2.5.2 Wave breaking

The maximum sustainable field amplitude in the plasma is given by the limit at which the fluid approximations break down (electron trajectories cross leading to loss of wave coherence). The fluid electrons reach the phase velocity of the wave causing a density singularity (and eventually trapping of electrons in the wake as will be discussed below). The cold, non-relativistic wave breaking field is $E_{wb} = m_e c\omega_p/e$ which can be obtained from the Poisson equation [73]. In the relativistic case (for laser amplitudes of $a_0 > 1$), this limit is extended to $\tilde{E}_{wb} = E_{wb}\sqrt{2(\gamma_p - 1)}$[73, 90]. Note that this one-dimensional treatment has further limitations as it does not consider particle motion in the transverse dimensions [91].

### 2.5.3 Energy gain

Electrons which are trapped in the correct phase of the wakefield structure are accelerated and may reach large energies. The maximum value is limited by the length over which the acceleration process takes place and the strength of the accelerating field throughout the acceleration process. An approximation for the latter can be given by the wave breaking field shown above. The maximum acceleration length is the shorter of the dephasing length $L_{dp}$ (distance travelled by an electron before it reaches a decelerating and defocusing region in the wake) and the laser depletion length $L_{pd}$ (distance at which the laser pulse energy has been depleted and the pulse can no longer drive a wakefield). The dephasing length scales as[4] $L_{dp} \simeq \lambda_p^3/\lambda_0^2$ [92] and is, therefore, proportional to $\propto n_e^{-3/2}$ favouring operation at lower electron density which implies acceleration over larger distances. Note that the exact value depends on the operation regime and dimensionality of the analysis. Lu *et al.* [89]

[4]This result can be found by approximating the duration over which acceleration occurs to be the fraction of the acceleration length $\lambda_p/2$ over the difference between particle and phase velocity $(\beta_e - \beta_\phi)c$, where $\beta_e \simeq 1$ and $\beta_\phi \simeq 1 - n_e/(2n_c)$. Multiplying the time by the electron velocity gives the dephasing length $L_{dp} \simeq \lambda_p n_c/n_e$.

give a phenomenological three-dimensional analysis which shows that wakefield size ($R \simeq 2\sqrt{a_0}/k_p$) and dephasing length ($L_{dp} \simeq (2/3)(\omega_0^2/\omega_p^2)R$) scale with the laser amplitude. The pulse depletion length (depletion to $1/e$) can be found by equating the energy of the laser pulse and the energy needed to sustain the wakefield. For a Gaussian pulse with matched duration this quantity was found to be $L_{pd} \simeq 8.7(k_0/k_p)^2 2/a_0^2$ for $a_0 \ll 1$ or $L_{pd} \simeq 8.7(k_0/k_p)^2$ for $a_0 \gg 1$ [93]. Therefore, pulse depletion scales as $\propto n_e^{-1}$.

Multiplying the maximum field by the acceleration distance shows that the energy gain is proportional to $W \propto n_e^{-1}$ (assuming the dephasing length is shorter for the given density).

Note that the laser pulse has to be able to drive the wakefield over this maximum distance which for low densities can be problematic due to laser pulse diffraction. Self-guiding of the pulse or the use of pre-formed plasma waveguides as seen in [94] (guiding of 100 ps pulses over 24 Rayleigh lengths at $1 \times 10^{13}\,\mathrm{W\,cm^{-2}}$ and $1 \times 10^{14}\,\mathrm{W\,cm^{-2}}$ using an axicon channel causing shock expansion), [95] (guiding of 100 fs pulses over 11 Rayleigh lengths in a broad intensity range between $1 \times 10^{8}\,\mathrm{W\,cm^{-2}}$ and $1 \times 10^{16}\,\mathrm{W\,cm^{-2}}$ using both straight and capillary tubes to form a parabolic density profile), [96] (guiding over 6 cm at an intensity of above $5 \times 10^{16}\,\mathrm{W\,cm^{-2}}$ using a long-lasting (100 ns) channel from a capillary discharge in hydrogen), [97] (generation of 20 cm long, low density channels at $n_{e,0} \sim 2 \times 10^{17}\,\mathrm{cm^{-3}}$ using an optical field ionisation approach), and [98] (guiding of 40 fs long laser pulses at intensities of $6 \times 10^{17}\,\mathrm{W\,cm^{-2}}$ over 10 cm at $n_{e,0} \sim 1 \times 10^{17}\,\mathrm{cm^{-3}}$ using optical field ionisation) can mitigate this obstacle [37].

A further obstacle to energy gain is beam loading. This effect is caused by a high charge electron bunch which modifies the shape of the accelerating electric field due to its own Coulomb field. However, if appropriately controlled, the beam loading effect can positively influence the beam properties as shown in [50] where mono-energetic peaks of high charge ($\sim 0.5\,\mathrm{nC}$) were created using a laser duration of 30 fs and amplitude of $a_0 = 2.6$ in a hydrogen-nitrogen gas target of different doping concentrations and electron density between $n_{e,0} = 1 \times 10^{18}\,\mathrm{cm^{-3}}$ and $5 \times 10^{18}\,\mathrm{cm^{-3}}$.

Chapters 3 and 4 of this thesis both study the electron energies that can be achieved with the respective mechanisms. Chapter 3 discusses the implications of using non-uniform plasmas for the dephasing length (and, therefore, for the energy). Chapter 4 presents work that could be used in combination with guiding channels to reach higher energies in future experiments.

### 2.5.4 Electron trapping and injection mechanisms

Electrons can be injected into wakefields by several mechanisms. The condition which has to be satisfied in all cases for an electron to be trapped is that its velocity must be larger than the wakefield's phase velocity. In a one-dimensional picture, the Hamiltonian describing a relativistic electron in a wakefield is given by [90]

$$\mathcal{H}(\gamma_z, \xi) = \gamma_z m_e c^2 \left(1 - \frac{v_z v_{ph}}{c}\right) - e\Phi = \mathrm{C} \ , \tag{2.74}$$

where $\gamma_z$ is the relativistic Lorentz factor, $v_z$ is the electron's velocity, $v_{ph}$ is the wake's phase velocity, $\xi$ is the co-moving spatial coordinate[5], and C is a constant. Here, the defining equation for a closed system[6] in Lagrangian mechanics, $-\partial\mathcal{L}/\partial t = d\mathcal{H}/dt = 0$ was used.

This equation is rearranged (using normalised potential values $\Phi' = e\Phi/(m_e c^2)$ and $\mathcal{H}' = \mathcal{H}/(m_e c^2)$) to give the velocity as function of $\xi$ [99]:

$$\beta_z(\xi) = \beta_{ph}\gamma_{ph}^2(\mathcal{H}_0' + \Phi'(\xi)) \pm \gamma_{ph}\sqrt{\gamma_{ph}^2(\mathcal{H}_0' + \Phi'(\xi))^2 - \gamma_\perp(\xi)^2} \ . \tag{2.75}$$

It describes closed (trapped) as well as open (untrapped) electron orbits which are drawn using a specific value of $\mathcal{H}_0$ (see Fig. 2.3). Open orbits (curves depicting solutions that have one solution for each $\xi$ value) represent particles which are oscillating in the wakefield (or make up the wakefield) whereas orbits with more than one solution for a given $\xi$ represent trapped particles which can be accelerated. The minimal and maximal values of $\gamma$ that lead to trapping are [90]

$$\gamma_{\min} \simeq (1 + \beta_{ph})\gamma_{ph}^2 \Delta\Phi' \tag{2.76}$$

$$\gamma_{\max} \simeq \frac{\Delta\Phi'}{1 + \beta_{ph}} + \frac{\beta_{ph}}{2\Delta\Phi'} \ , \tag{2.77}$$

where $\Delta\Phi'$ is the potential difference. The difference between those values gives the maximal energy gain possible in the wakefield.

This idealised one-dimensional model which introduced trapping does not yet explain which mechanisms can cause particles to be injected in real scenarios. These mechanisms can be roughly separated into five categories. All have the same goal—to satisfy the trapping condition by creating optimal initial conditions for electrons.

[5]Note that this equation has been transformed to the co-moving frame using a Galilean transformation.

[6]This assumes that the plasma is already created and no matter is created or eliminated from the system.

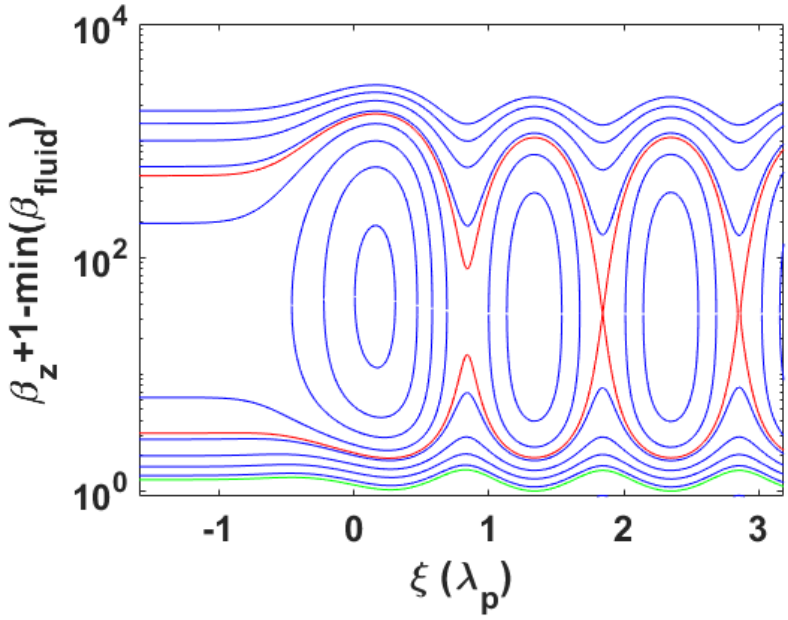



Figure 2.3: Solutions to Eq. 2.75 showing closed and open electron orbits drawn for various initial electron energies ($\mathcal{H}_0$). The separatrix is shown in red and the fluid background velocity (electrons initially at rest) is shown in green. The peak of the laser pulse is located at 0 and has an amplitude of $a_0 = 1$.

#### 2.5.4.1 External injection

The first is external injection in which an externally generated beam is "inserted" into the wakefield. The electrons, if injected into the correct phase of the wake, already satisfy the trapping condition. Here, as discussed in the introduction to this thesis, high spatial and temporal precision is needed due to the small scales involved.

#### 2.5.4.2 Self-injection

The second category is self-injection of particles. This mechanism exploits the fact that background (fluid) electron trajectories intersect the separatrix (separating line between trapped and untrapped orbits) when the laser intensity is high enough. At high laser amplitudes this is caused by plasma wave breaking [91]. Typically, this method relies on self-focusing of laser pulses in higher-density plasma (where the critical power is lower) and is, hence, difficult to control. Using short pulse lengths ($d < \omega_p^{-1}$ with $\omega_p$ being the plasma frequency), mono-energetic beams can be produced in the GeV range [26–28] (see Tab. 2.1) but reproducibility remains an issue. Kalmykov *et al.* showed that a slowly expanding bubble eases the injection condition [100] and Mangles *et al.* studied the threshold experimentally [101] varying the prod-

uct of focal spot quality (influencing the laser pulse intensity) and energy as well as the plasma electron density for pulses of duration $d = 40\,\mathrm{fs}$. Recently, Kuschel *et al.* suggested that small density perturbations aid self-injection [102], shown using a $d = 28\,\mathrm{fs}$ laser pulse at $a_0 \simeq 2.2$ and scanning the electron density in both gas jet and gas cell targets.

Self-injection via wave breaking will be observed in simulations presented in Chapter 3, in addition to overlaying effects aiding further injection. Specifically, it will be shown how the trapping threshold can be temporarily altered by modifying the target medium. Although reproducibility of this process was not studied experimentally in this thesis, I will present others' findings showing that, using cluster targets, stable and reproducible electron beam parameters can be achieved.

#### 2.5.4.3 Ionisation injection

Ionisation injection mechanisms use the fact that the binding energy of electrons in atoms differ significantly. This means that a laser's electromagnetic field will free electrons from the atomic potential at different positions with some of them being released close to the intensity peak of the laser pulse. These electrons have momenta close to zero and (if the wakefield is strong enough) are trapped more easily than the background electrons which were ionised previously. A drawback of this scheme is that without careful preparation, the injection mechanism does not automatically stop and creates beams with a continuous energy spectrum. Experimentally, ionisation injection was first realised using dopant elements such as nitrogen, argon, neon [103], or carbon dioxide [104]. The former article made use of 30 fs laser pulses with power values up to 120 TW (intensity values up to $1.5 \times 10^{20}\,\mathrm{W\,cm^{-2}}$) at electron densities between $5 \times 10^{18}\,\mathrm{cm^{-3}}$ and $3 \times 10^{19}\,\mathrm{cm^{-3}}$. The authors showed that the charge of injected electron beams is increased by an order of magnitude through the optical field ionisation of the used noble gases and nitrogen. Furthermore, the authors observed an electron beam divergence decrease by a factor $\sim 2$. The latter article used pulses of 60 fs at 110 TW and a electron density of less than $1.5 \times 10^{18}\,\mathrm{cm^{-3}}$. Using a gas cell of 1.3 cm in length, they generated electron beams above 1 GeV using a carbon dioxide dopant (3%) whereas no electrons were observed in pure helium using the same laser parameters. Ionisation injection has shown to create "quasi-monoenergetic" peaks in the electron beam distribution with significant tails at lower energies in pure nitrogen between 400-600 MeV[105] where the authors used 30 fs pulses at a power of 80 TW and saw self-injected electrons above $n_e = 3 \times 10^{18}\,\mathrm{cm^{-3}}$. Using an injector stage and a separate accelerator stage has proven fruitful in overcoming the issue of continuous

injection: beams with $\sim 5\%$ energy spread have been detected where the nitrogen-doped (0.5%) helium gas target causing ionisation injection was limited to a region of 3 mm separated by 1 mm from the 5 mm long helium acceleration stage [106]. This experiment used a 60 fs pulse with peak powers of up to 200 TW and an electron density of $3 \times 10^{18}\,\mathrm{cm}^{-3}$.

#### 2.5.4.4 Injection through tailored density profile

These methods prepare the plasma density in a way that aids injection. For example, in density down-ramp injection the density is decreased in the target. This causes a local increase in wakefield wavelength ($\lambda_p \propto n_e^{-1/2}$). If the wavelength increases over time the phase velocity decreases correspondingly (neglecting the change in laser group velocity). This eases the trapping condition because over the density ramp region the electrons need to acquire less longitudinal momentum. This effect has been verified experimentally and shown to inject electrons in [107, 108]. Geddes *et al.* [107] show that electron injection depends on the sign of the density gradient into which the laser pulse (10 TW delivered over 47 fs at a peak electron density of $2.2 \times 10^{19}\,\mathrm{cm}^{-3}$) is focused, exhibiting great stability over many shots when optimised. Gonsalves *et al.* also show great stability and tuning of the electron bunches using a 40 TW pulse (over 38 fs) and a gas target combining a jet (for injection in the downramp) and capillary (for acceleration). Issues with this mechanism are continuous injection over the down-ramp region and quick dephasing due to the growing distance between trapped electrons and wakefield peak density. A numerical characterisation of the impact of the density ramp parameters is given in [109].

When the density drops significantly over a short distance (e.g. a density step created by placing a sharp obstacle in a gas jet), the fluid electrons, which are not trapped before the step, may be trapped in the new phase of the wakefield which has changed instantaneously. After the step, the injection process ceases resulting in narrow energy spread electron bunches, shown in [110] using a laser intensity of $I = 2.5 \times 10^{18}\,\mathrm{W\,cm}^{-2}$ and an electron density in a gas jet of $n_{e,\mathrm{peak}} = 6 \times 10^{19}\,\mathrm{cm}^{-3}$ which falls abruptly to below $4 \times 10^{19}\,\mathrm{cm}^{-3}$ from which it continues to fall gradually (as typical for a gas jet) and in [111] using a laser intensity of $I = 8.5 \times 10^{18}\,\mathrm{W\,cm}^{-2}$ and electron density values between $1.5 \times 10^{18}\,\mathrm{cm}^{-3}$ and $6 \times 10^{18}\,\mathrm{cm}^{-3}$ with a smaller, sharp density step. Recently, this method has been used to generate sub-percent energy spread levels with peak energies of $\sim 0.8\,\mathrm{GeV}$ [112] using a laser intensity between $I = 2.9 \times 10^{18}\,\mathrm{W\,cm}^{-2}$ and $I = 3.6 \times 10^{18}\,\mathrm{W\,cm}^{-2}$ and a 6 mm long constant

electron density profile at $n_e = 2.6 \times 10^{18}\,\mathrm{cm}^{-3}$ following a peak at $n_e = 5.0 \times 10^{18}\,\mathrm{cm}^{-3}$ with a downramp of $\sim 160\,\mu\mathrm{m}$.

#### 2.5.4.5 Injection using multiple pulses

This mechanism makes use of injector pulses which trigger injection for a short amount of time. The first proposal was that of two counter-propagating injector pulses of orthogonal polarisation compared to the driver (or "pump") pulse colliding at a fixed distance behind the driver pulse [113, 114]. This creates a slowly evolving ponderomotive beat wave which traps and heats electrons which are then be injected into the wake. Further analytical and numerical studies showed that electrons of narrow energy spread are created by using a beat between a driver pulse and a single injector pulse directly without the need for a third pulse [115, 116]. In all cases, it was assumed that the injector pulse has lower intensity than the driver pulse. This method has shown to successfully generate mono-energetic beams [117] using two collinear and counter-propagating 30 fs laser pulses ($I_{\mathrm{pump}} = 3.4 \times 10^{18}\,\mathrm{W\,cm}^{-2}$ and $I_{\mathrm{inject}} = 4 \times 10^{17}\,\mathrm{W\,cm}^{-2}$), focusing them at the edge of a 2 mm wide gas jet generating electron densities between $n_e = 7.5 \times 10^{18}\,\mathrm{cm}^{-3}$ (no self-injection detected without injector) and $n_e = 1.25 \times 10^{19}\,\mathrm{cm}^{-3}$ (broad electron spectrum from self-injection in contrast to injection using injector pulse). The injection mechanism also works when using counter-crossing beams rather than head-on collisions. This was shown in [118] where two 40 fs laser pulses of intensities $I_{\mathrm{pump}} = 3.0 \times 10^{18}\,\mathrm{W\,cm}^{-2}$ and $I_{\mathrm{inject}} = 8.0 \times 10^{16}\,\mathrm{W\,cm}^{-2}$ crossing at an angle of 135° (and 180° in a different configuration) were used at an electron density $n_e = 3.95 \times 10^{19}\,\mathrm{cm}^{-3}$ (below the self-injection threshold), as well as in [119] where two 30 fs laser pulses of intensities $I_{\mathrm{pump}} = 3.6 \times 10^{18}\,\mathrm{W\,cm}^{-2}$ and $I_{\mathrm{inject}} = 1.5 \times 10^{17}\,\mathrm{W\,cm}^{-2}$ crossing at an angle of 135° were used at an electron density $n_e = 1 \times 10^{19}\,\mathrm{cm}^{-3}$.

A scheme for controlled ionisation injection for electron-beam driven wakefields with laser pulses as injectors has been put forward in [120] suggesting the use of two pulses counter-propagating along the axis perpendicular to the drive beam propagation direction and colliding within the bubble to ionise electrons at rest which then satisfy the trapping condition. Similarly, Hidding *et al.* [121] propose the use of a diverging laser pulse propagating collinearly with a drive electron beam at a set delay. The laser pulse injects helium electrons through ionisation injection within the bubble for a short amount of time before it drops below a certain intensity threshold.

In laser-driven wakefields, a mechanism has been suggested [57] which uses two pulses which coherently add to create a wakefield strong enough to trap nitrogen

electrons over a short amount of time determined by the injector pulse's Rayleigh range, thus, creating a low-emittance beam. Chapter 4 of this thesis investigates the two-pulse ionisation injection (2PII) approach [57] experimentally. It will be shown that the use of an injector pulse "switches on" electron trapping if the pulse delay is within a specific range and that the polarisation of the injector pulse affects the beam parameters. In this two-pulse approach, a particular feature of ionisation injection (Section 2.5.4.3) plays an important role as well—to minimise the duration and volume of electron injection the laser amplitude is tailored such that the inner shell electrons of the dopant (nitrogen) are only ionised and, therefore, available for trapping when the injector pulse reaches its peak intensity. The large amplitude of the wakefield as well as the position in its potential at which the electrons are "born" are both favourable for satisfying the trapping condition.

## 2.6 Computational methods for simulating laser-plasma interactions

There are various methods of studying laser-plasma interactions computationally. When choosing the best method for each problem, one firstly has to consider which physical aspects can be modelled with each respective approach. Secondly, considerations regarding computational resources have to be made as choosing an appropriate method can speed up the simulation by orders of magnitude. For example, so-called fluid (magnetohydrodynamic) codes use the fluid velocity and density of the respective particle species and numerically integrate the functions over the simulation's spatial dimensions. However, the set of particles (fluid element) in a specific area is treated as an ensemble of equal velocity with the Maxwell-Boltzmann distribution dictating the pressure. This makes it impossible to account for effects such as particle injection into the wakefield rendering the method, despite its computational efficiency, ineffectual for these purposes.

One can resort to a kinetic approach, solving the combined set of the Vlasov equation for each species' distribution function $f(\mathbf{r}, \mathbf{p}, t)$

$$\frac{\partial f}{\partial t} + \mathbf{v} \cdot \nabla f - e(\mathbf{E} + \mathbf{v} \times \mathbf{B}) \cdot \frac{\partial f}{\partial \mathbf{p}} = 0 \tag{2.78}$$

which is an adaptation of the collisionless Boltzmann equation, and the Maxwell equations. Due to the kinetic nature of the equations, a six-dimensional phase space has to be used making the approach computationally expensive. Substituting the distribution function with the plasma moments recovers the fluid approach.

In this thesis, the particle-in-cell (PIC) computation method was used to study the physics of plasma wakefields. This method is well established and is widely used in the literature. For example, PIC simulations were used for the first detailed study of the physics behind the non-linear wave-breaking ("bubble") regime [22].

### 2.6.1 Fundamentals of the PIC method

The PIC approach uses a grid on which information about electromagnetic fields is stored and macro-particles representing a (large) number of particles of a species which interact with the fields within each grid-cell. This is possible because the ratio of charge to mass which determines the object's acceleration under the Lorentz force

$$\frac{d(\gamma \mathbf{v})}{dt} = \frac{Q}{M}(\mathbf{E} + \mathbf{v} \times \mathbf{B}) \tag{2.79}$$

is identical between a macro-particle and the sum of all real particles it represents:

$$\frac{Q}{M} = \frac{\sum_i q_i}{\sum_i m_i} \ . \tag{2.80}$$

Here, $Q$ is the macro-particle charge and $M$ is the macro-particle mass. Interpolating forces from grid vertices rather than calculating each particle's interaction with all other particles due to (long range) Coulomb forces reduces the computational effort from $\mathcal{O}(N^2)$ to $\mathcal{O}(N)$, where $N$ is the number of macro-particles used within the simulation. Due to the finite grid resolution, unphysical effects such as numerical particle heating [122] can occur - especially if the cell size is larger than the Debye length. Specifically, this occurs when a macro-particle moves too quickly due to the insufficient resolution which, in turn, has an effect on the field computation. This effect reinforces itself through the fields' influence on nearby particles.

Another restriction comes from the relation between the temporal and spatial resolutions of the simulation which is necessary to ensure that light cannot propagate more than one cell per time interval. This is called the CFL (Courant-Friedrichs-Lewy) condition [123] and reads

$$\Delta t < \frac{1}{c\sqrt{\sum_i 1/\Delta x_i^2}} \ , \tag{2.81}$$

where $\Delta$ denotes the spatial ($x$) and temporal ($t$) increment size and $i$ indexes the spatial dimensions.

Macro-particles are initialised at random locations before entering the simulation loop. Each macro-particle has an associated weight corresponding to the species density in the given location. When modeling density gradients, the number of particles

per cell is usually kept constant but their weights are varied. Due to the macro-particle's finite extent it has also a pre-defined shape (e.g. top hat, triangular, spline interpolation). The order of the interpolation affects the accuracy of the simulation and its run time. The charge and current density of the particles are written as

$$\rho_j(\boldsymbol{r}) = \sum_i q_i S(\boldsymbol{r}_j - \boldsymbol{r}_i), \tag{2.82}$$

$$\boldsymbol{J}_j(\boldsymbol{r}) = \sum_i q_i \boldsymbol{v}_i S(\boldsymbol{r}_j - \boldsymbol{r}_i), \tag{2.83}$$

where $S(r_j - r_i)$ describes the effective shape (interpolation method) of the particles, $i$ is the macro-particle index and $j$ is the cell index. Then, using Gauss' law

$$\nabla \cdot \mathbf{E} = \frac{\rho}{\epsilon_0} \ , \tag{2.84}$$

the electric field is computed on the grid. As long as charge is conserved (and no magnetic monopoles exist initially), only two of the Maxwell equations, Ampere's law

$$\frac{\partial \boldsymbol{E}}{\partial t} = c^2(\nabla \times \boldsymbol{B}) - \frac{\boldsymbol{J}}{\epsilon_0}, \tag{2.85}$$

and Faraday's law

$$\frac{\partial \boldsymbol{B}}{\partial t} = -\nabla \times \boldsymbol{E} \tag{2.86}$$

have to be solved in the iterations after initialisation. This is shown in appendix A.3. The simulation loop in PIC codes consists of four main steps:

- First, the electromagnetic fields are updated using Ampere's law and Faraday's law. On the grid this is done using a finite-difference-time-domain (FDTD) method. Here, the grid arrangement used to discretise the Maxwell equations is called the Yee grid [124] where the magnetic field information is stored at a location shifted by half a cell length with respect to the electric counterpart.

- Second, the electromagnetic fields are interpolated to the macro-particle locations from which the Lorentz force can be obtained.

- Third, the location and velocity of the particles are updated (push) according to the force acting on them. This is done through numerical integration. To achieve higher accuracy than, say, an Euler method, a "leapfrog" (which achieves second order accuracy in the same number of computational steps) can be used where some quantities are defined on a grid which is shifted by half a step size: i.e. $\mathbf{x}_{n+3/2} - \mathbf{x}_{n+1/2} = \mathbf{v}_{n+1}\Delta t$.

- Fourth, the moments (charge and current) are updated according to the particles' new positions in phase space.

Some examples of widely used PIC codes are OSIRIS [125], EPOCH [126] and Smilei [127]. All of these codes were used to obtain results presented in the following chapters of this thesis.

### 2.6.2 Moving window frame

When studying wakefields (especially when looking at the evolution of an accelerated electron bunch) it is necessary to cover distances of millimetres or even centimetres with the simulation box. To avoid numerical errors the resolution has to be sufficiently high - in this work even up to the nanometre scale. This great difference of many orders of magnitude between cell size and the extent of the region of interest makes simulations almost infeasible as they are computationally too expensive with current systems. However, one can - due to the nature of the problem - take a smaller simulation box and move it using a Galilean transformation following the laser pulse as it propagates through the plasma. When the trailing boundary of the simulation box reaches particles and fields it will absorb them using an appropriate boundary condition. From the leading boundary new particles will be initialised at every time step.

# Chapter 3

# Wakefields in a cluster plasma

Typically, laser wakefield experiments are conducted using a gas jet or a gas cell to produce the target medium. While gas cells are more suited for experiments at low electron densities, gas jets can produce electron densities that are orders of magnitude higher, albeit over a smaller distance.

**Generation and characterisation of clusters** When gas jets are operated at certain conditions (the specifics of which will be discussed further below) such as a high backing pressure, atomic clusters can form in the isentropic expansion of the gas streaming through the nozzle due to the conversion of thermal energy to directed kinetic energy which results in a decrease of temperature [128, 129]. The formed clusters are held together by inter-atomic or inter-molecular van der Waals forces. The effect of clusterisation was first characterised by Hagena [130] who empirically found a parameter ($\Gamma^*$) that gives a condition for the presence of clusterisation for a specific gas at specific nozzle parameters. In an updated form this parameter reads [131]

$$\Gamma^* = k(d/\tan\alpha)^{0.85} p_0/T_0^{2.29} \ , \tag{3.1}$$

where $k$ is an element-specific constant (e.g. 1700 for Ar and 2360 for $CH_4$), $d$ is the nozzle throat diameter in µm, $p_0$ is the backing pressure in mbar, and $T_0$ is the initial gas temperature in K. In order for clusterisation to occur, $\Gamma^*$ has to reach the onset value of $\sim 100 - 300$. Murakami *et al.* [132] experimentally probed the clustering condition for hydrogen across a temperature and pressure range and calculated from Hagena's work how the condition which indicates for which parameters clusterisation starts scales for different gases. The authors show that methane and argon have similar clusterisation thresholds (at fixed nozzle parameters) and that clusterisation occurs over a great range of temperature values at a backing pressure of $P_0 = 40\,\mathrm{bar}$.

Lu *et al.* [133] conducted experiments studying cluster sizes for methane at high backing pressure of up to 84 bar which they measured using a Rayleigh scattering[1] diagnostic. They measured methane cluster radii between 1 and 7 nm. Tao *et al.* [134] investigated how using a planar nozzle geometry relates to Hagena's scaling and determined argon cluster sizes both experimentally and theoretically. The authors also extended the applicability range of Hagena's model to larger cluster sizes of $10^3$ to almost $10^7$ atoms per cluster, a range relevant for many experiments. More recent studies, such as those conducted by Aladi *et al.* [135] and Grieser *et al.* [136] used techniques such as Rayleigh and Mie scattering to estimate the cluster electron density and diameter. They obtained argon cluster diameters of 16 nm for a 12 bar backing pressure [135] and hydrogen cluster diameters of $\sim$ 27.1 nm at 16 bar. Recently, a study showed absolute electron density measurements for argon clusters giving values between $0.5 \times 10^{21}$ and $3 \times 10^{21}\,\mathrm{cm}^{-3}$ which is on the order of the critical density (see section 2.4.4) for $\lambda_0 = 800\,\mathrm{nm}$ [137]. These studies show that slight changes in set-up greatly influence the cluster diameter and electron density. These results show that methane, argon, and even hydrogen form clusters across a great range of conditions relevant for laser-driven wakefield experiments.

**Applications** The interaction of high-density clusters and laser pulses has been of interest to researchers for a long time and the cluster evolution caused by the interaction has been studied extensively [138–146] with focus on topics such as soft x-ray or EUV emission [147, 148] putting special emphasis on high harmonic generation [149–152] or even nuclear fusion [153]. Furthermore, it has been shown by Tajima *et al.* [154] that polarisation effects in clusters modify the dispersion relation of an electromagnetic wave showing that a "cluster mode" exists in which the phase velocity is reduced compared to a uniform plasma of the same average electron density $\langle n_e^{\mathrm{cl}} \rangle = \langle n_e^{\mathrm{u}} \rangle$.

Electrons can be accelerated in wakefields that are created in such clusterised plasma using, for example, argon [145, 155, 156] or methane [157]. For the sake of clarity, the term "plasma cluster" will be used in this chapter to describe an accumulation of atoms closely bound together by van der Waals forces that have been ionised and the term "cluster plasma" will be used to describe an accumulation of plasma clusters well separated by a distance much larger than the plasma cluster diameter.

[1] Rayleigh scattering is the process of elastic scattering of light off of targets smaller than the optical wavelength.

**Laser-cluster interaction** Of great importance for all processes mentioned above is the complex interaction dynamics between the expanding cluster and the laser field. The way clusters react to laser pulses (cluster polarisation, heating, expansion, disintegration) and the way laser pulses react to clusters (absorption, scattering) both depend on many parameters such as the cluster size, cluster electron density, cluster composition, laser pulse intensity, and laser pulse duration. Hence, to find an accurate description of the laser-cluster interaction process, detailed experimental studies across a large parameter space are required.

While many aspects of the laser-cluster interaction are difficult to probe experimentally due to the small size of the clusters and the short time-scales involved, there are specific measurements that can shed some light on the involved processes. For example, the electron and ion distributions can be measured using spectroscopy after a cluster has disintegrated. However, this only gives data several microseconds after the laser has interacted with the cluster. X-ray spectroscopy, however, can be used to get a dynamic picture of electron behaviour during the interaction process via the temporally resolved detection of x-rays [158]. Another property that can be measured is the laser energy absorption after interacting with a cluster plasma [159–161]. Unfortunately, a great number of experiments in the literature have not accurately characterised all necessary cluster parameters such as diameter, peak density, density distribution, or mean cluster separation. This makes it difficult to compare the results to available models (see below).

The interaction process is typically separated into three stages:

1. plasma generation (ionisation),
2. electron heating and expansion (or displacement) of the electron cluster,
3. and (ion) cluster disintegration[2].

To describe ionisation, I will follow the terminology of Last and Jortner [162] who distinguish between "inner" and "outer" ionisation. The process of ionising atoms in a cluster without the electrons leaving the cluster is called "inner ionisation". These electrons are called "quasi-free". Understandably, this process depends on

[2]Disintegration is not relevant for the studies conducted in this thesis due to the short time scales involved in wakefield physics. Significant disintegration would only occur after the relevant wake has completely passed the ion.

the intensity of the incident light as well as the cluster properties. It was found that the ionisation potential $W$ of atoms in clusters is reduced through nearby ions by $\Delta W_j = -(4q_j/d_{ii}) \exp\{(-d_{ii})/(2\lambda_D)\}$ ($q$ is the charge, $d_{ii}$ is the mean ion-ion distance and $\lambda_D$ is the Debye length) aiding enhanced field ionisation and allowing for inner shell ionisation at lower than typical laser intensities [163, 164]. In addition to the effect of enhanced field ionisation in a cluster, electron-impact ionisation, where free electrons collide with atoms and transfer their energy during the collision, may contribute to the overall degree of ionisation[3]. One of the few studies looking at ultra-fast ionisation dynamics (few femtoseconds) at high intensities ($I = 1 \times 10^{18}\,\mathrm{W\,cm^{-2}}$) [165] finds, using molecular dynamics simulations, that high ionisation levels are reached within a few femtoseconds (before the laser pulse intensity peak has been reached), in agreement with data presented in Appendix C.2. The authors studied Xe and $CD_4$ clusters. The study also shows that the degree of "outer" ionisation, which describes the process of electrons leaving the quasi-neutral cluster, is building up very quickly (a few femtoseconds after the inner ionisation saturates) for high intensities. Due to outer ionisation, a positive charge builds up within the cluster creating an attractive force for electrons that have left the cluster. The difference between "inner" and "outer" ionisation is illustrated in Fig. 3.1. The figure also shows the different stages of the ionisation and expansion process typically found at medium laser intensities ($1 \times 10^{15}\,\mathrm{W\,cm^{-2}}$ to $1 \times 10^{16}\,\mathrm{W\,cm^{-2}}$). In this regime, the laser energy is strongly absorbed in the presence of quasi-free electrons [166] further aiding inner ionisation. One of the main mechanisms responsible for this effect is inverse bremsstrahlung. At higher laser intensities (as will be discussed in the following sections) large parts of the the (inner) ionised electron bulk are oscillating in the laser field at an amplitude so large that they leave the ion cluster causing an increased Coulomb explosion response [165]. The quiver amplitude or excursion length $x_q = \sqrt{I}\lambda^2/c^2$ can be up to ten times larger than the cluster diameter (the effective value is reduced due to the ion bulk's attractive electrostatic force). I will show later that, at high laser intensities, the ionisation and expansion process happens on the order of a few laser cycles which means that the relevant effects unfold on a timescale of $\ll 100\,\mathrm{fs}$.

Trying to explain the observations made in experiments, such as the dependence of the absorption on the laser pulse length as seen in Xe and Ar clusters [167], many research groups conducted simulations and created phenomenological models. One of

[3]Appendix C.2 shows that this mechanism has negligible impact on the inner ionisation for the cluster parameters used in this thesis.

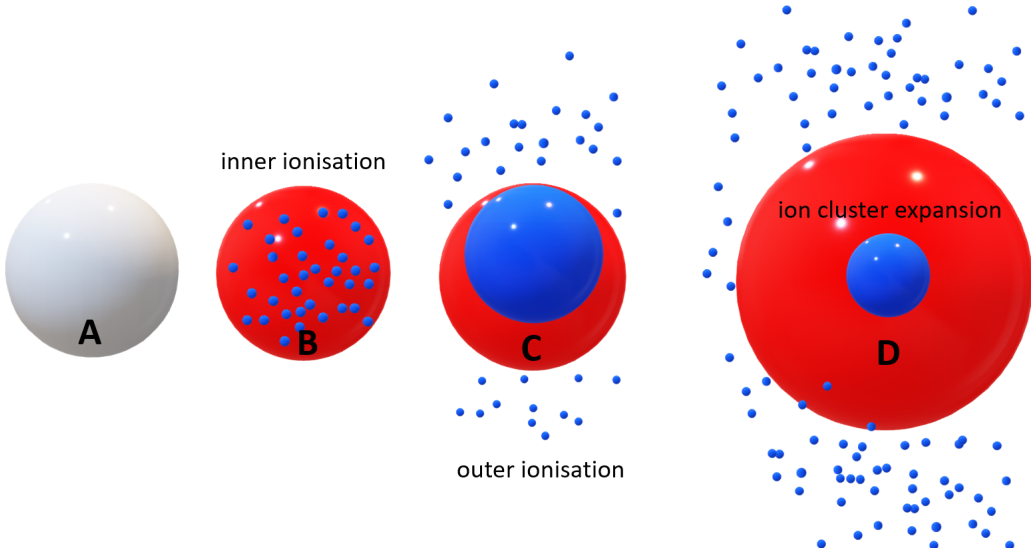



Figure 3.1: Simplified illustration of cluster expansion as found in the literature. The white sphere represents a neutral cluster, the red sphere represents the ion cluster and the blue spheres represent single electrons (small) and a larger volume occupied by electrons (large). The different stages of the ionisation and expansion process are shown from left to right. The duration of each stage and the magnitude of the electron oscillations in the laser field depend on the instantaneous pulse intensity and laser frequency. Reproduced from [164].

the earliest successful and often cited models which was able to explain a multitude of experimental results for moderate intensities was the nanoplasma model by Ditmire *et al.* [129]. It describes the hydrodynamic expansion of the cluster through efficient heating of the electrons by the laser pulse. This model, considering clusters with diameters larger than the Debye length (the authors consider a plasma of electron temperature $T_e = 1000\,\mathrm{eV}$ and solid density) describes expansion due to two effects. On the one hand, it is argued that the mean free path of some hot electrons is long enough such that they can escape which increases the charge imbalance of the cluster leading to rapid expansion of the positively charge ion cluster (Coulomb explosion). On the other hand, the pressure of the ionised and heated electrons forces an expansion which causes the cold ions to follow at the plasma sound speed $v \propto \sqrt{ZT_e/m_i}$ [129] ($Z$ is the atomic number and $m_i$ is the ion mass). The authors assume uniform temperature over the cluster and argue that the laser pulse deposits energy mainly via collisional inverse bremsstrahlung. Heating is shown to be most efficient when the cluster electron density is $n_e = 3n_{crit}$, where $n_{crit}$ is the critical density as shown in the previous chapter. The assumed continuous expansion of the electron bulk leads to a density decrease until the resonance is reached at which the laser absorption is

strongest. The resonance frequency is called Mie plasmon frequency [168]. If the laser frequency is much smaller than the Mie frequency, the electrons can shield the laser field. If the laser frequency is much larger than the Mie frequency, the laser field can penetrate into the cluster but inverse bremsstrahlung is not effective [169] (the energy gained by the electrons scales as $\omega_0^{-2}$). Effective absorption of light at the resonance is due to the fact that the plasma dielectric constant approaches a resonance value which causes the field and the heating rate inside of the cluster to be strongly increased [129]. The assumption of a uniform dielectric sphere in a constant field is only applicable if the electron excursion forced by the laser field is small and the diameter significantly smaller than the laser wavelength. The nanoplasma model further assumes that the expansion itself is uniform which (as will be shown in 3.1.2.2) is not valid (or at least not applicable on the relevant time-scales of tens of femtoseconds) for the cases studied in this thesis. According to Tisch *et al.* [170] the nanoplasma model is valid for "large (thousands of atoms), high Z clusters" as opposed to other cases where the electrons can escape the ion cluster. However, their study considers laser intensities of up to $I < 1 \times 10^{16}\,\mathrm{W\,cm^{-2}}$, not considering the effect of electron excursion due to higher laser fields. Furthermore, it was found using a one-dimensional numerical study [171] that the ponderomotive force of laser pulses as low as $I \sim 1 \times 10^{15}\,\mathrm{W\,cm^{-2}}$ can strongly modify the plasma hydrodynamics through compression of the cluster leading to modifications to the resonance condition.

According to a different model, the nonlinear laser absorption model by Kundu and Bauer [172], absorption is particularly high at $I = 7 \times 10^{15}\,\mathrm{W\,cm^{-2}}$ for a cluster density of 20 times the critical density (lowest density studied in their article). This resonance model is dominant at short time scales (few laser cycles) before the expanding cluster's electron density drops sufficiently such that the linear resonance effect at the Mie frequency becomes significant (typically after few hundreds of femtoseconds).

The laser-cluster dynamics have also been studied numerically, for example using a Monte Carlo simulation approach [173] finding enhanced inner shell excitation in the clusters. A different study [174] using classical dynamics simulations describes how a majority of all unbound electrons is removed from Xe clusters via "quasiresonance energy enhancement" at intensities of $I = 1 \times 10^{16}\,\mathrm{W\,cm^{-2}}$, which causes a Coulomb explosion. Deiss [164] presents a thorough numerical analysis of the laser-cluster interaction process for short pulses ($\tau = 61\,\mathrm{fs}$) of moderate intensity $I = 4.3 \times 10^{15}\,\mathrm{W\,cm^{-2}}$ discussing ionisation and polarisation dynamics of a single cluster. A semi-classical approach which treats inner-atomic dynamics self-consistently finds a strong difference in the ratio between inner and outer ionisation between different laser wave-

lengths [175]. Further numerical tools used in the literature are molecular dynamics simulations [165] which can give a microscopic description of the many-particle dynamics and particle-in-cell simulations [176] which can be used to study larger clusters compared to molecular dynamics simulations due to the resource-friendly architecture (run time in PIC codes scales with number of particles $N$ rather than $N^2$) as discussed in the previous chapter. The authors in [176] find that the electric field of the cluster imposes a phase shift between the electron oscillation and the laser field oscillation causing efficient energy absorption via the laser dephasing heating (LDH) mechanism in Ar and Xe clusters. Inverse bremsstrahlung is found to be negligible in the regime studied and great differences in outer ionised electron excursion amplitudes are found comparing laser intensities of $I = 4.4 \times 10^{14}\,\mathrm{W\,cm^{-2}}$ and $I = 6.7 \times 10^{15}\,\mathrm{W\,cm^{-2}}$.

A recent study goes so far as to question the impact that small-scale clusters have on the strength of the laser absorption process [177] for pulse lengths shorter than 100 fs showing that the laser-cluster interaction is far from a solved problem. The lack of phenomenological models universally applicable to different regimes is largely due to the sensitivity of the involved processes to the cluster and laser parameters.

This chapter is structured as follows: The first part investigates how the structure of wakefields is changed by introducing a cluster plasma target at moderate laser intensity levels ($a_0 = eA_0/(m_e c) < 1$), where $e$ is the elementary charge, $A_0$ is the peak value of the laser vector potential $\mathbf{A}$, $m_e$ is the electron mass, and $c$ is the speed of light in vacuum. Experimental observations using a single-shot frequency-domain holography diagnostic are presented in Section 3.1.1. These findings are supported by the computational study of the process using fully relativistic two-dimensional particle-in-cell simulations in Section 3.1.2 as well as a quasi-analytical one-dimensional approach incorporating strong density perturbations discussed in Section 3.1.3 which does not depend on the quasi-static approximation conventionally used to describe non-linear wakefields. The second part of this chapter investigates how particles are trapped and accelerated in a wakefield in a cluster plasma driven by a high-intensity laser pulse ($a_0 = 5$). Both sections are followed by discussions of the obtained results and interpretations of their applicability and impact. The results of Section 3.1 have been published in [178] and the results of Section 3.2 have been published in [179].

## 3.1 Wakefield structure in the weakly non-linear acceleration regime

The motivation for the work presented in this section stems from data taken during an experiment which was conducted at the ASTRA high-power laser facility [180]. The main objective of this experiment was to investigate the capabilities of a single-shot oblique-angle frequency-domain holography diagnostic proposed by Kasim *et al.* [181] which differs from commonly used measurement techniques such as shadowgraphy [182] or frequency-domain holography [183] as will be laid out in the next section. Due to the gas jet parameters used, an interesting effect was studied unintentionally. As I will discuss further below, there is a strong case for arguing that the gas target actually consisted of nanometre-sized methane clusters.

The observations of the wakefield structure from analysis of the experimental data are compared to two-dimensional particle-in-cell simulations and a one-dimensional quasi-analytic model showing that the wavefronts of the wakefield are curved backwards—the opposite of what is expected in plasma of uniform electron density distribution—and that the distance between consecutive wakefield electron density perturbations decreases with increasing distance behind the driving laser pulse. The results are found to have interesting implications for the use of cluster targets in wakefield acceleration experiments: it will be shown that the dephasing length—one of the major limiting factors in wakefield acceleration experiments [73]—could be increased using cluster targets.

Some of the experimental data used in this section has also been analysed and presented in [184]. The interpretation used in [184] to explain the experimental observations is partially based on the theory of modified electromagnetic wave propagation due to cluster polarisation forces by Tajima *et al.* [154] and partially based on beam loading effects. However, Kasim's arguments follow a different narrative to what is found from data analysis in this thesis in which I will argue that Tajima's theory is only partially applicable and that beam loading is unlikely given the laser parameters.

### 3.1.1 Experimental data

In the experiment, a laser pulse of 45 fs full-width at half-maximum (FWHM) duration, focused to an FWHM spot size diameter of 29 µm, was used to drive a wakefield. Note that the FWHM is related to a Gaussian beam's $1/e^2$-radius as $w_0 = \mathrm{FWHM}/\sqrt{2\ln(2)}$. The peak intensity of the beam was $1.1 \times 10^{18}$ W cm$^{-2}$ ($\pm 9\%$), or, using the expression for the normalised laser amplitude $a_0 \equiv$

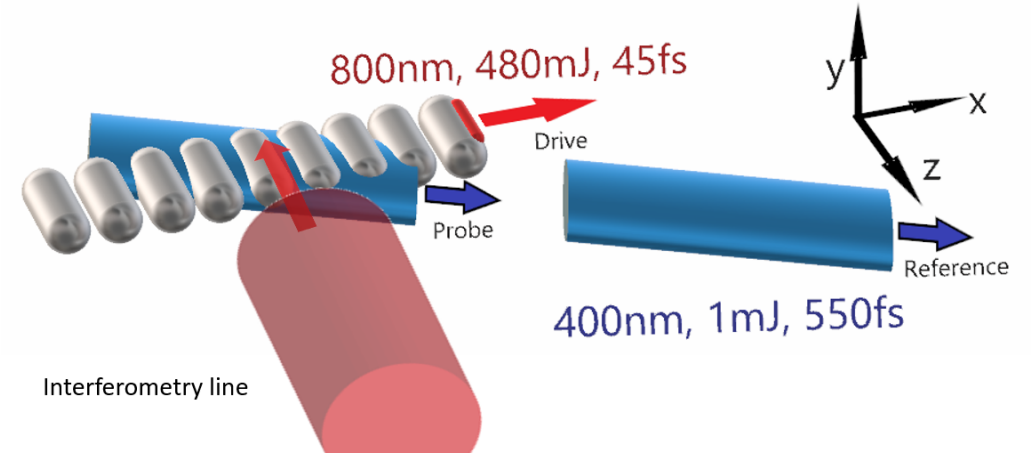



Figure 3.2: This schematic depicts the single-shot oblique-angle frequency-domain holography diagnostic and a transverse optical probe used in the experiment conducted at the ASTRA laser facility. First, the $2\omega$-reference pulse (blue) passes through the target chamber centre (TCC). Then, 1.5 ps later the $2\omega$-probe pulse (also blue) propagates through the TCC along the same axis as the reference pulse which crosses the $x$-axis at an angle of 8° and captures the wakefield (grey) created by the drive pulse (red). The electron density variations imprint a phase shift onto the probe pulse. The perpendicular interferometry probe is used to measure the electron density.

$8.55 \times 10^{-10}(I\lambda^2[\mathrm{W\,cm^{-2}}\mu\mathrm{m}^2])^{1/2}$ (here, $I$ is the intensity in $\mathrm{W\,cm^{-2}}$ and $\lambda$ is the laser wavelength in µm), $a_0 = 0.72\,(\pm 4.5\%)$[4]. The uncertainty in the peak intensity was obtained from the calibrations conducted in [184].

The path of the pulse was crossed by a perpendicular interferometry probe and two diagnosing pulses at a crossing angle of 8°. A schematic of this set-up is shown in Fig. 3.2. The target was created within the vacuum chamber from a gas jet operated at backing pressures between 7 and 14 bar leading to a range of electron densities from $3.5 \times 10^{18}\,\mathrm{cm^{-3}}$ to $1.1 \times 10^{19}\,\mathrm{cm^{-3}}$. The gas used for the data analysed in this thesis was methane. With equation 3.1 it becomes apparent that for the backing pressure values used, methane streaming from a nozzle will clusterise to form clusters of large peak electron density. For example, argon (with the element-specific k parameter of 1650) begins to cluster at around 2 bar [185]—methane has a significantly higher $k$ parameter of 2360 [131]. The corresponding Hagena parameter is $\Gamma^* \sim 40000$ (a value much larger than the clusterisation onset threshold) using $T = 293$K, $d = 1000$µm, $\alpha = 15°$, and $p_0 = 7000$mbar.

[4]The error propagation is obtained as follows. Given a function $z = f(x)$ the error is written as $\delta z = |f'(x)|\delta x$. Therefore, $\delta I/I = \delta a_0 2a_0/a_0^2$ and $\delta a_0/a_0 = \delta I/(2I)$.

The plasma electron density for each shot was obtained using the perpendicular (interferometry) probe pulse of 550 fs duration with a frequency doubled laser wavelength of $\lambda_0 = 400\,\text{nm}$. The probe was split and recombined with a slight misalignment causing interference fringes on a charge-coupled device (CCD) sensor [186]. The phase shift picked up by some photons in the probe while travelling through plasma (caused by differences in optical path length) was extracted following a method first introduced by Takeda *et al.* [187]. A Fast Fourier Transform (FFT) is applied to the raw intensity data. One of the two sidebands of the Fourier transformed intensity signal is isolated which clears the data of the high-frequency fringes associated with the laser frequency. Shifting the isolated peak to the central position and performing an inverse Fourier transform gives the signal for the intensity associated with the sideband $I_{sb}(x, y) = I_0 e^{-i\Phi}$. The phase angle is obtained using

$$\Phi = \tan^{-1}\left(\frac{\text{Im}\{I_{sb}\}}{\text{Re}\{I_{sb}\}}\right) \ . \tag{3.2}$$

This value is limited between -$\pi$ and $\pi$ which makes it necessary to unwrap the data to remove unphysical discontinuities. A schematic of the process using a synthetic fringe pattern is shown in Fig. 3.3.

From the phase information the electron density can be calculated assuming cylindrical symmetry using the inverse Abel transform [188, 189]

$$f(r) = -\frac{1}{\pi}\int_r^R \frac{\partial g(y)}{\partial y}\frac{1}{\sqrt{y^2 - r^2}}dy \ , \tag{3.3}$$

where $f$ is a function corresponding to the reconstructed density, $g$ is a function corresponding to the measured phase shift, $r$ is the distance between the object axis (along $x$) and a point on the integral phase distortion path $g(y, x)$, and $R$ is the object radius which is often set to infinity. A schematic of the variables involved is shown in Fig. 3.4. To obtain the real electron density value $n_e$ from $f$, a pre-factor of $\lambda_0 n_{\text{cr}}/\pi$ has to be multiplied with the function $g$ which comes from the relation of the refractive index in plasma (see Appendix A.4), where $\lambda_0$ is the probe wavelength and $n_{\text{cr}}$ is the associated critical density.

A real interferogram from the experiment is presented in Fig. 3.5 clearly showing the ionisation front of the drive laser pulse (propagating towards the right-hand side). The corresponding phase shift was obtained for the region highlighted in the left panel.

The interferometry probe is not able to capture the wakefield structure because the pulse's passing time through the plasma column is longer than the time over which the density perturbations propagate more than a plasma wavelength. Single-shot

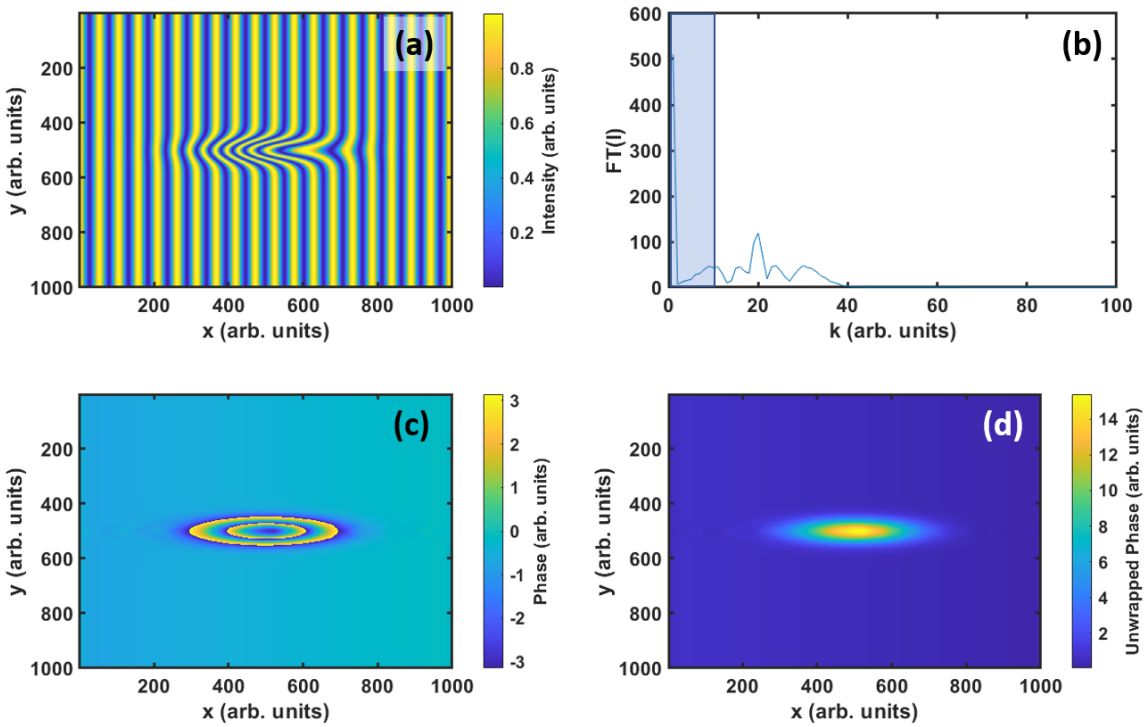



Figure 3.3: This figure shows the steps of the phase reconstruction algorithm. A synthetic interference pattern (a) is created from which the Fourier transform of the intensity is calculated (b). Here, only one of the two symmetric parts of the Fourier transform is shown. The blue shaded area is the part that is being removed from the signal and the side peak at $k = 19$ is shifted to the central zero position. The inverse Fourier transform of the shifted signal returns the sideband intensity from which the phase angle information can be extracted (c). This data is then unwrapped to give the final phase shift (d).

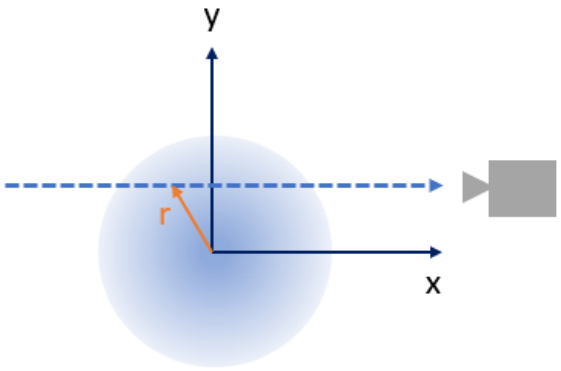



Figure 3.4: Schematic of variables involved in Abel transform for a cylindrically symmetric distribution. The dashed blue line is the line of sight.

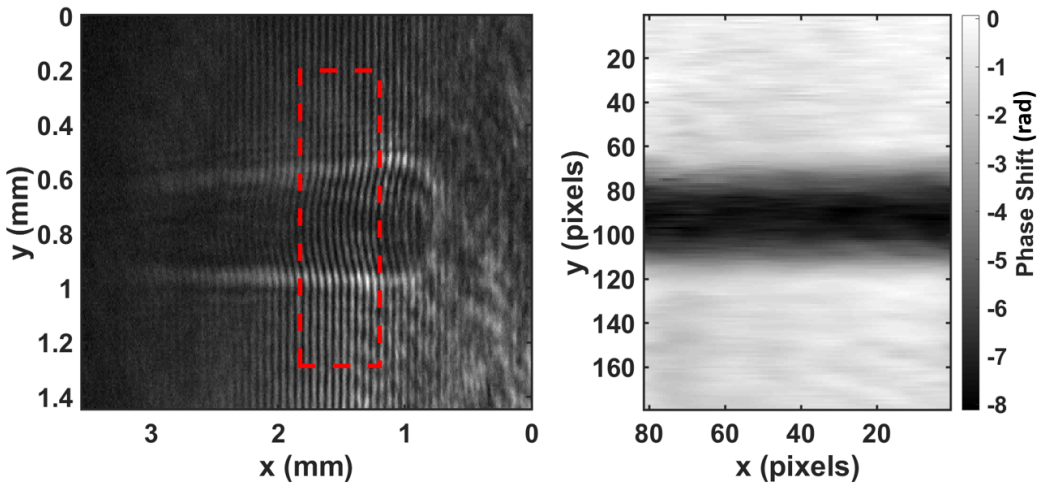



Figure 3.5: Data obtained from the perpendicular interferometry probe. The left part shows the interferogram, in which the ionisation front of the propagating laser as well as fringes from the pulse interfering with itself after passing through a Mach-Zehnder interferometer, can be seen clearly. The phase shift on the right-hand side was extracted from the area indicated by the dashed red rectangle in the left panel and is given in radian.

frequency-domain diagnostics [190, 191] have proven to be useful tools with which wakefield structures can be measured. The frequency-domain holography (FDH) method in which the diagnosing pulses co-propagate along the same axis as the driver has been used to produce snapshots of wakefield structures [183, 192]. However, due to the co-propagation, the results may blur significantly through an effect called "group velocity walk-off" where the wakefield structure slips backwards over the propagation distance with respect to the probe pulse. To diagnose the evolution of the wakefield Dong *et al.* used an oblique-angle frequency-domain streak camera (FDSC) [192] where the reference and probe pulses penetrate the plasma column at an angle. The spectrometer is oriented such that the wakefield evolution is encoded within the frequency information through a chirp (change of frequency between front and back of the pulse).

In the experiment analysed in this section, a modified FDH diagnostic was used in which the reference and probe pulses propagated at an angle with respect to the driver pulse and in which the spectrometer was oriented such that a snapshot of two spatial axes was taken rather than an FDSC video of the wakefield evolution. In detail, the phase was measured across the $x$-$y$-plane rather than the $x$-$z$-plane (see axis definition in Fig. 3.2). Both frequency-doubled 1 mJ diagnosing pulses were equally chirped in frequency and arrived at the target chamber centre with a time difference

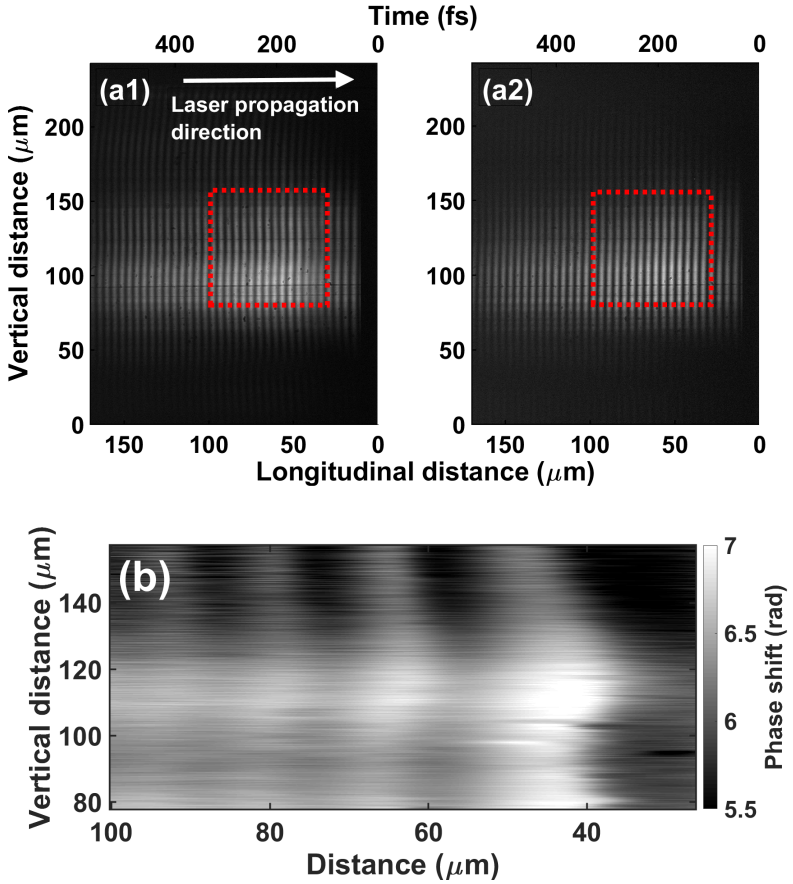



Figure 3.6: This figure shows a spectrogram (intensity signal from spectrometer CCD) obtained from the interference of the chirped reference and probe pulses using the oblique-angle FDH diagnostic. Panel (a1) shows interference after the probe has propagated through plasma. Panel (a2) shows an equivalent measurement for a shot in which no gas was used. The drive pulse propagation direction is from left to right. The $x$-axis was mapped from laser wavelength to time (upper $x$-axis) using calibration data from [184]. This axis was converted to distance using the approximate laser group velocity (lower $x$-axis). The bottom panel shows the reconstructed (unwrapped) phase in which the wakefield structure within a cluster plasma is visible. The axes limits are indicated by the dashed red rectangle in the upper panels.

of $\sim 1\,\mathrm{ps}$, the "reference" pulse arriving before the wakefield had been created and the "probe" pulse overlapping with the density perturbations and drive pulse. This overlap caused a phase shift to be imprinted onto the probe. It is important to note that the reference and probe pulses were not strong enough to ionise the gas target or perturb the wakefield. After exiting the interaction region, the interference of the reference and probe pulse was measured using a spectrometer the result of which can be seen in Fig. 3.6(a). The intensity signal obtained by the spectrometer is

$$I(y,\omega) = |E_{\mathrm{ref}}(y,\omega)|^2 + |E_{\mathrm{pr}}(y,\omega)|^2 + E^*_{\mathrm{ref}}(y,\omega)E_{\mathrm{pr}}(y,\omega) + E_{\mathrm{ref}}(y,\omega)E^*_{\mathrm{pr}}(y,\omega)\ , \quad (3.4)$$

where $E$ is the complex electric field corresponding to the respective laser pulse. Writing these fields as

$$E_{\mathrm{ref}}(y,\omega) = A_{\mathrm{ref}}(y,\omega)e^{i\Phi_{\mathrm{ref}}(y,\omega)}\ , \quad (3.5)$$

and

$$E_{\mathrm{pr}}(y,\omega) = A_{\mathrm{pr}}(y,\omega)e^{i[\Phi_{\mathrm{pr}}(y,\omega)+\omega\tau]}\ , \quad (3.6)$$

where $A = |E|$ is the amplitude, $\tau$ is the arrival time difference between the two pulses and $\Phi$ is the phase of the respective pulse, gives

$$I(y,\omega) = A_{\mathrm{ref}}(y,\omega)^2 + A_{\mathrm{pr}}(y,\omega)^2 + 2A_{\mathrm{ref}}(y,\omega)A_{\mathrm{pr}}(y,\omega)\cos\left[\omega\tau + \Delta\Phi(y,\omega)\right]\ . \quad (3.7)$$

For equal amplitudes

$$I(y,\omega) = 2A(y,\omega)^2\left\{1 + \cos\left[\omega\tau + \Delta\Phi(y,\omega)\right]\right\}\ . \quad (3.8)$$

From this equation one can see that in the frequency domain an interference pattern with period $2\pi/\tau$ is present. If the second pulse obtains a phase shift by travelling through a plasma the information will be encoded within $\Delta\Phi$. Taking the Fourier transform of equation 3.8 gives the signal $\mathcal{F}[I(\omega)] = \tilde{I}(t)$ in the time domain consisting of a central peak corresponding to the amplitude values of the electric field (autocorrelation term) and two peaks corresponding to the mixed terms positioned at $t = \pm\tau$. Isolating one of the symmetric side peaks, shifting it to zero, and taking the inverse Fourier transform modifies equation 3.8 to

$$I(y,\omega) = A(y,\omega)^2 e^{i\Delta\Phi(y,\omega)}\ . \quad (3.9)$$

Dividing this by the "null shot"-data $I_0(y,\omega)$ (corresponding data obtained from using the same algorithm on a shot in which no plasma was created) gives $\exp\{i(\Delta\Phi - \Delta\Phi_0)\} = \exp\{i(\Delta\Phi^*)\}$ from which the phase difference can be obtained

using equation 3.2. The result using the two interferograms from Fig. 3.6(a) is shown in Fig. 3.6(b). Note, that the position of the drive pulse propagation axis was not measured in the experiment and is not given in Fig. 3.6(b). This is because only the density perturbation caused by the driver has an effect on the probe pulse properties, not the driver itself. Therefore, going forward, the argument is being made that the line along $x$ with the largest phase shift magnitude is the propagation axis.

Using the null shot as a reference makes it possible to remove the artificial phase shift signal which is caused by the diagnostic itself rather than the laser-plasma interaction. The results obtained from the oblique-angle diagnostic show a wakefield structure that differs in two ways from what is found in experiments using a uniform density target.

First, the "horseshoe" structure is inverted which means that the wavefronts curve in the opposite direction (backwards in the frame of the propagating laser pulse) to what would be predicted theoretically in a uniform plasma[5].

Second, the wavelength of the plasma perturbation increases from left to right (towards the first wake behind the laser pulse). The observed first and second plasma wavelengths were found to be consistently larger than the theoretically predicted value of $2\pi c/\omega_\mathrm{p}$ (where $\omega_\mathrm{p}$ is calculated using the average electron density) throughout a great variety of shots at different average plasma electron density values (see Fig. 3.7). This shows the reproducibility of the effect of clusters causing an increased first wakefield wavelength.

It has to be noted that, due to the angle between the drive and diagnosing pulses, there exists a group velocity difference which causes a relative slip along the $x$-axis resulting in a blur within the phase acquisition. The geometrical idea behind this is shown in Fig. 3.8. The difference in velocity along the $x$-axis between wakefield and probe pulse caused by the angle of incidence $\alpha$ leads to a blur of the radially symmetric (good approximation for wakefields) structure with radius $r$, given as a shift $s(r) = \pm r \tan(\alpha/2)$ (for details of the derivation see Appendix C.1). This error is consistent across the observed (projected) dimension and, thus, does not alter the qualitative interpretation of the wakefield structure. The blur is illustrated using a mathematical computation whose results are shown in Fig. 3.9. First, a spheroid is created with radially decreasing density. The spheroid's extent in the $y$ and $z$ dimensions (same axis convention as above) is equal (rotational symmetry about the

[5]The forwards curvature in uniform plasma wakefields is an effect linked to the relativistic electron mass increase in regions of strong laser fields. Therefore, the plasma wavelength increases close to the laser axis.

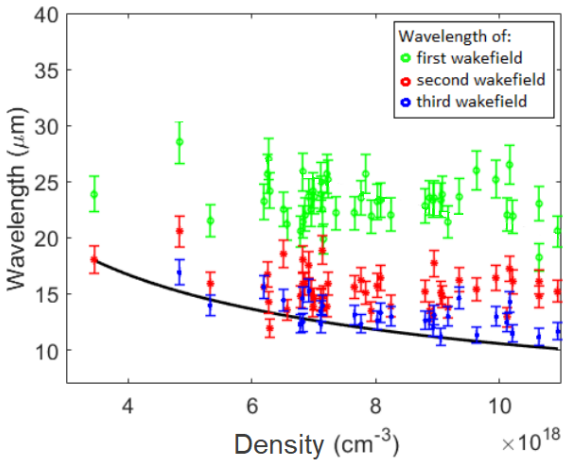



Figure 3.7: Results of wakefield wavelength measurement. The magnitude of the first, second and third wavelength is plotted against the electron density which was obtained from the interferometry diagnostic. The plot shows data from several shots. The theoretical value for a uniform plasma is indicated using a black curve. The values were obtained from an on-axis measurement of the distance between successive phase minima. The error bars were obtained from pixel-on-CCD to time conversion parameter ($b = (1.81 \pm 0.12)$ pix/fs) calibration. Figure modified from [184].

$x$-axis) while it is smaller along $x$. The top left panel shows an integration along the $z$-axis in a resting frame, showing the ideal case of a perfect blur-free detection. The other panels show what a chirped probe pulse propagating at an angle of incidence of 8°, 20°, or 45° would detect (note that axis has changed from $x$ to $\lambda$ as the spectrometer detects the wavelength of the probe). Using a coordinate transformation (see Appendix C.1), one can compute the intersection of an object in $x$-$y$-$z$ space with a plane in $y$-$\lambda$ space propagating the values in both coordinate systems at a given velocity and angle after each time step. For example,

$$x = u(\lambda - \lambda_0)\cos(\alpha) + t\left(c_{\text{probe}}\cos(\alpha) - c_{\text{wake}}\right) \ , \tag{3.10}$$

where the chirp factor $u$ converts from wavelength to distance, $c$ is the respective velocity, $\alpha$ is the angle of incidence, $t$ is the time, $\lambda$ is the wavelength of the probe pulse, and $\lambda_0$ is the central wavelength of the probe pulse. In the remaining three panels in Fig. 3.9, the integration is over time instead of space. With increasing angle the blur becomes stronger. Two important conclusions can be drawn. First, the $y$-axis values are not directly dependent on the blur. Second, the distance between the periodic density perturbations is not affected as the shift is the same for all frequencies, allowing for a quantitative measurement of the wakefield wavelength. A solution to overcome this blur is to use a modified Abel inversion [181], in which

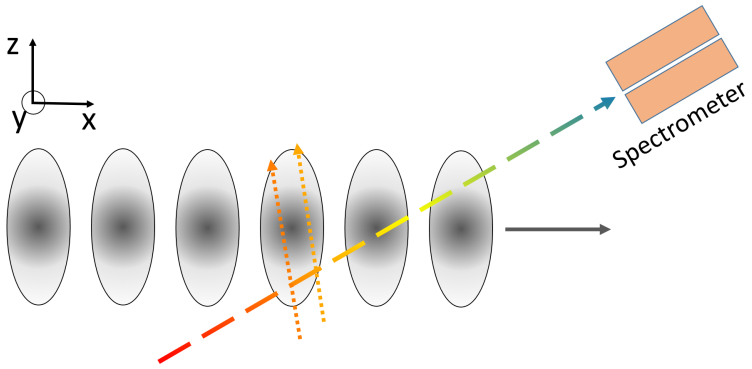



Figure 3.8: Schematic showing a phase acquisition slip due to the difference in velocity projected onto the $x$-axis of wakefield and probe. The probe pulse slice measured in the spectrometer is shown as the dashed line with colours representing the frequency chirp. Two paths of sight are shown as dotted lines in different shades of orange corresponding to particular wavelengths of the probe. These paths symbolise the relative shift of the probe pulse in the frame of reference of the wakefield.

the group velocity difference is accounted for. This formula differs from Eq. 3.3 by a term $\cosh\left(ka\sqrt{y^2 - r^2}\right)$ within the integral.

### 3.1.2 Two-dimensional particle-in-cell simulations

In order to get a better understanding of the process causing the modifications to the wakefield structure, I used a particle-in-cell code to study the interaction. For this task, the fully relativistic code OSIRIS [125] was used. Even though three-dimensional simulations are in principle available, they proved infeasible for simulating this particular interaction due to the high computational cost associated with the spatial and temporal resolution required to study nanometre-sized objects at the same time as wakefield structures which cover tens of micrometres. Since the experimental diagnostics did not measure any cluster parameters, estimates had to be taken from the literature to feed the simulation input. As was shown in the introduction, cluster sizes can range (depending on the conditions) between 1 nm and 10s of nm with electron density values on the order of the critical density for $\lambda_0 = 800\,\mathrm{nm}$. Since a large-scale parameter scan was not feasible, two values for each of those parameters (four configurations) were chosen in this section (details in section 3.1.2.2).

#### 3.1.2.1 Modifications to OSIRIS code

In order to probe the interaction of a laser pulse with randomly distributed plasma clusters, the particle density distribution options in OSIRIS - mainly written in For-

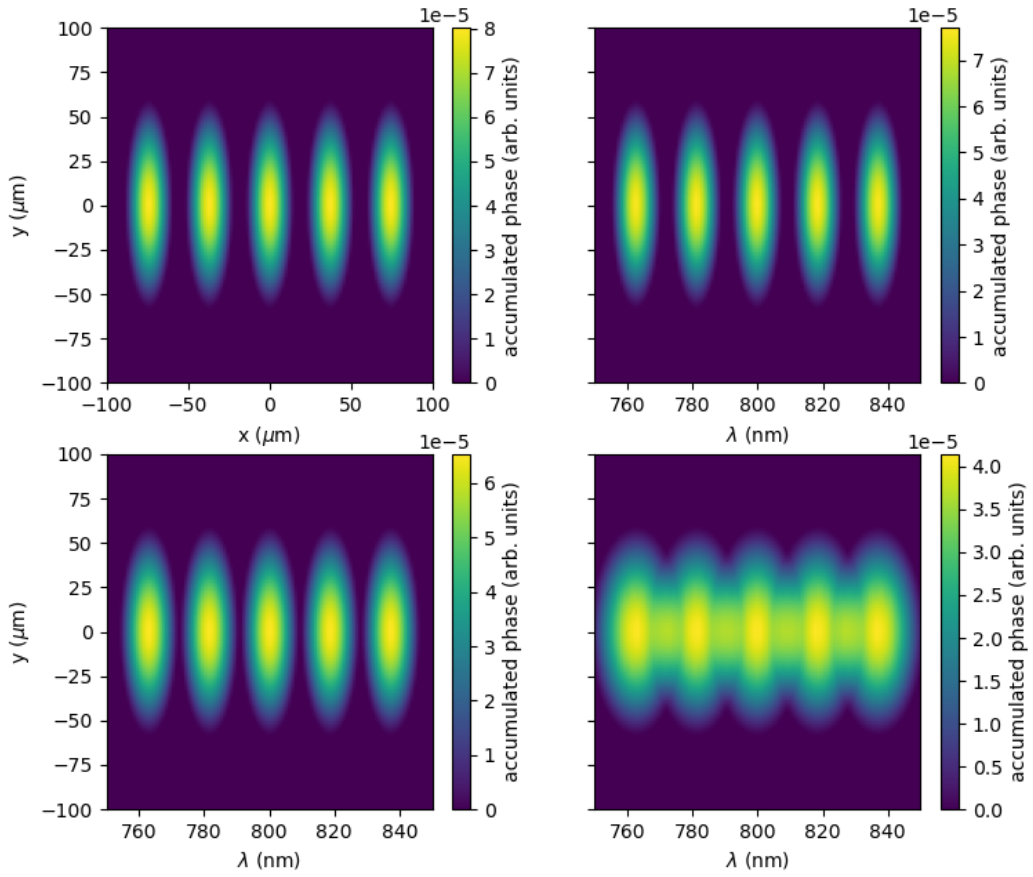



Figure 3.9: Accumulated phase by integration of periodic spheroid structures (synthetic wakefield signal). In the top left panel the integral is taken over the $z$ coordinate of the static wakefield structure leaving an image of the phase plotted over the $x$ and $y$ axis. In the remaining panels the integral is taken over the time coordinate emulating the phase imprinted onto a chirped probe pulse with a central wavelength of 800nm propagating at an angle of 8° (top right), 20° (bottom left), and 45° (bottom right) with respect to the density perturbation's propagation direction.

tran 90 and Fortran 2003 - had to be modified. A staggered grid of clusters was implemented using an analytic function to describe the particle density distribution across the whole simulation area. This function can, for example, consist of a periodically repeating pattern caused by the use of a modulo operation making the cluster separation a function depending on the cluster's (uniform) number density, cluster diameter, and the average particle density within the simulation box. Even though this option is available, realistic modelling of the clusterisation process requires randomness of the clusters' initialisation positions. To this end, the OSIRIS module **m_psource_std** was modified (see Appendix B.1 for code). Within this module, the subroutine **read_input_std()** was extended to be able to read the parameters

- cluster shape (i.e. "square", "sphere")
- cluster density
- cluster average density
- cluster width (diameter of sphere or side length of cube)
- cluster xmin, ymin, zmin (start of cluster initialisation in dimension $i$)
- cluster xmax, ymax, zmax (end of cluster initialisation in dimension $i$)
- cluster ramp xmin (start of linear density ramp)
- cluster ramp xmax (end of linear density ramp)
- cluster seed (necessary for pseudo-random number generation)

whose values can now be assigned in the input deck. After reading the parameters from this input deck, the subroutine creates a pseudo-random array from the input seed to feed the **random_number()** subroutine. The next step is to compute the cluster volume from the *cluster width* parameter which depends on the shape and dimension of the simulation. Then, the plasma volume is computed which does not necessarily have to be equal to the simulation box volume. Using the cluster volume, the plasma volume and the other input parameters, the number of total clusters that have to be initialised can be easily computed. The total cluster number is then used for allocating the size of the **cluster_center** array. Next, this array is filled with randomly distributed positions within the chosen input limits which allows for decoupling the total simulation box from the plasma filled box. Before this variable

is passed on to other subroutines, a bubble sort algorithm is applied to the $x$-values for better efficiency in parallelised codes.

In the case of initialisation of a linear particle density ramp, the process of determining the cluster centre positions is less trivial (see Appendix A.5). The equation governing the cluster positions is found to be

$$x_c = x_0 + \sqrt{\frac{R}{V_n}}\Delta x \ , \tag{3.11}$$

where $x_c$ is the cluster centre position, $R$ is a random number with uniform distribution between 0 and 1, $V_n$ is the ratio of ramp volume over total volume $V_n = V_r/V_{tot}$, and $\Delta x$ defines the ramp length.

The **get_den_value_std()** subroutine initialises the particles and loops over all cells and all cluster centre values in the simulation when it is called. The sorting algorithm mentioned above reduces the runtime of the simulation when operating on several cores. This is done by limiting the loop indices (which correspond to the centre values of the clusters) to values that are within the cells being addressed by the current node that has called the **get_den_value_std()** subroutine. The above-mentioned subroutines are called within the function **inject_std()** for every particle species that is defined in the input deck. This function also accounts for the number of macro-particles per cell for each species.

#### 3.1.2.2 Results of simulations

The clusters initialised at the right simulation boundary (moving to the left in the co-moving frame) had a circular shape, radius of $r_{cl} = 12.7\,\text{nm}$, electron temperature of $T_e = 10\,\text{eV}$ and peak electron density of $n_{\text{cl}} = 1.5\,n_{\text{cr}} = 2.61 \times 10^{21}\,\text{cm}^{-3}$ where $n_{\text{cr}} = \omega_0^2 m_e \epsilon_0 / e^2$ is the critical density of plasma for the drive pulse frequency $\omega_0$. The total electron density (averaged over the simulation box) was $\langle n_e \rangle = 0.004\,n_{\text{cr}}$ $= 6.97 \times 10^{18}\text{cm}^{-3}$ which is within the range of plasma densities measured in the experiment. The normalised laser amplitude $a_0$ was set to 0.72. The polarisation of the laser was linear and its vector was parallel to the simulation plane ($\vec{E_0} = (0, E_y, 0)$). The laser pulse had a Gaussian shape in both longitudinal and perpendicular directions. The FWHM duration of the pulse was 45 fs and the transverse FWHM was 32 µm. Because a high resolution was needed to resolve the cluster structure, 160 cells per laser wavelength (corresponding to 14000×12000 cells) were used with $16 \times 16$ electron macro-particles per cell and $4 \times 4$ ion macro-particles per cell. The particle boundaries were absorbing and the longitudinal (transverse) field boundaries were

of type "Lindman"[6] [193] ("open"). To satisfy the Courant-Friedrichs-Lewy (CFL) condition [123]

$$\frac{1}{\Delta t^2} \geq \sum_i \frac{c^2}{\Delta x_i^2} \qquad \longrightarrow \qquad \Delta t \leq \sqrt{\frac{\left(\frac{x}{n_x}\right)^2 \left(\frac{y}{n_y}\right)^2}{\left(\frac{x}{n_x}\right)^2 + \left(\frac{y}{ny}\right)^2}}\,, \tag{3.12}$$

where $\Delta x_i$ is the length of a spatial step in dimension $i$, $t$ is the temporal step, $n_x$ and $n_y$ are the numbers of cells per distance unit $x$ and $y$, respectively, which define the size of the simulation box in each direction, a simulation time-step of 16.6 as had to be used[7]. The plots in this section show data taken at the last simulation iteration corresponding to 0.42 ps of propagation within the plasma.

Two simulations of the same average electron density are compared in Fig. 3.10, one using a cluster plasma (panels (a), (b), (c), and (e)) and one using a uniform plasma distribution (panels (d) and (f)). In the top panel, the initially over-dense clusters (injected from the right-hand boundary of the simulation box) start expanding as soon as they start interacting with the laser pulse (in relative terms, the laser pulse propagates towards the right-hand side). Closer investigation of these density patterns reveals that the electrons oscillate around the positively charged ion clusters to form dipole-like structures synchronised with the laser field (see Fig. 3.11). Within one half-oscillation of the laser field, the majority of electrons associated with an ion cluster are located on one specific side of this ion cluster depending on the sign of the perpendicular electric field. The electrons within this oscillating cloud spend a significant amount of time outside of the ion cluster which causes the repulsive Coulomb force to drive an explosion of the electron bunch which prevents a large fraction of the electrons from being recaptured by the ion cluster. Therefore, over the distance of a few µm, more and more electrons are dissociated from their original ion cluster and move around "freely". With increasing distance, the magnitude of the electrostatic forces of neighbouring clusters seen by the electrons increases which, in return, further reduces the effect of the confining electrostatic potential to the vicinity of the respective cluster of origin. As this number density of dissociated electrons continues to increase behind the laser pulse to the left (see Fig. 3.11), the plasma frequency increases accordingly. This causes the plasma wavelength to decrease until all clusters have homogenised, at which time it matches that of a uniform plasma of the same average density.

[6] This free-space boundary condition allows launching of arbitrary waves into the computational region and separation of ingoing and outgoing waves.

[7] Note that $c = 1$ in OSIRIS units.

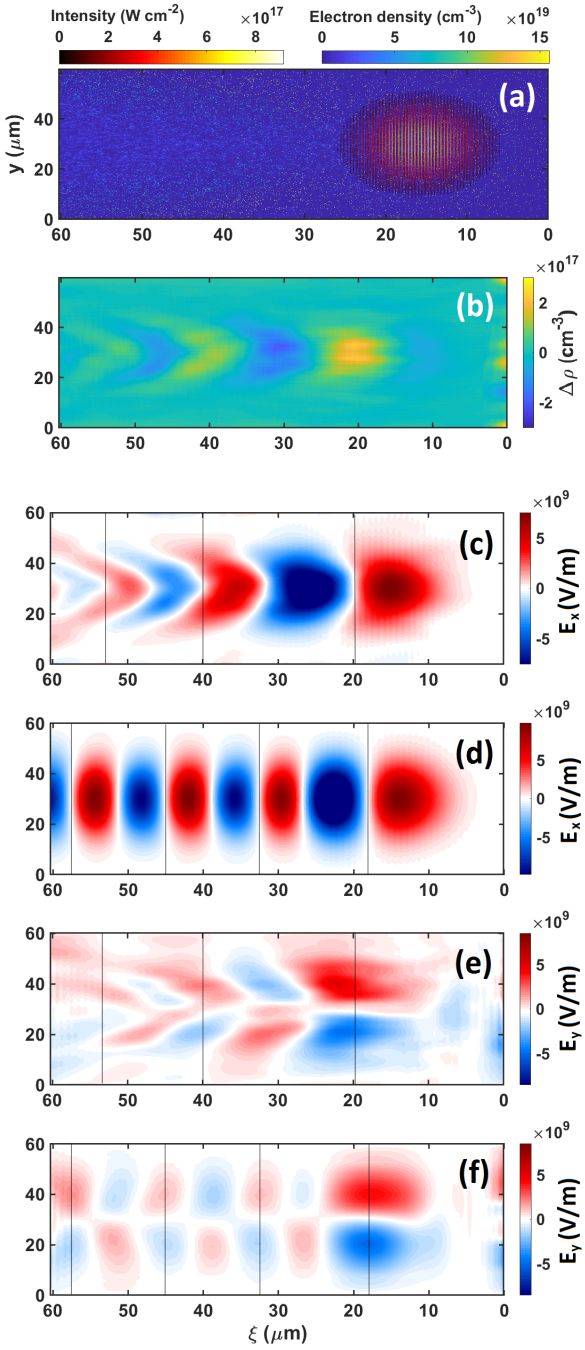



Figure 3.10: Results of the 2D moving window particle-in-cell simulations. The laser pulse propagates towards the right. Panel (a) plots the electron density and the laser intensity in a cluster plasma. Panel (b) shows perturbations in the filtered charge density caused by the laser pulse interacting with the cluster plasma. The longitudinal electric field caused by the density perturbations is shown for a cluster plasma in panel (c) and for a uniform plasma in panel (d). The transverse electric field is shown for a cluster plasma in panel (e) and for uniform plasma in panel (f). The laser duration for both simulations was 45 fs. The average electron density was $6.97 \times 10^{18}\,\mathrm{cm}^{-3}$.

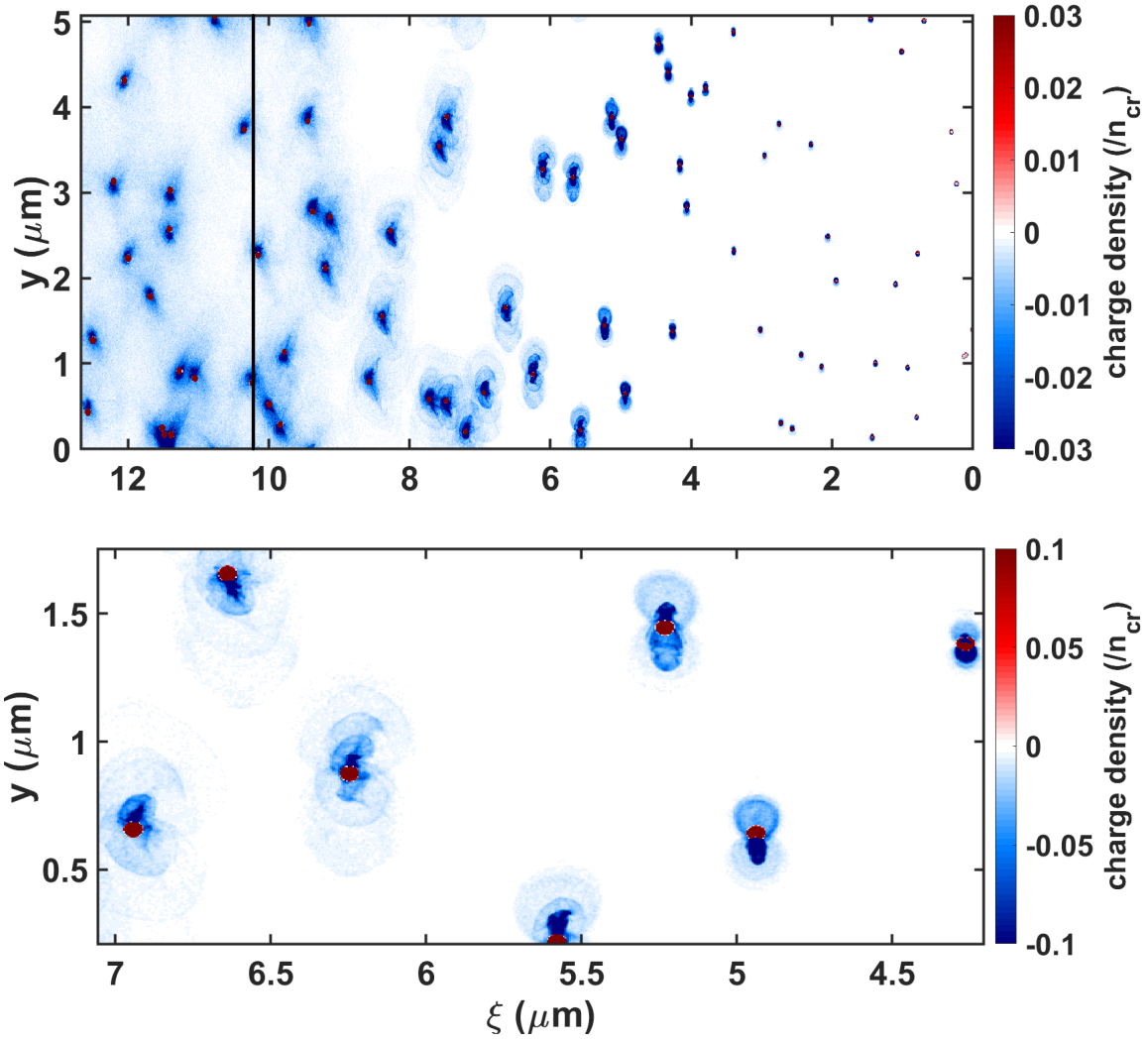



Figure 3.11: Close-up of electron and ion charge density from a PIC simulation plotted in the region in which clusters interact with the laser pulse. The laser pulse is centered at $\xi = 17\mu$m and, therefore, outside of the shown box. The (right) FWHM location of the laser front is indicated by the black vertical line in the upper panel. Ion clusters are plotted in red, electrons in blue. The circular clusters were initialised with a peak density of $1.5 \times n_{cr}$ and radius of 12.7nm. The top window shows the increase of "free" electron density towards the left. The bottom window (closer zoom) shows the periodic event of electrons being ripped out of the cluster followed by the Coulomb explosion mechanism.

Panel (b) of Fig. 3.10 shows the perturbations in the charge density $\Delta\rho$ in a cluster plasma. In this plot, the wakefield structure is clearly visible. Panel (c) plots the corresponding longitudinal electric field for the cluster simulation and panel (d) shows the results of the same diagnostic for a uniform plasma simulation. The electric fields have been smoothed using a two-dimensional Gaussian smoothing kernel with a standard deviation of 350 cells (corresponding to 1.75 µm) to average the quickly varying fields from the cluster oscillations. The wakefield wavelength is measured from these results. The vertical lines in the plots indicate the boundaries between complete oscillations of the plasma wave. Calculating the theoretical uniform plasma (Langmuir) wavelength as is given in [73] for a plasma electron density of $n_e = 6.97 \times 10^{18}\mathrm{cm}^{-3}$ gives a value of $\lambda_p = 12.6\,\mu\mathrm{m}$. This result is close to the measurements made from the simulations in the uniform case ($\lambda_{p,1} = 14.9\,\mu\mathrm{m}$, $\lambda_{p,2} = 12.5\,\mu\mathrm{m}$, and $\lambda_{p,3} = 12.5\,\mu\mathrm{m}$ for the first three wavelengths) but differs from the values obtained from the cluster simulations ($\lambda_{p,1} = 20.1\,\mu\mathrm{m}$ and $\lambda_{p,2} = 13.3\,\mu\mathrm{m}$). Comparing the results of Fig. 3.10 to the experiment (approximately 23 µm and 17 µm) at corresponding electron density shows that the simulation wavelengths are slightly shorter. This could be linked to the cluster conditions and cluster filling fraction (ratio of cluster plasma to background uniform plasma) which were not measured in the experiment.
The shape of the wakefield in the cluster simulation is observed to behave in a similar manner to what is found from the experimental results (Fig. 3.10(b)). Again, the wavefronts curve into the direction opposite of the laser propagation direction and the first plasma wavelength is larger than those trailing it. In contrast, the uniform wakefield results confirm that—as was expected—the wakefield wavefronts curve (marginally) forwards.

The transverse electric field is depicted in panels (e) and (f), where the same Gaussian smoothing kernel has been applied as for the longitudinal electric field. The magnitude of the laser pulse's electric field along the $y$-direction is larger than the vertical field caused by the wakefield. For this reason, the wakefield's electric field had to be extracted from the simulation diagnostic—the result of which is shown in panels (e) and (f). In order to isolate the laser field's imprint, the Fourier transform of the data was taken after which the high-frequency components corresponding to the laser oscillations were removed. After this, an inverse Fourier transform was applied which resulted in the fields shown. This method is equivalent to applying a low-pass filter that has a specific cut-off frequency at $\omega_c < \omega_0$.

Even though the experiment did not study electron acceleration and no particles were (self-)injected in the simulations due to the insufficient laser amplitude, it could

be of interest to discuss how externally injected electrons behave in the wakefield (i.e. how the beam properties are preserved). A qualitative estimate of the change in beam emittance was made from the available simulation data in Fig. 3.10. Keeping the normalised transverse root mean square emittance $\epsilon_{\mathrm{n,rms}} = \frac{1}{m_0 c}\sqrt{\langle y^2\rangle\langle p_y^2\rangle - \langle y p_y\rangle^2}$ (average taken over all electrons in beam cross section) small requires the radial extent of the focusing fields to be larger than the electron beam waist. Assuming typical electron beam diameters of a few µm, this condition is indeed satisfied in both uniform and cluster plasma for the transverse and focusing fields shown in the two bottom panels of Fig. 3.10. Furthermore, similar vertical field strengths will lead to similar transverse emittance. This is fulfilled for both cases analysed. The last condition that has to be met to ensure high beam quality for externally injected electrons is that there needs to exist a region in which accelerating longitudinal fields overlap with focusing transverse fields. This is the region in which the electron beam is efficiently accelerated and preserves its emittance. One sees in panels (c), (d), (e), and (f) that such a region does indeed exist for both simulations with the difference that for the cluster case this particle bucket is decreasing in size for subsequent wakes. These conditions allow for preserving the electron beam emittance. However, there is another factor that may degrade the emittance: the clusters are randomly distributed which means that, even though the fields allow, on average, for the emittance to be preserved, strong microscopic fluctuations of the electric fields caused by ion clusters influence some parts of the electron beam stronger than others. This "collision" with the ion cluster can worsen the effective emittance of the propagating electron beam.

To further investigate the origin of the wakefield curvature, three additional PIC simulations were run. These had a limited vertical extent corresponding to a horizontal slice through the large scale simulations above. Here, a plane wave laser pulse (Gaussian duration of 45 fs) was used. The laser amplitude was varied between the values 0.9, 0.72, and 0.5 in the simulations shown in Fig. 3.12. The simulation box consisted of $12000 \times 1000$ cells with $32\times32$ electron macro-particles and $2\times2$ ion macro-particles within each cell. The time step satisfied the CFL condition ($\Delta t = 11.9\,\mathrm{as}$) and the electromagnetic field boundary conditions at the top and bottom boundary were periodic. The results show that the plasma wavelength scales with the laser pulse amplitude—the higher $a_0$, the smaller $\lambda_p$. The measured values are shown in Tab. 3.1. This scaling can be explained when considering that the cluster expansion is also a function of the laser amplitude. If the laser pulse electric field increases, the electrons start their expansion earlier which leads to a higher free electron plasma density. Here, "free" means that the electron ceases to be bound to the cluster and

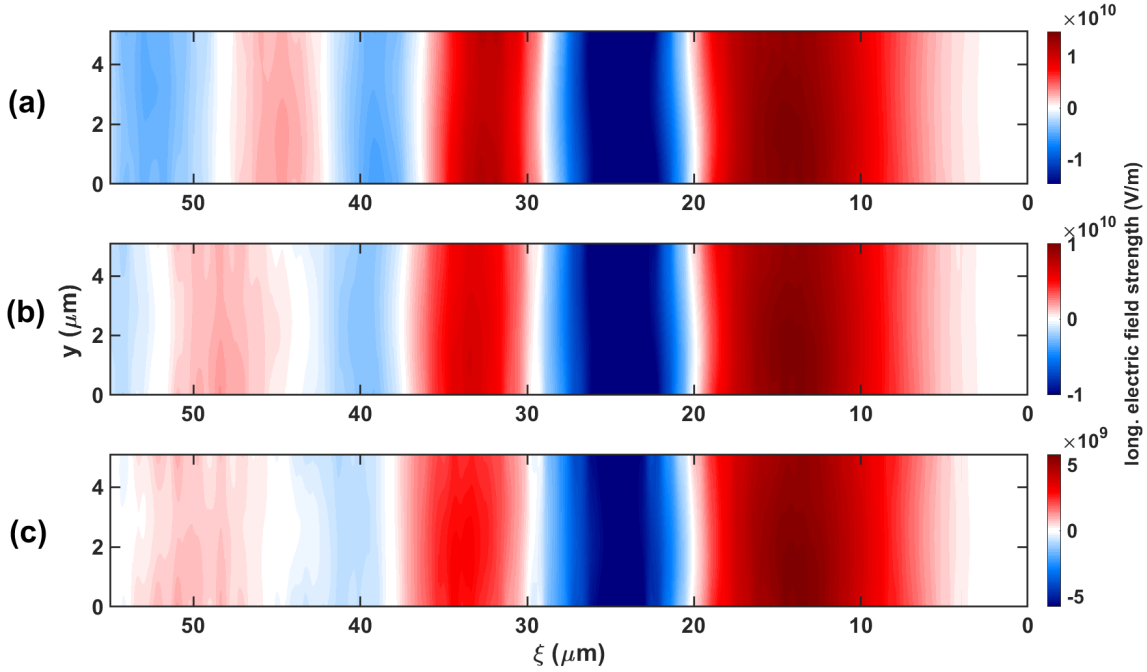



Figure 3.12: Longitudinal electric field results from two-dimensional PIC simulations for various laser pulse amplitudes. The laser amplitudes are (a) $a_0 = 0.9$, (b) $a_0 = 0.72$, and (c) $a_0 = 0.5$. The electric field is smoothed over 350 cells. The laser pulse is centered at 17µm.

| Simulation | $a_0$ | 1st wavelength (µm) | 2nd wavelength (µm) |
|---|---|---|---|
| (a) | 0.9 | 16.5 | 11.6 |
| (b) | 0.72 | 17.6 | 14.3 |
| (c) | 0.5 | 18.2 | 16.2 |

Table 3.1: List of first and second wakefield wavelengths for different laser amplitudes.

| Simulation | cluster radius (nm) | cluster electron density ($/n_{cr}$) |
|---|---|---|
| (a) | 6.4 | 1.5 |
| (b) | 12.7 | 1.5 |
| (c) | 6.4 | 0.7 |
| (d) | 12.7 | 0.7 |

Table 3.2: List of cluster parameters for the study of cluster expansion.

stops contributing to the polarisation effect within the cluster. These results can be understood in the context of the proportionality between the plasma wavelength and the free electron density ${\lambda_p}^{-1} \propto \sqrt{n_e}$ which is in accordance with the wavelength increase observed in the simulations. It should be noted that the measured wavelengths are shorter than those obtained from the full-scale simulations which is likely to be due to the use of periodic boundary conditions[8] and the lack of a vertical component in the ponderomotive force. The curvature of the wakefield can now be linked to the simulations by arguing that the electron plasma wavelength is shortest on the laser propagation axis and increases symmetrically towards both sides (in $y$-direction) due to the decrease in laser amplitude of a Gaussian laser pulse. Since the decrease in intensity is continuous the increase in electron plasma wavelength is also continuous which leads to a wakefield curvature towards the back.

Next, the impact that varying the cluster parameters has on the cluster expansion properties has to be considered. To this end, four additional simulations with varying cluster parameters were conducted. These parameters are listed in Tab. 3.2.

Fig. 3.13 shows that the initial cluster parameters have a significant impact on the expansion pattern of the cluster plasma. The white function overlaid on each panel is the electron density of a respective line-out (averaged over 50 cells along y to capture enough clusters) through the centre of the simulation box (on-axis). Clusters of high electron density (panels (a) and (c), $n_e = 1.5\, n_{cr}$) show early expansion if compared to the laser pulse position. Clusters of lower electron density ($n_e = 0.7\, n_{cr}$) are seen to expand slower when interacting with a laser of $a_0 = 0.72$ than their respective high density counterparts. This is expected because the Coulomb force (acting on a test charge on the edge of the cluster) between the cluster electrons scales as $F_c \propto n_{cl} r_{cl}$ where $r_{cl}$ is the cluster radius[9]. This is applicable whenever large clouds of electrons are collectively dislocated from the ion cluster by the Lorentz force. However, panel (b) exhibits a behaviour that is not easily explainable since its expansion pattern is

[8]Periodic boundary conditions prevent the particle density to decrease by being lost to regions outside of the box as particles exiting one boundary are re-initialised at the other boundary.

[9]The charge within a sphere scales as $\propto r^3$ and the field drops as $\propto r^{-2}$.

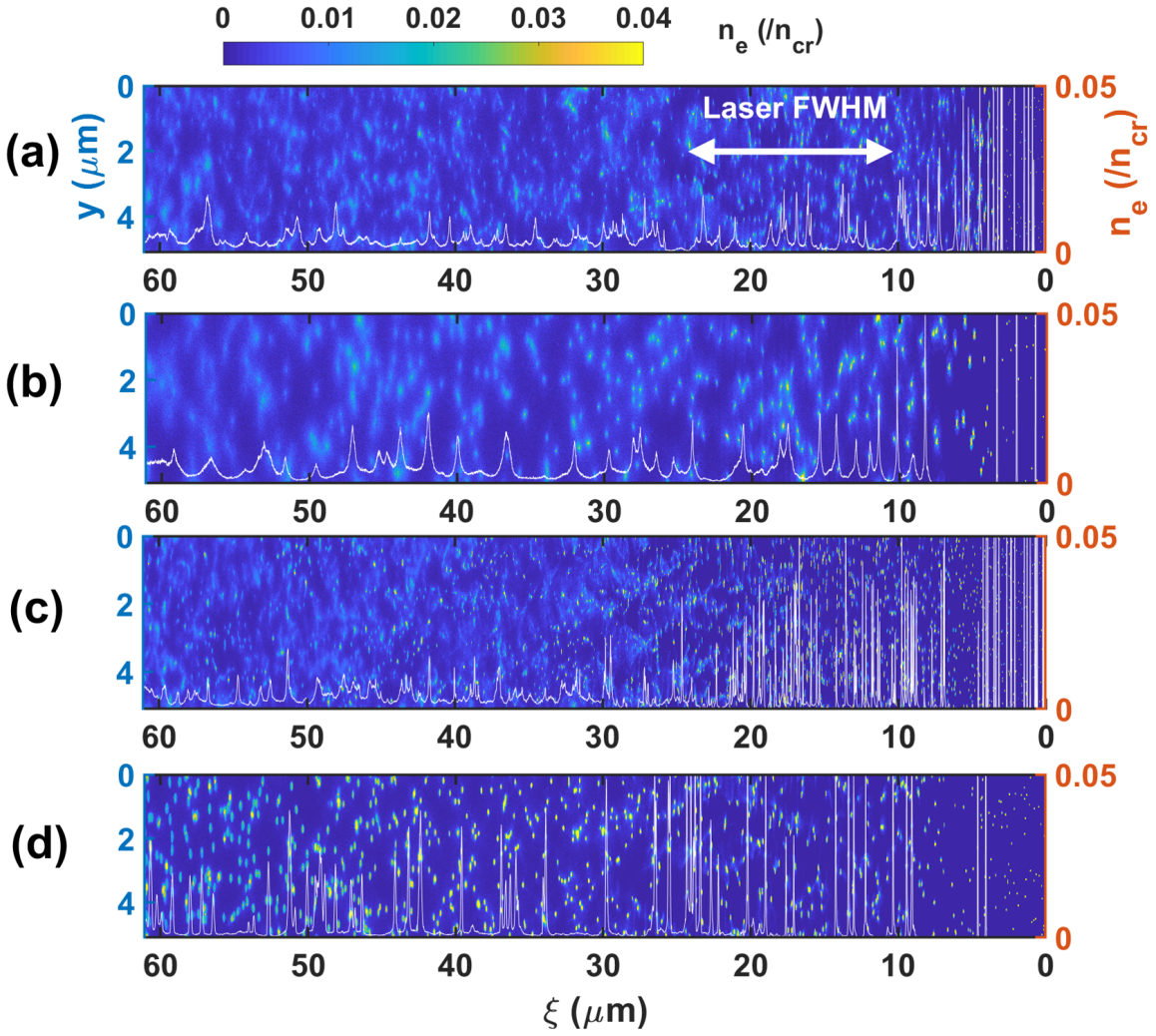



Figure 3.13: Electron density plots of four two-dimensional PIC simulations with varying cluster parameters. A horizontal lineout averaged over 50 cells in the centre is shown by the overlaid white curve. The initial cluster parameters are (a) $n_{cl}/n_{cr} = 1.5$, $r = 6.4$nm, (b) $n_{cl}/n_{cr} = 1.5$, $r = 12.7$nm, (c) $n_{cl}/n_{cr} = 0.7$, $r = 6.4$nm, and (d) $n_{cl}/n_{cr} = 0.7$, $r = 12.7$nm. The 45 fs laser pulse is centered at 17µm (as indicated by the white double arrow in the top window). The normalised laser amplitude for all simulations was $a_0 = 0.72$.

the slowest despite having a larger cluster radius. One explanation for this could be that the larger radius leads to a prolonged overlap of electrons and ions inhibiting efficient Coulomb explosion. The results show that by controlling cluster parameters in the plasma the wakefield properties are also controlled.

### 3.1.3 Quasi-analytic one-dimensional model

In this section, I will show how it is possible to give a one-dimensional description of the non-linear wakefield evolution in a cluster plasma by solving a commonly used set of equations consisting of Ampere's law, Gauss's law, and the equation of motion without resorting to the commonly used quasi-static approximation. The results are shown to support the findings of experimental data and two-dimensional PIC simulations.

Methods for computing the non-linear wakefield evolution [194, 195] generally depend on the condition that the temporal derivative of the quantities studied vanishes ($\partial/\partial\tau() = 0$) which means that these quantities evolve to a negligible extent in comparison to the derivatives with respect to the co-moving spatial variable $\xi = x - v_g t$. Here, $\tau = t$ is the time in the new frame, and $v_g$ is the group velocity of the laser pulse. This assumption is called the quasi-static approximation [196, 197]. In what follows, this generalisation cannot be used since, as dictated by the nature of clusters, the electron plasma density fluctuates strongly over space $\xi$ and time $\tau$.

Other authors studying uniform plasmas have followed the approach to integrate the continuity equation

$$\frac{\partial n}{\partial \tau} = 0 = \frac{\partial}{\partial \xi}[n(\beta_g - \beta_x)c] \tag{3.13}$$

to get an analytic expression for the number density. Since this is not valid for the cluster case, the differential equations governing Ampere's law (with Maxwell's addition)

$$\frac{\partial E_x}{\partial t} = -\frac{j_x}{\epsilon_0} = \frac{e n_e \beta_x c}{\epsilon_0}\hat{x} \tag{3.14}$$

and Gauss's law

$$\frac{\partial E_x}{\partial x} = -\frac{\rho}{\epsilon_0} = \frac{e(n_i - n_e)}{\epsilon_0}\ , \tag{3.15}$$

and the equation of motion in the co-propagating frame of reference (for derivation see Appendix A.6)

$$\frac{1}{c}\frac{\partial}{\partial \tau}(\gamma\beta_x) = \frac{\partial}{\partial \xi}\left[\tilde{\Phi} - \gamma\left(1 - \beta_g\beta_x\right)\right] \tag{3.16}$$

have to be solved simultaneously using a numerical scheme. In the equations above, $n_e$ is the electron density, $\beta_x$ is the normalised relativistic longitudinal electron velocity,

$j_x$ is the corresponding current, $E$ is the electric field, $\epsilon_0$ is the vacuum permittivity, $\rho$ is the charge density, $\gamma$ is the Lorentz factor, $c$ is the speed of light in vacuum, and $\tilde{\Phi} = (e\Phi)/(mc^2)$ is the normalised electrostatic potential. To proceed, Ampere's law and Gauss's law are combined into one equation giving

$$\frac{\epsilon_0}{ec}\frac{\partial E_x}{\partial t} = \left(n_i - \frac{\epsilon_0}{e}\frac{\partial E_x}{\partial x}\right)\beta_x \ , \tag{3.17}$$

where $n_i$ is the ion density. This equation, however, has to be modified to change into a co-moving frame of reference (Eulerian transformation). To do this, one uses the equations

$$\frac{\partial}{\partial x} = \frac{\partial \tau}{\partial x}\frac{\partial}{\partial \tau} + \frac{\partial \xi}{\partial x}\frac{\partial}{\partial \xi} = \frac{\partial}{\partial \xi} \ , \tag{3.18}$$

and

$$\frac{\partial}{\partial t} = \frac{\partial \tau}{\partial t}\frac{\partial}{\partial \tau} + \frac{\partial \xi}{\partial t}\frac{\partial}{\partial \xi} = \frac{\partial}{\partial \tau} - v_g\frac{\partial}{\partial \xi} \tag{3.19}$$

with which equation 3.17 becomes

$$\frac{1}{c}\frac{\epsilon_0}{en_0}\frac{\partial}{\partial \tau}E = \left(\frac{n_i}{n_0} - \frac{\epsilon_0}{en_0}\frac{\partial E}{\partial \xi}\right)\beta_x + \frac{\epsilon_0}{en_0}\frac{\partial}{\partial \xi}(\beta_g E) \ . \tag{3.20}$$

Here, $n_0$ is a reference electron density introduced for normalisation purposes. Equations 3.16 and 3.20 can be normalised using $\tilde{E} = eE/(mc\omega_p) = \omega_p\epsilon_0 E/(en_0 c)$, $\tilde{p}_x = p_x/mc$, $\partial/\partial\tilde{\tau} = 1/\omega_p\,\partial/\partial\tau$, and $\partial/\partial\tilde{\xi} = c/\omega_p\,\partial/\partial\xi$. This gives

$$\frac{\partial}{\partial \tilde{\tau}}(\tilde{p}_x) = -\tilde{E} - \frac{\partial}{\partial \tilde{\xi}}(\gamma - \tilde{p}_x\beta_g) \tag{3.21}$$

and

$$\frac{\partial}{\partial \tilde{\tau}}\tilde{E} = \left(\frac{n_i}{n_0} - \frac{\partial \tilde{E}}{\partial \tilde{\xi}}\right)\beta_x + \frac{\partial}{\partial \tilde{\xi}}(\beta_g \tilde{E}) \ . \tag{3.22}$$

This is the system of coupled partial differential equations (PDE) which need to be solved numerically to describe the wakefield behaviour in a cluster plasma. Typical PDE solvers such as the fixed (non-adaptive) stencil[10] approximation routines very quickly run into numerical instabilities when encountering strong parameter fluctuations. Therefore, to overcome this issue, a more stable method has to be used. Weighted essentially non-oscillatory (WENO) solvers [198] are tailored to the problem of large gradients in the computed parameters making them the optimal choice for the cluster case. A WENO scheme is a high-resolution numerical method developed to

[10]In this context, a stencil is a specific arrangement of points (nodes) from which a function can be numerically approximated. An example of two stencils to approximate $f(x_i)$ could be $S(f(x_{i-3/2}), f(x_{i-1/2}), f(x_{i+1/2}))$ and $S(f(x_{i-1/2}), f(x_{i+1/2}), f(x_{i+3/2}))$.

specifically solve hyperbolic[11] PDEs. It is an extension to the ENO scheme which uses a combination of many stencils instead of choosing a single one leading to a smoother numerical flux [199]. Both methods avoid including cells with discontinuities into the stencils for approximating the result. This is done through the use of an adaptive method automatically shifting the stencils into regions of optimal local smoothness of the function. This also helps to avoid oscillations at discontinuities in a stencil as described by the Gibbs phenomenon [200].

Generally, fluid computations of plasma behaviour have difficulties when encountering regions of vacuum [201, 202]. Analogously, in order to give a physical meaning to the quantities used (i.e. $\beta_g$ or $\omega_p$), a reference (background) density had to be used in the WENO scheme. This is why in addition to the clusters of peak density $n_{cl} = 1.5 \times n_{cr}$ (in contrast to the PIC simulations) a background density layer of $n_0 = 0.001 \times n_{cr}$ was introduced. Another issue was modelling the cluster expansion which was not feasible by using a pressure term as the method quickly ran into numerical instabilities. However, it was possible to analyse the expansion curve from the PIC simulations (see Fig. 3.13) and to artificially expand clusters according to it. The initialised clusters had a super-Gaussian shape $e^{-(x/r)^6}$ to avoid numerical issues associated with the use of a step function. The clusters then expanded according to the function

$$r(\xi) = \kappa - (\kappa - r_0) \sqrt[10]{\frac{\tanh\left(\frac{\xi}{\zeta} - 1\right) + 1}{2}} \,, \tag{3.23}$$

where $\kappa = 0.70\,\mu\text{m}$ defines the magnitude of expansion, $r_0$ is the initial radius, $\xi$ is the co-moving spatial dimension and $\zeta = 1\,\mu\text{m}$ is a scale parameter. This equation can be used to get the peak density decrease associated with expansion which is proportional to

$$n \propto n_{cl} \frac{r_0}{r(\xi)} e^{-[\xi/r(\xi)]^6} \,. \tag{3.24}$$

Figure 3.14 compares the model function (according to which the clusters are forced to expand) to PIC simulation data. The model should not be taken as an exact representation for two reasons. Firstly, as seen from PIC simulations (Fig. 3.13) the expansion depends on the exact cluster parameters which can not be directly mapped from a 2D simulation to a 1D model. Secondly, the expression in Eq. 3.24 does not describe the sole contribution to the electron density distribution as the electrons are also directly affected by the laser pulse which pushes the electrons away from the ion

[11] Hyperbolic PDEs have in common that solutions are wave-like which means that a perturbation of the initial condition propagates at finite speed.

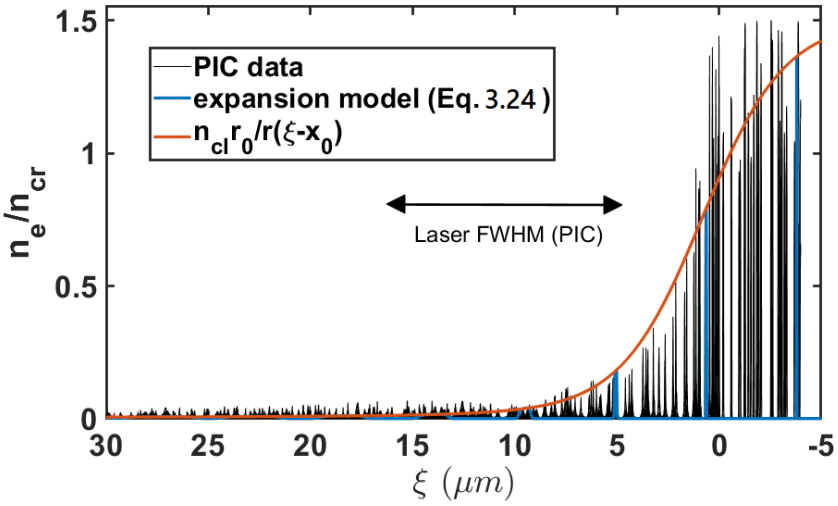



Figure 3.14: Comparison of cluster density as observed in particle-in-cell simulations (black) and the analytic curve used for the one-dimensional model (orange). The latter represents the average of the peak values of the clusters. Additionally, the forced expansion model is plotted in blue which acts as a base function around which electrons may fluctuate after interacting with the forces present. The PIC simulation cluster parameters are $n_{cl}/n_{cr} = 1.5$ and $r = 6.4$nm.

cluster distribution via the ponderomotive force. This leads to a compression of the electron distribution and a corresponding build up of electrostatic forces. This compression may cause occasional larger peak values (as observed in the PIC simulation).

Equations 3.21 and 3.22 were solved numerically using[12] a fifth order WENO advection operator [203]. The method used 10000 cells with a time step satisfying the CLF condition. The FWHM cluster radius $r$ was 70.8 nm and the average electron density is $\langle n_e \rangle = 0.0081 \times n_{cr}$ which includes the background density of $n_0 = 0.001 \times n_{cr}$. These values are both larger than what was used in the PIC simulations as a consequence of the one-dimensional geometry which requires a higher number density of clusters (number of clusters per plasma wavelength—not particle density within one cluster) compared to two-dimensional simulations to have a comparable impact while at the same time preventing numerical errors from the insufficient resolution of a single cluster. The first of these two arguments can be understood looking at the cluster filling fraction $f = V_{cl}/V_{box}$, where $V_{cl}$ is the total volume occupied by clusters

[12]My collaborator B. Spiers arranged the WENO solver function for use in a solver loop which took the normalised equation parameters as input and updated them accordingly under the CFL condition using Matlab.

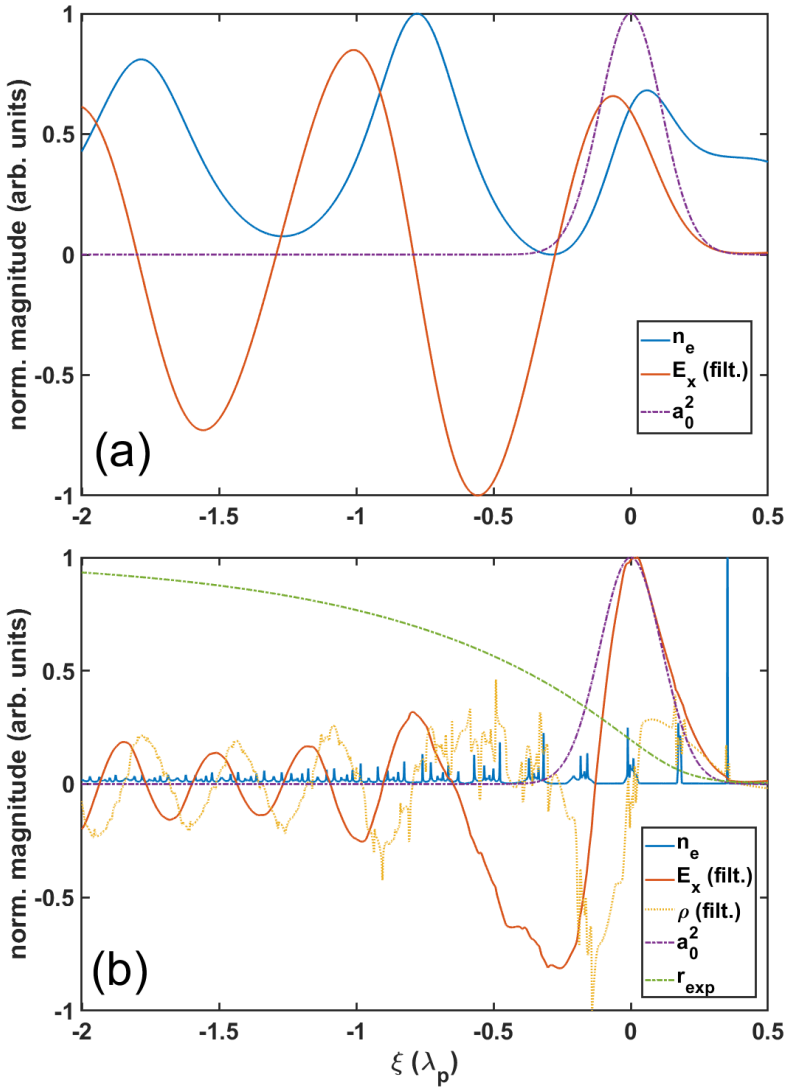



Figure 3.15: Results of the one-dimensional WENO scheme. Electron density, longitudinal electric field strength, and laser field strength are shown for a uniform plasma (top panel) and a cluster plasma (bottom panel). The top panel acts as a reference solution where $\xi$ is normalised to the theoretical value of $\lambda_p$ for the corresponding uniform electron density. In the bottom panel, clusters are injected from the right-hand side into the background density. They artificially expand according to the expansion function $r_{exp}$. The electric field was smoothed using a Gaussian smoothing kernel. The uniform (background) plasma is $n_e = 0.001 \times n_{cr}$. The averaged electron density in the cluster simulation is $\langle n_e \rangle = 0.0081 \times n_{cr}$.

and $V_{box}$ is the total volume within the simulation box. The number of clusters scales as $N_{cl} \sim V_{box}/s^D$, where $s$ is the separation between clusters and $D$ is the dimension. The volume of a cluster scales as $\sim w^D$, where $w$ is the cluster width. The total volume of all clusters scales as $\sim V_{box}(w/s)^D$ which gives $f \sim (w/s)^D$. Hence, if the cluster width is smaller than the cluster separation then the total electron density increases from 2D to 1D for similar parameters.

Applied to a uniform plasma (only background plasma without clusters), the WENO scheme is able to reproduce the well-known shape of a wakefield [194, 195] as is shown in the upper panel in Fig. 3.15 in which the normalised values for electron density, longitudinal electric field, and laser amplitude are shown. The plasma wavelength which was again measured from the electric field's trough position values is $\sim 1$ (normalised to $\lambda_{p,u} = 2\pi c/\omega_p$) as expected. In order to be able to compare the results of the obtained wavelengths to the cluster simulation, the $x$-axis of the lower panel was normalised to $\lambda_{p,u}$ as well. The results show that the cluster plasma wakefield wavelength decreases towards the left of the simulation box where the clusters have expanded almost completely. Converting to real units, the cluster plasma wavelengths are 19.7 µm, 10.1 µm, 8.6 µm and 8.5 µm. These values are obtained after applying a Gaussian smoothing kernel to the longitudinal electric field that has a standard deviation of 250 cells (in real units 2.21 µm) which is on the order of the cluster separation. The results can be compared to the theoretically predicted value for a uniform plasma of the same average electron density which is 8.9 µm. The small difference between this value and the smallest wavelength in the cluster case may be due to the filtering of the data. It is important to note that the strong perturbations in electron density close to the ion cluster cause a significant difference between the values of $n_e$ and $\rho$ which is not generally the case in a uniform plasma.

### 3.1.4 Discussion

Tiwari *et al.* [204] showed using a two-dimensional theoretical model that the presence of clusters embedded into a background plasma leads to an expansion of the plasma wavelength through a modification of the dispersion relation of electrostatic waves. They found that this effect scales with the cluster size and the degree of clusterisation within the plasma. Experimental results, two-dimensional PIC simulations, and a WENO solver presented in this section also show an increase in the (first) plasma wavelength when a short laser pulse interacts with a cluster plasma in agreement with the theory established in [204]. However, it has to be noted that this theory only offers a good description of the physical picture in a region in which the electrons have

not undergone significant Coulomb explosion which depends on the laser intensity and cluster parameters. Another distinction is that the theory describes a plasma in which there exists a background plasma. In the investigation presented in this section, the main contribution to the change in electron plasma wavelength rather seems to be an increase in "free" electron density. As long as electrons are bound to their cluster of origin the propagation of an electron plasma wave is inhibited. The more electrons are dissociated, the more prevalent the collective behaviour caused by the laser ponderomotive force.

As was explained in section 3.1.3, there are certain factors that make it difficult to directly compare cluster models in different dimensions (beyond the dimensional analysis which was presented for the scaling of certain cluster parameters). This also holds for the comparison between a "real" three-dimensional cluster and the two-dimensional particle-in-cell simulations presented in this chapter. Especially, it has to be noted that, due to the boundary conditions in a two-dimensional simulation, a cluster is essentially a rod extending to infinity in the dimension perpendicular to the simulation plane (similar to the representation of a Gaussian laser pulse which is not defined in the third dimension). This impacts the cluster expansion and the associated cluster electron density distribution, which in three dimensions would decrease more quickly than in two. Vice versa, the background density would increase more slowly behind the laser pulse, leading to an even stronger effect on the increased wakefield wavelength. Furthermore, accelerated electrons are less likely to scatter from ion clusters in the wakefield in three-dimensions. A similar argument can be made about the energy deposition during the interaction between a cluster and a laser pulse which is larger in two dimensions than in three because of the larger ratio between volume occupied by the cluster and that occupied by the laser pulse. The use of circular polarisation in simulations would have complicated matters even further because electrostatic cluster forces in the third dimension, which are important for the correct modelling of all points mentioned above, would have not been considered. Therefore, all simulations used linear polarisation.

A useful effect that could be exploited using wakefields in cluster plasmas is the prolongation of the electron acceleration mechanism which is limited by the dephasing length $L_{dp} \simeq (\lambda_p c)/(2(c - v_g))$—the distance over which particles are accelerated until they reach electric fields of opposite sign inhibiting acceleration. If the acceleration length can be "stretched", electrons can achieve higher peak energies. Another contribution to an increased dephasing length is the change in laser group velocity as described in [154] as will be discussed in section 3.2.5. However, further studies

have to be undertaken to see whether the pulse depletion from the interaction with clusters (over a distance longer than what can be simulated at present time given the high resolution) counteracts the positive effects described above.

## 3.2 Cluster electron self-injection and acceleration in the non-linear wakefield regime

Electrons cannot be trapped in low amplitude wakefields below the wave-breaking threshold (such as those presented in the previous section) without any external means of injection (see section 2.5.4). In contrast, when the amplitude of ultrashort laser pulses is raised to relativistic levels, it is possible for electrons to be self-injected. In what follows, I will show the impact of the presence of a cluster plasma on the electron self-injection mechanism in the "bubble" regime. The main results of this section have been published in Reference [179].

The creation of relativistic electron beams from clustered gases such as methane and argon has been studied experimentally showing that the features of the beams are different to what is found through acceleration in a uniform density plasma. Among these features are an increased accelerated charge [156, 205], higher peak energies [156, 205], better reproducibility [157], and a broad energy spectrum [145, 155–157, 205, 206]. Two groups argue [145, 205] that the acceleration mechanism is due to direct laser acceleration[13] (DLA). However, it has to be noted that their results hold for very specific conditions and cannot generally be applied to electron acceleration from cluster targets due to the following reasons: in one case clusters of 0.24 µm diameters were used in the simulation (which is significantly larger than what other groups observed and what is used in this chapter) [145]; in the other case [205] the laser pulse duration was 80 fs which is rather long for an electron density of $2 \times 10^{19}\,\mathrm{cm}^{-3}$. Furthermore, the study in [205] used simulations with a resolution of 1 cell per cluster diameter and 9 particles per cell (which makes it impossible to reliably model effects such as the impact of cluster expansion and laser absorption) and a non-randomised grid for the cluster initialisation. I will argue below that the injection process observed in many experiments (with similar clustering conditions and matched laser duration) is likely to be due to a different mechanism than DLA.

[13]Direct laser acceleration occurs when the laser pulse overlaps with trapped electrons. The mechanism is based on the increased transverse momentum from betatron oscillations in the plane of polarisation being converted to longitudinal momentum via the $\mathbf{v} \times \mathbf{B}$ force.

Using high-resolution particle-in-cell simulations, I will describe how particles are trapped and accelerated in a cluster plasma and how the mechanism compares to electrons generated from non-linear wakefields at high densities in uniform plasmas. In addition, the properties of a high-intensity laser pulse propagating in a cluster plasma are investigated.

### 3.2.1 Numerical challenges

In order to resolve the dynamics of the nanometre-sized clusters, the resolution of the simulation (just like in the previous section) had to be sufficiently high. This means that, depending on the cluster parameters used in each cluster plasma simulation, the number of cells per laser wavelength ranged between 125.0 and 188.5 making three-dimensional simulations of several consecutive plasma wavelengths infeasible. Even at the relatively high densities mostly used in this study of $n_e/n_{cr} = 0.004$ which keeps the bubble dimensions small, a three-dimensional moving window simulation would require approximately $10^{11} - 10^{12}$ cells. Even the two-dimensional simulations presented here are limited in how far the laser is able to propagate within the plasma due to the short timestep enforced by the Courant-Friedrichs-Lewy condition (see eq. 3.12).

Often, wakefield simulations in uniform plasma use a resolution of as few as 15 cells per wavelength in the direction of laser propagation and somewhat less in the perpendicular directions. However, I have found that numerical dispersion within the commonly used finite-difference time domain (FDTD) methods strongly influences the results of the uniform plasma simulations which has an impact on the laser group velocity—a parameter relevant for the accurate description of electron trapping and acceleration. Fig. 3.16 highlights two important features through varying parameters in the following way:

- increasing the resolution while keeping the resolution ratio between the two simulation dimensions constant,
- increasing the resolution in $x$-direction but decreasing it in $y$-direction, and
- changing the number of macro-particles per cell.

First, particles are only self-injected in panel (a) which represents a simulation that is distinct from all others through its low resolution in the laser propagation direction. Second, the laser group velocity is lower in panel (a) than in all other cases causing a lower phase velocity of the wake and, therefore, relaxing the trapping condition. The

difference in position of the back of the first bubble is 3.3 µm accumulated over a time span of 0.5 ps which leads to $\Delta v_g/c = 0.022$. This error significantly influences the dephasing length and, hence, the results for the maximum energy that can be reached in an accelerator stage. Andriyash *et al.*[207] get sufficiently close to the theoretical group velocity estimate using an FDTD Maxwell solver at around 62.5 cells per laser wavelength in direction of laser propagation. Using the Yee solver method in OSIRIS, it was found that the artificial numerical dispersion is sufficiently damped at the $x$-resolution used in Fig. 3.16(b-d) which was 37.7 cells per wavelength compared to 12.6 cells per wavelength in panel (a). This is why in what follows, the number of cells used in each simulation will be stated. Neither the resolution in $y$-direction which was varied from 6.3 to 33.9 cells per wavelength nor the number of macro-particles per cell which was varied from $8 \times 8$ to $32 \times 32$ seem to have a significant impact (within the used limits) on the laser group velocity and injection mechanism.

### 3.2.2 Simulation parameters

To simulate wakefield behaviour in a cluster plasma, I used the cluster class introduced in section 3.1.2.1 within the fully relativistic OSIRIS code [125]. The two-dimensional simulations used a moving window. The simulation parameters are shown in Tab. 3.3. The grid size was adapted depending on the cluster diameter studied and had a maximum size of $15000 \times 8400$ cells corresponding to 188.5 cells per laser wavelength in the longitudinal ($x$) direction and 164.9 cells per wavelength in the transverse ($y$) direction. In addition to the high resolution, the cluster simulations also incorporated a great number of macro-particles per cell (mppc) to further reduce numerical heating [122]. The simulations testing argon clusters used $32 \times 32$ electron macro-particles per cell (mppc) while the hydrogen simulations used $16 \times 16$ electron mppc. All ions were initialised with $8 \times 8$ mppc. Due to the different requirements for resolving small structures in uniform background simulations, there were 37.7 cells per wavelength in the longitudinal ($x$) direction and 12.6 cells per wavelength in the transverse ($y$) direction. The plasma was simulated with $8 \times 8$ electron mppc and $2 \times 2$ ion mppc. The macro-particles were absorbed when reaching the simulation boundary. The electromagnetic field boundaries were of type "Lindman" longitudinally and "open" transversally to allow for outflowing fields using a moving window. The time-step of the simulation was chosen to satisfy the Courant-Friedrichs-Lewy condition which was described in Eq. 3.12.

A laser amplitude of $a_0 = 5$ ($I = 5.34 \times 10^{19}\,\mathrm{W\,cm^{-2}}$) at focus was used in all simulations. The laser pulse was linearly polarised parallel to the simulation plane

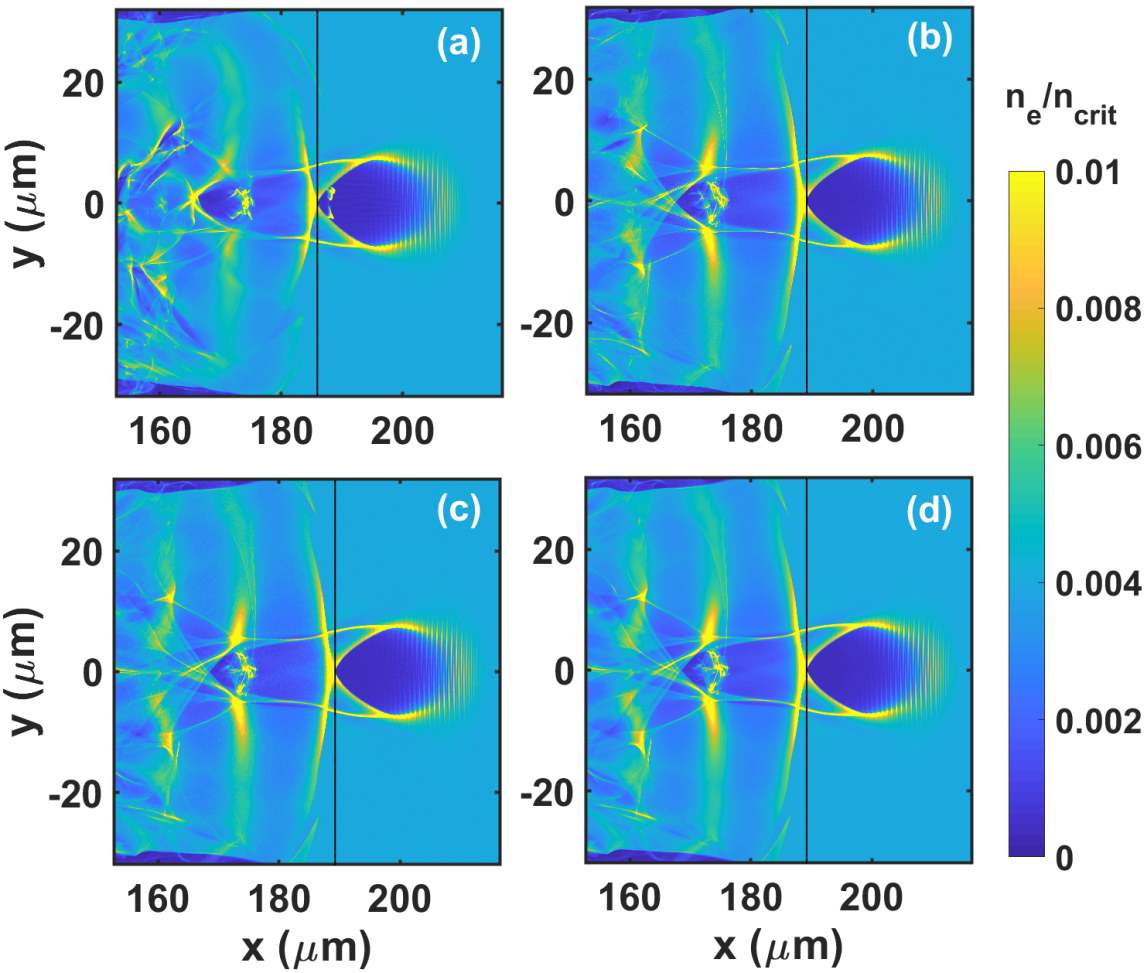



Figure 3.16: Comparison of simulations using different resolution and macro-particle numbers after a propagation time of 0.5 ps. Simulation (a) uses a low resolution of 12.6 cells per wavelength in the $x$-direction and 11.3 cells per wavelength in the $y$-direction with 16×16 electron macro-particles per cell (mppc). Simulation (b) uses 37.7 cells/$\lambda$ ($x$-dir) and 33.9 cells/$\lambda$ ($y$-dir) with 8×8 mppc. Simulation (c) uses 37.7 cells/$\lambda$ ($x$-dir) and 6.3 cells/$\lambda$ ($y$-dir) with 8×8 mppc. Simulation (d) uses 37.7 cells/$\lambda$ ($x$-dir) and 6.3 cells/$\lambda$ ($y$-dir) with 32×32 mppc. The black vertical lines show the position of the bubble's rear point.

and had a Gaussian shape in the longitudinal (temporal) and transverse (spatial) directions. The average electron density parameter shown in Tab. 3.3 of $0.004\,n_{\mathrm{cr}}$ ($n_{\mathrm{cr}}$ is the critical density) is equivalent to an SI value of $6.97 \times 10^{18}\mathrm{cm}^{-3}$ for a laser wavelength of 800 nm. The clusters were initialised from the boundary as a plasma with $T_e = 10\,\mathrm{eV}$ and $T_i = 0\,\mathrm{eV}$. The ionisation levels were found from test simulations which looked at the microscopic cluster ionisation process as well as an equivalent full-scale simulation (see Appendix C.2 for results). Due to the computational cost associated with the ionisation module and the matching results of the pre-ionised and neutral cluster simulations, I continued with the pre-ionised clusters for the parameter scan.

| # | Type | $P_{\mathrm{L}}$ | $d$ | $w$ | $n_{\mathrm{cl}}/n_{\mathrm{cr}}$ | $d_{\mathrm{cl}}$ | Gas | $\langle n_e \rangle / n_{\mathrm{cr}}$ |
|---|---|---|---|---|---|---|---|---|
| | - | [TW] | [fs] | [µm] | - | [nm] | - | - |
| A | unif. | 196 | 30 | 12.7 | - | - | $Ar^{16+}$ | 0.004 |
| B | cl.(s) | 196 | 30 | 12.7 | 1.5 | 12 | $Ar^{16+}$ | 0.004 |
| C | cl.(r) | 196 | 30 | 12.7 | 1.5 | 12 | $Ar^{16+}$ | 0.004 |
| D | unif. | 332 | 30 | 16.6 | - | - | $H^+$ | 0.004 |
| E | cl.(r) | 332 | 30 | 16.6 | 1.25 | 18 | $H^+$ | 0.004 |
| F | cl.(r) | 332 | 30 | 16.6 | 5.0 | 18 | $H^+$ | 0.004 |
| G | cl.(r) | 332 | 30 | 16.6 | 0.75 | 18 | $H^+$ | 0.004 |
| H | cl.(r) | 332 | 30 | 16.6 | 2.5 | 24 | $H^+$ | 0.004 |
| I | unif. | 332 | 30 | 16.6 | - | - | $H^+$ | 0.002 |
| J | cl.(r) | 332 | 30 | 16.6 | 1.25 | 24 | $H^+$ | 0.002 |
| K | unif. | 126 | 15 | 10.2 | - | - | $H^+$ | 0.004 |
| L | cl.(r) | 126 | 15 | 10.2 | 1.25 | 24 | $H^+$ | 0.004 |

Table 3.3: This table lists the parameters used for the PIC simulations. The peak normalised laser amplitude for all simulations was $a_0 = 5.0$. $P_L$ is the laser power, $d = d_{\mathrm{FWHM}}$ is the laser (intensity) FWHM duration, $w = w_{\mathrm{FWHM}}$ is the laser (intensity) FWHM-spot diameter, $n_{\mathrm{cl}}/n_{\mathrm{cr}}$ is the cluster peak electron density normalised to the critical density, and $d_{\mathrm{cl}}$ is the cluster diameter. "unif." means uniform density distribution, "cl.(s)" means periodically arranged clusters defined by an analytic function are used, and "cl.(r)" means clusters of randomised positions are used.

The cluster sizes shown in the simulation parameter table are similar to results found in [136, 208]. In these articles argon and hydrogen gas jets were studied and measurements of cluster radii between 8 nm and 20 nm are presented for backing pressures between 12 bar and 16 bar.

### 3.2.3 Wakefield behaviour

Before looking at how electrons are trapped and accelerated in cluster plasmas, it is useful to study the wakefield structure and its evolution and how it differs to the case of a uniform plasma. The relevant parameters for all simulations used below are found in Tab. 3.3.

Simulations A, B, and C differ in the type of plasma the laser pulse is propagating in. While simulation A uses a uniform plasma, simulations B and C use a cluster plasma. The clusters in simulation B are arranged in a specific periodic pattern[14] (shifted rows or hexagon structure) while the clusters in C are randomly distributed. Both, B and C, have the same average electron density as simulation A. The electron density after 0.76 ps is displayed in Fig. 3.17. It shows that all cases have entered a regime similar to the bubble regime found in References [22, 23]. The clusters damp the electron response which causes a smoothing of the wake structures longitudinally and transversally. The randomness in simulation C further enhances this effect to a point where the regions of increased locally averaged electron density (wake peaks) fade towards the left (rear) of the simulation box. Furthermore, the symmetry of the bubble is slightly distorted. From these simulations, it is seen that the effect of cluster randomisation is important to get a more realistic description of the process[15].

At the point where the laser is at focus the intensity is highest and the major and minor axes of the electron cavity (behind the laser pulse) are of similar extent. The bubble radius can be expressed as $R \simeq 2\sqrt{a_0}\lambda_p/(2\pi)$ as was found phenomenologically by Lu *et al.* [89]. At the simulation time step shown, the radius is of similar extent across all simulations. However, after the focus the ponderomotive force decreases which affects the expulsion of electrons associated with random clusters more strongly than in the other two cases as will be shown below. Due to the strong local fluctuations in electron density (and electric field), it is more difficult to determine a radius for these (later) cases. On-axis quantities, however, such as the longitudinal electric field and the associated acceleration length for trapped electrons can be measured from the simulations.

Figure 3.18 shows the results of tracking the temporal evolution of the relative position of the peak accelerating field. In a uniform plasma and after the laser pulse has propagated through a linear density ramp (which reaches constant density after

[14] The clusters are staggered in shifted rows at an inclination angle of $\alpha = 26.57°$ (forming a hexagon structure). The closest distance between cluster centers is $a/2 = 246.4\,\text{nm}$ which is smaller than the laser wavelength.

[15] This chapter (and the associated published article [179]) shows, to my knowledge, the first use of randomised cluster injection in PIC codes.

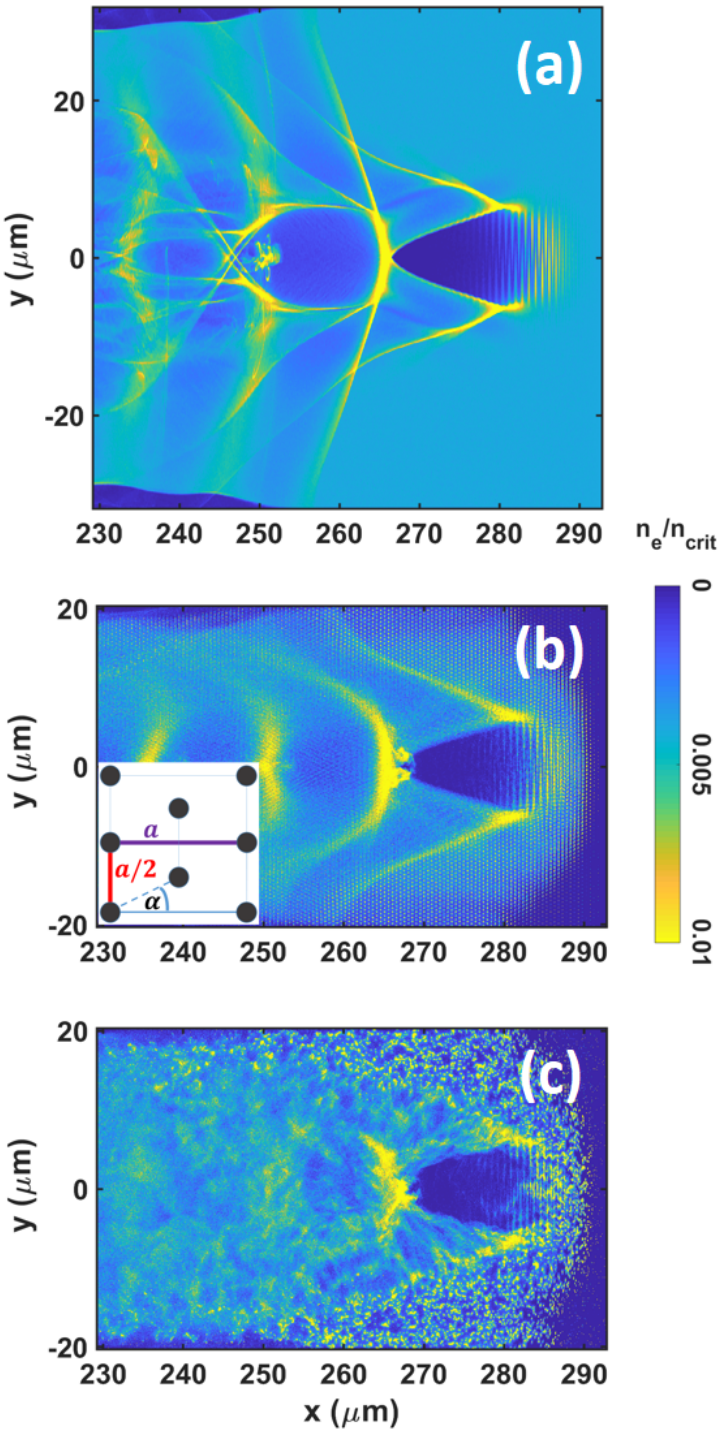



Figure 3.17: This figure shows the electron density normalised to critical density for (a) a uniform plasma (simulation A), (b) a plasma of clusters arranged in a staggered grid (simulation B), and (c) a plasma of clusters with random positions (simulation C) after 0.76 ps. All parameters are according to Tab. 3.3. The laser pulse propagates to the right-hand side. The inset schematic in (b) shows the geometric arrangement of the clusters.

time step 2 up to which the bubble radius decreases) a continuous slip towards the back of the simulation box is observed. This is due to the difference between the laser group velocity and the simulation box propagation velocity (equal to the speed of light in vacuum). In a randomised cluster plasma the position strongly fluctuates from time step to time step[16] which has interesting implications for the trapping condition of electrons in the vicinity of the bubble. The maximum value of this field is also tracked and shown in panel (b) of Fig. 3.18. The imperfect evacuation of the cluster electrons from the bubble and the strong damping effects in the cluster simulation cause a lower peak value than present in the first wake in the uniform plasma. However, in terms of peak magnitude, the cluster electric field is similar to the second wake in the uniform plasma into which electrons are observed to be injected. Therefore, arguments about peak electron energy of accelerated bunches will be based on similar accelerating fields.

The simulations also show that the maximum acceleration length, defined as the distance in which the longitudinal electric field is negative (accelerating), also fluctuates very strongly in the cluster case. The largest and smallest values differ by over 20 µm. This causes enhanced trapping because particle trajectories that would have been outside the separatrix now exist within an accelerating field for a longer duration. Later, I will show that this is also dependent on the cluster parameters. In the uniform case, the pattern shows a mirrored behaviour to the position of the maximum electric field which shows that the wakefield structure evolves coherently.

To visualise the impact of the clusters on the accelerating structures, the shape of the longitudinal electric field is shown in Fig. 3.19(a) (uniform), Fig. 3.19(b) (clusters with $n_{\mathrm{cl}}/n_{\mathrm{cr}} = 1.25$), and Fig. 3.19(c) (clusters with $n_{\mathrm{cl}}/n_{\mathrm{cr}} = 5.0$). The wakefield in the uniform plasma is highly non-linear and exhibits signs of beam loading in the second bucket. Introducing clusters the fields become asymmetric with respect to the laser propagation axis - an effect that increases strongly with cluster electron density (or cluster separation which is the other side of the same coin assuming constant average electron density). Furthermore, strong local field oscillations are seen at the point where the laser interacts directly with the clusters.

Now, after having looked at the impact of clusters on the accelerating field, it is also important to see how the clusters themselves evolve while and after interacting with the short laser pulse. Figure 3.20 shows the ion and electron density plotted in

[16]Note that time step in this context corresponds to a data dump rather than a computational time step of the simulation routine.

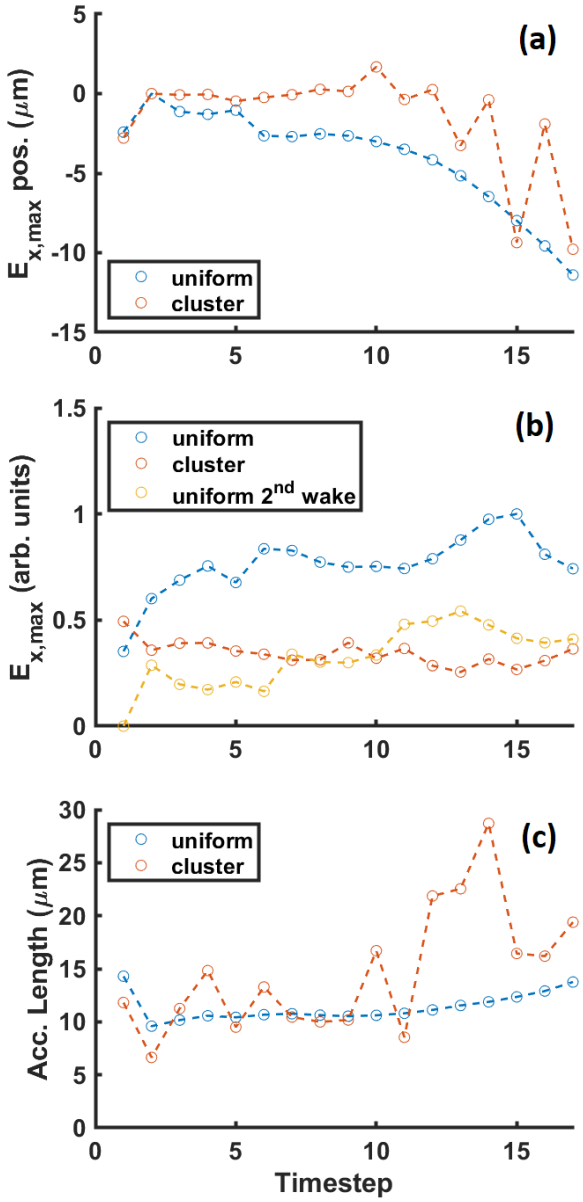



Figure 3.18: Comparison of the wakefield evolution in a uniform and a cluster plasma (simulations D and E - see Tab. 3.3). Panel (a) shows the position of the maximum accelerating longitudinal field plotted against time. The zero (reference) value on the $y$-axis was chosen to be at time step 2 where the maximum plasma density has been reached after the density ramp. Panel (b) shows the normalised peak accelerating electric field strength for cluster and uniform cases as well as the value for the second wake in the uniform case. Panel (c) shows the maximum acceleration length, defined as the distance between troughs where the electric field in the first bubble is negative (and thus accelerating). Here, one time step corresponds to 0.25 ps in simulation D and to 0.26 ps in the other simulations. All values are taken from a line-out on the laser propagation axis.

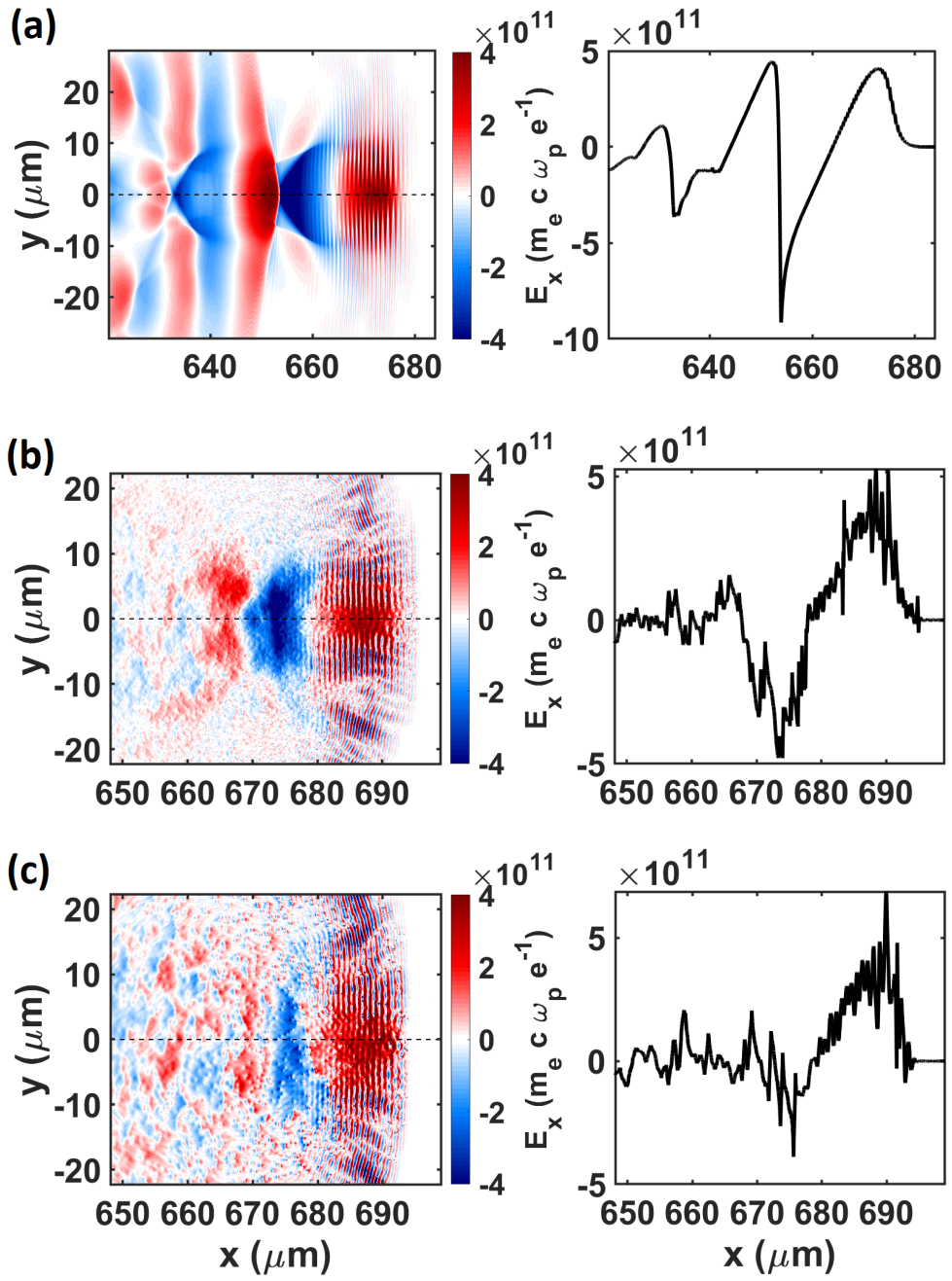



Figure 3.19: This figure shows the shape of the longitudinal electric field of simulations D (top row), E (middle row), and F (bottom row). The right-hand side column presents line-outs of the laser propagation axis at $y = 0$.

different colours to distinguish the evolution of the ion clusters from the electrons. At the beginning of the interaction, electrons oscillate as a unit within the ion cluster in phase with the laser field showing slight (hydrodynamic) expansion. When the laser field strength and the ponderomotive push are strong enough the electrons start to fully separate from the ion cluster and experience strong repulsive Coulomb fields in addition to the laser field. The associated expansion of the electrons causes homogenisation of the electron density distribution. Electrons that were formerly bound together in the same cluster are now experiencing attractive forces of different ion clusters (which can at this stage be approximated as point sources) and repulsive forces from electrons of other clusters. The larger the diameter of the cluster the longer the electrons stay associated with the respective ion cluster. However, when the different species are finally separated the Coulomb explosion effect is more pronounced because of the large amount of charge contributing to the effect. The ions also experience a Coulomb explosion which happens more slowly due to the high mass as can be seen towards the back of the simulation box. The gradient of the expansion process scales with the peak ion charge density in the cluster as the Coulomb force $F_c \propto \rho_{cl} \times r_{cl}$, where $\rho_{cl}$ is the cluster charge density and $r_{cl}$ is the cluster radius.

It can be seen in the top panel of Fig. 3.20 that a stream of electrons is flowing into the bubble centrally from the right-hand side. This is due to the presence of regions of higher density caused by the randomised initialisation position (clusters of clusters). This aids the presence of favourable trajectories for electron injection and it can be seen that many electrons have accumulated at the back of the bubble.

### 3.2.4 Electron trapping and acceleration

To understand why experiments conducted in cluster plasmas have shown increased bunch charge and peak energy levels as well as a broad energy spectrum, it is important to study what the mechanism is that causes electron trapping in these environments, how it scales with the cluster and laser parameters and how it differs from conventional self-injection in the bubble regime.

Fig. 3.21 shows trajectories of particles injected into a wakefield for both the cluster and uniform plasma cases. From the large number of macro-particles in the simulation, the relevant trajectories were selected using a filter. This removed all particles that were below a specific longitudinal momentum (and were not accelerated within the wakefield). A previous study [205] reported strongly enhanced betatron oscillation[17] and resonant coupling of the trapped particles to the laser electric field when

[17]This term describes electrons oscillating within the bubble to create synchrotron radiation [209].

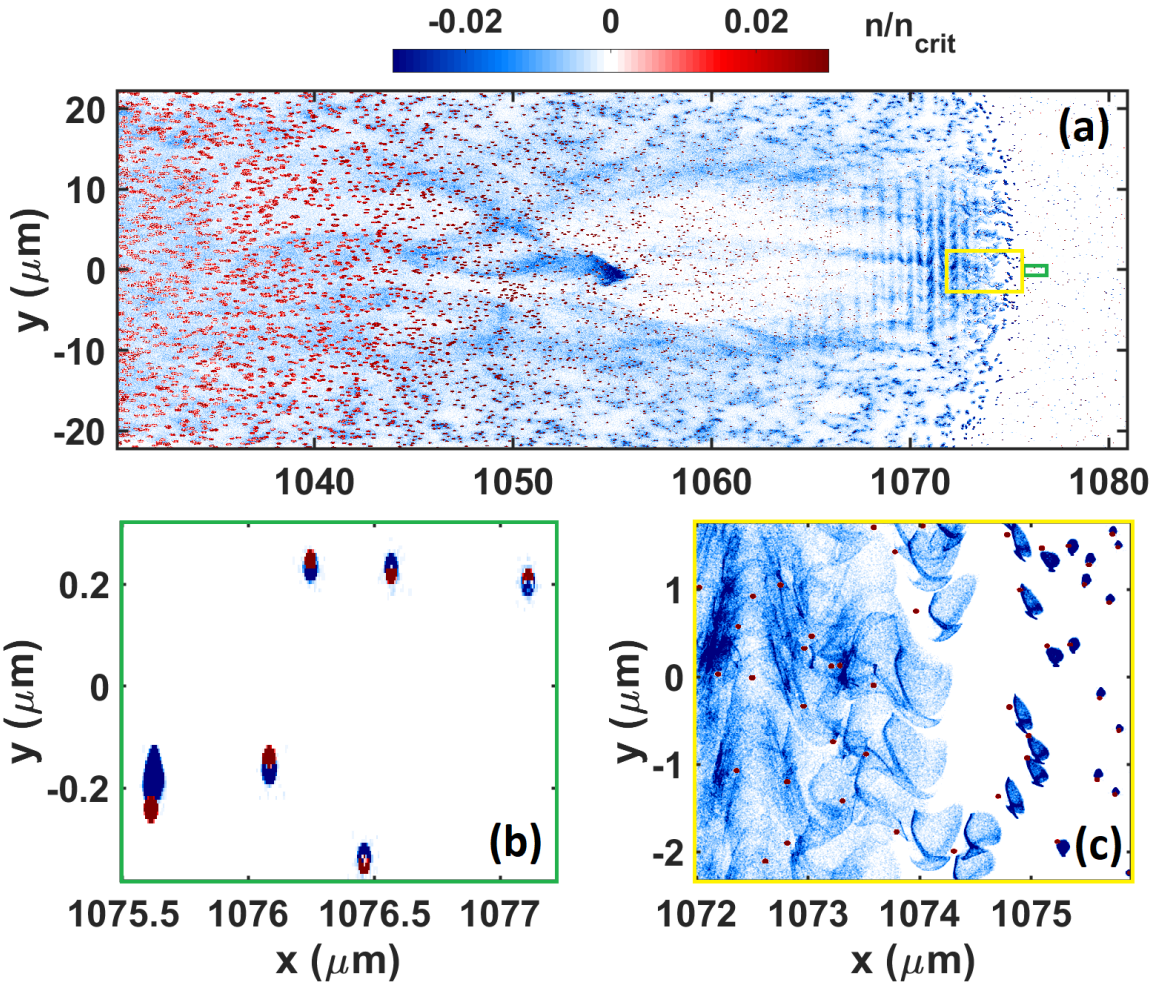



Figure 3.20: Normalised charge density of simulation G after 3.57 ps. The laser propagates towards the right edge of the simulation box. Panel (a) shows the wakefield structure formed by plasma electrons. The ion clusters (red) expand towards the back of the simulation box (left) through the Coulomb explosion mechanism. The green and yellow boxes indicate the areas shown in panels (b) and (c). Panel (b) shows a snapshot of the hydrodynamic expansion of the clusters in the region where the laser electromagnetic fields are of low magnitude. Panel (c) shows the region in which the clusters encounter the ponderomotive force pushing them forwards (towards the right) and away from the ion cluster and the Lorentz force causing an oscillatory motion about the cluster centre depending on the sign of the electric field at the respective position. Additionally, the Coulomb explosion lets the electron bunches expand on the order of a few µm.

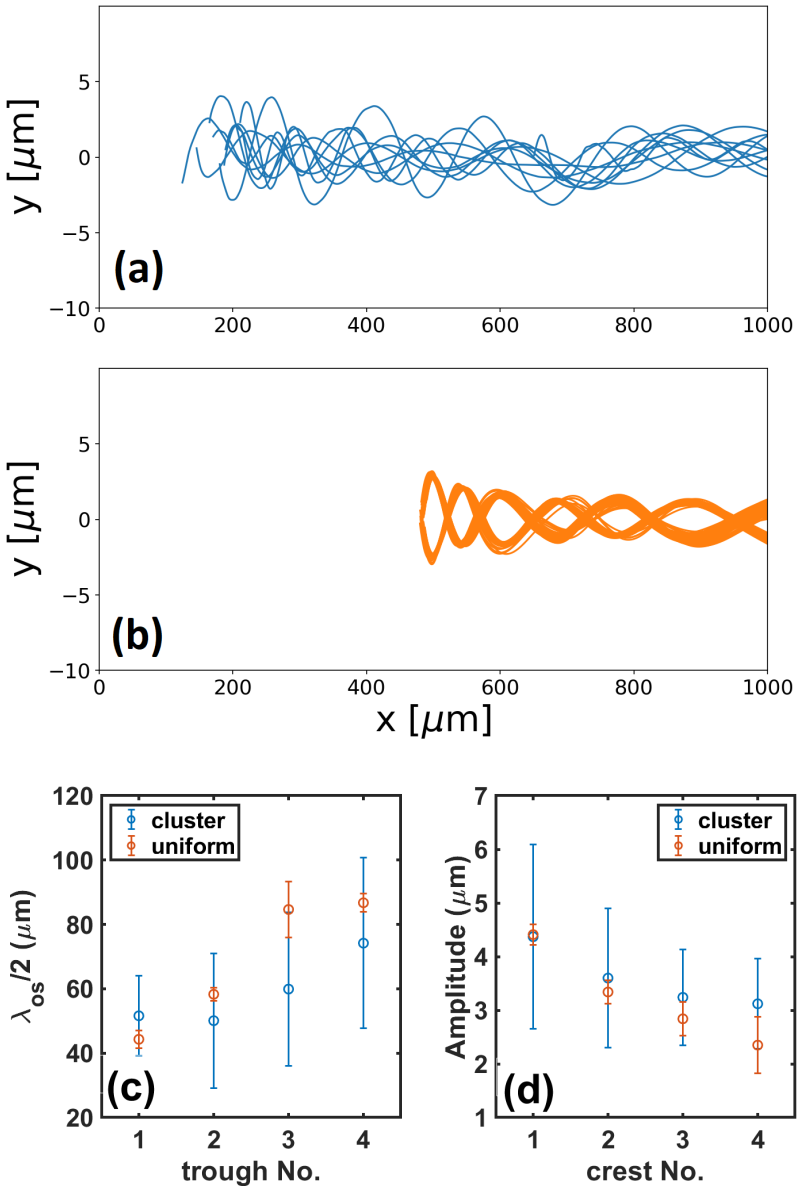



Figure 3.21: This figure shows particle trajectories of trapped electrons starting at the point of injection into the wake for the cluster (a) and uniform (b) case. Panels (c) and (d) show the half-wavelength distances and oscillation amplitude plotted against the trough (and crest) number of the electron trajectory. The error bars show the standard deviation obtained from the 10 randomly selected tracks displayed in (a) and (b).

compared to a uniform simulation. As mentioned in the introduction to this section, it was argued that in the cluster case direct laser acceleration converted great parts of the transverse momentum into longitudinal momentum. In the high-resolution study presented in this chapter, this effect was not observed. The oscillation amplitude was similar in both cases with the mean value decreasing with increasing simulation time. The same holds for the wavelength of the oscillation which increased over time indicating an increasing longitudinal momentum. Note that the oscillations start at different points in the simulation in the cluster case leading to a phase shift that has been subtracted in the wavelength analysis.

In the uniform plasma, the trapping condition, which states that the electrons need to have a forward-directed velocity at least equal to the phase velocity of the wake, is fulfilled over a short duration. This is evident when looking at Fig. 3.22(a) in which the injection length for the tracked particles is on the order of 10 µm. In the cluster plasma, injection starts early on (close to where the maximum average density is reached after the ramp) and continues throughout the entire simulation even though the intensity of the laser decreases. The $y$-position at which the trapped electrons were injected is localised to two regions in the uniform case and spread over the entire vertical bubble extent in the cluster case as shown in the histogram. Therefore, the uniform self-injection pattern resembles the injection ring with a radius similar to the laser spot size which was found in Reference [24]. The cluster injection does not show this feature. In contrast, many trapped electrons are born in the central region on-axis and are not pushed out by the laser pulse's ponderomotive force because they are bound in the cluster potential in the initial interaction region. Then, once the electrons have left the vicinity of the cluster the injection process can be compared to ionisation injection where particles are born in a region in which the intensity of the laser pulse is higher and where the wakefield potential favours injection. The longer electrons stay associated with the cluster the larger is the potential difference needed for injection[18] which was described by Pak *et al.* [210] as $\Delta\bar{\Psi} = \sqrt{1 + (P_\perp/mc)^2}/\gamma_\phi - 1$, where $P_\perp$ is the perpendicular electron momentum, and $\gamma_\phi = (1 - (v_\phi/c)^2)^{-1/2}$. Another process that can aid the injection in a cluster plasma is the strong attractive force of ion clusters acting on electrons whose trajectory intersects with the high field region. This may increase the longitudinal momentum for some electrons while decreasing it for others. This aided injection process using an ion nano-particle was studied in [211]. Even though the clusters used here are much smaller, it can be

[18]This statement is true up to the position where the electric field goes through zero.

argued that even small increments can add up stochastically enhancing the trapping probability of some electrons.

The perpendicular electron momentum at the point of injection also differs between the uniform and cluster cases. In the uniform case, the symmetric injection process causes two distinct regions of positive and negative momentum. In the cluster case electrons have a larger range of perpendicular momenta even if the trapping condition is modified by replacing the standard phase velocity equation [89]

$$v_\Phi = v_g - v_{etch} \simeq c\sqrt{1 - \left(\frac{\omega_p}{\omega_0}\right)^2} - c\left(\frac{\omega_p}{\omega_0}\right)^2 \tag{3.25}$$

with a modified wakefield phase velocity which will be described in the context of the increase of the laser group velocity/wakefield phase velocity in a cluster plasma (see section 3.2.5). The fact that there exist particles with zero perpendicular momentum implies that they have experienced equal perpendicular impulse between initialisation and trapping. In a wakefield context, this is achievable if the electrons stay on a central path through the bubble or if they experience fluctuating perpendicular forces (which can be caused by distortions through cluster fields). The observed perpendicular momentum explains the high standard deviation of the oscillation amplitude of injected electrons in Fig. 3.21(a).

The relative position in the co-moving frame at which electrons are injected over time shows that in the cluster case the electrons are indeed (as argued when looking at the electric field shape's evolution) trapped at fluctuating positions. For example, the green crosses in panel (g) of Fig. 3.22 which are taken at similar times show trapping occurring over several µm. Similar to density down-ramp injection, electrons can be more easily trapped when the acceleration region suddenly increases. The observation of electrons trapped over an extended period of time (indicated by the multi-coloured crosses in Fig. 3.22(g)) and with various transverse momentum values (indicated by the closely connected blue markers in Fig. 3.22(d) and (e)) is directly linked to the behaviour of the maximum electric field position of the wake and the acceleration length as seen in Fig. 3.18 (strongly fluctuating orange markers showing a repeated increase and decrease of the distance between an electron approaching the wake and the relative wake position). An electron following a trajectory that can be trapped at time $t_1$ does not necessarily have to be trapped slightly later at $t_2$ because of the rapid evolution of the wakefield which is associated with the random nature of the cluster positions. The asymmetries in the electric field seen in Fig. 3.19(b) can even result in two electrons equidistant from the laser propagation axis "born" at

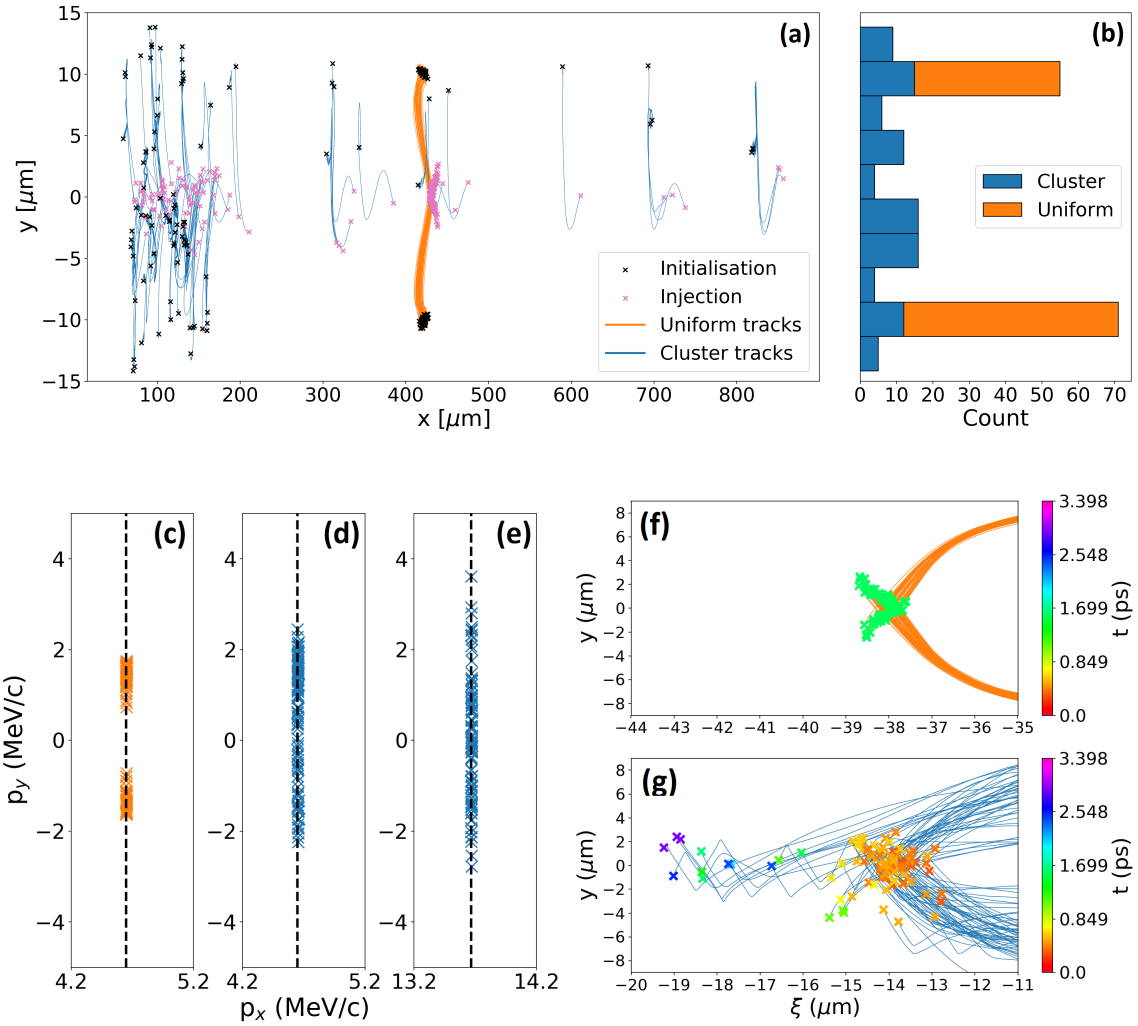



Figure 3.22: This figure presents the analysis of the electron injection behaviour. Panel (a) shows the positions of particle injection (pink) and the corresponding initialisation positions (black) for uniform and cluster plasmas (simulations D and G). Panel (b) shows the number of particles initialised within a given range of the $y$-coordinate. The perpendicular momentum of the particles at the time of injection (threshold calculated using eq. 3.25) is presented for uniform plasma (panel (c)) and cluster plasma (panel (d)). Panel (e) shows the same (cluster plasma) data with a new threshold calculated from the higher laser group velocity in section 3.2.5. Panels (f) and (g) compare the injection positions in a co-moving frame travelling at the speed of light for the uniform and cluster case. The colour of the 'x'-markers corresponds to the time at injection.

the same time experiencing different trapping conditions. These features lead to an unpredictable and fluctuating injection volume.

The acceleration process depends on cluster parameters as is shown in the plot of the longitudinal momentum in Fig. 3.23. These results, taken at the end of each simulation, show a broad spread in accordance with some of the observations made in the experimental campaigns studying wakefields in cluster targets. The momentum data shows several branches (most pronounced in panels (b) in which the cluster electron density was highest and (d) in which the cluster diameter was largest) which each correspond to a new injection event supporting the above arguments. The cases with high cluster electron density and large diameter also have the lowest maximum longitudinal momentum which is due to the lower peak electric field. Another observation is that the spatial extent of accelerated electrons is larger than in the other simulations. The narrowest spatial extent of accelerated electrons is seen in simulation J in which the average plasma electron density was halved compared to the other simulations. The largest peak momenta are seen in simulations E and G which have slightly over- and undercritical clusters, respectively. Their cluster electron density and radius are smaller than those in simulations F and H which means that their electric field structure is smoother with a larger peak value.

The perpendicular momentum of the electrons can give information about laser etching which is more prevalent in panels (g) and (i). To see this effect, one has to look at the perpendicular[19] electron momentum on the right-hand side which shows the electron response to the laser pulse. The impact of the laser field indicated by rapid electron oscillations causing positive and negative momenta can be clearly seen. The effect of laser etching can, therefore, also be observed in the momentum response which, in the case of panels (g) and (i) shows an absence of oscillating electrons at the leading (right) edge followed by a rapid increase of momentum towards the back of the pulse (a few microns further to the left) corresponding to a sharp edge in laser intensity. This sharp intensity edge is a typical feature of pulse etching. In the simulation of smaller average electron density (panel (j)), this effect is smallest because less energy is used freeing cluster electrons.

The number of particles accelerated to a specific momentum is plotted in Fig. 3.24 for several simulations. There is great similarity in the curves for simulations E and G apart from the central peak in G at which charge has accumulated at medium

[19]In principle, an effect could be seen in the longitudinal momentum too, but the effect is very small on the scale of the momentum values of the accelerated electron bunches.

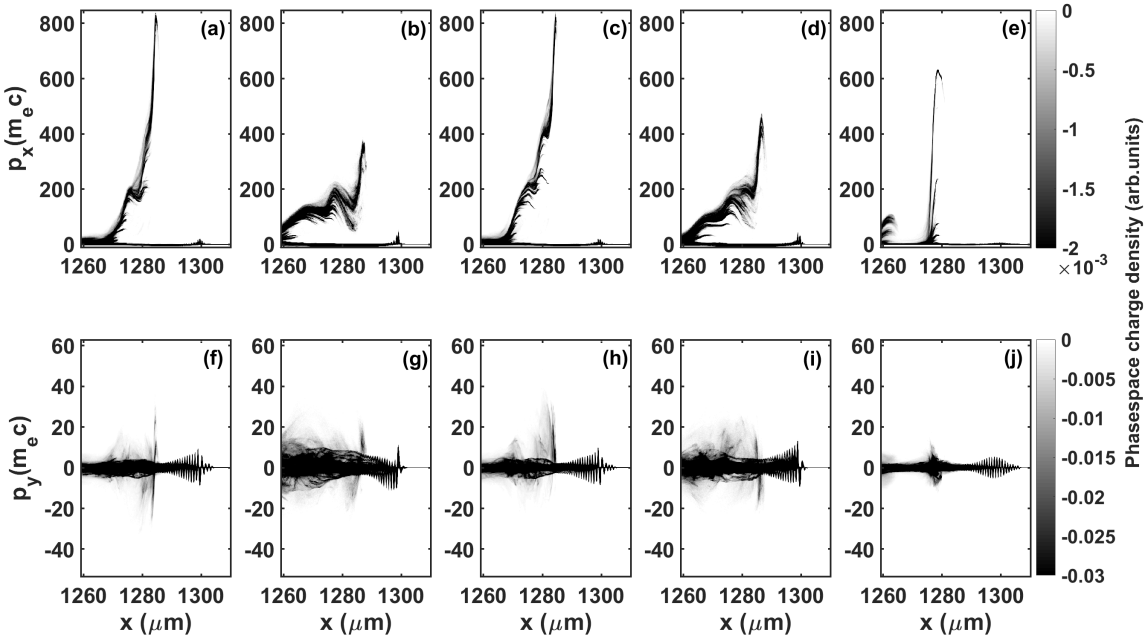



Figure 3.23: This figure shows the $x$-$p_x$ and $x$-$p_y$ phasespace density of simulations with different cluster parameters. The data was taken after 4.33 ps. Panels (a) and (f) correspond to simulation E, (b) and (g) to F, (c) and (h) to G, (d) and (i) to H, (e) and (j) to J.

momentum values. The peak in simulation J has mono-energetic features due to the reduced background levels at lower momenta. The histogram in the lower panel shows the energy of the tracked macro-particles which are spread out reaching up to 400 MeV.

#### 3.2.4.1 Electron beam charge calculation

Due to its two-dimensional nature, the simulation data obtained from the PIC simulations has some limitations. For example, it is not possible to easily extract the amount of charge that lies within the trapped electron beam without making assumptions about the third dimension. The code is normalised such that the third dimension is an infinitely long, periodic extension of the two-dimensional "projection" data. Here, I will describe how it is possible to extract real charge values from the simulation data and which assumptions limit the accuracy of the values obtained.

First, the accelerated beam has to be isolated from background electrons. This can be done by using a four-dimensional data set of $[x, y, p_x, n_e]$ and only considering data above a certain $p_x$ threshold. Alternatively, the simulation can be set up such that the plasma slab ends at a certain distance and the beam propagates out of this

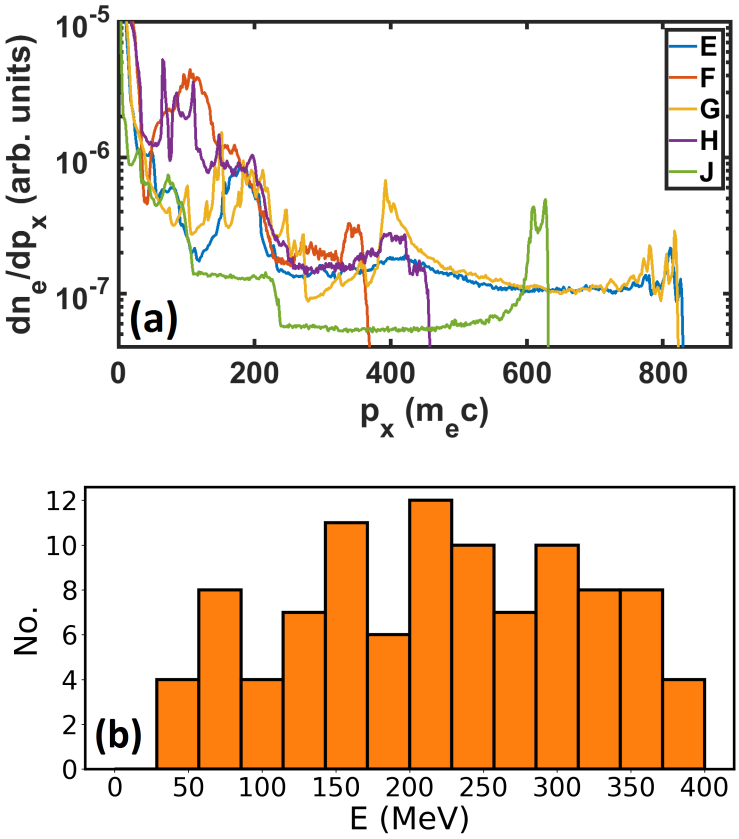



Figure 3.24: Panel (a) compares the charge density of all particles within the simulation box (plotted against the longitudinal momentum) for different simulations. Panel (b) is a histogram of the energy distribution of 100 injected macro-particles from simulation E. All results were obtained after 4.33 ps.

region into a vacuum. After isolation of the accelerated beam, the following routine can be applied: The integrals of the charge density as well as its square along the transverse dimension for a given $x$-cell is taken:

$$\int n_e dy \sim 2 n_0 w_0 \ , \tag{3.26}$$

$$\int n_e^2 dy \sim 2 n_0^2 w_0 \ . \tag{3.27}$$

The parameter $w_0$ can be rewritten as

$$w_0 \sim \frac{\left(\int n_e dy\right)^2}{2 \int n_e^2 dy} = \frac{4 n_0^2 w_0^2}{4 n_0^2 w_0} \ . \tag{3.28}$$

The particle number in a two-dimensional structure in $y$-$z$-space which can be approximated using a cylindrically symmetric distribution function is

$$\begin{aligned} N dx \sim \pi w_0^2 n_0 dx &= 2 n_0 w_0 \frac{\pi}{2} w_0 dx \\ &= \int n_e dy \frac{\pi}{4} \frac{\left(\int n_e dy\right)^2}{\int n_e^2 dy} dx \\ &= \frac{\pi}{4} \frac{\left(\int n_e dy\right)^3}{\int n_e^2 dy} dx \ . \end{aligned} \tag{3.29}$$

This expression can be found at every point in $x$-direction and taking the integral (or the sum) over $dx$ results in the particle number. However, there are errors associated with the approximation that every $dx$ slice is cylindrically symmetric. No assumption on the symmetry of the total beam was made.

The result is independent of the parametrisation of the density profile, beamwidth, and shifts from the axis. The results are exact for a top-hat beam profile with half-width $w_0$. For a Gaussian beam profile, the factor $\pi/4$ in the last line of equation 3.29 needs to be replaced with $1/\sqrt{2}$. Therefore, the calculated value is correct within 10% for any super-Gaussian distribution at each $x$-slice within the simulation box. Figure 3.25 shows a plot of these three distribution functions.

It is possible that there is more than one bunch being accelerated. If there is no overlap between the beams (separation distance $s \gg w_0$) then - assuming two Gaussian beams - an additional factor of $f = 1/2$ arises. For perfect overlap ($s = 0$) between the beams the charge calculation is accurate. For $s$ values that lie in between, the factor is (see Appendix A.7)

$$f = \frac{1 + e^{-\frac{1}{2}(s/w_0)^2}}{2} \ . \tag{3.30}$$

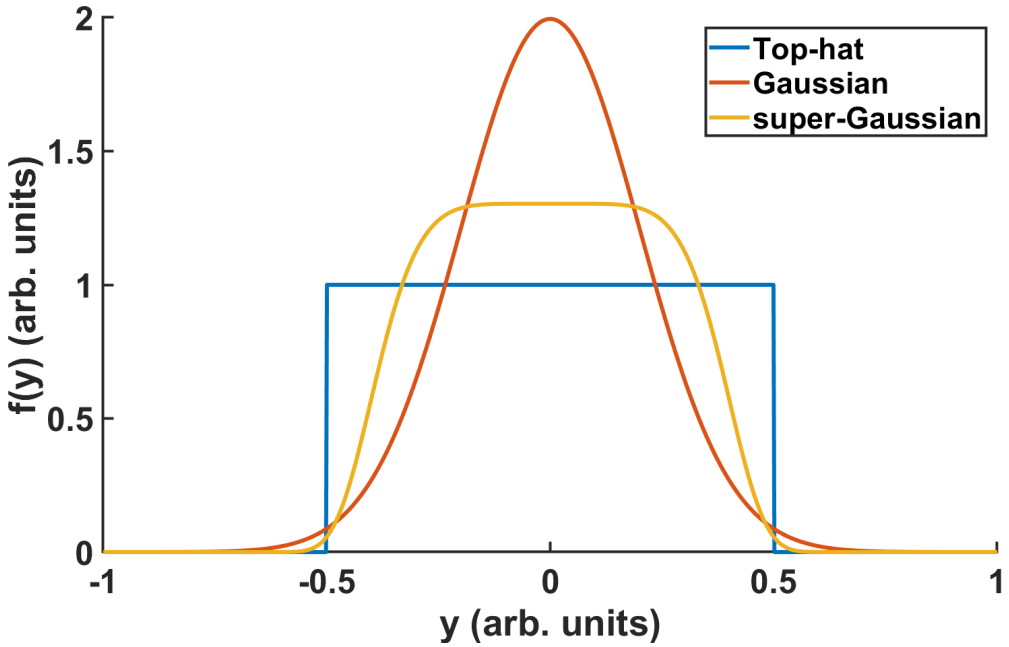



Figure 3.25: Distribution functions for which the cumulative charge of the particle beam can be determined to be within a 10% uncertainty interval.

The electron beam charge found for each simulation using this method is shown in Tab. 3.4.

| Simulation | D | E | F | G | H | I | J | K | L |
|---|---|---|---|---|---|---|---|---|---|
| Q ($> 80\%$) | 8.0* | 7.2 | 1.6 | 5.4 | 9.1 | 15.2 | 7.6 | 6.0* | 9.6 |
| Q ($> 500\, m_e c$) | 0.0 | 22.1 | 0.0 | 18.1 | 0.0 | 0.0 | 7.9 | 0.0 | 12.8 |

Table 3.4: This table lists the charge accelerated within the highest 20% of momentum and above 500 $m_e c$ for different simulations. All values are given in units of pC. The asterisk indicates that the value was calculated from an earlier time step in simulations D and K compared to all other simulations due to dephasing and charge reduction of electrons at later time steps.

#### 3.2.4.2 Quantitative comparison

The cluster experiment conducted in [157] (in chapter 4 of this reference) has well-characterised beam parameters which is why it is chosen for quantitative comparison to the simulation data I have presented above. The author used a 10 TW laser pulse with a duration of 37 fs. The maximum laser amplitude was $a_0 = 3.9$. The nanometre-

sized methane clusters created an average plasma electron density $\langle n_e \rangle$ with values between 0.8 and $2.2 \times 10^{19}\,\mathrm{cm}^{-3}$. The electrons were measured above a cutoff energy of 45 MeV and showed a large energy spread. The highest peak electron energy measured in the cluster experiments was 249 MeV($\pm$8 MeV). The lowest peak electron energy measured was not explicitly stated but can be read from the plot to be between 60 and 80 MeV. Compared to these values, simulation E in this chapter found a peak electron energy of 389.5 MeV. The charge in the experiment was measured to be between 2 and 48 pC (depending on electron density and position of focal spot) which is on the same order of magnitude as the 7.2 to 22.1 pC from the simulation (depending on the measurement cut-off as shown in Tab. 3.4). An alternative approach which used a peak energy-dependent relative[20] cut-off was also tested, in which the charge measurement is truncated below the relative energy value obtained from dividing the lower experimental cut-off energy ($E_{\mathrm{co,exp}} = 45\,\mathrm{MeV}$ below which no data was taken) by the experimental peak energy and multiplying by the simulated peak energy. This means that

$$Q = 0 \text{ for } E < E_{\mathrm{co,sim}} = E_{\mathrm{peak,sim}} \frac{E_{\mathrm{co,exp}}}{E_{\mathrm{peak,exp}}} \ . \tag{3.31}$$

Here, the impact of taking a charge measurement with a truncated spectrum is relativised (charge measurements where the peak energies are low are stronger affected by a constant energy cut-off). When the experimental peak energy is high, the relative cut-off is smaller than when the experimental peak energy is low. The measurement using two representative energy peak values from the experiment yields $Q_{\mathrm{sim}} = 25.1\,\mathrm{pC}$ for an experimental peak energy of $E_{\mathrm{peak,exp}} = 80\,\mathrm{MeV}$ or $Q_{\mathrm{sim}} = 79.6\,\mathrm{pC}$ for an experimental peak energy of $E_{\mathrm{peak,exp}} = 200\,\mathrm{MeV}$. This method gives higher charge values because a greater part of the low energy tail of the spectrum contributes to the total beam charge.

### 3.2.5 Analysis of laser pulse properties

The laser propagation properties in a cluster plasma were found to differ from the well-known case in a uniform plasma [154]. The dispersion relation is modified by a restoring force due to the polarisability of the cluster:

$$n^2(k,\omega) \equiv \frac{c^2k^2}{\omega^2} = 1 - \frac{p\omega_p^2}{\omega^2 - f\omega_p^2 + i\gamma\omega} - \frac{q\omega_p^2}{\omega^2} \ . \tag{3.32}$$

[20] Here, the relative value is not pre-set but depends on the ratio between the lower experimental energy cut-off and the experimental peak energy selected.

Here, p is the "packing" ratio of cluster volume to the entire volume, f is a factor of order unity which is related to the geometry of a cluster, q is the ratio between the background plasma density and the cluster electron density, $\omega_p$ is the oscillation frequency within a cluster, and $\gamma$ is the damping rate of plasma oscillations. This leads to the "cluster mode" which allows a laser pulse to propagate in plasma of even highly overcritical clusters.

It has to be mentioned that the theory of cluster polarisation does not describe the process of cluster disintegration. However, at intensity values used in wakefield acceleration, this process starts early on in the laser-cluster interaction and its strength depends on the cluster parameters. It can be argued that at the leading edge of the laser pulse the impact of the polarisation effect should be more pronounced in simulations using clusters of higher electron density and size. The reason for this would be that the electrons stay associated with the respective ion cluster for a longer time whereas at the back of the laser, the high charge leads to fast expansion through the Coulomb explosion mechanism. However, the deterioration of the laser shape prevents accurate measurements of the group velocity in plasmas of high electron density clusters. The velocity of the intensity peak on the other hand is measured more easily. Taking a line-out through the laser propagation axis and measuring the position of the intensity envelope's central peak at initialisation ($t = 0$) gives a reference value to which later measurements are then compared.

The peak velocity values for cluster $v_{mp} = 1.0004\,c$ (simulation G) and uniform $v_{mp} = 0.9993\,c$ (simulation D) plasmas are found by comparing the reference value to the peak position at the last time step. It is important to note that this apparent superluminal velocity is an artefact caused by the way the velocity is measured. To obtain the value, the change in position of the intensity peak was measured between two time steps. The peak of highest intensity moves faster than $c$ due to red-shifted photons[21] at the front edge of the laser pulse overlapping with unshifted photons due to the difference in group velocity. This locally increases the intensity causing a shifted peak at the leading part of the pulse. The difference between the two measurements indicates that, in the cluster case, either the etching velocity is lower or the group velocity is higher, both of which have an impact on the wakefield's phase velocity. Similar results from other cluster simulations suggest that the laser pulse

[21] The frequency shift of photons in electron density gradients [212, 213] is an important effect associated with laser pulse propagation in a plasma. The "red-shift" is a manifestation of photon deceleration and is associated with the energy loss from driving a wakefield while preserving the photon number within the pulse [214, 215].

group velocity does not strongly depend on cluster parameters within the range of values studied in this chapter.

This result indicates that through the use of cluster targets a (slight) increase in dephasing length $L_{dp} \simeq (1-(v_g - v_{\rm etch})/c)^{-1} R$ is obtained. Here, $v_g$ is the laser group velocity, $v_{\rm etch}$ is the laser etching velocity[22], and $R$ is the bubble radius. The quantity $R$ was observed to fluctuate strongly in the cluster case. Therefore, some trapped electrons experience an increase in dephasing length leading to higher peak energy. Furthermore, a larger group velocity also increases the dephasing length. The change in wakefield phase velocity $v_\Phi \simeq v_g - v_{\rm etch}$ from $v_\phi^{\rm unif}$ to $v_\phi^{\rm cl}$ causes an increase of the dephasing length by a factor

$$\frac{L_{dp}^{\rm cl}}{L_{dp}^{\rm unif}} = \frac{1 - v_\phi^{\rm unif}}{1 - v_\phi^{\rm cl}} \ . \tag{3.33}$$

Earlier, I mentioned that the simulations using denser and larger clusters suffer a stronger impact when it comes to the depletion (etching) of the front of the laser pulse (see Fig. 3.23). However, this is not the case for the etching velocity itself. The Fourier transform of the perpendicular electric field $E_y(x, y)$ shows (Fig. 3.26) that dense (panel b) and large (panel c) clusters do not cause a red-shifted spectrum as strongly as the simulations using lower cluster peak density (panels d,e) or even the uniform simulation (panel f). This result means that an efficiently driven wakefield exists in simulations D, E, and G, whereas energy must be lost via a different mechanism in simulations F and H. It is argued in [146] that the observation of strong etching is related to the increased resonant laser absorption at high electron density clusters. In addition, photon scattering from overcritical targets depletes the laser without driving a wakefield efficiently. The energy loss over time is plotted in Fig. 3.27 and is observed to be larger in simulations F and H than in simulations E and G. At the same time, the red-shifted peak is not pronounced as strongly. The strongest (relative) energy depletion of the laser pulse is found for lower initial energy in both uniform (K) and cluster (L) cases. A reduced average electron density (I,J) leads to a smaller depletion effect.

[22]While propagating in plasma, the front of a laser pulse can be abrased with a velocity $v_{\rm etch} \propto \omega_p^2/\omega_0^2$ [216]. This means that the laser is depleted after propagating over a distance of $L_{etch} \simeq c\tau_{\rm FWHM}\omega_p^2/\omega_0^2$. This effect is called laser etching.

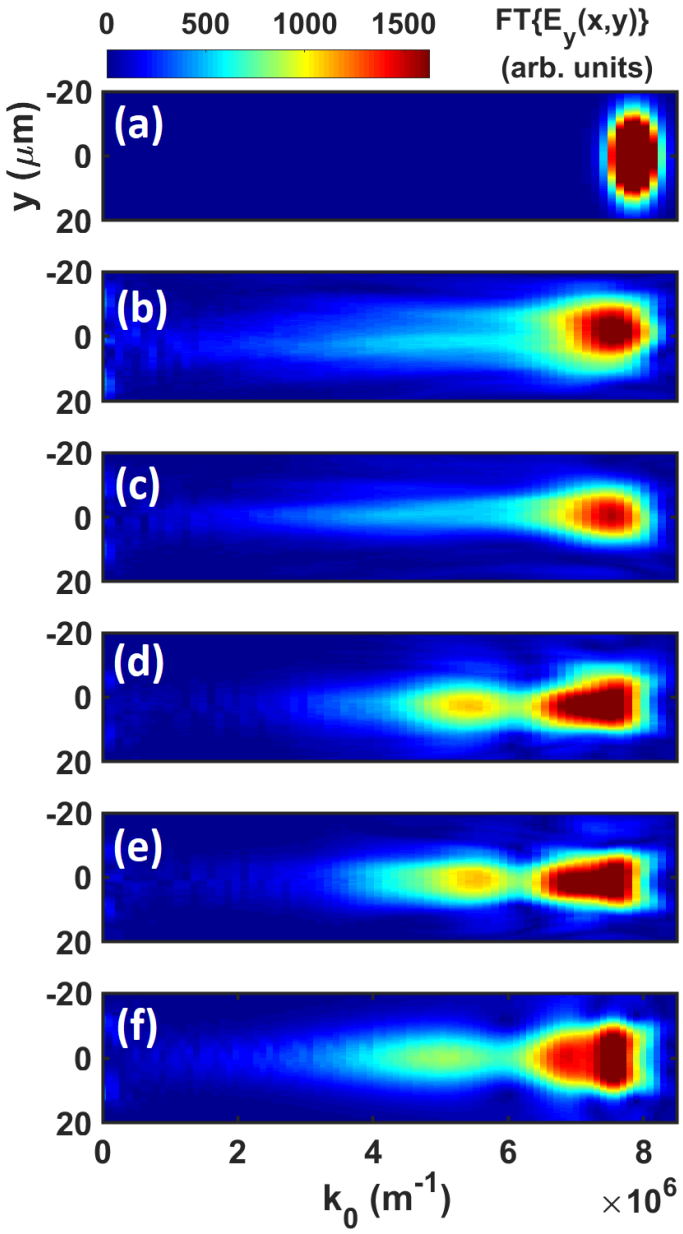



Figure 3.26: This figure shows the Fourier transform of the perpendicular electric field $\mathcal{F}[E_y(x,y)] = \tilde{E}_y(k,y)$ at the first time step (panel a) and after 4.33 ps (b-f). Panels (b-e) show results using different cluster parameters and panel (f) shows data from a uniform simulation. The normalised cluster electron density is 5 (panel b, simulation F), 2.5 (panel c, simulation H), 1.25 (panel d, simulation E), and 0.75 (panel e, simulation G). The relative normalised number density of clusters in the simulation box is 0.15 (b), 0.17 (c), 0.6 (d), and 1 (e) resulting in the same average charge density. The reference wave vector value for a laser of wavelength $\lambda_0 = 800\,\mathrm{nm}$ is $k_0 = 7.85 \times 10^6 \mathrm{m}^{-1}$ in vacuum and $k_0 = 7.84 \times 10^6 \mathrm{m}^{-1}$ in plasma of $n_e = 0.004\, n_{cr}$.

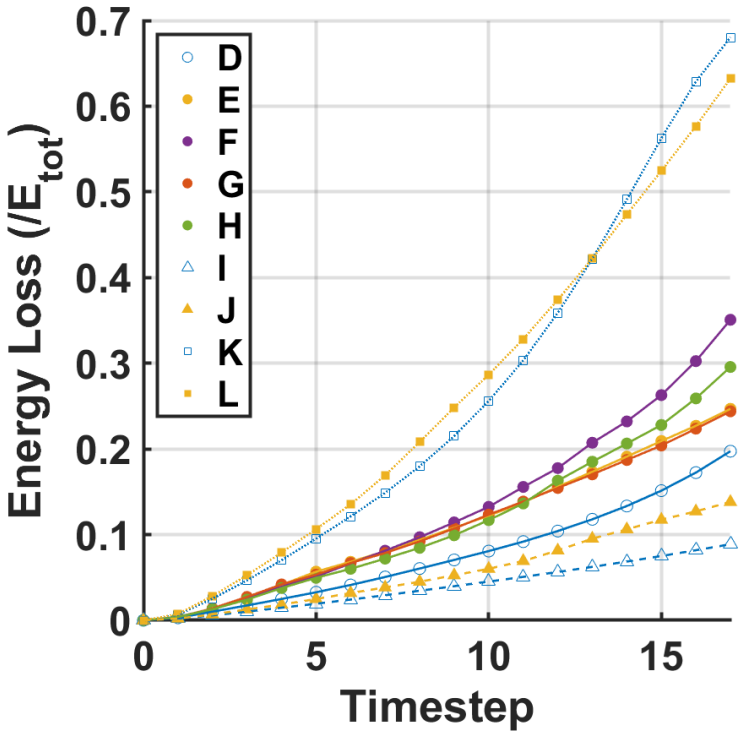



Figure 3.27: This figure shows the evolution of laser pulse energy loss normalised to its initialisation value. Hollow marker objects represent the use of a uniform plasma whereas filled marker objects represent a cluster plasma. Triangles represent simulations using half the plasma electron density ($0.002\,n_{cr}$). Squares represent the use of laser pulses of reduced energy (18.9% of the value of all other simulations) delivered in a pulse of half the duration (15 fs). The parameters of each simulation are listed in Tab. 3.3. One time step corresponds to 0.25 ps in simulation D and to 0.26 ps in all other simulations.

## 3.3 Summary and conclusion

This chapter presented an analysis of the shape of a wakefield in a cluster plasma as well as a high-resolution numerical study of the interaction of a high-power laser pulse with a cluster plasma of randomised cluster locations. The first section comprised both experimental and numerical results which showed that the first electron plasma wavelength is increased for low laser amplitudes driving a weakly non-linear wakefield which can lead to an increase in dephasing length. The second section showed that there exists an injection mechanism that differs from electron self-injection in a uniform plasma and has some similarities to ionisation injection. In simulations the electron bunches generated from cluster targets were found to exhibit features similar to those observed in earlier experiments, and which had remained unexplained. This process of continuous electron injection leads to accelerated bunches with large

quantities of charge accelerated to high energies that create betatron emission from undulation within the wakefield (which is one of the main applications that electron beams from cluster targets may have). It was shown that tuning the cluster parameters gives control over various aspects of electron acceleration which can be done with different gas targets, jet nozzles, backing pressures, and various other parameters. Furthermore, the enhanced group velocity of the laser pulse extends the dephasing length provided that energy depletion is mitigated.

# Chapter 4

# Experimental study of electron injection using a two-pulse ionisation injection scheme

As discussed in section 2.5.4, self-injection of electrons through the wave-breaking mechanism in the non-linear regime can create electron bunches of high charge. The duration over which injection occurs can be long and uncontrollable causing large energy spreads. This is an issue for real-world applications such as radiotherapy [64] which strive for mono-energetic beams of high charge and low emittance. This is why the idea of finding new mechanisms leading to the trapping of electrons in plasma wakefield accelerators has found a lot of attention in the recent past. For example, modifications to the plasma profile such as strong and localised density gradients can be utilised to create a narrow region within which trapping occurs. These methods have been shown to be capable of creating beams of narrow transverse momentum spread [107] and high reproducibility [110]. In 2021, near-GeV electrons with an energy spread of $\ll 1\%$ have been reported using a tailored density profile [112]. Other approaches [103, 210] have used the large separation of successive ionisation levels in some elements to inject particles at specific positions in the wakefield potential causing an eased trapping condition as was described in the previous chapter.

The idea of using two laser pulses to separate the injection and acceleration processes of electrons in wakefields has been proposed in various schemes. One of the earliest methods [217] suggested the use of two orthogonally propagating pulses where the second locally alters the trajectories of some electrons to enable trapping. In 1997, Esarey *et al.* [218] modified the method and proposed a head-on collision of two injector pulses. This collision causes trapping into a wakefield which has been created by a third pump laser pulse. Almost a decade later, an experiment successfully showed

stable low-emittance electron beams injected through a collision of two pulses [117].

In 2014, Yu *et al.* [219] and Xu *et al.* [220] both proposed to use two laser pulses of different wavelengths separating the electron injection process from the wakefield excitation in a slightly different manner to achieve low emittance electron beams. Here, the beams are co-propagating at a set separation distance rather than counter-propagating. This scheme can be difficult to implement experimentally considering one has to have access to a facility allowing for the simultaneous use of laser pulses with parameters such as (in the case of Xu *et al.* ) a spot size of $w_1 = 0.64\,\mu\text{m}$ and pulse duration of $\tau_1 = 7\,\text{fs}$ at a wavelength of $\lambda_1 = 80\,\text{nm}$ for the injector and $w_0 = 10\,\mu\text{m}$, $\tau_0 = 18\,\text{fs}$, and $\lambda_0 = 800\,\text{nm}$ for the drive pulse.

In 2013, the two-pulse ionisation injection (2PII) scheme was introduced by Bourgeois, Cowley and Hooker [57] which uses two pulses of the same wavelength with a longitudinal separation of $\lambda_p$. The wakefields driven by the pulses add coherently to create a large wakefield amplitude over a short amount of time aiding the trapping of nitrogen electrons. The duration over which the injector pulse is able to free the sixth and seventh nitrogen electrons is tailored using a specific (comparably short) injector Rayleigh length and laser amplitude slightly above the ionisation threshold. The dissipation of energy (local decrease in intensity) quickly terminates the injection process leading to a narrow electron spread. The trapped electron beam is then, depending on the driver pulse amplitude, accelerated in a (quasi-)linear wakefield. The simulations in the 2PII paper showed the creation of electron bunches with a charge of 5 pC, mean energy of 370 MeV, and a relative energy spread of 2%.

Acceleration in low amplitude wakefields is advantageous as unwanted self-injection is avoided. Furthermore, it is possible to guide the drive pulse in a controlled environment such as a plasma channel [97, 98] allowing for long acceleration lengths.

In 2019, experimental results of a two-colour scheme ($\lambda_0 = 800\,\text{nm}$, $\lambda_1 = 400\,\text{nm}$) were reported [221]. In the experiment the main laser pulse was split into a 1.9 J, $w_0 = 25\,\mu\text{m}$ drive pulse and a 0.1 J, $w_0 = 2.5\,\mu\text{m}$ injector pulse. While the drive beam consistently self-injected and accelerated electrons on its own, charge and cutoff energy[1] boosts were reported (strongest effect when using p-polarisation) for a perfect overlap of the two pulses compared to the case with a delay between the pulses as well as the case without splitting the beam leaving only the driver pulse. It has to be noted that this work operated in the nonlinear regime.

[1]No significant enhancement in (charge density) peak energy was found. These values stayed consistently at $\sim 100\,\text{MeV}$.

This chapter presents work done towards achieving electron acceleration using the 2PII mechanism and is structured as follows. In Section 4.1, I will discuss important aspects of the planning process of the experiment. Then, I will describe the diagnostics that were used to conduct the experiment probing the 2PII mechanism and present the results of the campaign. In Section 4.2 I will discuss two-dimensional particle-in-cell simulations and how they relate to the experimental findings giving an outlook of possible improvements. Section 4.3 gives a summary of the findings and discusses future work. The contents of this chapter are currently being prepared for submission to a peer-reviewed journal.

## 4.1 Experimental investigation of the 2PII mechanism

To attempt the experimental verification of the 2PII scheme, a grant proposal was written in autumn 2019 with the objective to get access to the HERCULES high-power laser facility at the Center for Ultrafast Optical Science (CUOS) at the University of Michigan in Ann Arbor. The experiment was scheduled to take place in 2020 but had to be delayed to early 2021 due to the travel restrictions linked to the COVID-19 pandemic. Many scientists assisted in conducting this experiment without whom it would not have been possible to get results in such a short amount of time. I want to highlight the support by the two Target Area Officers from the University of Michigan, Yong Ma and Paul Campbell, who committed to many hours of work during the experiment and who shared their valuable experience.

### 4.1.1 Experimental considerations and restrictions

When planning an experiment, one often has to consider limitations that make it impossible to recreate the perfect conditions such as those in the simulations conducted in the article first discussing the 2PII scheme [57]. Restrictions (or deviations from optimal conditions) can apply to many experimental parameters such as laser pulse shape, laser pulse duration, available laser pulse energy, delay between pulses, laser beam alignment, plasma density profile, availability of optical components at laser facility, vacuum chamber size, *et cetera*.

To conduct an experiment seeking to produce an electron beam using the 2PII injection scheme, one has to consider dependencies between parameters in the design stage. A useful quantity when comparing electron beam properties (for convenience I

call this meta-quantity $\Omega$) depends - amongst other parameters - on the beam's normalised energy spread $\Delta E/E_{\mathrm{peak}}$, the accelerated charge $Q$, and the radial normalised root-mean-square emittance

$$\epsilon = \sqrt{\langle r^2 \rangle \langle p_r^2 \rangle - \langle r p_r \rangle^2} \ , \tag{4.1}$$

where $\langle rp \rangle = \overline{rp} - \overline{r}\,\overline{p}$. Here, the bar means taking the average over all particles in the accelerated bunch. In an idealised case (Gaussian beam shape, perfect spot, parallel beam propagation) this is a function

$$\begin{aligned} \Omega = F \Big[ & d_\eta, w_{0,\eta}(f_\eta, D_\eta, \lambda_{0,\eta}; n_e); a_{0,\eta}(w_{0,\eta}, P_\eta); z_{R,\eta}(w_{0,\eta}, \lambda_{0,\eta}); \\ & \lambda_p(n_e^{\mathrm{A}}, n_e^{\mathrm{B}}; d_\eta); \Delta t(\lambda_p); \Delta r_\eta; P_\eta(E_\eta, d_\eta); \dots \Big] \end{aligned} \tag{4.2}$$

where the index $\eta = \{\mathrm{inject}, \mathrm{drive}\}$ is used to indicate that the function depends on the properties of both pulses. The parameters used here are the laser pulse duration $d$, the laser spot size $w_0$, the focal length of the focusing optic $f$, the diameter of the collimated beam $D$, the laser wavelength $\lambda_0$, the electron density of species A $n_e^A$ and species B $n_e^B$, the normalised laser amplitude $a_0$, the laser pulse power $P$, the Rayleigh length of the focused beam $z_R$, the plasma wavelength $\lambda_p$, the temporal separation between the two pulses $\Delta t$, the relative radial separation of the two pulses at focus $\Delta r$, and the laser pulse energy $E$.

Nowadays, Ti:sapphire laser facilities that are able to deliver enough power to the target in order to test the 2PII scheme typically have a compressed laser pulse duration on the order of $d_{\mathrm{FWHM}} \simeq 30\,\mathrm{fs}$. This automatically imposes limits on the remaining interconnected properties of the parameter space in which the scheme can be observed. For example, the plasma wavelength has to be large enough such that the laser pulse does not strongly interfere with the injected electron bunch in the accelerating field of the wake. Hence, the total electron density has to be chosen accordingly and is limited to a value $n_e \lesssim 1 \times 10^{19}\,\mathrm{cm}^{-3}$. This, in turn, poses a limit on the laser pulse spot size $w_0$ and, therefore, on the parabolic mirrors used to focus the beam. To create a stable wakefield into which electrons are injected, the spot size needs to be roughly matched to the plasma wavelength for optimal exploitation of the 2PII scheme. When introducing more restrictions such as a maximal focal length $f$ (due to the vacuum chamber size), limited variation in beam diameter $D$, or power limits, one quickly finds oneself in a very narrow parameter space suitable for 2PII operation.

### 4.1.2 The HERCULES high-power laser facility

The HERCULES laser is an 800 nm Ti:sapphire system that delivers up to 9 J to the target chamber in a 30 fs (FWHM) pulse which gives a peak power of 300 TW. This allows for splitting the beam while each part retains enough power to be used for the 2PII scheme. The collimated beam diameter entering the experimental vacuum chamber was 10.16 cm. Due to vacuum chamber size restrictions, the maximum focal length that could be used was $\sim 2$ m.

### 4.1.3 Generating two collinear pulses

In the experiment conducted at CUOS, it was important to reduce spatial and temporal beam jitter in order to achieve optimal beam overlap spatially and optimal delay control temporally. This meant that it was necessary to split the beam as late as possible (preferably within the final vacuum chamber). After considering various beamline designs, I decided that the most effective way of doing this was to use a 5.08 cm diameter pickoff mirror that would split the beam into two parts of area (or intensity) ratio $\sim 1:3$. As typical mirror holders would block a significant part of the second ring-shaped beam, the pickoff mirror was glued onto a thin post of 0.64 cm diameter - a construction which allowed for control of the roll, pitch, and yaw of the mirror. The mount is shown in Fig. 4.1.

The question of which beam to use for which of the two purposes—driving the low amplitude wakefield and injecting electrons into the wakefield—had to be answered with all available optics in mind. The final decision was made when it became clear that, due to space constraints, the incoming beam could not be telescoped down to a diameter of 5.08 cm. This meant that, in order to have a drive beam Rayleigh range comparable to the acceleration distance (using the parabolic mirror of $f = 2.03$ m focal length), the beamlet containing 25% of the total power had to be used due to its smaller diameter $D = 5.08$ cm giving a larger ($1/e^2$ intensity) spot size

$$w_0 = \frac{2}{\pi}\lambda\frac{f}{D} \ = 20.4\,\mu\text{m} \ , \tag{4.3}$$

which is on the lower end of what the 2PII mechanism can tolerate as indicated by preliminary particle-in-cell simulations. This choice puts a constraint on the minimum energy used in the total beam as the drive pulse should (according to the theory) reach a normalised laser amplitude of $a_0 \approx 1$ to support the trapping mechanism as shown in the theoretical study in reference [57].

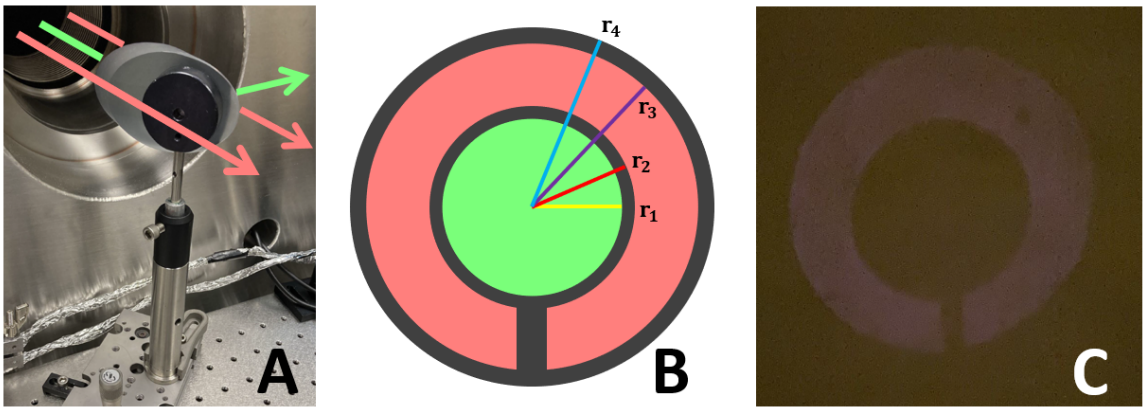



Figure 4.1: Panel A of this figure shows a photograph of the pickoff mirror mounted on a custom-made holder installed in the target chamber. The arrows symbolise the beam paths. Panel B shows the beam cross-sections after the split has occurred (not to scale). The green part is used as drive beam and the red part is used as injector beam. The black areas correspond to energy which is lost. The energy corresponding to area $(r_4^2 - r_3^2)\pi$ is lost due to the frame of a quarter wave plate installed further down-stream in the beamline. The energy corresponding to area $(r_2^2 - r_1^2)\pi$ is lost due to the imperfect orientation of the pickoff mirror. The energy corresponding to the black horizontal rectangle connecting the two black circles at the bottom is lost due to the post holding the pickoff mirror. Panel C shows a photograph of the scattered light of the injector pulse (after the split) being reflected from a sheet of paper.

If the ratios $R_1$ (energy preserved after the split at the pickoff mirror) and $R_2$ (energy preserved after the split at the pellicle which is used to generate a probe beam) are known, then the energy needed to reach the wanted amplitudes at focus is

$$E_{\text{tot}} = \frac{E_d}{\epsilon R_1 R_2} \ , \tag{4.4}$$

where $E_{\text{d}}$ is the drive pulse energy and $\epsilon$ is the efficiency of beam transportation to the target (including all losses at mirrors).

Equation 4.4 considers that $E_d/(R_1R_2) > E_i/(1-R_1)$ which is true for the configuration considered in this experiment.

The driver energy is given by the product of pulse duration $d_d$ and pulse power $P_d$ (I will omit the subscript as the calculation holds for both pulses):

$$E = Pd \ . \tag{4.5}$$

The instantaneous peak pulse power is defined by

$$P = \iint I(x,y)dxdy = \zeta A I_0 \ , \tag{4.6}$$

where $\zeta$ is a factor depending on the pulse shape, $A$ is the focal spot area of the pulse, and $I_0$ is the peak intensity at focus. For a Gaussian pulse, $A$ is given by

$$A = w_0^2\pi = \left(\frac{\text{FWHM}}{\sqrt{2\ln 2}}\right)^2 \pi \ , \tag{4.7}$$

with $w_0$ being the radius at which the intensity of a Gaussian pulse drops to $1/e^2 \simeq 0.135$. $I_0$ is expressed in terms of the normalised laser amplitude $a_0$ as

$$I_0 = \frac{a_0^2 \times 10^4}{(8.55 \times 10^{-10})^2 \lambda_{\mu\text{m}}^2} \ [\text{Wm}^{-2}] \ , \tag{4.8}$$

where the pulse's wavelength $\lambda_{\mu\text{m}}$ is in units of µm.

The actual pulse length was characterised by the laboratory's laser scientists using auto-correlation to be $d = 39\,\text{fs}$ rather than its nominal value of 30 fs. Therefore, the total energy required to generate a wakefield of $a_0 = 1$ at a focal spot radius of $w_0 = 20.4\,\mu\text{m}$ using the drive pulse was $E_{\text{tot}} = 5.65\,\text{J}$. This number was calculated using an estimated efficiency of $\epsilon = 0.4$ (measured in previous experiments at HERCULES). The actual efficiency was measured in air during low power mode operation using a calorimeter to quantify the losses at various optics throughout the beamline.

In this mode, the energy of the pulse before the compressor chamber was measured by the laser scientists (using a calorimeter) to be 1.85 mJ with a standard deviation

of $\sigma = 0.209\,\mathrm{mJ}$. The energy of the drive pulse after the final optic was $0.192\,\mathrm{mJ}$ with $\sigma = 0.021\,\mathrm{mJ}$. The energy of the injector pulse without a quarter-wave plate in the beamline was $0.335\,\mathrm{mJ}$ with $\sigma = 0.05\,\mathrm{mJ}$. Introducing a quarter-wave plate reduced the energy[2] to $0.282\,\mathrm{mJ}$ with $\sigma = 0.025\,\mathrm{mJ}$. The energy efficiency is calculated from the formula

$$\epsilon = \frac{E_f}{E_i} \frac{1}{\prod_k (1 - L_k)}, \tag{4.9}$$

where $E_f$ and $E_i$ are the final and initial measured energy values and $L_k$ is the loss when the beam is split at optic $k$. The driver efficiency was calculated using a factor originating from the energy loss at the pickoff mirror $L_1 = 0.75$ and a factor originating from the energy loss in the pellicle $L_2 = 0.04$. Its value is $\epsilon_d = 0.43$. The injector efficiency was calculated using $L_1 = 0.25$ (opposite split ratio). Without the wave plate it is $\epsilon_i = 0.24$ and with the wave plate it is $\epsilon_i^* = 0.20$.

Due to the imperfect nature of experiments, the spot sizes depend to a great extent on the quality of alignment. Therefore, higher energy values are required to account for those larger spot sizes. Optimally, control over the fraction $P_i/P_d$ is needed to find the desired peak intensity of both pulses, especially as in the present case three-quarters of the energy goes into the beam of significantly smaller spot size (this will be further discussed in Section 4.1.7.3).

The 2PII mechanism requires that both beams go through the same focal point and propagate along the same axis. To achieve this, a hole was drilled into the short focal length ($f = 38.8\,\mathrm{cm}$) gold off-axis parabolic mirror (OAP) which was closer to the target chamber centre (TCC). Care was taken that the drive beam could pass without being clipped at the hole's edges while the full injector ring was reflected from the OAP's gold surface.

### 4.1.4 Target chamber layout

The layout of the optical components and beamlines within the target vacuum chamber is shown in Fig. 4.2.

The target chamber had an area of $0.97\,\mathrm{m} \times 3.75\,\mathrm{m}$. The incoming beam was split into two parts using a pickoff mirror as described in the previous section. The outer part (injector) was reflected from a mirror to be incident on a deformable mirror[3] (DM) whose motors optimised the wavefront of the beam (see Section 4.1.7.2). From the DM the beam was reflected and passed through a quarter-wave plate. After being

[2] This reduction is mainly caused by clipping of the beam on the edge of the mount whose diameter was slightly smaller than that of the ring-shaped top-hat beam.

[3] A deformable mirror is also commonly referred to as adaptive optic (AO).

reflected from a further mirror, the beam was focused using a 388 mm focal length OAP which had a hole drilled through its centre. The beam reflected from the pickoff mirror (driver) was guided through a delay stage and arrived on the 2.03 m focal length parabola which focused the beam through the OAP hole so that it overlapped with the injector in the gas cell. A pellicle with reflectivity of 4% was introduced into the drive beamline which split off the probe for the interferometry diagnostic. To have control over the pulse's arrival time, the probe also passed through a delay stage. The probe beam exited the chamber to be characterised on the diagnostic table (see Section 4.1.7.1).

A focal spot imaging system consisting of a lens, a mirror and a CCD was mounted on a translation stage behind the gas cell to be moved out of the beamline during high power shots (see Section 4.1.7.3). A 1.03 T magnet and two Lanex[4] screens were located at the down-stream end of the chamber behind the gas cell to deflect and measure accelerated electrons. The fluorescent intensity signal was measured using two cameras placed outside of the chamber. The Lanex screens were placed within a housing of matte black aluminium foil (with cut outs for the chamber windows) to keep any laser light from saturating the CCDs. To measure the beam pointing stability (see Section 4.1.7.4) the leak-through light from the sixth mirror in the drive beamline was reflected out of the chamber. It was then focused and recollimated using a lens. A CCD was used to measure the focal spot position.

Another translation stage was introduced just before the gas cell (not shown in Fig. 4.2) which allowed for moving a mirror into the injector beamline and reflecting the focusing beam into a microscope objective. The beam then propagated through a lens just inside the target chamber and was imaged onto the wavefront sensor on the diagnostic table (see Section 4.1.7.2).

[4] "Lanex" is the commercial name for rare earth intensifying screens.

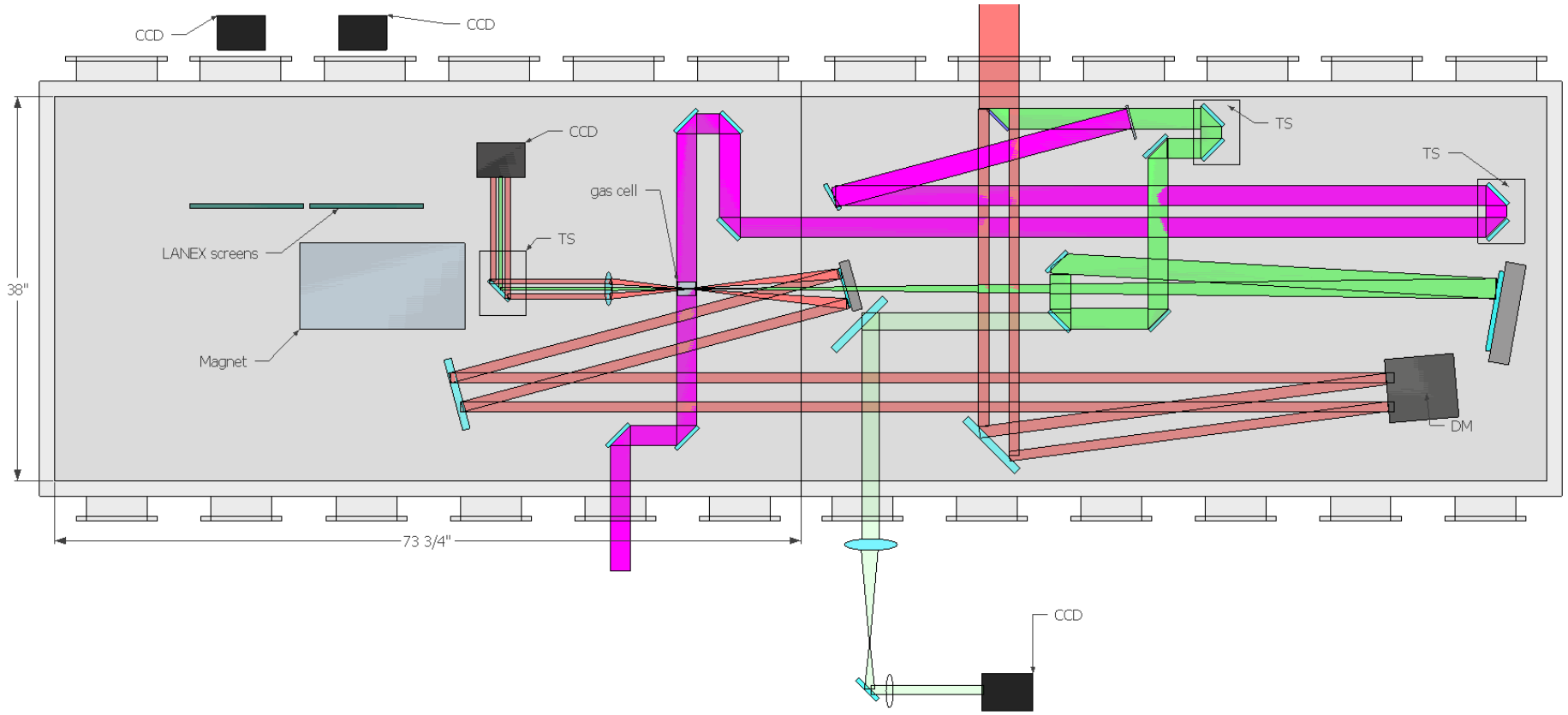



Figure 4.2: This figure shows the layout of the beamlines and placement of optics in the HERCULES gas target vacuum chamber. The driver beam is depicted as green, the injector beam as red, and the probe beam as pink. "DM" stands for deformable mirror which is used to optimise the focal spot. "TS" stands for translation stage used for modifying the pulse arrival times.

| $M_{He} : M_{N_2}$ | 90 : 10 | 95 : 5 | 97 : 3 |
|---|---|---|---|
| $A_{He} : A_N$ | 81.81 : 9.09 | 90.48 : 9.52 | 94.17 : 5.83 |
| $A^*_{He} : A^*_N$ | 32.15 : 7.14 | 39.59 : 4.17 | 43.31 : 2.68 |
| $n_{e,He} : n_{e,N}$ | 64.29 : 35.71 | 79.17 : 20.83 | 86.61 : 13.39 |

Table 4.1: Atom and electron ratios obtained from three different He-$N_2$ mixtures. $M$ stands for molecules, $A$ stands for atoms, $A^*$ stands for atoms normalised such that the ionised electrons (2 from He and 5 from N) add up to 100%, and $n$ stands for electrons. It is assumed that 5 electrons are ionised from each nitrogen atom.

### 4.1.5 Gas selection

The original 2PII article simulates the process for a hydrogen-nitrogen mixture with a set (hydrogen) electron density of $2.0 \times 10^{18}\,\mathrm{cm}^{-2}$ doped with 5% nitrogen atoms (in addition). Assuming that in the relevant region the drive pulse ionises five electrons from the nitrogen atom, the total ratio between electrons from hydrogen and nitrogen is $n_{e,H}/n_{e,N} = 100/25 = 4$. In the experiment conducted at the CUOS, a helium-nitrogen mixture was used instead to avoid complications with handling hydrogen. Since nitrogen is a diatomic molecule a conversion factor has to be included when choosing the gas ratio. The electron ratio is linked to the molecule ratio through the formula

$$\frac{n_{e,He}}{n_{e,N}} = \frac{M_{He}}{5M_{N_2}} \tag{4.10}$$

where $M$ stands for the number of respective molecules in the mix. Conveniently, the factor of two in atom number per nitrogen molecule cancels with the factor of two in electron number per helium atom in equation 4.10. For the experiment, three gas bottles were bought with different ratios of helium to nitrogen molecules. Table 4.1 shows how these ratios correspond to atom and electron numbers assuming 5 electrons are ionised from each nitrogen atom.

### 4.1.6 Gas cell design

Two different gas cells were designed for the experiment. Gas cell 1 (GC1) was 3D printed and had a (inner) length of 10 mm, width of 10 mm, height of 5 mm and entrance and exit pinholes of $\sim 200\,\mu$m diameter. The second gas cell (GC2) had equal width and height but its length was a function of height due to an inclined back wall with a maximum length of 5 mm and a minimum length of 2 mm. Therefore, instead of a pinhole, a slit was used. The slit had a width of $\sim 0.5$ mm.

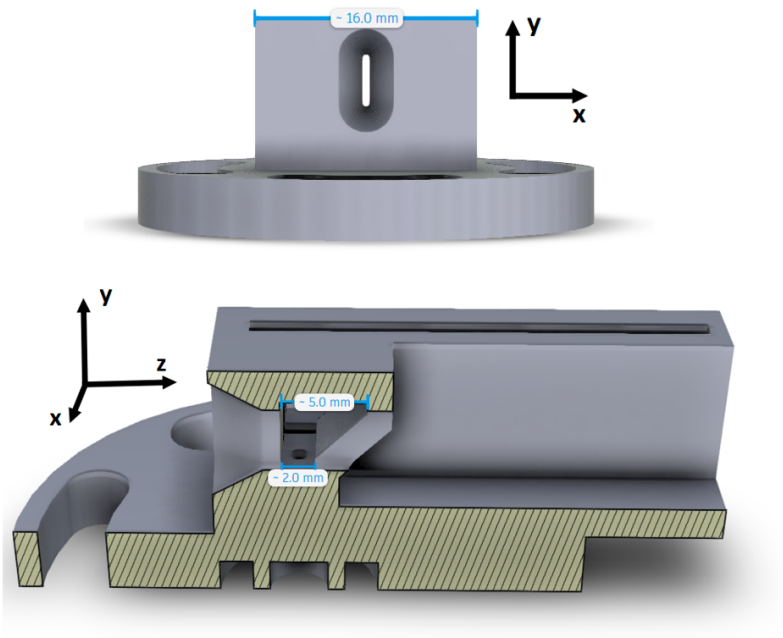



Figure 4.3: This figure shows two perspectives of the CAD drawings for gas cell 2. The front view shows the slit through which the laser pulses enter. The side view presents a cross-section in which the inside of the chamber can be seen. The long slit on top of the gas cell is there for the insertion of a glass window for probing purposes. The laser propagation direction is towards the right (increasing $z$ values).

The design of the inclined back wall of GC2 can be seen from the CAD drawings which are presented in Fig. 4.3. The gas streamed into the cell through two holes located at the bottom of the cell.

### 4.1.7 Diagnostics

This section will present the relevant diagnostics which were used to obtain the data of this experiment as presented in Section 4.1.8.

#### 4.1.7.1 Measuring electron density

The electron density in the plasma was probed using an interferometry diagnostic. The pink beam in Fig. 4.2 which was split from the green drive pulse using a pellicle of 4% reflectivity was used as probe pulse. The delay stage in the probe beam path was used to adjust the timing such that the probe pulse arrived at the gas cell at the same time as the drive and injector pulses. The probe pulse passes through two windows on either side of the gas cell and exits the target chamber to be measured

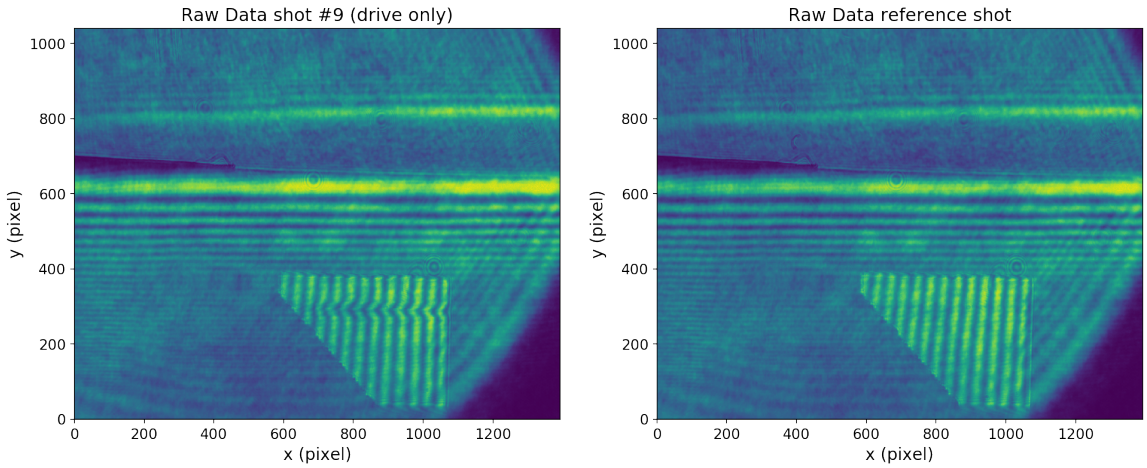



Figure 4.4: Raw intensity data as measured by the interferometer CCD for a shot with drive pulse only (left-hand side) and a reference shot (right-hand side). The gas cell (GC2) is seen at the bottom of the images. The laser pulse enters the gas cell from the right edge. Horizontal fringes are due to the clipping of the beam at the gas cell.

using an interferometer. In this experiment, a shearing interferometer was used in which the part of the probe beam which passes through the gas cell windows interferes with the part of the probe beam which passes above the gas cell without picking up a phase shift. This is done by using a prism to spatially invert the pulse on one arm while keeping the pulse unchanged on the other arm. A slight misalignment of the pointing angle of one of the beams causes a fringe pattern through the interference of the wavefronts on the CCD.

When plasma is created in the gas cell, a phase shift is imprinted on the probe which will result in a local change in fringe curvature. Figure 4.4 shows the signal measured on the interferometer CCD with and without plasma. For density analysis, the region of the plasma column is isolated (same for respective pixels in the reference data).

The density reconstruction using the Abel inversion (see Section 3.1.1) is very sensitive to noise. For example, the location of the symmetry axis used in the algorithm or the data quality (background noise, resolution issues, *et cetera*) impacts the density values obtained from the analysis. Given these sources of error, the generalised Abel inversion [222] is a superior method over the standard Abel inversion in which symmetric and asymmetric parts of the phase shift data are separately reconstructed and then recombined. The generalised Abel transform was used to compute the density value from the cropped phase image where either half (split along the plasma

| | OAP | MO | lens |
|---|---|---|---|
| o (mm) | 2980 | -57.8 | 723.23 |
| f (mm) | 387.7 | 4.03 | 490 |
| i (mm) | -445.5 | -3.77 | -1519.5 |
| M | -0.153 | 0.065 | -2.101 |

Table 4.2: Distances of object and image from focusing optic, focal length and magnification for all three components used in the imaging line. The measurement precision is limited to full millimetres. Decimal points arise from subtraction of exact focal lengths or calculated image distances.

"channel" centre) of the phase map was taken. An error estimate of this routine will be given in Section 4.1.8.1.

The density values for shots with and without injector pulse are shown in Fig. 4.5. The effect of the annular injector beam (short Rayleigh length) creating a conical plasma is seen while the drive beam (long Rayleigh length) creates a plasma column on-axis.

#### 4.1.7.2 Measuring wavefront for adaptive optics optimisation

The injector pulse's focal spot and its wavefront were optimised using an ILAO Star 200 B100 deformable mirror. For this purpose, another imaging system had to be built. This array of mirrors, lenses, and a microscope objective imaged the injector pulse onto a HASO4 wavefront sensor.

The lens equation

$$\frac{1}{o} + \frac{1}{i} = \frac{1}{f} \tag{4.11}$$

relates the distance $o$ between the object and the focusing optic, the distance $i$ between focusing optic and image, and the focal length $f$ of the focusing optic. The associated magnification is $M = -i/o$. This magnification should result in an image size on the HASO which fills the maximum CCD area (to get a high resolution) while leaving enough room for detecting distortions caused by moving a motor in the DM. The CCD area was $4.56\,\mathrm{mm} \times 3.64\,\mathrm{mm}$. In order to get an appropriately sized image while being restrained by the target chamber layout, the following three focusing optics were used: the injector OAP, a microscope objective and a lens. The resulting magnification was obtained by multiplying the magnification factor of each component.

Table 4.2 presents the relevant distances and focal lengths. The object being imaged was the beam (shape) at the DM's surface. After being focused by the OAP down-stream, the injector rays were reflected using a mirror which was mounted on

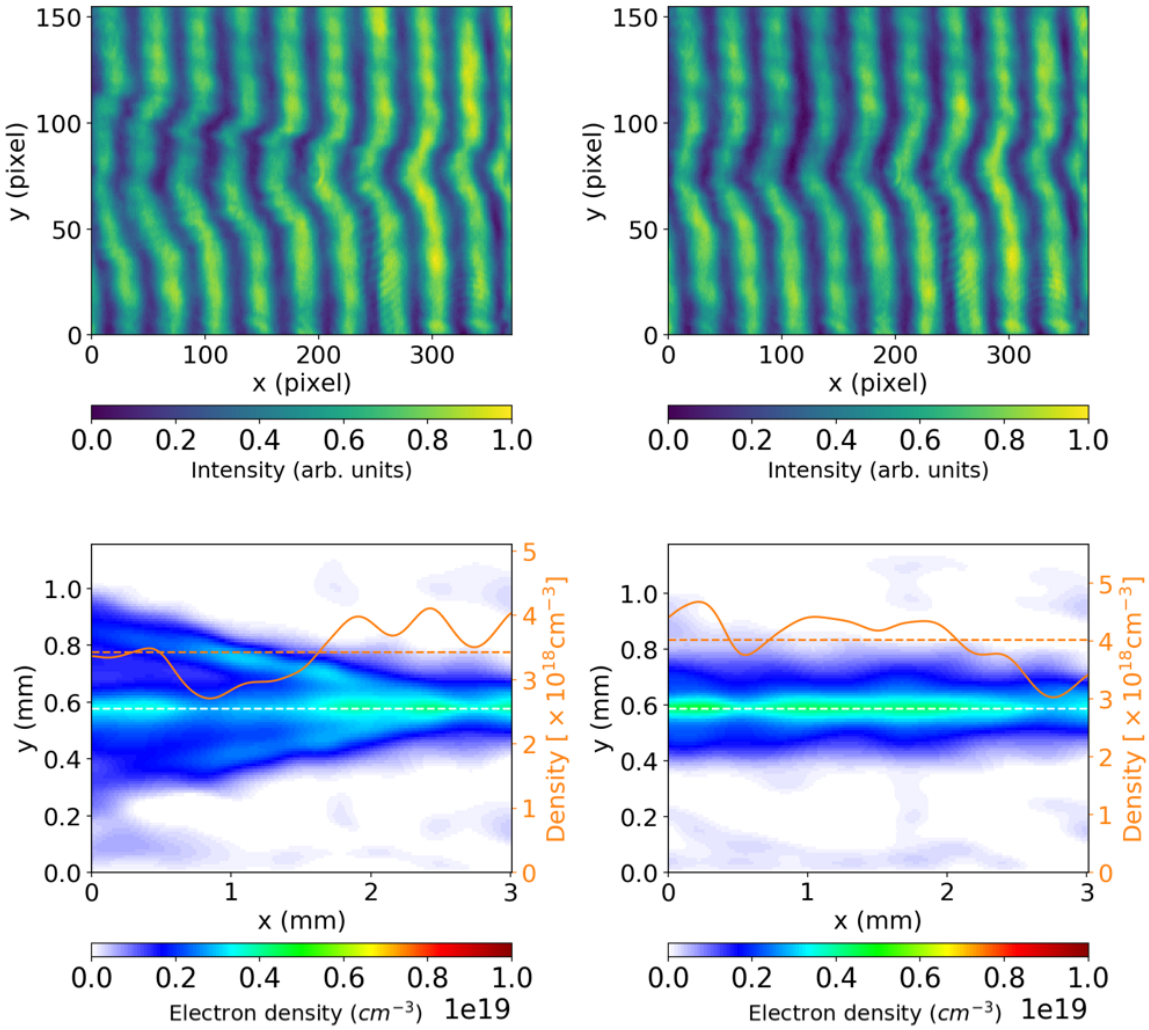



Figure 4.5: Cropped intensity plot from interferometer CCD (top panels) for a shot with (left panels) and without (right panels) injector pulse. The electron density is plotted (bottom panels) as obtained from the numerical Abel transform method, where the white dashed line shows the symmetry axis, the orange line shows the electron density value at the symmetry axis and the orange dashed line shows the average electron density along the symmetry axis. The laser pulses are propagating from right to left. The bottom left electron density profile is obtained from analysing the top left interferometry image through a phase shift analysis and subsequent Abel transform. The same holds for the right-hand side panels.

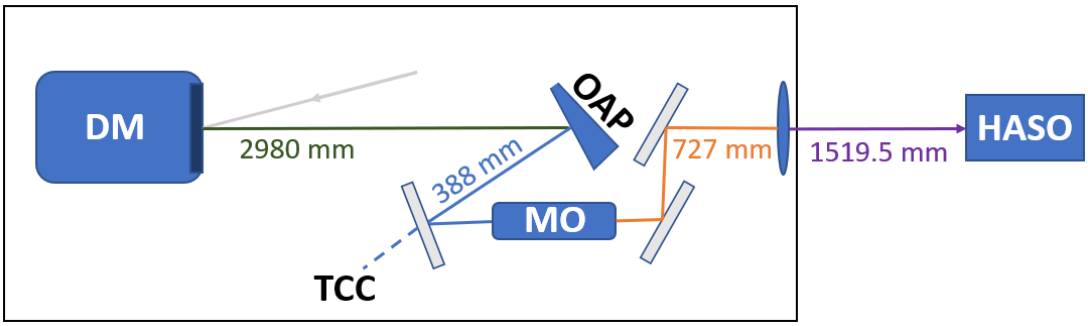



Figure 4.6: Schematic of the imaging system for the injector wavefront optimisation. The black border encloses parts which are inside of the vacuum chamber.

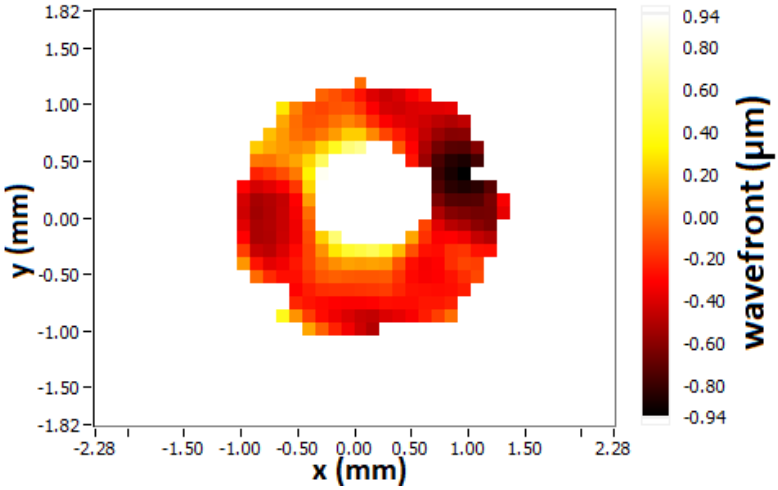



Figure 4.7: This figure shows the wavefront values on the CCD after being corrected for refractive errors by the *Wavetune* software.

a motorised vertical translation stage (so that it could be moved into the beamline under vacuum) 5.02 cm before the TCC onto a microscope objective (MO) placed at the same distance. The beam then propagated through the chamber via a mirror system and was focused outside of the chamber using a lens. The arrangement and measured distances between optics are schematised in Fig. 4.6.

Going through this system the wavefront of the image was then measured using the wavefront sensor. A wavefront measurement of the annulus beam imaged from the DM surface is shown in Fig. 4.7.

The size of the image on the wavefront sensor roughly matches the calculated image size of $101.6\,\text{mm} \times \text{M} = 101.6\,\text{mm} \times (-0.153) \times (0.065) \times (-2.101) = 2.1\,\text{mm}$ which is a value that is handled well by the optimisation algorithm.

*Wavetune* software controlling the deformable mirror's actuators was used in com-

bination with the PHARAO focal spot optimisation package to optimise the focal spot.

#### 4.1.7.3 Measuring focal spot properties

To measure the focal spot properties, another imaging system was built. It used a lens to collimate the expanding pulse after it had passed through the target chamber centre. The focal spot shapes were measured using a CCD during low power operation of the HERCULES laser at 10 Hz to avoid damaging any parts of the camera. In this low power mode, the beam still propagates through the laser amplifiers but they are not pumped thus not amplifying the low power pulse. Although this method preserves the pulse profile to a greater extent compared to not sending it through the amplifiers, it has to be said that the intensity distribution can not be assumed to stay identical when operated at maximum power. Therefore, the analysis below can only give an estimate of the peak intensities reached by either pulse at focus. The lens was on a motorized translation stage which was moved out of the beamline before high-power operation of the laser.

A calibration was performed to find the magnification of the focal spot using a high-resolution *USAF 1951* target and a laser alignment diode. The first method used the printed calibration lines on the *USAF 1951* target whose separation was measured on the CCD. Comparing the measurement of pixels between horizontal lines on the CCD to the resolution values given with the target in µm between lines a conversion factor of 0.61 to 0.64 pixels/µm was found (the uncertainty stems from the imperfect step between black and white on the image). The real size of each pixel of the CCD is 16.8 µm horizontally and 19.6 µm vertically. Multiplication gives a magnification of 10.25 to 10.75.

A second calibration method used the focal spot of the laser pulse seen on the CCD. The motorized stage was used to move the beam across the screen and the encoded motor values were compared to the observed shift. This method gave a magnification of 10.23. Going forward a mean magnification of $m = 10.41 \pm 0.29$ was used.

The image of both laser pulses captured by the CCD is shown in Fig. 4.8. To get to an estimate for the normalised laser amplitude, I numerically integrated the intensity values of each row (column) to give a vertical (horizontal) pulse profile. Then, I fitted a Gaussian function to the integrated data. The $w_0$-width values obtained using this method and the resulting intensity calculations can only be used as a rough estimate for the following reasons:

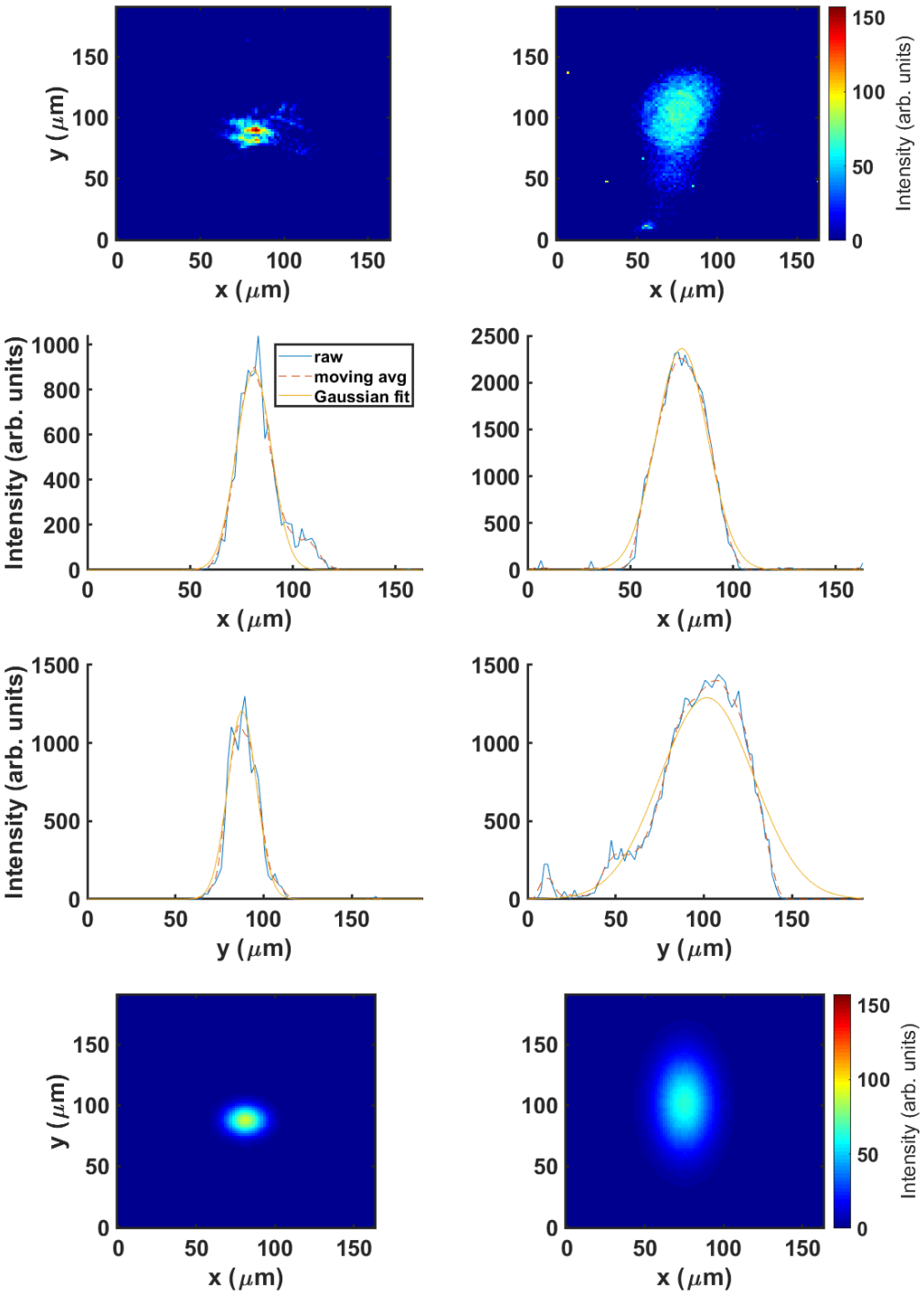



Figure 4.8: This figure shows the focal spots under vacuum (top row) of the injector (left panel) and drive (right panel) beam on a CCD as measured by the imaging system during low power operation (amplifiers not pumped). The left panel was obtained with additional filters inserted into the beamline before the compressor to prevent saturation of the CCD. The middle rows show the integrated intensity for either beam in $x$ and $y$-directions. The bottom row shows the reconstructed focal images.

For the injector, the peak intensity value is larger compared to the peak of a focal spot reconstructed by multiplying the orthogonal fitted Gaussian functions (see bottom left panel in Fig. 4.8). The issue here is that the absolute intensity is computed from the $w_0$ values of the Gaussian function which are 16.29 µm (horizontal) and 17.03 µm (vertical). Using these values a normalised amplitude for the beam is found using the total beam energy (calculated from the transport efficiency $\epsilon_t$ and the split ratio), the pulse length, the focal spot area, and a rearranged version of equation 4.8. Following the formulae for the instantaneous peak power

$$P_0 = E\frac{2\sqrt{\ln 2}}{\sqrt{\pi}\tau_{\mathrm{FWHM}}} \tag{4.12}$$

and the intensity

$$I_0 = \frac{P_0}{\sqrt{2\pi}\sigma_x\sqrt{2\pi}\sigma_y} \ , \tag{4.13}$$

where $\sigma$ is the beam profile's standard deviation and given a total laser energy of 9 J the normalised laser amplitude is found to be $a_0 = 1.88$. However, to get the hot spot amplitude, I normalised the synthetic focal spot to contain the same energy as the experimental image. Comparing the maximum intensity values of those two focal spot images gives an experimental peak value which for the injector is 1.76 times higher than the reconstructed peak value which was used to compute $a_0$. Therefore, the peak of the injector's hot spots can be estimated to be at $a_0 = 1.88 \times \sqrt{1.76} = 2.49$. Both values, 1.88 and 2.49, are high enough to ionise the sixth and seventh electrons of the nitrogen atom. At this point, it should be made clear that in the 2PII method [57] the injector pulse not only locally ionises those electrons, it also temporarily increases the wakefield's amplitude allowing the ionised electrons to be trapped. As shown in the cited article, the optimal delay between the two pulses for this constructive wakefield amplification to occur is one plasma wavelength.

For the driver, it was observed that the brightness level on the CCD (in 10 Hz low power mode) was reduced after the chamber was pumped to vacuum. At the same time, an astigmatism was introduced (as seen in the focal spot image) causing an elliptical beam shape. While the horizontal spot size remained fairly constant at $w_0 = 25.1$ µm, the vertical spot size fluctuated due to the jitter from measurement to measurement (which were performed at 10 Hz). In the most extreme case it was $w_0 = 53.3$ µm. This gives an $a_0$ value of 0.71 using the energy from the calibration conducted in air.

The pulse profiles deviate from perfect Gaussian distributions as seen in Fig. 4.8 which means that the peak intensity values calculated from the fits are only an approximation. An alternative and more direct method to obtain the peak intensity values was also tested. In the area where the CCD pixels were strongest illuminated, the raw pixel intensity values were measured and divided by the total (summed) pixel intensity on the screen

$$\iota = \frac{\max\left(I_{i,j}\right)}{\sum_{i,j} I_{i,j}} \ , \tag{4.14}$$

where $i$ and $j$ are pixel indices. The background pixel intensity was $I_{\mathrm{bg}} = 0$. This ratio $\iota$ was then divided by the area of one pixel $A_{\mathrm{pix}}$ and multiplied by the power of the respective pulse $P$ (at full power operation). The intensity of the peak is, therefore, given by

$$I_{\mathrm{peak}} = \frac{\iota P}{A_{\mathrm{pix}}} \ . \tag{4.15}$$

Using this method, the injector pulse had a peak intensity corresponding to $a_0 = 2.46$ and the drive pulse had a peak intensity corresponding to $a_0 = 0.75$. The peak values obtained using this method differ by up to 6% from the previous method.

The theoretically predicted Airy disk [223] FWHM spot size for a focused top-hat beam profile can be found (see Appendix A.10) to be $w_{0,i} = 3.1\,\mu\mathrm{m}$ for the injector (which is much smaller than the observed value) and $w_{0,d} = 32.9\,\mu\mathrm{m}$ for the driver.

In order to visualise the origin of the injector's poor beam quality (high $M^2$ value[5]), the impact of different beam shapes and noise profiles on measured focal spots were analysed using a symplectic[6] envelope model [224]. This model uses the fact that the paraxial Helmholtz equation with Hermite-Gaussian solutions can be reduced to the same form as the time-dependent Schrödinger equation for a quantum harmonic oscillator (with Hermite functions being eigenstates). Therefore, the solution of the time evolution of a wave function can be related to the time evolution of transverse modes of the electric field. Analytical and numerical methods to obtain the intensity profile of a focusing beam at any given point in propagation direction using this approach are discussed in Reference [225].

Fig. 4.9 shows the focusing of:

[5]The $M^2$ value describes the deviation of a laser beam profile from the behaviour of an optimal Gaussian beam.

[6]A set of symplectic equations has a Hamiltonian structure.

- a Gaussian beam

$$\propto \exp\left\{-\frac{\sqrt{x^2+y^2}}{2\sigma^2}\right\}, \tag{4.16}$$

- a circular top-hat beam

$$\propto \Theta(R-\sqrt{x^2+y^2}) \tag{4.17}$$

with $\Theta$ being the Heaviside function ($\Theta(x \geq 0) = 1$ and $\Theta(x < 0) = 0$) and $R$ being the outer radius of the top-hat,

- a circular top-hat annular beam

$$\propto \Theta(R-\sqrt{x^2+y^2}) - \Theta(r-\sqrt{x^2+y^2}) \tag{4.18}$$

with $r$ being the inner radius of the cut-out,

- a circular top-hat annular beam with sinusoidal oscillations (to emulate the impact of the DM motors)

$$\propto \exp\left\{-\left(\sqrt{x^2+y^2}-R\right)^2/\sigma^2\right\}\cos\left\{4\arctan\left(\frac{y}{x}\right)\right\}^2, \tag{4.19}$$

where $\sigma$ is related to the width of the ring,

- as well as the previous two beam shapes with noise patterns of type

$$\propto A \times \exp\{i\left(\mathcal{GF}_3\left(\mathcal{R}[0,1]\times a\right)\right)\}, \tag{4.20}$$

where $A$ is one of the amplitude functions used above, $\mathcal{GF}_3$ denotes a Gaussian filter over $3\times3$ pixels, $\mathcal{R}$ is a matrix of random numbers between 0 and 1 of the size of the image and $a$ is a quantity determining the amplitude of the noise.

It can be seen that the occurrence of oscillation patterns and noise in the phase structure of the beam results in energy being lost from the focal spot into the surrounding area.

The injector pulse's beam divergence[7] can be measured by looking at the change in radius of the annular beam along the beam propagation ($z$-) axis. Fig. 4.10 shows one of the injector images taken at a specific distance away from the focus. Here, the annular structure and the impact of the motors of the DM can be seen. To calculate

[7]To be precise, the term beam divergence is mostly used in the literature to describe the angle of the spot size evolution of a Gaussian pulse rather than the evolution of the location of the maximum intensity of an annular beam but for the purposes of this chapter, I will adapt the definition.

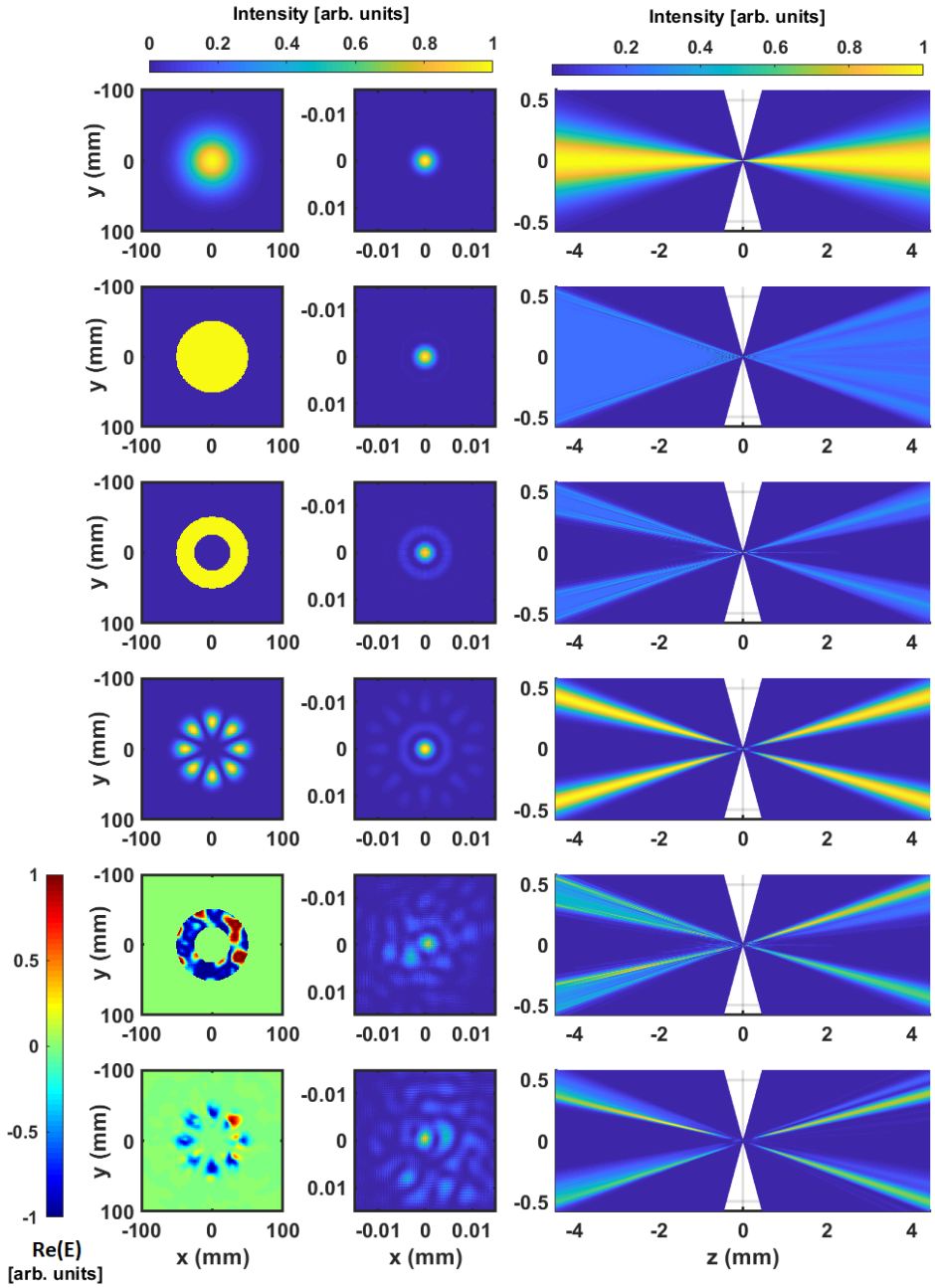



Figure 4.9: Beam intensity of collimated pulse before being focused (left panels), intensity of beam at best focus (middle panels), and side view of beam intensity evolution going through the focus (right panels). The two panels on the bottom left of the figure show the real part of the electric field (showing the fluctuations due to noise) and have, therefore a different colour axis. The lack of data in the central part of the right-hand side panels is due to the auto-rescaling mechanism of the algorithm to keep important features resolved at all times.

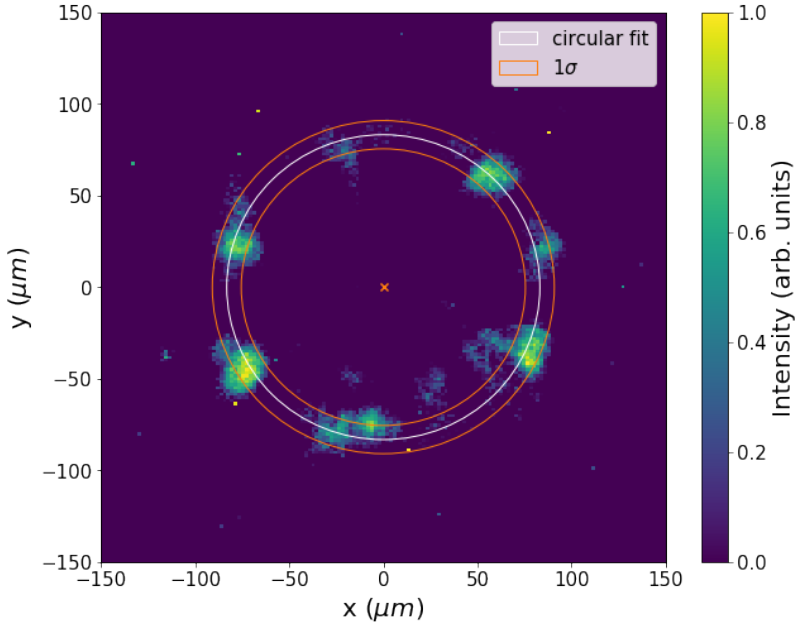



Figure 4.10: Intensity distribution of injector beam measured by focal spot camera at 1.6(±0.05) mm from focus. The centre of a fitted circle (white line) is shown as orange 'x'. The width of the fitted Gaussian at the same radius is shown as orange line.

the beam divergence, the data was fitted using a least squares method at four different $z$-positions separated by 200 µm each. At all of these locations a ring structure was clearly visible (closer to the focus the annular structure could not easily be identified by the model). The function used for fitting the data was

$$f(I_0, x_0, y_0, R, r) = I_0 \exp\left\{ -\frac{\left(\sqrt{(x-x_0)^2 + (y-y_0)^2} - R\right)^2}{2\sigma^2} \right\}, \tag{4.21}$$

where the centre position of the circle is $(x_0, y_0)$, the radius is $R$, and the standard deviation of the Gaussian is $\sigma$ (which is not to be confused with the uncertainty of the fit itself).

Details of the fitting procedure can be found in Appendix A.9. Next, the obtained values of the radius $R$ were fitted using a linear model to get the divergence of the beam. The results of both fits are shown in Fig. 4.11.

The linear fit function is $f(z) = 0.054z - 3.32$ with an RMSE[8] of 0.16 µm (calculated from the residuals of the four data points). The beam divergence half-angle of the maximum intensity of the annular beam is $\theta \simeq \arctan(0.054) = 3.09°$. This

[8]The root-mean-square error measures the difference between observed and fitted values.

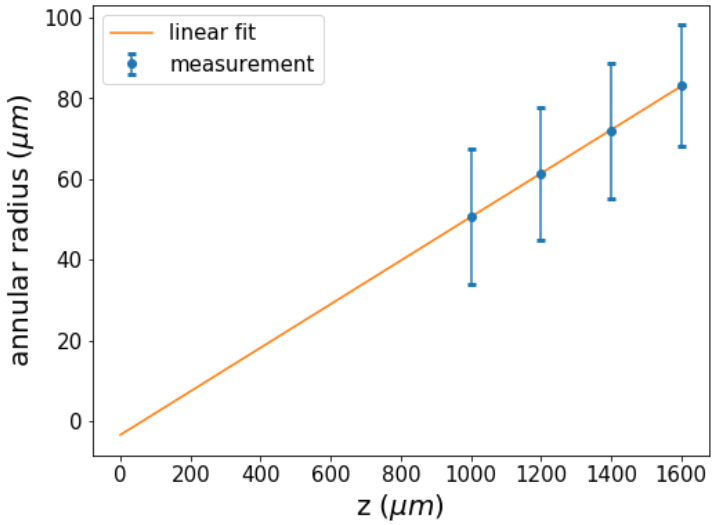



Figure 4.11: This figure shows the relationship between measurements of the radius of the annular beam obtained from a circular fit (see Fig. 4.10) and the distance from focus along the beam propagation axis $z$. The error bars originate from the intensity oscillations along the beam circumference. The $z$-axis zero value position has an uncertainty of 100 µm (which is the interval at which focal spot measurements were taken around the focal spot). A least squares linear fit is plotted in orange.

measurement can be compared to a geometric analysis. Taking the arctangent of the ratio between the position of the beam on the final focusing optic $r$ and its focal length $f$, it can be seen that the half-angle $\theta = \arctan(r/f)$ at which the intensity peak can be found (far away from focus) is predicted to be at $\theta \geq 3.74°$ (inner boundary of annular beam at $r = 2.54\,\text{cm}$). Using the measured divergence angle of 3.09°, the spot size of a diffraction-limited (top hat) laser pulse is written in the paraxial approximation as

$$w_0 = \frac{\lambda}{\pi\theta} = 4.7\,\mu\text{m} \tag{4.22}$$

which is larger than the theoretically predicted value of a focused top-hat. Using the divergence value from geometric optics, the expected spot size becomes $\leq 3.9\,\mu\text{m}$. However, it has to be kept in mind that the pulse observed does not have an ideal top-hat shape. Due to the inner part of the beam being removed, the focal spot will further deviate from this theoretical value. A formula for the intensity distribution of an annular beam is given in [226] (see Eq. 16 in the article). However, this theory only holds for Gaussian distributions rather than top-hat beams.

#### 4.1.7.4 Measuring spatial jitter

During alignment, it was seen that the drive pulse pointing was fluctuating much stronger than the injector pulse due to the greater number of optics used and the larger focal length of the focusing optic. Since spatial overlap of the two pulses is important for the 2PII mechanism, it is necessary to have information about this property on every shot. As the imaging system is prone to damage if used during high power operation another imaging system had to be built outside the main beamline from which the pointing properties could be inferred. To this end, I used the light leaking through the second last mirror in the drive beam-line before the parabolic mirror. This light was reflected out of the chamber using a mirror. On the outside of the chamber, a lens was mounted close to the chamber window which focused the light onto the diagnostic table. Then, the focal spot was imaged onto a CCD using another lens.

For calibration purposes, 159 low-power shots were taken and measured on both the focal spot imaging camera in the main beamline as well as the leak-through system. The position at which the (fitted) peak intensity was measured on the camera in the leak-through path was then plotted against the pre-calibrated detection values (given as deviation angle) on the focal spot imaging camera (see Fig. 4.12). A linear fit of these data points was used to create a map which allowed to get an estimate of the spatial drive beam jitter from the leak-through measurement. The linear fits are $\alpha = f(x) = 8.01 - 0.17x$ and $\beta = g(y) = -32.31 + 0.28y$, where $\alpha$ and $\beta$ are measured in µrad and $x$ and $y$ are measured in pixel. The corresponding RMSEs calculated from the residuals (difference of measurement $\alpha$ (or $\beta$) and fit $f$ (or $g$) at any given position on camera 2) are 2.28µrad (or 2.20µrad). This method allows to infer the deviation angle of the drive beam at the focal spot from a position measurement (measured in pixel and mapped via correlation function) on a camera in the leak-through path during high power operation.

#### 4.1.7.5 Measuring temporal pulse delay

Precise control of the temporal delay between drive pulse and injector pulse is of utmost importance when conducting a 2PII experiment. Therefore, the timing had to be measured whenever a beam was realigned which typically occurred after 25 shots (at a frequency of $< 1/60$ Hz). The first method of measuring the relative timing between the pulses was to observe the position of the ionisation fronts caused by the

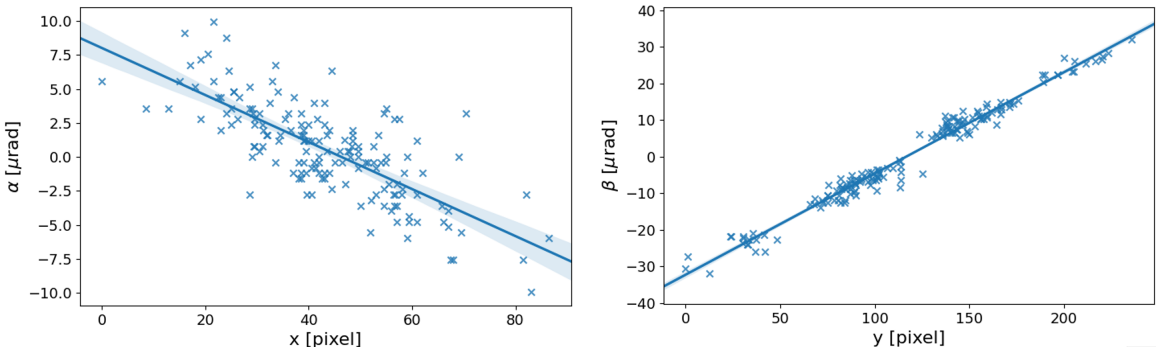



Figure 4.12: Correlation measurements and fits between focal spot imaging camera and leak through camera for the drive pulse position. The left-hand side panel maps the horizontal position of the focal spot as measured on the leak through CCD ($x$) to the horizontal deviation angle of the drive beam focal spot under vacuum at the target chamber centre ($\alpha$). The right-hand side corresponds to the vertical deviation angle $\beta$ and the measured position $y$, respectively. Measurements are plotted using the 'x' marker, the fits are plotted using the dark blue line, and the 95% confidence interval of the fit is plotted using the light blue shaded area. The uncertainty from magnification on the deviation angle axes is 2.8%.

beams in the gas cell[9]. Whenever the probe beam passes the gas cell (perpendicularly) at the same time as the other beams, interferograms or shadowgrams such as those shown in Fig. 4.13 are obtained. If the probe pulse delay (or path length) is increased, the other beams have travelled further in the gas cell when the probe arrives and a longer plasma column can be observed. By blocking either beam, the position of the other beam is obtained and vice versa. Using a delay stage in the drive pulse beamline, the position in the propagation direction of the beams is measured separately. This measurement routine was precise enough to proceed to the next method.

As shown in Fig. 4.14 an interference pattern can be observed on the focal spot image when both pulses are overlapped spatially and temporally. By moving the delay stage in the drive pulse beamline, the overlap in propagation direction could be found to a precision of approximately 10 µm. The minimal step size of the motors used was 1 µm which caused a 2 µm path length difference due to the double-pass nature of the delay stage.

[9]This method is limited in accuracy because of the varying intensity values with changing distance from the focus as well as different intensity values of different pulses. This causes the ionisation front to appear at slightly different positions.

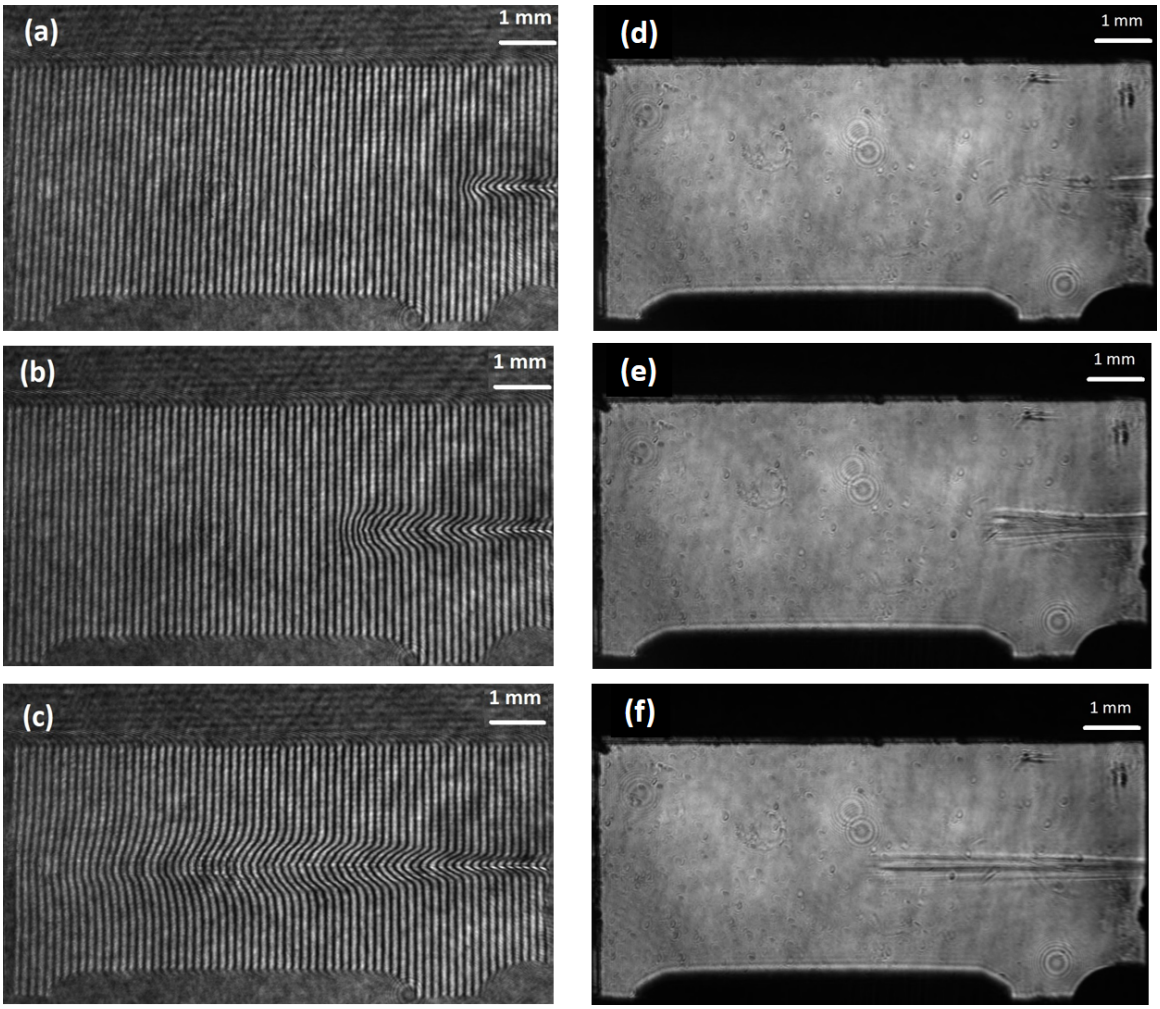



Figure 4.13: Images of the gas cell (GC1) window used for timing where the laser pulse enters from the right-hand side. Panels (a), (b), and (c) show interferograms whereas panels (d), (e), and (f) show shadowgrams of the plasma formed by the drive and/or injector pulses. Shown are six separate shots with varied delay stage motor positions in the probe pulse beamline. The probe delay is increased from the top row to the bottom row. Panels (a) and (f) show the phase shift of the probe pulse due to the plasma caused by the drive pulse (injector blocked), panels (d) and (e) show the same caused by the injector (driver blocked), and panels (b) and (c) show the same caused by driver and injector pulses overlapping spatially and temporally.

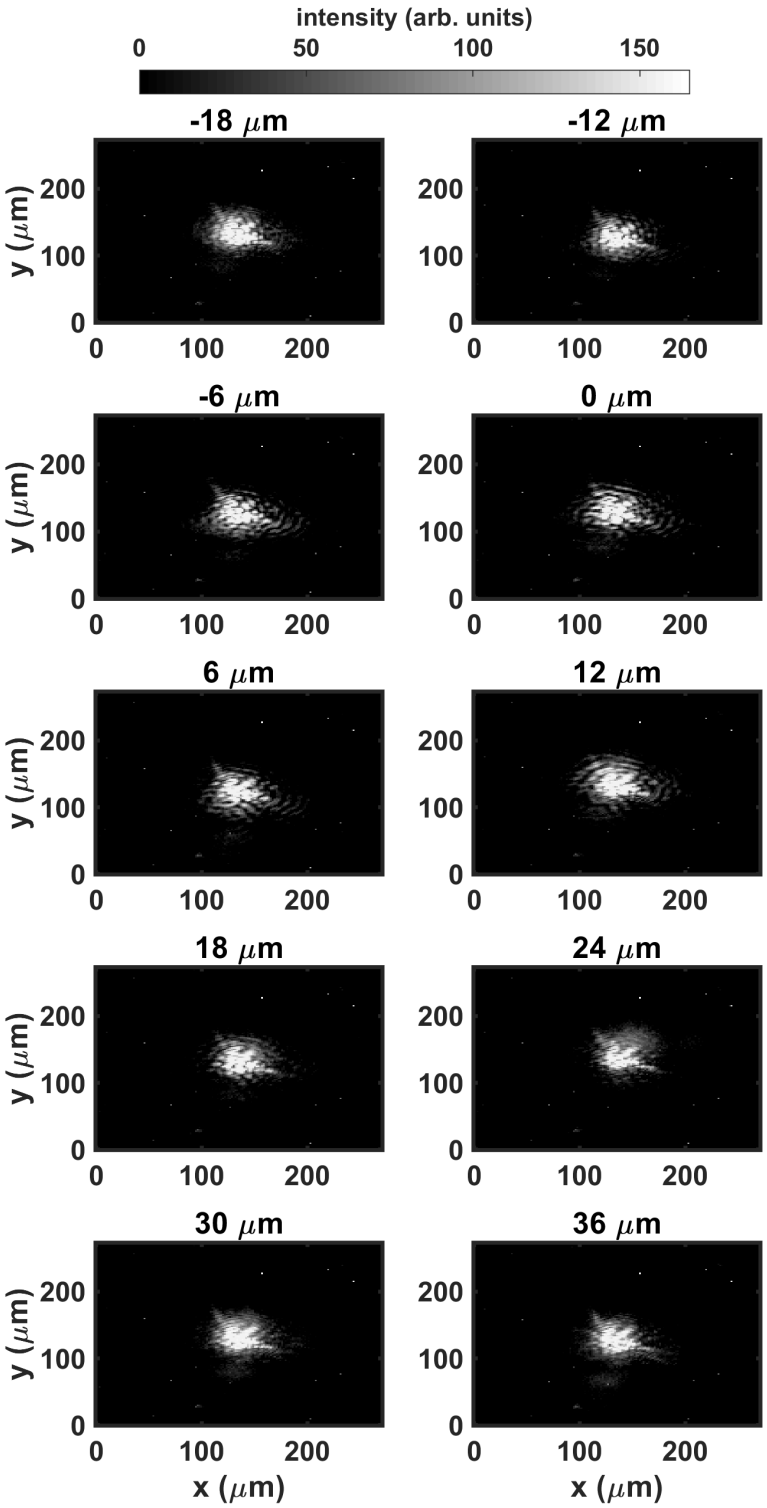



Figure 4.14: This graph shows an image of the focal spots of the injector and drive beams overlapping in the target chamber centre during low power operation. The title of each subplot indicates the path length difference caused by the motion of a motorised delay stage. Fringes caused by the temporal overlap of both beams can be seen to disappear at high values of delay.

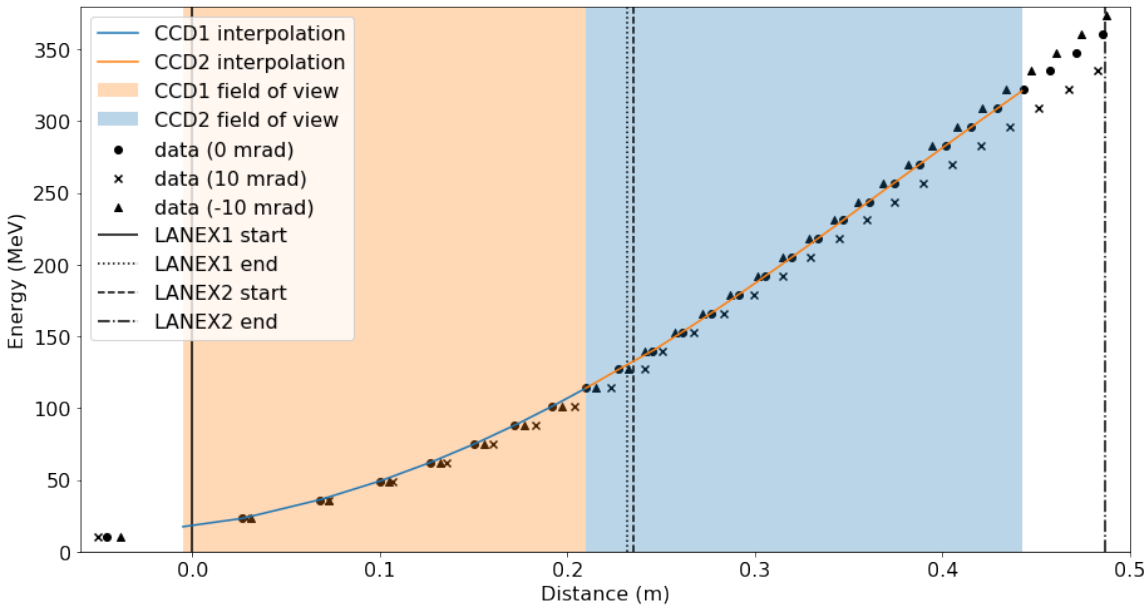



Figure 4.15: Energy calibration curve for electron trajectories. Data points correspond to intersection of trajectories with the Lanex screens for 0 mrad (circle), 10 mrad (cross), and -10 mrad (triangle) horizontal divergence angles.

#### 4.1.7.6 Measuring accelerated electron bunch energy

The energy and charge of accelerated electrons were measured on two scintillating Lanex screens. These screens emit light in proportion to the charge of electrons with which they interacted. The electron beam is deflected passing through a magnet with a central magnetic field of 1.02994 T (manufacturer precision) located behind the gas cell as seen in Fig. 4.2. Two cameras are used to take images of either of the scintillating screens at each shot. The electron trajectory and therefore its intersection point with the screen differs depending on the particle's energy and angle of incidence.

To calibrate the screens, a simulation of the interaction was run which was written by a collaborator at CUOS [227]. A three-dimensional relativistic Boris pusher [228, 229] was used to compute the electron trajectories passing through a magnet including fringe fields outside the magnetic gap of the dipole. The geometry of the experimental set-up was measured and included in the model. Using the data points of the intersection of the electron trajectories with the screens, I created a map from the CCD's pixels (corresponding to a specific Lanex screen position) to electron energy values for given beam divergence angles. Fig. 4.15 shows the non-linear map from distance to energy as seen by both CCDs.

As mentioned above, the divergence angle was also taken into account in the cali-

bration model. Divergence in the horizontal plane causes electrons of the same kinetic energy to appear at different areas on the Lanex screen broadening the observed spectrum. Divergence in the vertical plane can be observed on the Lanex screen but has a negligible impact on the energy calibration.

#### 4.1.7.7 Measuring properties related to electron bunch charge

In addition to the (uncalibrated) charge detection through integrating the brightness over the image of the Lanex screen, two further diagnostics were tested whose measured quantities are related to the magnitude of the accelerated charge. These were

- a B-dot probe measuring electromagnetic pulses (EMP) from the interaction of an electron beam with the chamber wall, and
- two photomultiplier tubes (PMT) measuring X-rays from bremsstrahlung.

The B-dot antenna picks up EMPs which are generated by electrons interacting with the chamber wall and exciting a resonant mode [230]. The magnitude of the EMP signal is proportional to the magnitude of the charge [231]. The probe consists of a wire bent to a loop and is therefore sensitive to any change in magnetic field which is oriented perpendicularly to the plane of the circle. The signal measured is a voltage corresponding to the induced current within the loop.

The PMTs measure weak (low intensity) photon signals through photon conversion using a scintillator and electron generation using a photocathode. They then amplify the signal through an array of dynodes and anodes through secondary electron emission. The radiation picked up by the PMTs originates from electrons interacting with the chamber wall and lead shielding via the bremsstrahlung effect where charged particles are deflected in atomic potentials of the target material. A larger particle number interacting with the material leads to a higher flux (given a specific electron energy). The PMTs are located behind the chamber wall.

### 4.1.8 Results

After the set-up was finished, high-power shots were taken using all laser amplifiers to reach the full $\sim 9\,\mathrm{J}$. The experimental parameters of the runs presented in this chapter are listed in Table 4.3. All runs used gas cell GC2 as the injector pulse blew a hole of 4 mm in diameter in the back wall of GC1 after a small number of shots in preliminary test runs. The acceleration length using GC2 was $\sim 4\,\mathrm{mm}$ as the laser

| Run | Gas | Average Electron Density | Polarisation | Gas Cell |
|---|---|---|---|---|
| I | He with 3% $N_2$ | $4.45 \times 10^{18}\,\mathrm{cm}^{-3}$ | circular | GC2 |
| II | He | $4.55 \times 10^{18}\,\mathrm{cm}^{-3}$ | circular | GC2 |
| III | He with 3% $N_2$ | $4.32 \times 10^{18}\,\mathrm{cm}^{-3}$ | linear | GC2 |
| IV | He with 5% $N_2$ | $4.87 \times 10^{18}\,\mathrm{cm}^{-3}$ | linear | GC2 |

Table 4.3: This table presents the parameters for all experimental runs discussed in this chapter.

beams were aligned through the longest part of the gas cell and the injector was focused at $\sim 1\,\mathrm{mm}$ into the gas cell.

One part of showing that electrons indeed originate from the 2PII mechanism rather than just ionisation injection or self-injection is to prove that there are no electrons trapped and accelerated in the wakefield caused by either of the two pulses on their own (while the other pulse is blocked). When single pulse electron injection was attempted at electron densities of $n_e > 1 \times 10^{19}\,\mathrm{cm}^{-3}$, the drive pulse was found to be able to inject electrons on its own. The reason for this is that at higher electron density the pulse is more prone to self-focusing which can increase the intensity to a level at which self-injection can occur. At sufficient electron density, electron injection was found to occur for mixtures of He and $N_2$ as well as for pure He. In contrast, the injector pulse was not able to inject and accelerate electrons (to values above the detection threshold) at any gas pressure[10] which is due to its short focal length and the associated beam breakup which prevents stable pulse propagation over a sufficiently long distance as was shown by Thomas *et al.* [85].

For the 2PII test, a gas pressure was selected at which neither of the pulses separately were able to inject and accelerate electrons. In Run I, 13 reference shots were taken from which

- 5 shots used only the drive pulse and were taken before the start of the delay scan,
- 5 shots used only the drive pulse and were taken after the end of the delay scan,
- 3 shots used only the injector pulse and were taken after the end of the delay scan.

[10]Preliminary runs showed that if the injector was propagating in front of the driver, even electron self-injection of the driver was inhibited.

All of them were taken at a gas backing pressure 0.689 (±0.003) bar, which was left unchanged throughout Run I, and show no detectable electron signal which is confirmed through data collected by PMTs and B-dot probe as will be shown below. The threshold of detectable electron signal is given by an intensity pattern on the Lanex screens which shows a clear distinction between signal and noise. More specifically, after background subtraction, the remaining noise fluctuations were consistently around 100 counts which is why a threshold of 300 was chosen above which a peak was identified as an electron bunch. Figure 4.16 presents the different steps of the data analysis routine. First, the raw data was summed over the divergence angle to give a two-dimensional data set of intensity counts as a function of beam energy. Then, the background was subtracted which was obtained from a shot which did not have an accelerated electron bunch. Various filtering techniques (here, a Gaussian filter of smoothing kernel size $\sigma = 15$ pixels and a moving average (MA) filter with a window size of 54 pixels) were tested which led to similar results. Using this method, electron beam properties such as the FWHM and the peak energy were obtained from all shots.

As a last step, one needs to account for the non-linearity of the energy dispersion and correct the measured intensity levels of the electron spectra. Every pixel on the CCD measures a specific intensity level on the Lanex screens. The intensity scales with the electron charge density interacting with the screen or, in other words, with how many electrons penetrate the screen per unit of distance (or area in two dimensions) rather than per unit of energy. However, as seen in Fig. 4.15, $\Delta E/\Delta x$ which is the electron energy interval covered within each unit of distance (pixel width) is not linear. If the energy interval per pixel increases towards the right-hand side of the Lanex screen, more electrons appear to be present at higher energy values. Therefore, I have computed the change in energy for every pixel from the interpolated energy calibration curve. This value was then used as a divisor for the intensity value observed at every pixel individually. Figure 4.17 shows the difference between the curves obtained before and after the intensity correction procedure for a shot with two peaks (shot 36) to see the impact in different regions.

#### 4.1.8.1 Run I

Figures 4.18 and 4.19 show raw electron spectra of shots of Run I. All shots shown here passed the criterion described above after being post-processed by the same algorithm including reference subtraction and filtering of high-frequency noise. The images in Fig. 4.18 show a single mono-energetic bunch accelerated to $\sim 200$ MeV. A

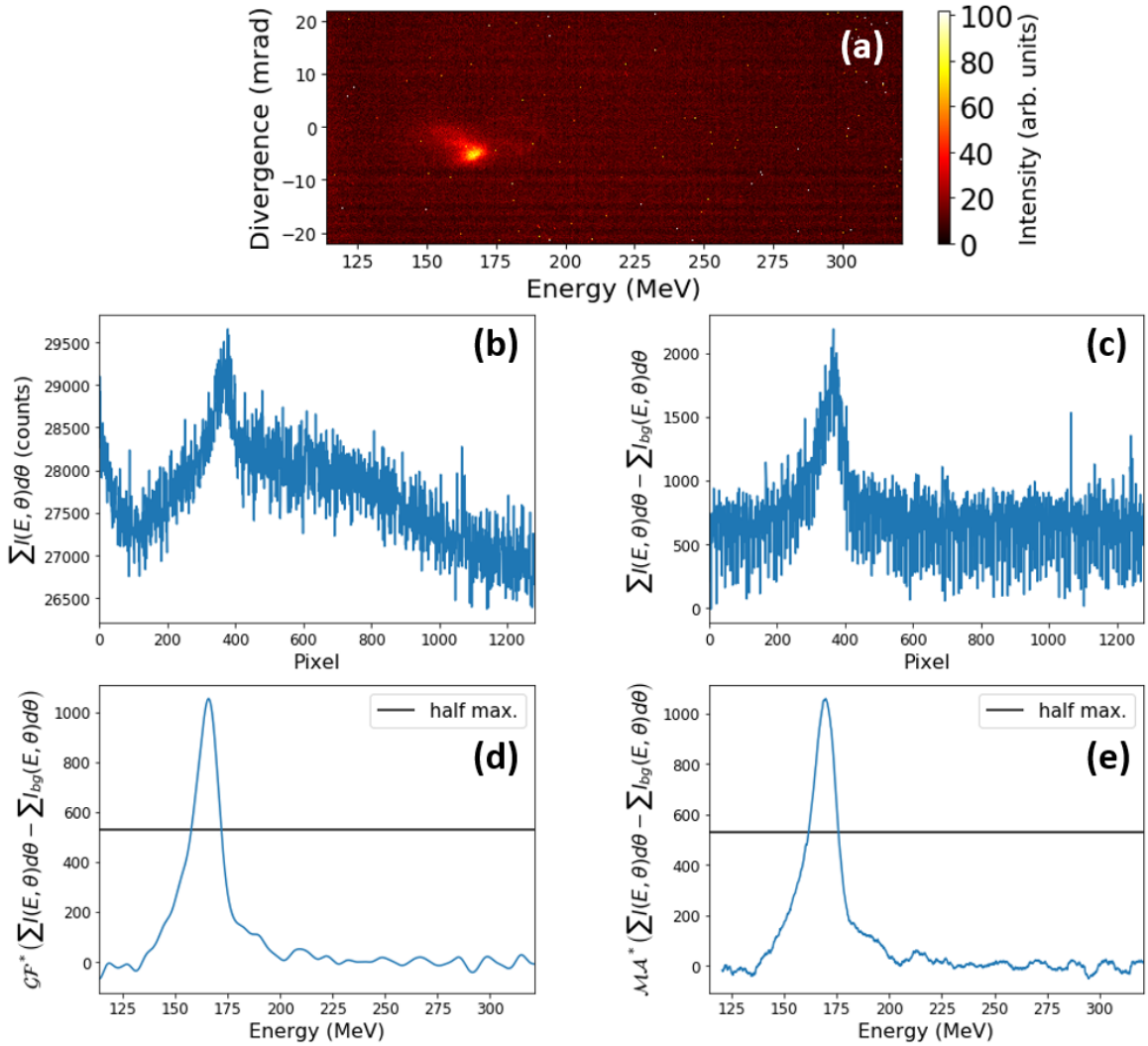



Figure 4.16: This figure shows various steps performed on raw intensity data from the Lanex screens. The raw data from screen 2 of shot 50 is shown in panel (a). Panel (b) shows the data obtained from summing the raw image over the divergence axis. Panel (c) shows the intensity values (all given in units of counts) after a reference image was subtracted. Panel (d) shows the background-subtracted data after applying a Gaussian filter to the data. Panel (e) shows the background-subtracted data after applying a moving average filter to the data with a window size of 54 pixels (no data available for the first 54 pixels). Panels (d) and (e) use the energy axis rather than pixel values. The asterisk indicates that the data was shifted such that the average remaining background value is centred at 0.

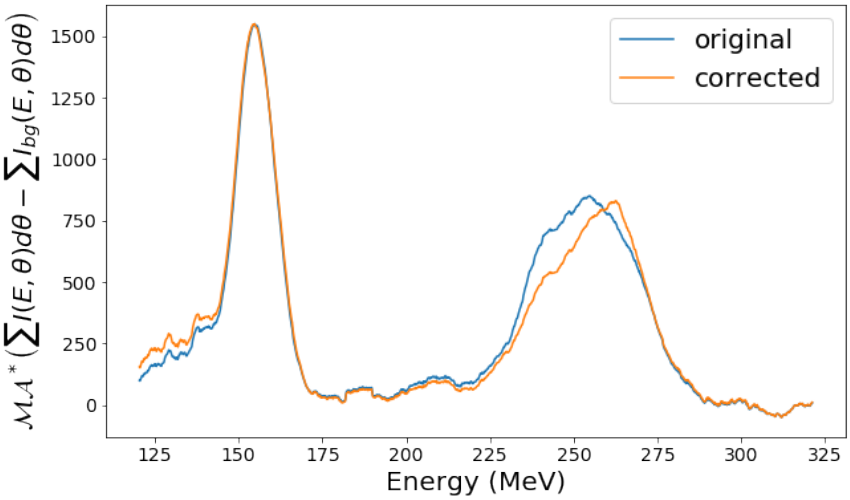



Figure 4.17: Electron energy spectrum from shot 36 before (blue) and after (orange) the intensity has been corrected for nonlinear dispersion.

second type of injection pattern was observed (Fig. 4.19) in which two bunches are accelerated with one beam having slightly higher peak energy (compared to the single bunch injection shots) and the second beam being separated by $\sim$ 100 MeV. The lower-energy beams appear to consist of an annular (and possibly radially oscillating) bunch indicated by branching into two peaks (on the high energy end).

Run I also included one shot (#020) in which the pattern was not well distinguishable and one shot (#056) with a broad energy spectrum.

The CCD-specific pixel to distance conversion value was used (obtained from measurements) in combination with the distance between interaction region (TCC) and position of the Lanex screen to give the divergence angle axis.

In order to study the origin of the observed beam patterns, analysis was performed correlating the electron beam parameters to

- pulse delay,
- laser pointing,
- laser pulse energy,
- and plasma electron density.

The position of the maximum intensity density of the energy spectrum[11] and the

[11]This can also be described as peak energy but to avoid confusion with the cutoff (peak) energy I will continue using the rather verbose but more precise terminology above.

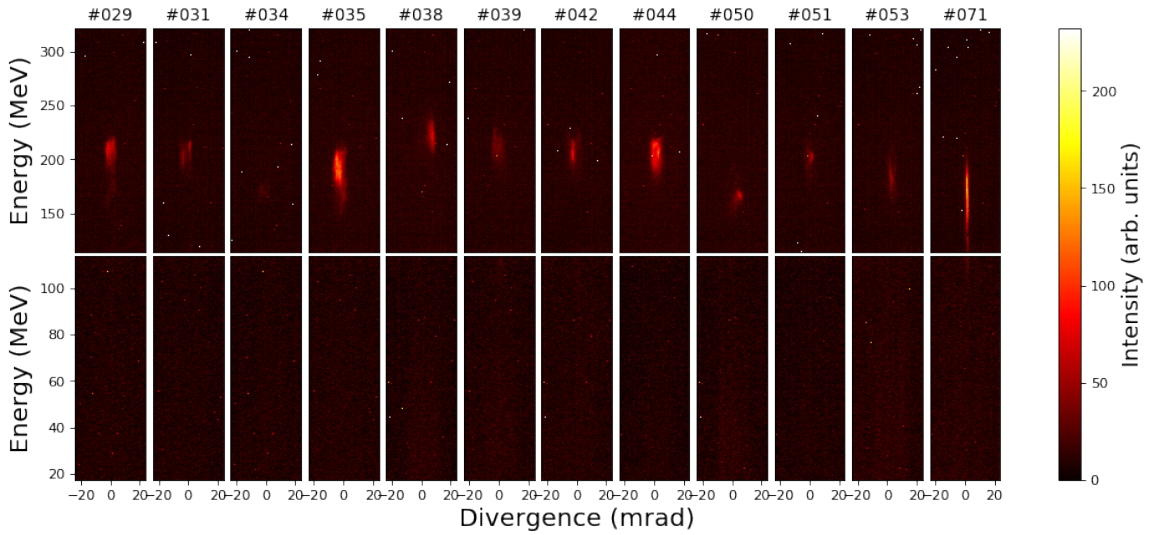



Figure 4.18: Intensity of signal on the Lanex screens captured by a CCD (with axes corresponding to energy against detected divergence) for shots showing one distinct electron bunch. These shots were taken over various pulse delay values (see Fig. 4.20).

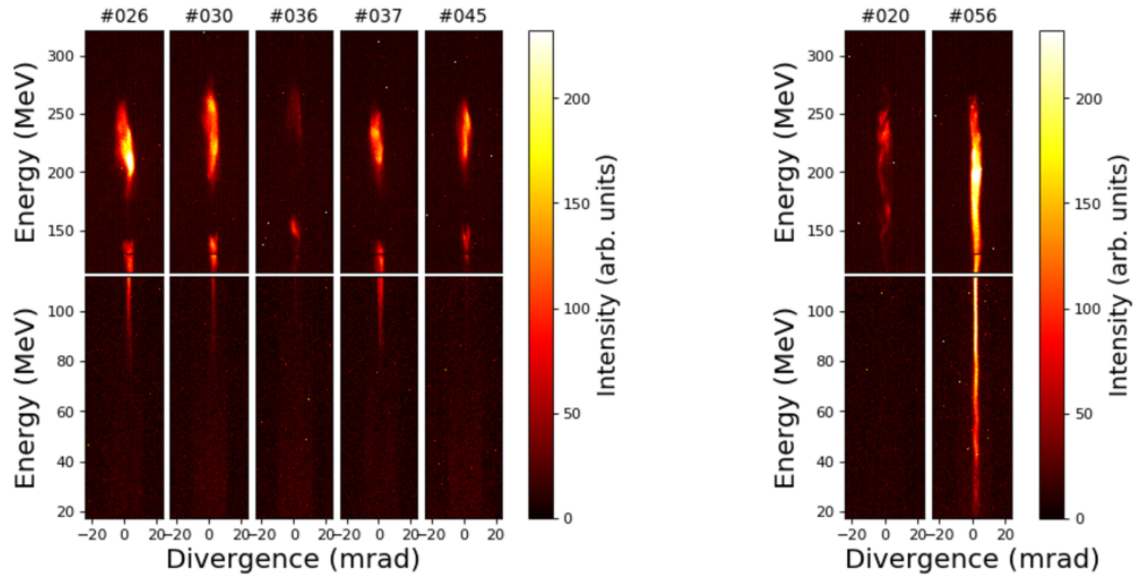



Figure 4.19: Intensity of signal on the Lanex screens captured by a CCD (energy against detected divergence) for shots showing two distinct electron bunches (left hand side) and shots exhibiting no easily distinguishable type (right hand side). These shots were taken over various pulse delay values (see Fig. 4.20).

corresponding FWHM of every spectrum in Run I were measured. Then, the delay between the injector pulse and the drive pulse was plotted against shot number (see Fig. 4.20). This shows how many shots were taken at each delay value. The delay is given by twice the distance of the motor readings of the (double-pass) delay stage. The overlap (null) position was estimated from finding the midpoint between on and offset of beam overlap from the occurrence of fringes on the focal spot camera (see Fig. 4.14). The overlap position was estimated to be correct to $< \pm 10\,\mu\text{m}$ with the error arising from the imprecise threshold for the fringe detection. Positive delay corresponds to the injector pulse trailing the drive pulse.

Figure 4.21 presents the results differently with the energy measurement and the normalised FWHM spread directly plotted against the pulse delay showing that, except for two shots (#20 & #71), the occurrence of electrons is limited to a region between a pulse delay of 13 µm and 25 µm. From these plots, it can be seen that electron injection and acceleration is more prevalent when the injector is trailing the drive pulse at a specific distance centred around a mean (influenced by the number of shots taken at each position and excluding shot #71[12]) of 17.2 µm. For values much larger or much lower than this distance electron injection is inhibited (in the tested range) indicating that 2PII was the causing mechanism. As a note, the plasma wavelength for the average peak density in this run $\bar{n}_{e,\text{peak}} = 4.45 \times 10^{18}\,\text{cm}^{-3}$ (results of density measurements will follow shortly) is $\lambda_p = 15.8\,\mu\text{m}$ which, according to the theory published in the 2PII article by Bourgeois *et al.* [57], is equal to the optimal pulse delay to observe the injection mechanism.

The divergence of the electron beam was obtained in a similar manner from the Lanex screen observation data as the energy values. The difference was that the sum was taken over the other dimension resulting in the intensity as a function of vertical position from which the divergence angle can be calculated after calibration. In addition, a comparison was made to taking a line-out along the energy value at maximum intensity. The results of these methods are shown in Fig. 4.22 for shot 26 which has a particularly large divergence. The FWHM was 5.6 mrad for the sum approach (panel b), 6.4 mrad using a Gaussian filter on the data to reduce noise (panel c), and 4.3 mrad when using a line-out at the energy of 209 MeV (panel d).

[12]Shot 71 can be explained through injection where the injector pulse is injecting into the next bucket which is a plasma wavelength behind (it will be shown that the laser energy and electron density were not significantly above average to be able to cause self-injection of the drive pulse).

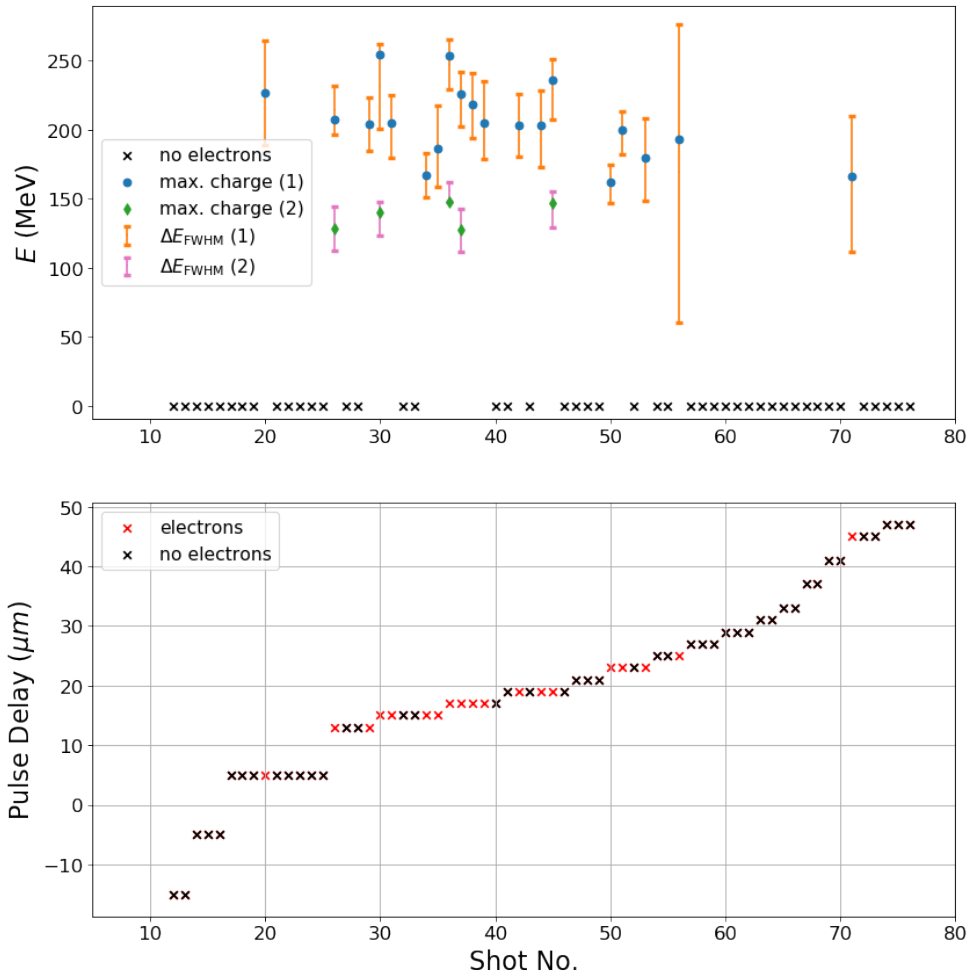



Figure 4.20: This figure shows energy values obtained from data analysis of Run I (top panel). The energy of the highest integrated charge density and the corresponding FWHM (whose limits do not necessarily have to be equally distanced from the peak) are plotted against shot number for the first and (if available) second bunches. The bottom panel shows the delay (spatial distance) between drive pulse and injector pulse for each shot of Run I.

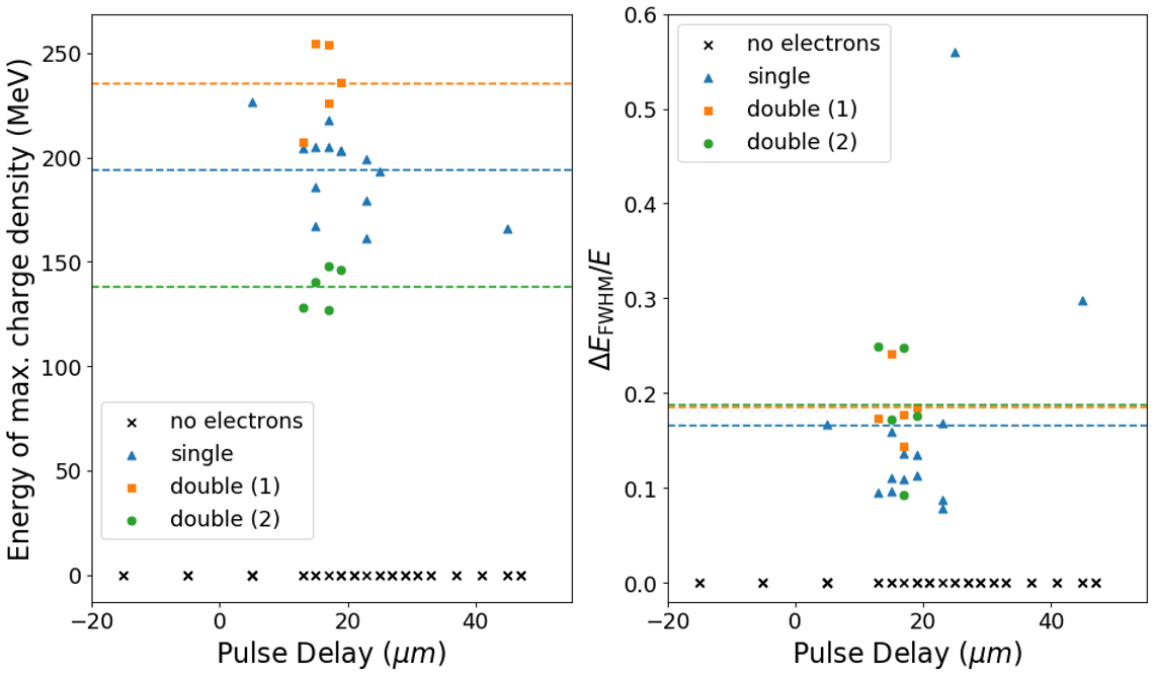



Figure 4.21: This figure shows the energy values of the highest integrated charge density for each shot plotted against pulse delay (left panel) and the corresponding FWHM energy spread normalised to the peak energy also plotted against pulse delay (right panel). The dashed lines correspond to the respective means of each group. All shots were taken in Run I. The pulse delay offset accuracy is within $< \pm 10 \mu m$ while the pulse delay accuracy is $< \pm 1 \mu m$. For the sake of clarity, the error bars for the energy measurement according to Fig. 4.23 are not displayed. These range between $-8.1\%$ and $+2.8\%$. The normalised FWHM values represent an upper limit as the (positive) error propagated from dividing through the erroneous peak value ($\Delta_+(\Delta E_{\mathrm{FWHM}}/E) = \Delta E_{\mathrm{FWHM}}/E \times \Delta E/E$) is much smaller than the measured artificial energy spread due to the beam divergence (up to $\sim -70\%$). There are multiple shots without electrons which are represented as one black 'x' marker as they were taken at the same delay.

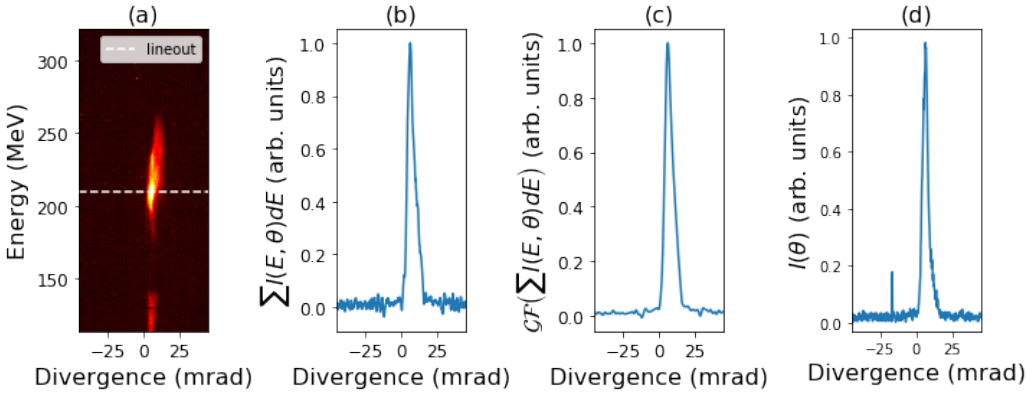



Figure 4.22: This figure shows the results of the divergence analysis. Panel (a) shows the raw intensity data (corresponding to electron charge density on Lanex screen) of shot 26. Panel (b) shows the data summed over the energy axis resulting in a function of divergence angle. A Gaussian filter was applied in panel (c) to reduce fluctuations in noise. Panel (d) shows the line-out at the energy position indicated in the raw data by a dashed line. The small spike on the left-hand side is due to a bright pixel (either due to a dead pixel or because of X-rays hitting the CCD).

For other shots in Run I similar values were measured with all beams having a divergence FWHM smaller than 10 mrad. It has to be noted that the summation approach did not give indicative results for low amplitude shots such as shot 34 due to the small signal to noise ratio. Here, the line-out approach was taken to get a result.

The beam divergence also has an impact on the uncertainty of the energy measurement. As was shown in Fig. 4.15, trajectories of electrons with equal energy but different divergence intersect with the Lanex screen at different positions. Given that all measured divergence values were within the ±10 mrad interval, the upper boundary for relative uncertainty from this source of error can be quantified using these simulated trajectories. Figure 4.23 shows the computed relative error for the second CCD (higher energy) from the interpolated function for each energy value (compared to the ±0 mrad values used in all axis labels). The kink seen in the data arises from the slit and offset between the two Lanex screens. The uncertainty of the energy axes caused by the beam divergence is, therefore, limited by +2.8% and −8.1%.

When measuring the relative FWHM values, Gaussian error propagation cannot be used as the errors of the three values (position of peak, as well as right and left half-maxima) are not independent. For a mono-energetic beam, the divergence causes a spread on the energy axis which increases the measured FWHM value. Assuming uncorrelated transverse and longitudinal momenta with an isotropic

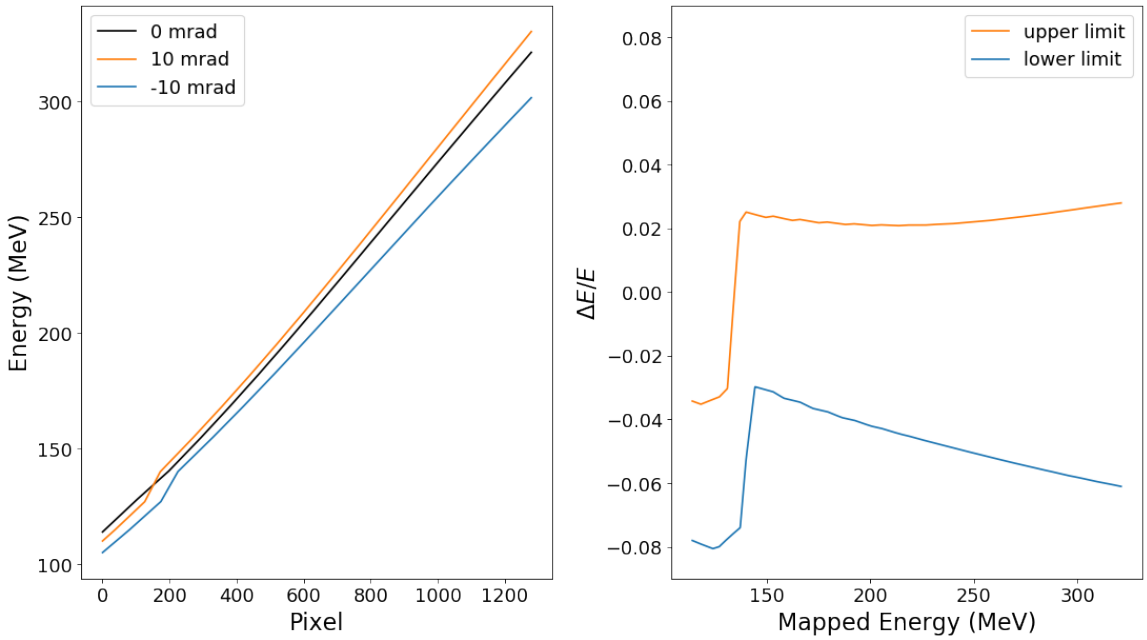



Figure 4.23: The left-hand side panel of this figure shows the interpolated pixel to energy conversion curves for different incidence angles obtained from simulated electron trajectories. The panel on the right-hand side shows the deviation in energy caused by a divergence angle of ±10 mrad normalised to the reference value (mapped energy) at 0 mrad.

distribution it is not possible to measure an energy FWHM that is smaller than the real value. This means that the measured values represent maxima. A quantitative analysis would depend on the exact trajectory of the electrons and therefore on the beam properties which cannot easily be inferred from the obtained data. To find a maximum lower error, one can perform the following steps. First, one takes a specific distance on the pixel axis (measured energy spread) from the left panel in Fig. 4.23. Then one relates this value to energy using the black curve which gives the upper measured limit. Finally, one reads the left pixel value using the orange curve and the right pixel value using the blue curve and subtracts these values which gives the narrowest energy distribution which can cause the measured spread using a beam of the given divergence. For example, using a measured energy spread of 20 MeV (measured between $200 - 220$ MeV), one finds a hypothetical minimum energy spread (producing the same measured result) of 5.9 MeV which is 70.4% smaller.

The spatial jitter measurement of the beam pointing was done as explained in Section 4.1.7.4. The 2PII mechanism can only be expected to occur when both pulses are not only temporally separated by a certain value but also their spatial overlap does not exceed a certain value. If the spatial overlap is not given, the wakefield amplitude does not add constructively and the ionisation and attempted injection processes do not take place at a location at which the electrons can be trapped. Due to the short focal length of the injector parabola, the injector pulse is stable with very limited shot to shot fluctuations ($\sqrt{\Delta x + \Delta y} \ll w_{0,\mathrm{inj}}$). The drive pulse fluctuations can, therefore, be used as an indicator of relative overlap between the two pulses. However, due to realignment between runs using motorised mirrors no absolute value can be given.

Figure 4.24 shows the jitter measurements of Run I distinguishing between shots in which electrons were injected and those in which this was not the case. The centre of mass for shots showing electrons is separated from the centre of mass of the other shots by 24.2 µm in $y$-direction and 4.9 µm in $x$-direction. While this indicates a trend the limited number of shots does not allow for a final conclusion based on statistical evidence for this run. Shots lacking electrons could be caused by fluctuations in other parameters rather than beam overlap. The injection of electrons even at large jitter values indicates that the injector pulse must have been partially guided by the driver's wakefield or must have had enough power to inject off-axis.

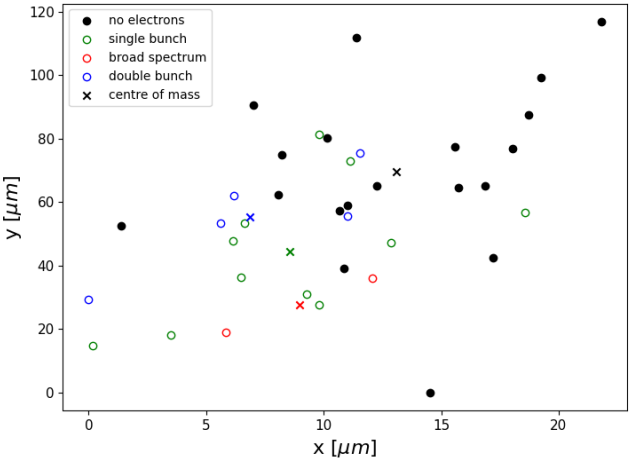



Figure 4.24: Measurement of relative drive pulse transverse position obtained from leak-through camera. The pixel to axis conversion was performed using data from Section 4.1.7.4. The data points have an uncertainty arising from the standard deviation of the correlation data which is $\pm 4.6\,\mu m$ ($x$) and $\pm 4.5\,\mu m$ ($y$). Shots 20 to 56 are plotted to make a valid comparison in a parameter space in which injection is likely to occur. The centre of mass of each species is indicated with an 'x' marker of the respective colour.

Analysis of the PMT and EMP signals gives additional information to interpret the electron spectra shown above. A sample read-out from the oscilloscope showing the laser energy (detected through a photodiode measurement of leak-through light before the compressor), the signals of both PMTs, and the EMP as measured by the B-dot probe are presented in Fig. 4.25 for shots 56 and 55. Shot 56 shows a distinct (negative) peak in both PMT signals which indicates the presence of electrons causing X-rays whereas shot 55 does not show the same feature.

A quantitative comparison across shots from Run I is shown in Fig. 4.26. No correlation between total laser energy and accelerated electrons can be found from this data (red markers which indicate the presence of electrons are distributed across the whole range of laser energies) supporting the argument for 2PII as it is unlikely that peaks in laser energy caused injection. On the other hand, a correlation between the PMT peak signal and the presence of electrons exists. The same holds for the EMP signal and the presence of electrons. This is shown by the mean values displayed using horizontal lines. The mean of all shots in which electrons were observed (red line) is larger in magnitude than the mean of shots in which no electrons were observed (black line). Furthermore, the mean over shots 26-56 (selected as in the

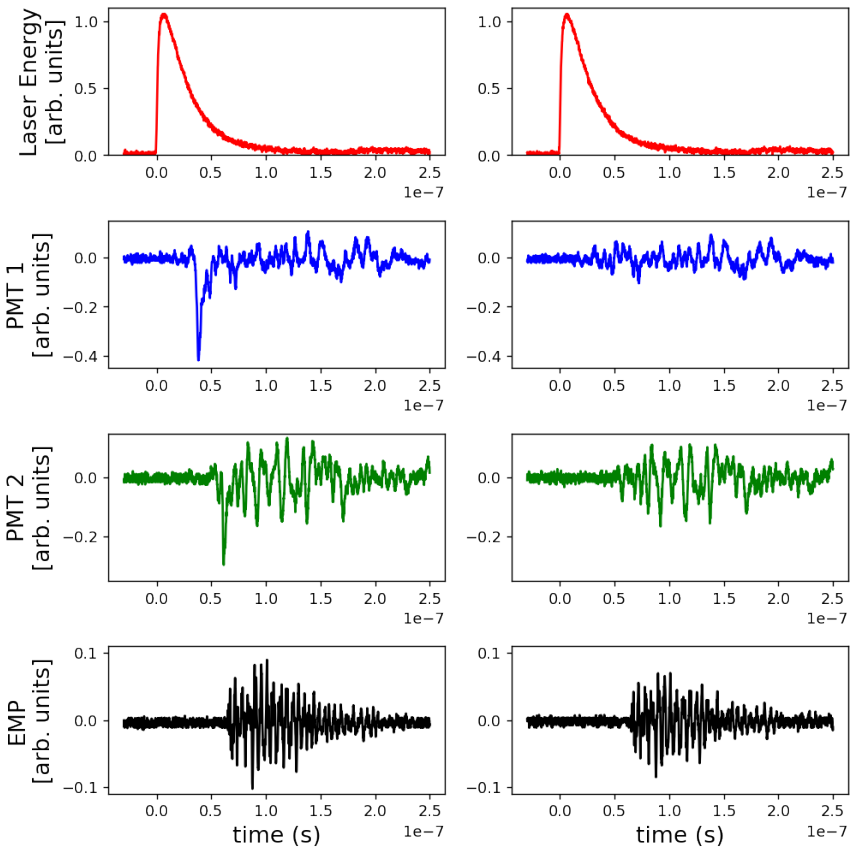



Figure 4.25: This figure shows oscilloscope signals from various diagnostics for shots 56 (electrons on Lanex screen, left-hand side panels) and 55 (no electrons on Lanex screen, right-hand side panels).

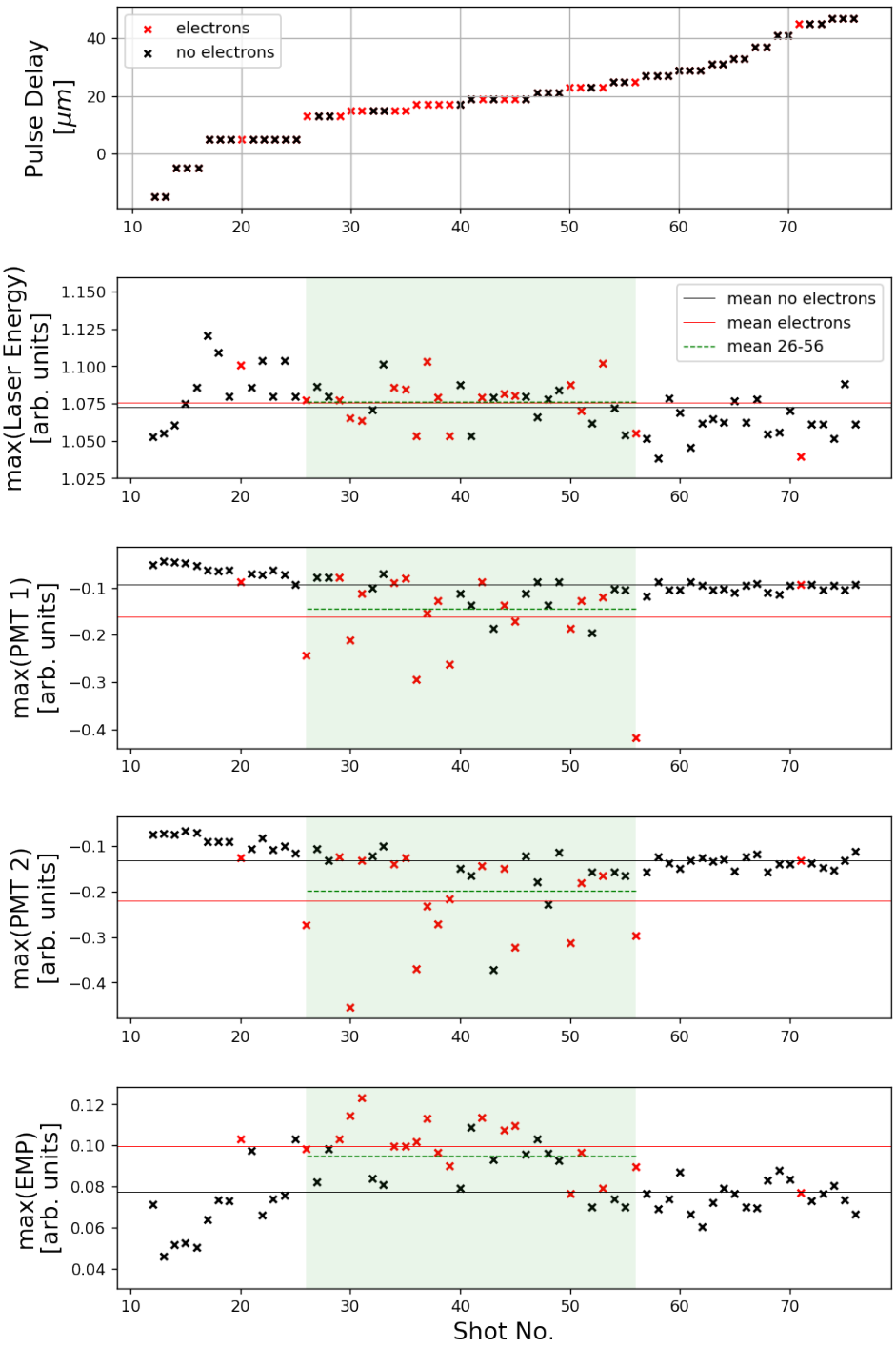



Figure 4.26: This figure shows oscilloscope readings of the peak values of measurements of total laser pulse energy (panel 2), generated X-rays measured by two different PMTs (panels 3 and 4), and EMP signal measured by the B-dot probe (bottom panel) for Run I. All red 'x' markers represent shots in which electrons were captured on the Lanex screen. All black ones do not feature electron traces. For convenience, the relation between shot number and pulse delay is displayed again (top panel).

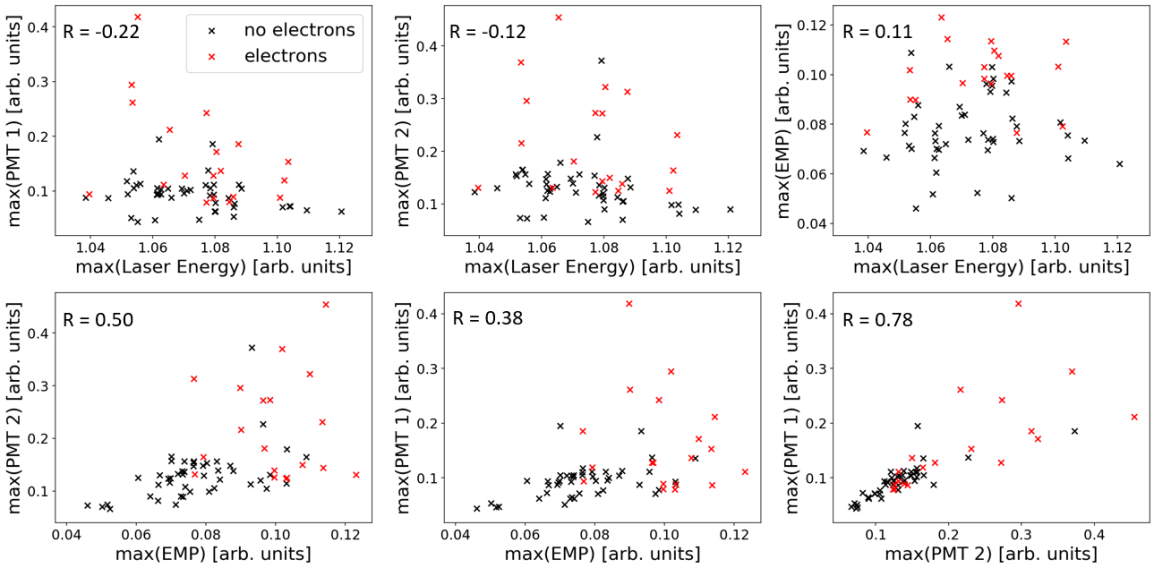



Figure 4.27: Correlations between absolute values of parameters presented in Fig. 4.26. The value $R$ given in the top left corner of each panel is the respective Pearson product-moment correlation coefficient between $x$ and $y$ values.

previous section) also had a larger magnitude than any of the shots outside of this region for both PMT diagnostics. This shows the impact of laser pulse delay on generated X-rays and on the accelerated charge incident on the chamber wall. To further compare the data, the correlation between all four parameters (laser energy, PMT 1, PMT 2, EMP) observed is shown in Fig. 4.27. The Pearson product-moment correlation coefficient [232] between the $x$ and $y$ parameters are given in the top left corner showing a strong linear correlation between the signals (X-rays) of the two photomultiplier tubes ($R = 0.78$). It is observed that all parameters have little correlation with the laser energy (except the laser energy itself). Further information can be gained when calculating the correlation of all four parameters with the electron bunch peak energy and the electron bunch charge (as discussed earlier, an electron bunch is "present" if the integrated intensity data—corresponding to the electron charge—has a peak that is at least three times higher than the average noise). Figure 4.28 presents the correlation plots for these values showing that the EMP signal is moderately correlated to the electron peak energy but not correlated to the magnitude of the charge in the electron bunch. The absolute peak signals from the photomultiplier tubes are moderately correlated to the electron bunch charge with Pearson coefficients of $R = 0.69$ (PMT 1) and $R = 0.53$ (PMT 2).

A further source (other than the laser energy) that could influence the occurrence

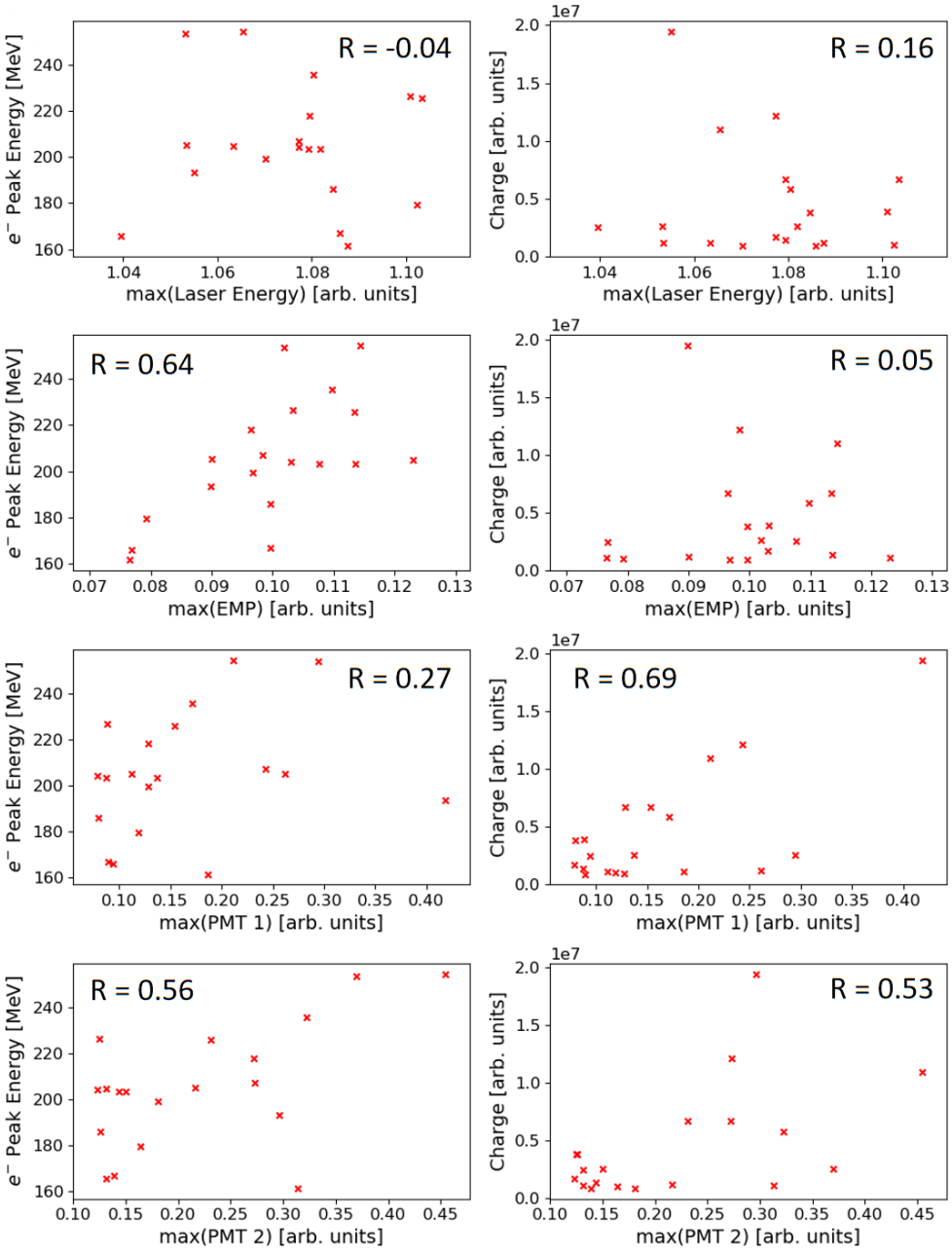



Figure 4.28: Correlations of absolute oscilloscope readings for laser energy, PMT 1, PMT 2, and EMP signals versus electron bunch peak energy and electron bunch charge. Since the latter two parameters would be ill-defined without the presence of electrons, only pre-selected shots in which electrons were observed are included in the analysis. The value $R$ given in the top corners of each panel is the respective Pearson product-moment correlation coefficient between $x$ and $y$ values.

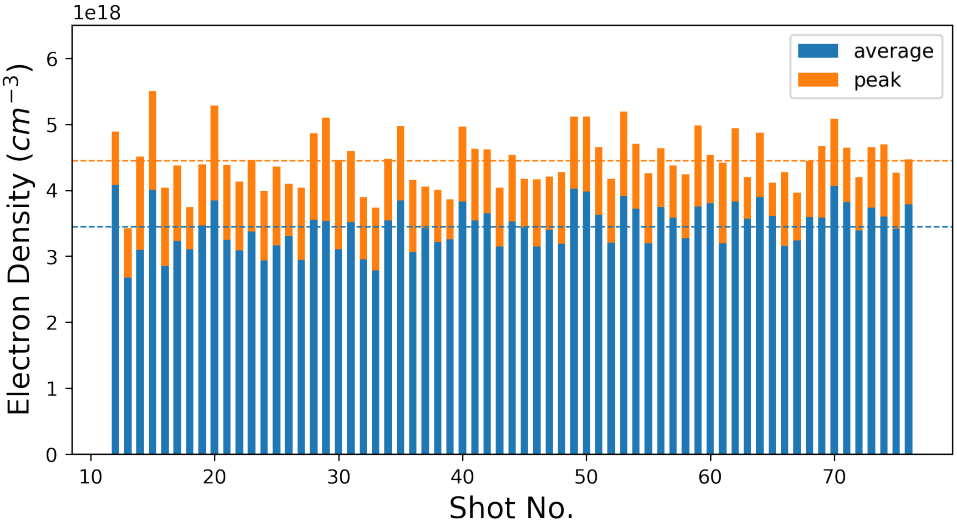



Figure 4.29: This figure shows the reconstructed electron density from the interferometry diagnostic for Run I. The peak values are shown in orange while the mean of the density along the symmetry axis of each shot is shown in blue. The dashed lines give the average of the respective values over all shots. The uncertainty in electron density arising from the error in the choice of certain parameters within the reconstruction routine is discussed in the text and the real value can be estimated to be between the measured value $n_e$ and $1.28 \times n_e$.

of electron injection is the electron density. Even though the backing pressure was kept constant over the entire run, shot-to-shot fluctuations of electron density can occur. As shown in Section 4.1.7.1, the electron density was measured using a probe pulse crossing the plasma column perpendicularly. The results of the density analysis for Run I are shown in Fig. 4.29.

The average peak value in Run I was $\overline{n}_{e,\mathrm{peak}} = 4.45 \times 10^{18}\,\mathrm{cm}^{-3}$ ($\pm 9.3\%$). The average mean value (taken over the symmetry axis) was $\overline{n}_{e,\mathrm{mean}} = 3.45 \times 10^{18}\,\mathrm{cm}^{-3}$ ($\pm 9.7\%$).

Before correlating the density measurement and electron spectra it is important to discuss the error boundaries from the reconstruction routine caused by human error. To this end, I varied specific parameters which had to be set within the data analysis over a range that was larger than can be expected to occur through human error. The values of these parameters (angle and translation of symmetry axis for Abel inversion and limits of the Fourier transform for peak isolation) were all important for the density analysis. For shot 28, the position of the symmetry axis was varied over 8 pixels and the rotation of the image with respect to the symmetry axis was varied over 2 degrees. Then, for fixed shift and rotation values the left and right limits of

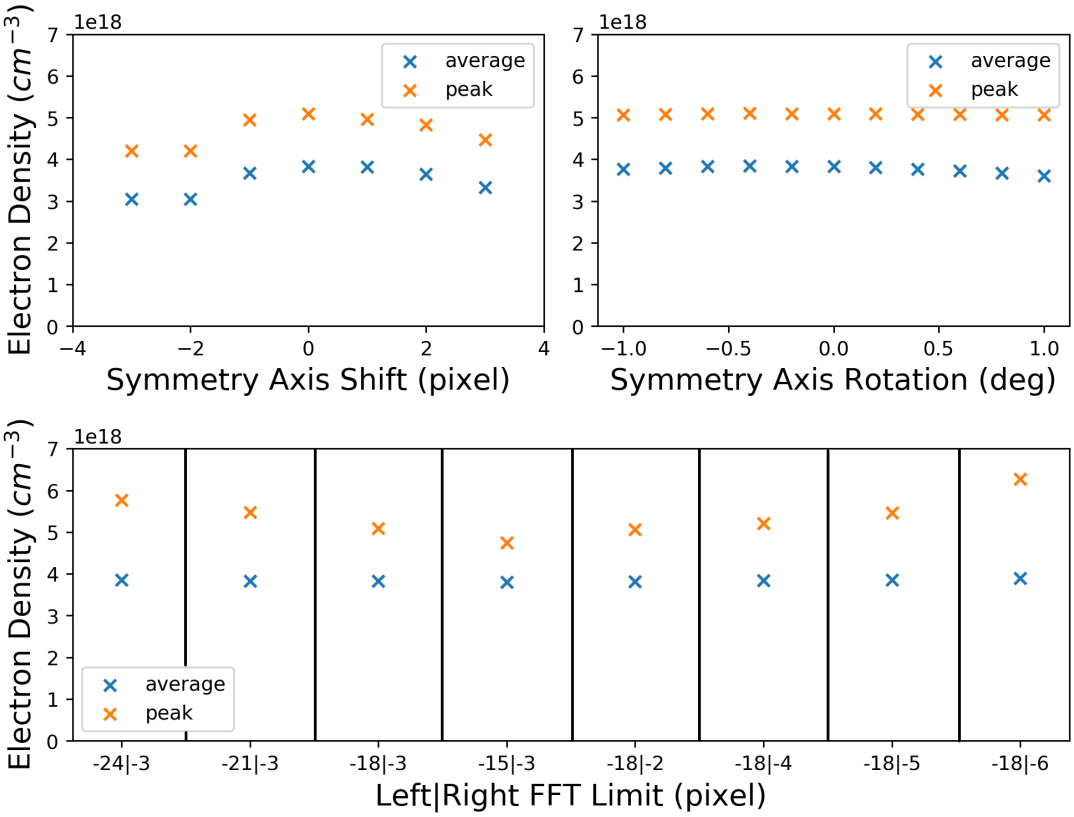



Figure 4.30: This figure shows the reconstructed electron density from the interferometry diagnostic for shot 28. The top left panel shows a variation of the symmetry axis shift (rotation at 0°, Fourier transform limits at -18|-3 pixels). The top right panel shows the density varied over the rotation of the image with respect to the symmetry axis (shift at 0 pixels, Fourier transform limits at -18|-3 pixels). The bottom panel shows the density at various settings of the limits of the Fourier transform (shift at 0 pixels, rotation at 0°).

the isolated Fourier transform data were shifted over 9 (left) and 4 (right) pixels with respect to the central peak at 0. The results are shown in Fig. 4.30.

The reconstructed electron density reduces with increasing shift of the axis as expected (due to the reduction of column radius in the Abel transform). The axis rotation has a negligible impact over the tested value range. The boundaries of the Fourier transform mask not only cause a variation in density value but also a change in continuity of the data. The two largest electron density values are at the largest left (-24) and right (-6) mask limits. However, these two values show a patchy structure with large fluctuations (which is the reason for the smaller magnitude in fluctuations of average density) and are therefore not be considered for the error estimation.

To estimate how the different error sources contribute when combined I took four

| Shift | Left FFT lim. | Right FFT lim. | $n_{e,\mathrm{peak}}$ | $\Delta n_{e,\mathrm{peak}}/n^*_{e,\mathrm{peak}}$ |
|---|---|---|---|---|
| -3 pixels | -15 pixels | -3 pixels | $3.88 \times 10^{18}\,\mathrm{cm}^{-3}$ | -0.22 |
| 3 pixels | -15 pixels | -3 pixels | $4.37 \times 10^{18}\,\mathrm{cm}^{-3}$ | -0.14 |
| -3 pixels | -21 pixels | -3 pixels | $4.64 \times 10^{18}\,\mathrm{cm}^{-3}$ | 0.09 |
| 3 pixels | -21 pixels | -3 pixels | $4.55 \times 10^{18}\,\mathrm{cm}^{-3}$ | 0.01 |

Table 4.4: Results of error approximation for the electron density reconstruction. $n^*_{e,\mathrm{peak}}$ is the peak value of the reference condition (no shift, no rotation, -18|-3 FFT limits).

parameter sets in which the respective parameters on their own had a maximum impact on the density value. Due to its small impact on the reconstructed electron density value the axis rotation error was not considered. The results are shown in Tab. 4.4. Note that an error of $-22\%$ for the real value corresponds to an error of $1/(1-0.22)-1 = +28\%$ for the measured value which is the upper error limit of the density reconstruction routine for this run. A further source of error associated with the phase shift measurement could be a deviation from cylindrical symmetry of the plasma channel which is not accounted for in the calculation above.

Using the electron density measurement, the last outstanding step of those described at the beginning of this section can be resolved to show that the injection is indeed depending on the laser pulse delay (rather than on density). In Fig. 4.31 the electron peak density is plotted against the bunch peak energy. Electrons are shown to be injected across the full range of density values present in the data with double and single bunches occurring at similar values. What can be noted is that the double bunches seem to follow a trend where both first and second bunch energy increases with increasing density. This trend does not seem to exist for the single electron bunches.

This concludes the investigation of Run I showing that electrons are more likely to be injected when the two laser pulses have a separation within a specific range. For convenience, I call this region injection space. Furthermore, the lack of accelerated electron bunches found in some shots within the injection space could be caused by a mismatch in spatial beam overlap at focus. It was observed that the EMP and X-ray signals were higher in the injection space - even if no electrons were detected on the Lanex screens in some of the shots. The reason for this could be the existence of electron beams that do not intersect with the Lanex screens either because they miss

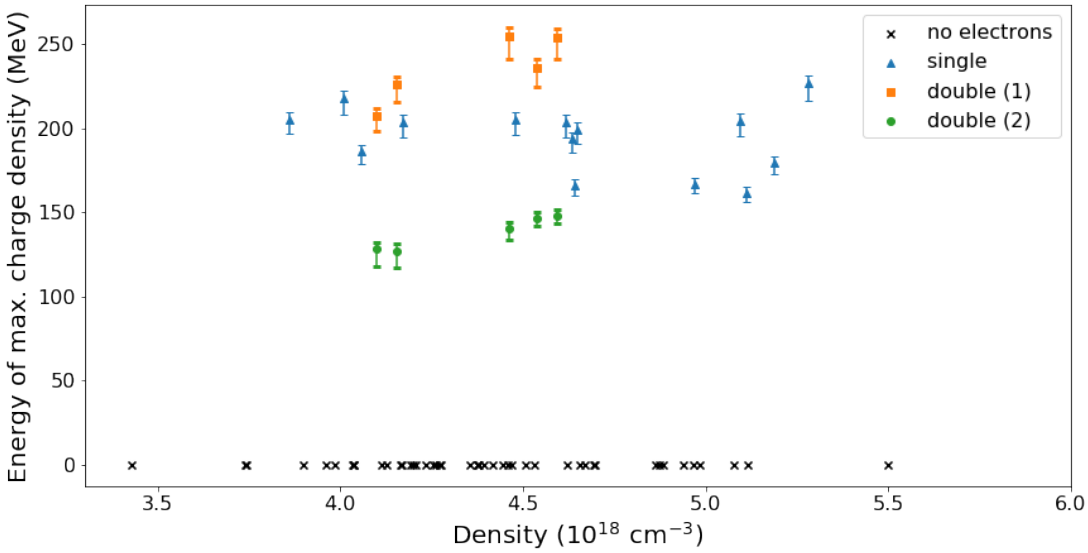



Figure 4.31: This figure shows the energy of the maximum charge density plotted versus the reconstructed electron density for data from Run I. For the sake of clarity, the error bars for the density measurement (only positive and up to +28%) are not displayed.

the entrance hole to the magnet or because they are injected but not trapped (which means that they are accelerated by the wakefield but not for a sufficiently long time) resulting in (weakly relativistic) bunches below the detection threshold.

#### 4.1.8.2 Run II

For the second run, the gas bottle with the helium-nitrogen mixture was exchanged for a bottle filled with pure helium. This meant that, without the presence of a dopant, tightly bound electrons to be injected by the injector pulse were not available.

Throughout the whole run in which the pulse delay was scanned as before, no electrons were detected on the Lanex screens. The electron density obtained from the interferometry data averaged over the first 10 shots was $\bar{n}_{e,\mathrm{peak}} = 4.55 \times 10^{18}\,\mathrm{cm}^{-3}$ ($\pm 3.6\%$)[13] which is slightly higher than observed in Run I. After those shots, the probe pulse was used to obtain data from a spectrometer analysing the plasma emission spectra which prevented any further density measurements.

The averaged laser energy over all shots was larger than in Run I by 2.7%. As shown in Fig. 4.32, no trace of enhanced X-ray levels were picked up by either PMT. The B-dot probe, however, showed significantly larger EMP signals than in Run I

[13] As in Run I this is the standard deviation of the measurements and does not explicitly include the 28% uncertainty from the reconstruction algorithm.

(mean over all shots of 0.12 vs 0.08) indicating the interaction of untrapped, low energy electrons with the chamber wall.

#### 4.1.8.3 Run III

Run III used the same gas mixture as Run I. The quarter-waveplate was rotated such that the polarisation of the injector pulse was changed from circular to linear. This means that the magnitude of the electric field is now oscillating as $\mathbf{E} = E_0 \cos(kz - \omega t)\hat{\mathbf{e}}_x$ and goes through zero which was not the case for light of (right-handed) circular polarisation with $\mathbf{E} = (1/\sqrt{2})E_0 [\cos(kz - \omega t)\hat{\mathbf{e}}_x + \sin(kz - \omega t)\hat{\mathbf{e}}_y]$. The peak instantaneous intensity is increased in the linear case (at equal average power) because the intensity oscillates between its peak value and zero. Therefore, to reach equal average intensity, the peak value must be larger.

The electron density obtained from the interferometry data averaged over the first 21 shots was $\bar{n}_{e,\mathrm{peak}} = 4.32 \times 10^{18}\,\mathrm{cm}^{-3}$ ($\pm 5.8\%$) and, therefore, slightly lower than in Run I. After this shot, the interferometer was again blocked to conduct the spectrometer measurement mentioned above. There were 5 control shots with the injector pulse blocked and 3 control shots with the drive pulse blocked none of which showed injected electrons.

The measurements of the electron bunch energy and its respective FWHM are shown in Fig. 4.33. The main difference observed between Run I and Run III is the occurrence of several shots with a broad electron spectrum in Run III. Half of the shots in which electrons are detected have an energy spread with FWHM of more than 20% of the peak value of the spectrum. The pulse delay region in which particles are accelerated is, on average, lower (closer to overlap) than in Run I. However, both regions are within the uncertainty interval of the delay measurement.

Plotting the shot number versus pulse delay (see Fig. 4.34) shows that in this run the delay was reset to obtain more data in the region in which electrons were found. The laser energy was stable and did not drift throughout the run.

From the jitter measurement data, no evidence can be found that the deviation from overlap is causing the absence of injection. Fig. 4.35 shows the occurrence of electron injection over a great range of drive pulse transverse position values (relative to fixed injector position). This figure only compares the shots within a specific delay region (from 6 µm to 18 µm) to remove bias from shots that may show a lack of electrons for a different reason than the one probed here.

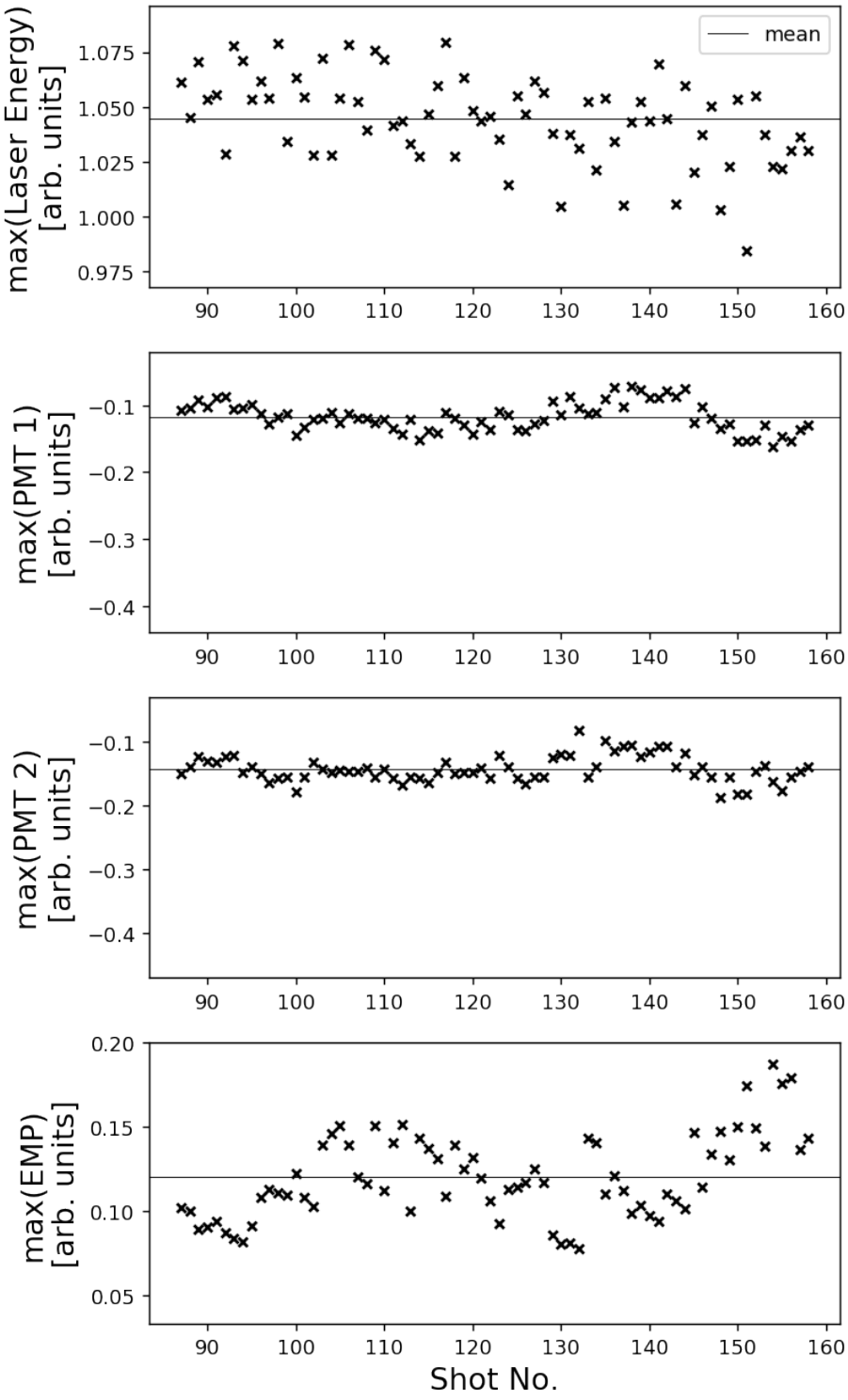



Figure 4.32: This figure shows oscilloscope readings for the peak values of measurements of total laser pulse energy (top), generated X-rays measured by PMTs (middle panels), and EMP signal measured by the B-dot probe (lower panel) for Run II.

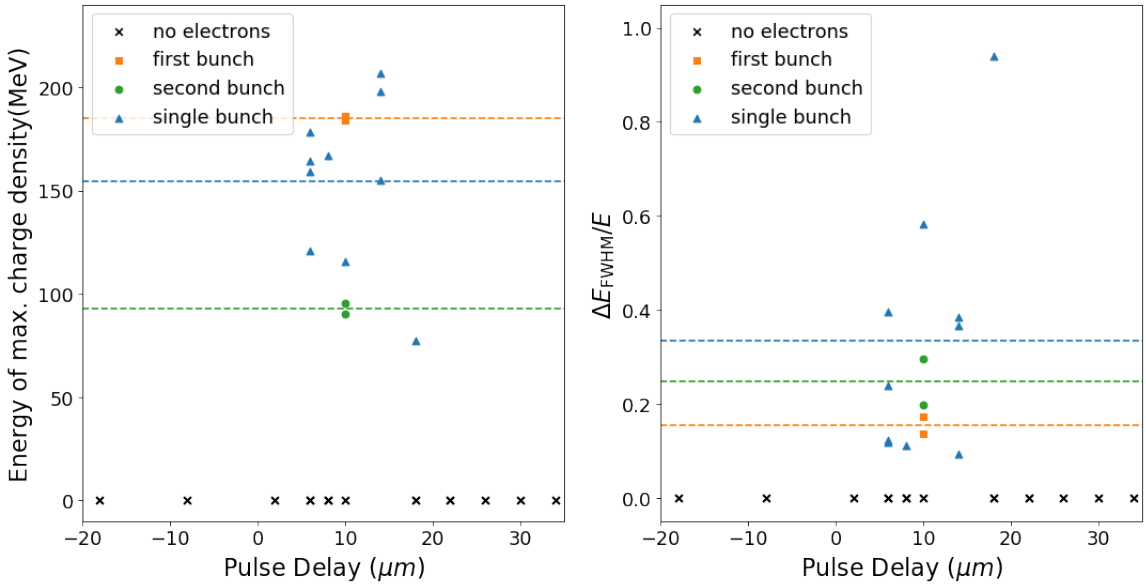



Figure 4.33: This figure shows the energy values of the highest integrated charge density for each shot plotted against pulse delay (left panel) and the corresponding FWHM energy spread normalised to the peak energy also plotted against pulse delay (right panel). The dashed lines correspond to the respective means of each group. All shots are from Run III. The pulse delay offset accuracy is within $< \pm 10 \mu m$ while the pulse delay accuracy is $< \pm 1 \mu m$. For the sake of clarity, the error bars for the energy measurement according to Fig. 4.23 are not displayed. These range between $-8.1\%$ and $+2.8\%$. The normalised FWHM values represent an upper limit as the (positive) error propagated from dividing through the erroneous peak value ($\Delta_+(\Delta E_{\mathrm{FWHM}}/E) = \Delta E_{\mathrm{FWHM}}/E \times \Delta E/E$) is much smaller than the measured artificial energy spread due to the beam divergence (up to $\sim -70\%$). There are multiple shots without electrons which are represented as one black 'x' marker as they were taken at the same delay.

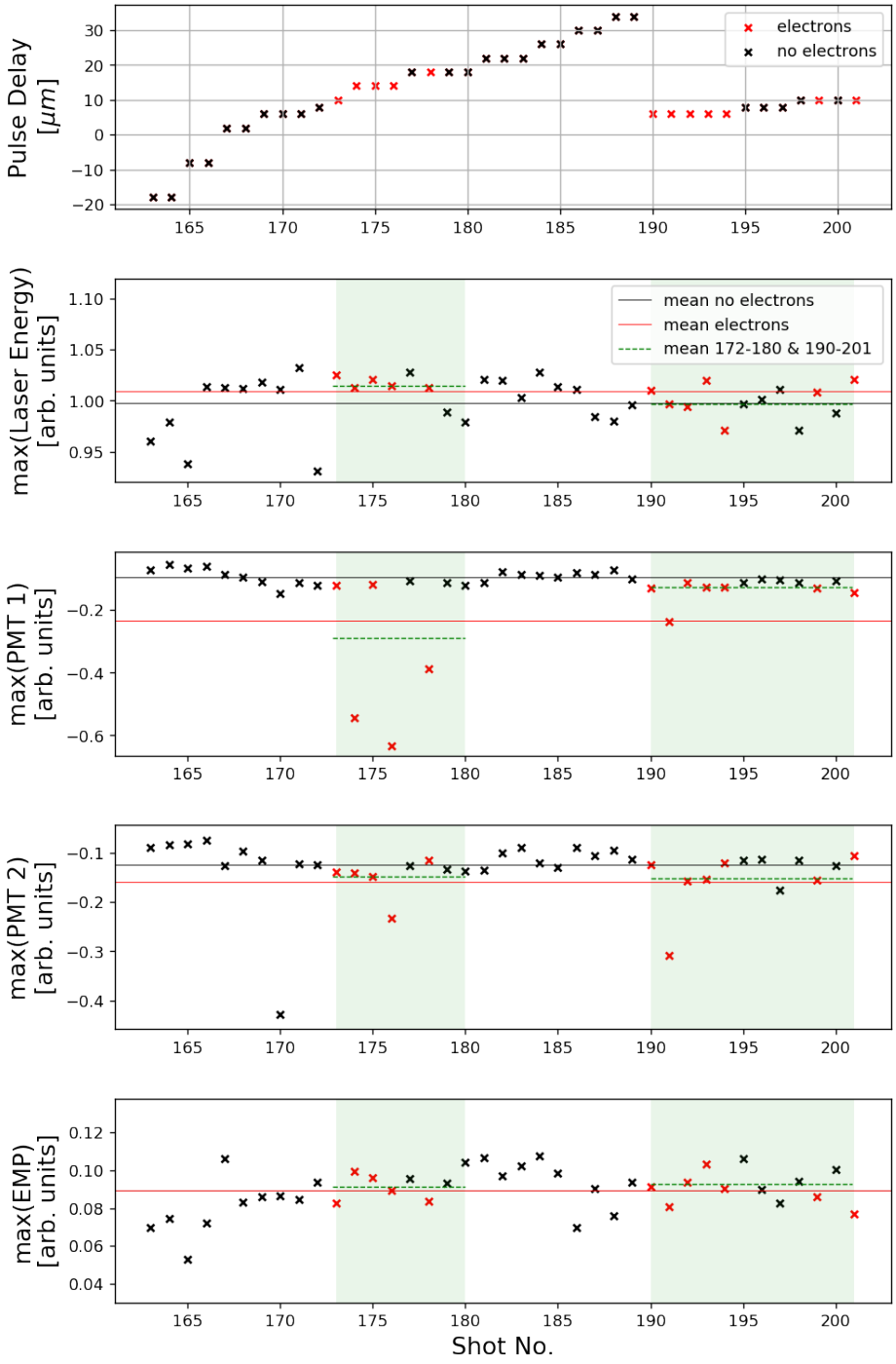



Figure 4.34: This figure shows the delay (spatial distance) between drive pulse and injector pulse for each shot of Run III. For shots in which electrons are observed on the Lanex screen, the 'x' marker is displayed in red. Below, the oscilloscope readings for the peak values of measurements of total laser pulse energy (panel 2), generated X-rays measured by PMTs (panels 3 and 4), and EMP signal measured by the B-dot probe (bottom panel) are shown.

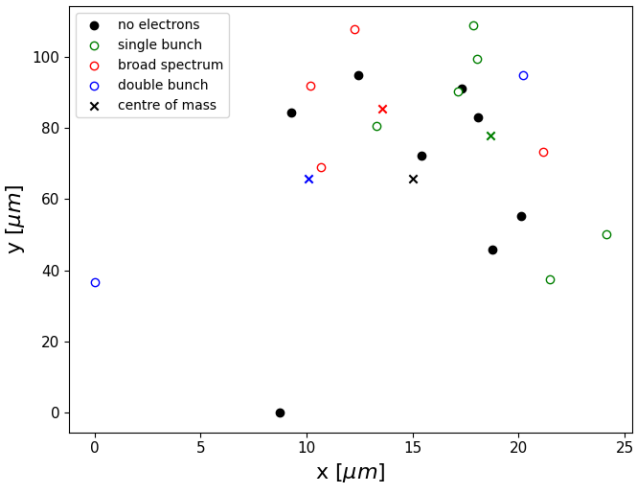



Figure 4.35: Measurement of relative drive pulse transverse position obtained from leak-through camera for all shots with delays between 6 µm and 18 µm taken in Run III. The pixel to axis conversion was performed using data from Section 4.1.7.4. The data points have an uncertainty arising from the standard deviation of the correlation data which is $\pm 4.6\,\mu m$ ($x$) and $\pm 4.5\,\mu m$ ($y$). Shots 173 to 180 and 190 to 201 are plotted to make a valid comparison in a parameter space in which injection is likely to occur. The centre of mass of each species is indicated with an 'x' marker of the respective colour.

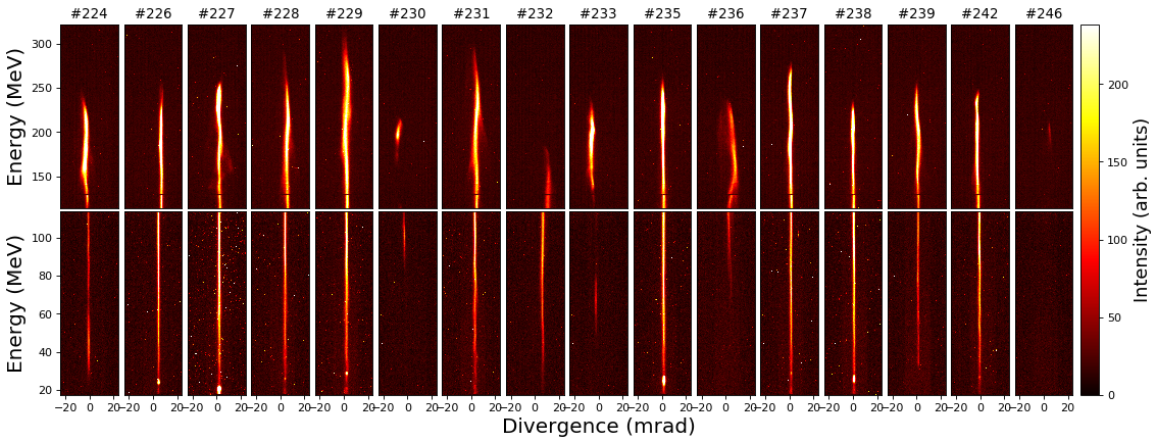



Figure 4.36: Intensity of signal on the Lanex screens captured by a CCD (with axes corresponding to energy against divergence angle) for all shots displaying electrons in Run IV.

#### 4.1.8.4 Run IV

Run IV used a gas mixture of 5% nitrogen and 95% helium and used a linearly polarised injector pulse (wave plate unchanged with respect to Run III). Furthermore, the backing pressure was raised from the previous run to 0.724 bar. As a consequence, the average electron density was slightly higher. From analysing shots 1 to 15 (for later shots the interferometry line was, again, blocked) the density obtained was $n_{e,\mathrm{peak}} = 4.87 \times 10^{18}\,\mathrm{cm}^{-3}$ ($\pm 8.2\%$). There were 5 control shots with the injector pulse blocked none of which showed injected electrons.

In contrast to the mono-energetic beams found in Run I, almost all shots showing electrons (see Fig. 4.36) have a broader energy spectrum (exceptions are shots 230 and 246) with maximum electron energies reaching values larger than 300 MeV.

Plotting the shot number versus pulse delay (see Fig. 4.37) shows that in this run electrons were only injected in a very narrow region of pulse delay variation (mainly between 16 and 22 µm with single events at 24 and 26 µm). This suggests that the injection mechanism is not likely to originate from the self-focusing effect caused by spatially overlapping beams as the region at which electron injection occurs would be stretched at higher electron density rather than narrowed.

Figure 4.38 shows the jitter measurement data with particles being, again, injected over a large range. Especially the vertical direction shows fluctuations of the focal spot of up to two times of the pulse's FWHM from one extremum to the other. Similarly, the absence of particle injection is also detected over a large space. As in previous runs, the fluctuations are stronger in the $y$-axis than in the $x$-axis.

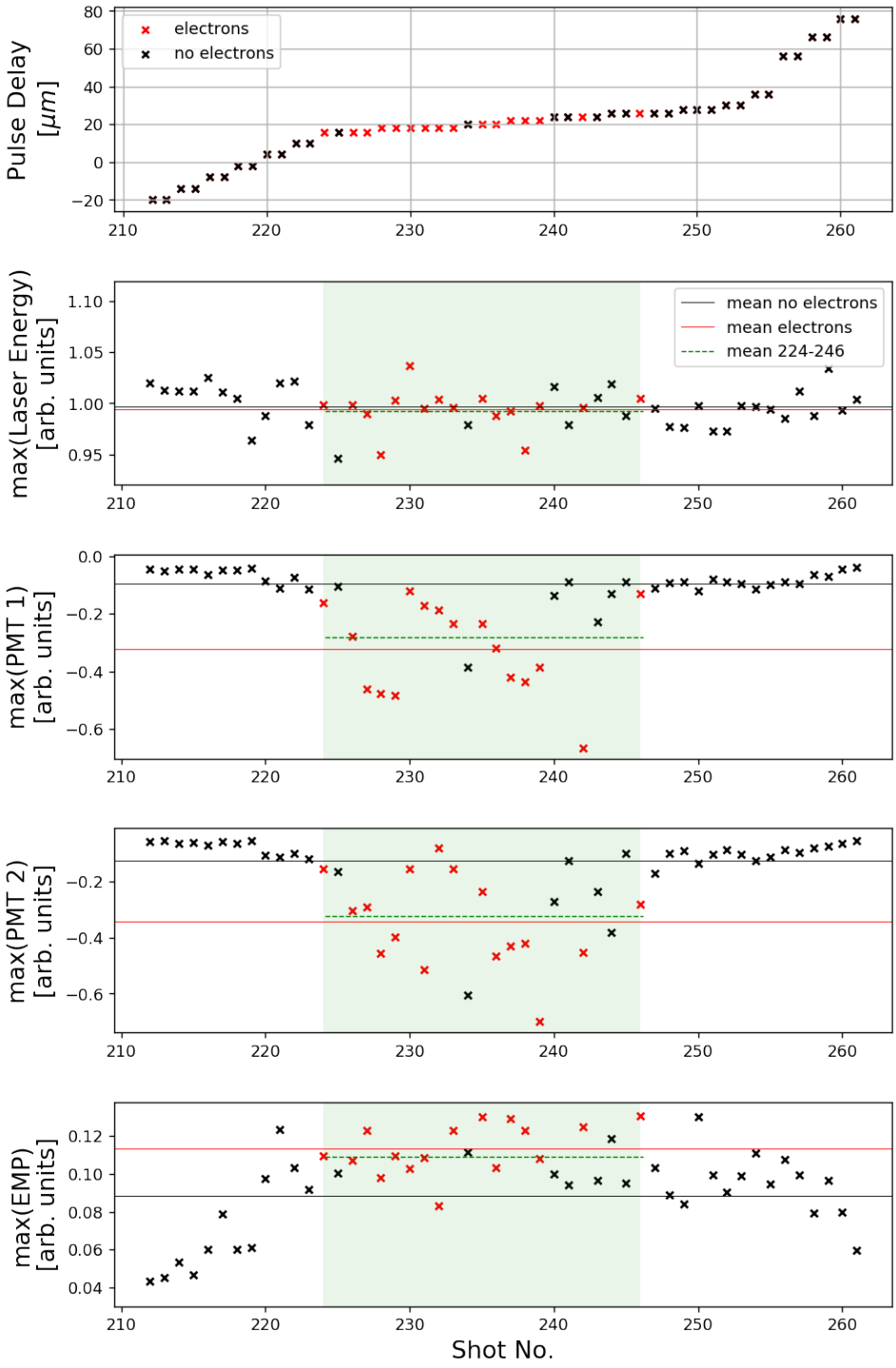



Figure 4.37: This figure shows the delay (spatial distance) between drive pulse and injector pulse for each shot of Run IV. For shots in which electrons are observed on the Lanex screen, the 'x' marker is displayed in red. Below, the oscilloscope readings for the peak values of measurements of total laser pulse energy (panel 2), generated X-rays measured by PMTs (panels 3 and 4), and EMP signal measured by the B-dot probe (bottom panel) are shown.

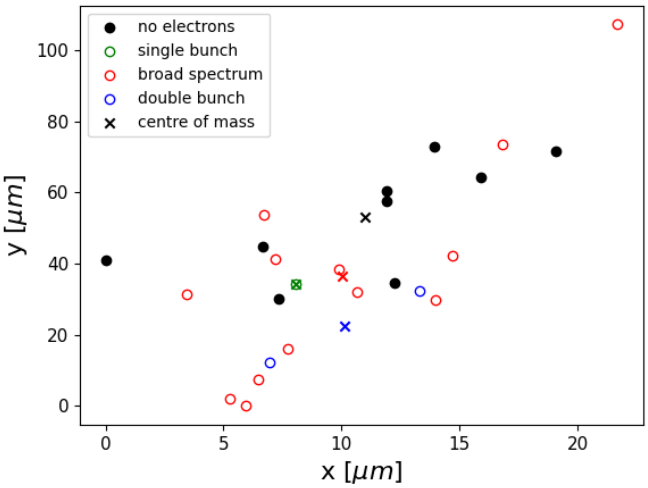



Figure 4.38: Measurement of relative drive pulse transverse position obtained from leak-through camera for all shots with delays between 16 µm and 26 µm taken in Run IV. The pixel to axis conversion was performed using data from Section 4.1.7.4. The data points have an uncertainty arising from the standard deviation of the correlation data which is $\pm 4.6$ µm ($x$) and $\pm 4.5$ µm ($y$). Shots 224 to 248 are plotted to make a valid comparison in a parameter space in which injection is likely to occur. The centre of mass of each species is indicated with an 'x' marker of the respective colour.

This feature is expected if one thinks about the motion of mirrors in the vacuum chamber. Vibrations (eg. from motors of vacuum pumps) cause small oscillations of the mirrors which are mounted using a vertical post. A side-ways motion of a mirror does not influence the beam pointing as strongly as a forwards motion which changes the incidence and reflection angles.

This section has shown that a narrow energy spread is a feature more strongly associated with a circularly polarised injector pulse. This can be explained by the difference in instantaneous peak intensity between a linear and circular pulse of equal average power which is higher in the former case but oscillates to a zero value. This means that the ionisation of the inner nitrogen energy levels (6 and 7) frees electrons in a wider region and over a longer duration than in the circular polarisation case. It was also seen that increasing the concentration of the nitrogen dopant from 3% to 5% narrowed the pulse separation region in which particles were injected.

## 4.2 Simulations

The mechanism was also studied using two-dimensional particle-in-cell simulations using the code EPOCH [126]. Although it is not possible to have a perfect representation of the experimental conditions, PIC simulations can help to understand the basic processes and limitations which occur in an experiment.

The quickly diffracting injector pulse and the acceleration length of 4 mm made it necessary to have a large simulation box. This made it unfeasible to conduct three-dimensional simulations which restricted the simulations to the use of linear polarisation only. In two dimensions it is difficult to accurately model the annular injector pulse, especially given the strong deviation from its optimal shape due to the impact of the DM motors and OAP focusing errors on the beam's phase front and intensity distribution. To approximate the shape of the incoming and outgoing injector beam, I used two separate pulses propagating at the experimentally measured divergence angle of the annular intensity peaks and crossing at the focus.

Since the laser amplitude threshold for electron self-injection is different in two-dimensional simulations compared to the real three-dimensional case I ran simulations at $n_e = 4.45 \times 10^{18}\,\mathrm{cm}^{-3}$ using helium doped with 3% nitrogen to find this threshold. It was found that the drive pulse did not inject at $a_0 = 0.63$ or below which is why this value was used in the simulation. This value is lower than the one found from the focal spot measurement ($a_0 = 0.71$). For the combined injector pulses the peak intensity was chosen to be $a_0 = 2.16$ where also no self-injection occurred. This value is within the range given from experimental observations.

A limitation of using a two-dimensional simulation model is that the intensity of the injector pulse lobes necessarily has to be too large away from focus such that it can be matched at the focus where the injection occurs. This is because the two pulses represent the entire annular beam. However, due to the divergence (half) angle of 3.1° (as observed in the experiment) the laser pulse has a negligible role in driving an on-axis wakefield at more than 1 mm away from focus (at this $z$ location the distance between the centre of the two beams will be apart by more than 100 µm). The spot size of each individual injector lobe was set to the value obtained from Fig. 4.10 $w_0 = 15.4\,\mu\mathrm{m}$.

The simulations presented here used 30 cells per laser wavelength (2625 cells total) in the longitudinal direction and 6.24 cells per laser wavelength (6013 cells total) in the transverse direction. In real units, the box had an extent of 70 µm in $z$-direction and 770.67 µm in $y$-direction. All particles were initialised as neutral nitrogen and helium

| Simulation | $\Delta z$ ($\lambda_p$) | $\Delta y$ (µm) | $a_{0,i}$ | $a_{0,d}$ | $n_e(1 \times 10^{18}\,\mathrm{cm}^{-3})$ |
|---|---|---|---|---|---|
| 1 | 1.25 | 0 | 2.16 | 0.63 | 4.45 |
| 2 | 1.0 | 0 | 2.16 | 0.63 | 4.45 |
| 3 | 0.75 | 0 | 2.16 | 0.63 | 4.45 |
| 4 | 0.5 | 0 | 2.16 | 0.63 | 4.45 |
| 5 | 0.25 | 0 | 2.16 | 0.63 | 4.45 |
| 6 | 0.0 | 0 | 2.16 | 0.63 | 4.45 |
| 7 | -0.5 | 0 | 2.16 | 0.63 | 4.45 |
| 8 | -1 | 0 | 2.16 | 0.63 | 4.45 |
| 9 | 0 | 10 | 2.16 | 0.63 | 4.45 |
| 10 | 0 | 30 | 2.16 | 0.63 | 4.45 |
| 11 | 0 | 50 | 2.16 | 0.63 | 4.45 |
| 12 | 0 | 0 | 1.98 | 0.63 | 4.45 |
| 13 | 0 | 0 | 1.8 | 0.63 | 4.45 |
| 14 | 0 | 0 | 2.16 | 0.55 | 4.45 |
| 15 | 0 | 0 | 2.16 | 0.5 | 4.45 |
| 16 | 0 | 0 | 2.16 | 0.63 | 4.0 |
| 17 | 0 | 0 | 2.16 | 0.63 | 3.5 |

Table 4.5: This table shows the parameters used in simulations 1 to 17. The position (delay) of the injector with respect to the drive pulse $\Delta z$ is given in units of the plasma wavelength. A positive value means that the injector is behind the driver. The vertical mismatch at the focal distance is given by $\Delta y$.

atoms and then ionised using the barrier suppression, multiphoton, and tunnelling ionisation mechanisms. The nitrogen species used 8 electron macro-particles per cell while the helium species used 4. The boundary conditions used were of type "simple_laser" for the left boundary to which electromagnetic fields can be attached and "open" for the other boundaries. All simulations shown used a moving window co-propagating with the laser pulses. To prevent unphysical injection at a sharp boundary, a linear density ramp was introduced with a length of 100 µm. The laser duration (FWHM) was set to 39 fs for all simulations to match the experiment.

A parameter scan was performed whose details are listed in Tab. 4.5. The delay between pulses, the relative $y$-position (perpendicular to propagation direction), both peak intensities, and the plasma density were scanned. The results are discussed below.

Figure 4.39 shows nitrogen electrons trapped in the wakefield for various pulse delays. All simulations had a $\sim 4$ mm propagation distance in plasma. At or close to temporal overlap of the pulses (panels 5 and 6) the trapped particle density is high

and spread out over a large area in subsequent buckets. At a separation of exactly one plasma wavelength between pulses (panel 2) the area covered by the electron beam is smallest. The electron beam has caught up with the decelerating region of the wakefield where the shape of the electric field components of both wakefield and laser pulse causes a transversal spread in the beam. The drive pulse peak amplitude at the last time step ranges between $a_0 = 0.75$ (panel 7) and 1.14 (panel 5) showing that beam overlap causes slight self-focusing before the injector diffracts.

The results are better understood when probing the kinetic energy values of the electrons within the simulations. Figure 4.40 shows the kinetic energy of electrons originating from the sixth and seventh ionisation levels from the nitrogen atoms. Similar features to those discovered in the experiment are visible. The only simulation that has only one energy peak without significant background noise is simulation 2 in which the laser pulses are separated by one plasma wavelength. Slight deviations from this separation (simulations 1 and 3) decrease the beam quality and peak energy. Similar to simulation 2, mono-energetic spectra around 100 MeV (although including significant amounts of electrons at low energy) are found at pulse separations of $0.5\lambda_p$ (panel 4) and $-\lambda_p$ (panel 8). At perfect laser pulse overlap (panel 6) two peaks are found with close resemblance to the double peak found in Fig. 4.19 (although not as strong a separation present between peaks in the simulation). The most strongly accelerated electrons reach values in excess of 200 MeV. When decreasing the total electron density (panels 16 and 17), the peaks become more strongly separated. When decreasing the injector pulse amplitude (panels 12 and 13) or drive pulse amplitude (panels 14 and 15) the more energetic peak decreases in magnitude while the other peak stays almost constant. Increasing the laser pulse separation in $y$-direction (spatial jitter) has the strongest impact of all parameter scans (panels 9, 10, and 11). The trapping is strongly inhibited at a separation of 50 µm ($\sim 3\lambda_p$).

It has to be noted that all macro-particles (corresponding to the sixth and seventh nitrogen electrons) in the box are tracked meaning that those expelled from the accelerating region as well as those that would have a divergence too big to be detected on a Lanex screen far away from the interaction region are also present in the histogram (e.g. electrons at top and bottom boundary in panel 8 of Fig. 4.39).

To see the impact on the injection process caused by the pulse separation in $y$-direction, the time evolution of simulation 10 (pulses on parallel paths apart by 30 µm) is shown in Fig. 4.41. The injector ionises nitrogen electrons and guides them in its own wakefield for a short amount of time. Of those electrons only a small number is trapped in the drive wakefield at the bottom edge of the region shown.

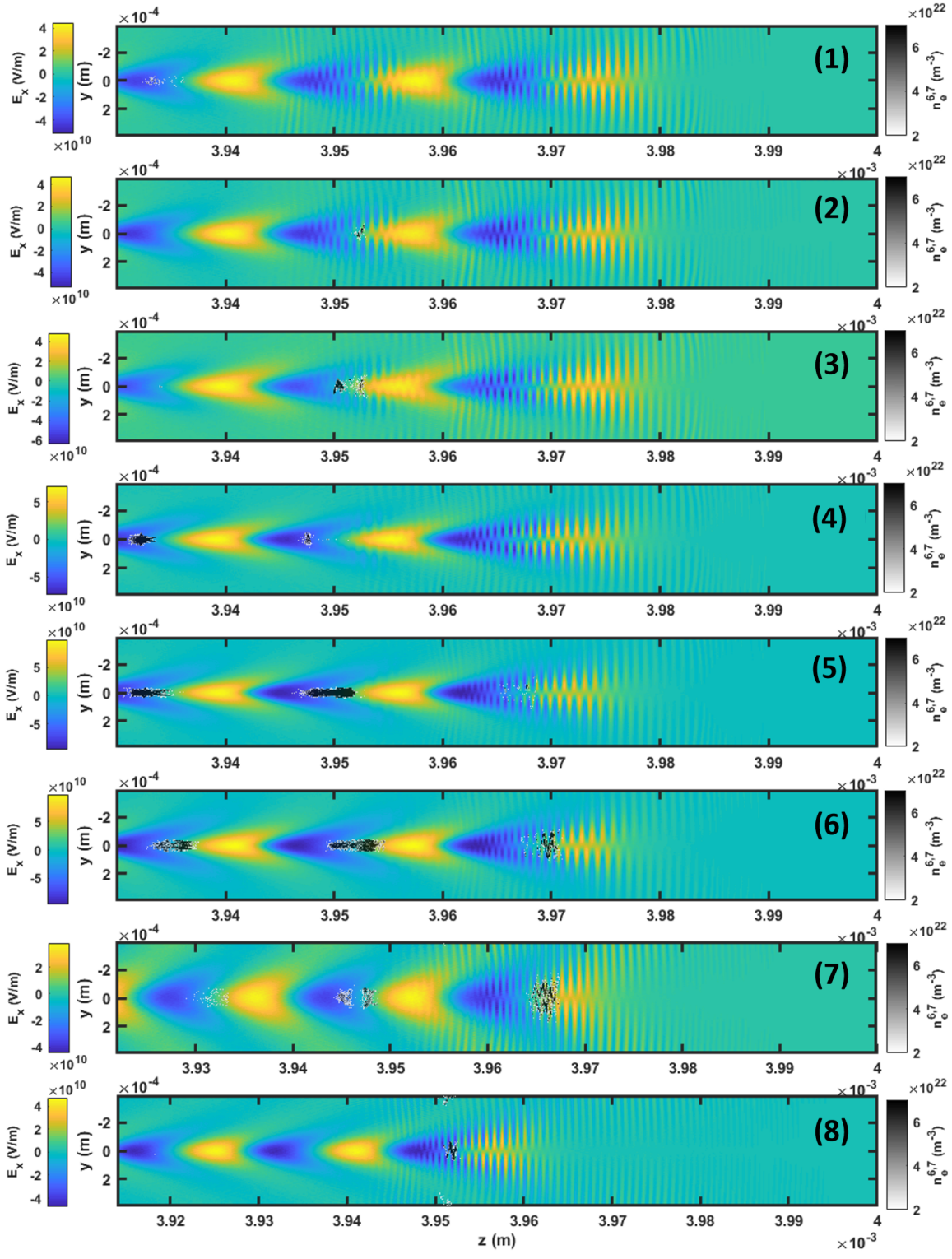



Figure 4.39: This figure shows the longitudinal electric field $E_x$ and the number density (above $2 \times 10^{22}\,\mathrm{m}^{-3}$) of the sixth and seventh nitrogen electrons after 4 mm of propagation (corresponding to 13.3 ps) obtained from PIC simulations. The separation in $z$ between the pulses was $1.25\lambda_p$ (simulation 1), $\lambda_p$ (2), $0.75\lambda_p$ (3), $0.5\lambda_p$ (4), $0.25\lambda_p$ (5), 0 (6), $-0.5\lambda_p$ (7), and $-\lambda_p$ (8).

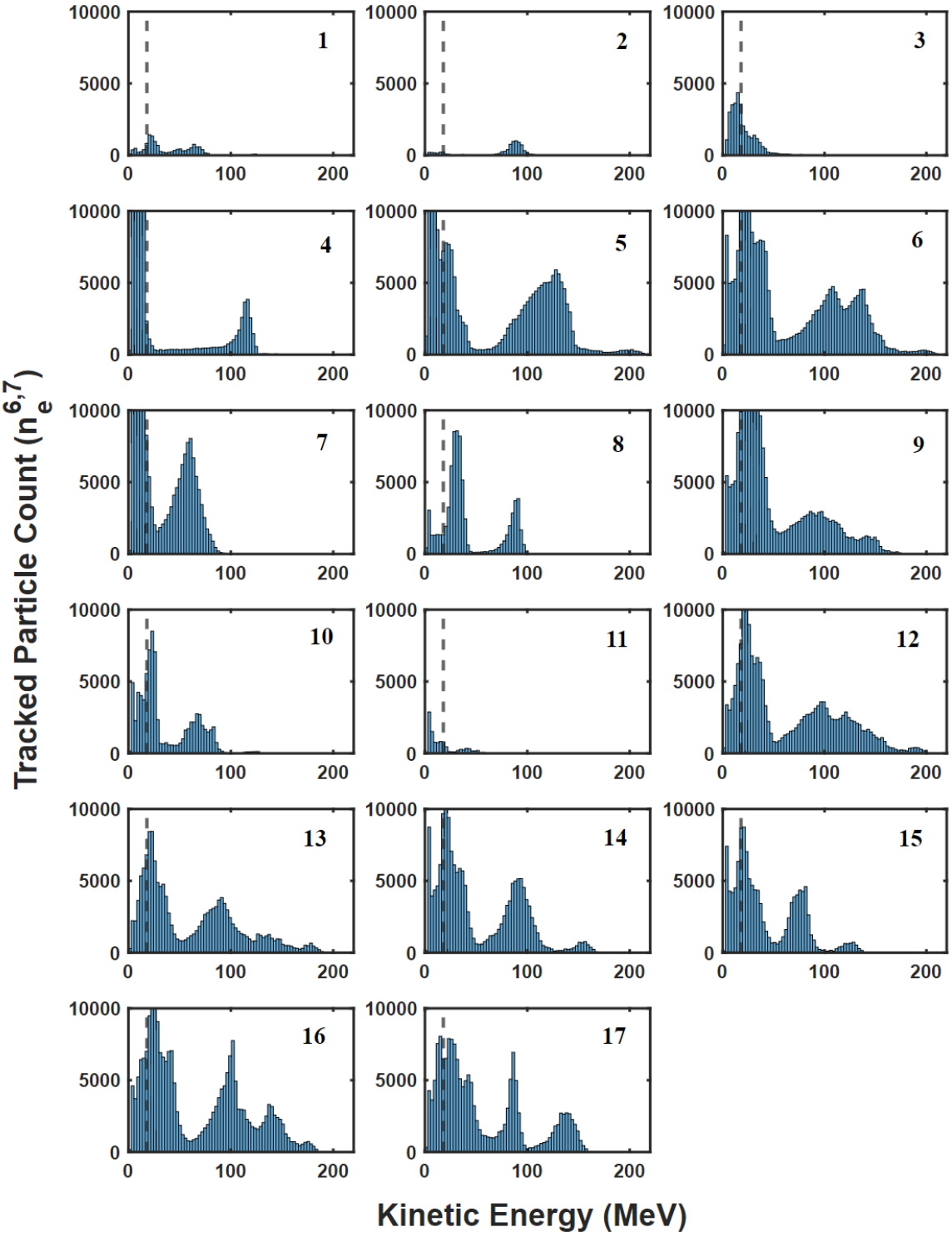



Figure 4.40: This figure shows the kinetic energy of the sixth and seventh nitrogen electrons within the PIC simulation box. The simulation parameters corresponding to each panel are listed in Tab. 4.5. The dashed vertical line corresponds to the detection cutoff in the experiment at $\approx 19\,\mathrm{MeV}$. The data was taken after 13.3 ps.

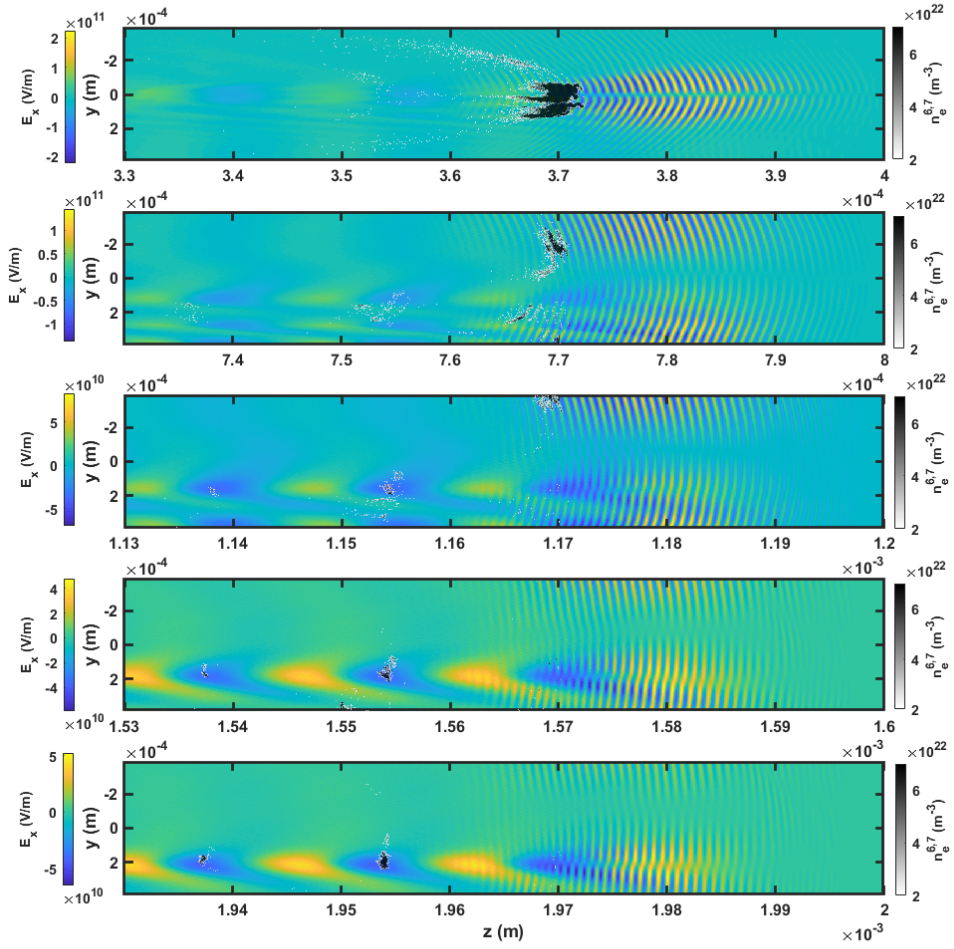



Figure 4.41: This figure shows the longitudinal electric field $E_x$ and the number density (above $2 \times 10^{22}\,\mathrm{m}^{-3}$) of the sixth and seventh nitrogen electrons for 5 time steps (1.3 ps, 2.7 ps, 4.0 ps, 5.3 ps, 6.7 ps) of simulation 10 where the drive pulse's $y$-position is shifted by 30 µm. Shown is the central region of the simulation box.

This observation supports the experimental data showing that trapping can occur even for significant jitter on the order of a spot size.

The peak energy and the charge injected into each wakefield for all simulations are plotted in Fig. 4.42. Both values are largest for pulse delays close to perfect overlap. Similar to the observations in the experiment, electrons are injected over a wide pulse delay interval (more than one plasma wavelength $\lambda_p \approx 16\,\mu\text{m}$) which is against the predictions brought forward in the 2PII paper [57].

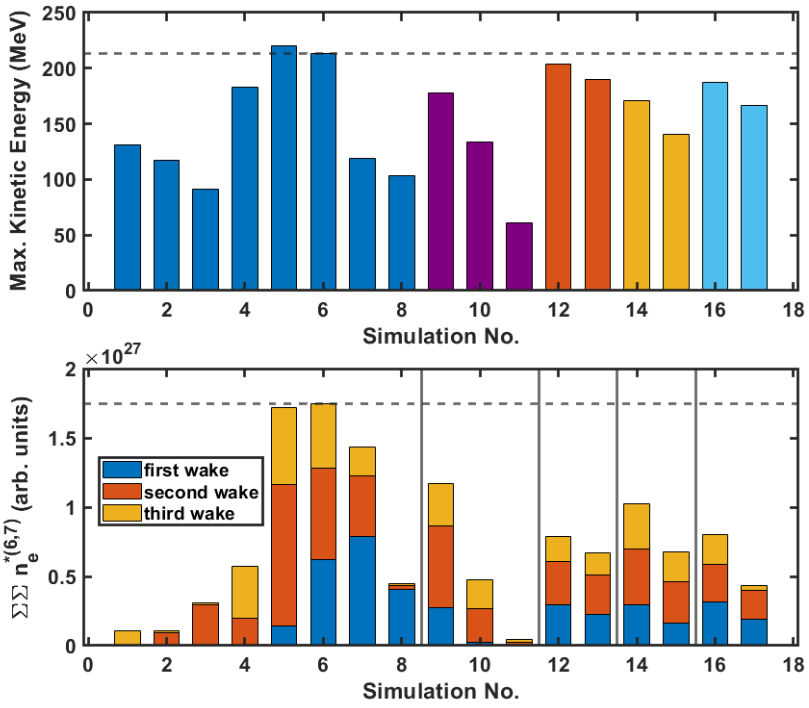



Figure 4.42: This figure shows the maximum kinetic energy of trapped particles and their particle density from PIC simulations. The colours in the top panel indicate the different parameter scans while the horizontal dashed line shows the comparison value of simulation 6. The bottom panel shows the particle number (sum over density) of the sixth and seventh nitrogen electrons within the wakefield region for all three wakes (stacked) seen in the simulations. Again, the dashed horizontal line shows the comparison value of simulation 6. The vertical lines separate the parameter scans. The numbering of the wakes is done from the drive pulse position. The third wake in simulation 17 is cut off due to the increased wave length at low density artificially reducing the charge. Note that the macro-particle density is directly proportional to the real density as all macro-particle weights of the studied species were found to be exactly equal in the simulations.

## 4.3 Conclusion

The results presented in this chapter are a first step towards decoupling the injection and drive process using two co-propagating pulses of the same wavelength for low energy-spread electron beam generation. Mono-energetic beams were observed using a circularly polarised injector pulse. There was a region of pulse delay (separation) between injector and driver in which particles were injected. Outside of this region injection was suppressed. The results do not give a clear indication of whether the 2PII mechanism of [57] was found as the injection region seems to be too broad in Run I but narrow enough in Run IV (which had a slightly higher average density, higher amounts of nitrogen dopant and linear instead of circular polarisation). The results indicate that the injection mechanism is indeed a two-pulse effect. Electrons are injected even when the drive pulse has a strong spatial jitter of one to two drive beam FWHMs as seen in the experiment and simulations. The reason for this effect could be a combination of guiding of the injector pulse in the drive pulse wakefield, injection from one injector lobe outside the focal region, and the evolution of a combined wakefield driven by both pulses during the injection period which then evolves into a wakefield mainly driven by the drive pulse (as seen in the simulations which start close to focus).

While the simulations in the 2PII Letter by Bourgeois *et al.* achieve energy spreads of $\Delta E/E = 2\%$, the experiments in this thesis only achieve spreads as low as $\Delta E/E = 7\%$ in the optimal case. The simulations conducted in this thesis which try to replicate the experimental conditions produce an energy spread of $\Delta E/E = 9\%$ which is even larger than the experimental observation. The 2PII article shows accelerated electrons of $E = 370\,\mathrm{MeV}$ after a distance travelled of $z = 6.4\,\mathrm{mm}$. After propagating $z = 3.6\,\mathrm{mm}$ the electrons have an energy of around $E = 250\,\mathrm{MeV}$ which is on the higher spectrum of—but comparable to—what is found in the experiment presented here (where the acceleration length was $z \leq 4\,\mathrm{mm}$) as was shown in Fig. 4.21. The normalised emittance (which was $\epsilon_{\mathrm{n,rms}} = 5\,\mu\mathrm{m}$ at the point of minimal energy spread in the 2PII Letter) was not retrievable in the experiment because no diagnostic measured the perpendicular momentum. The emittance calculated from the simulations presented in this chapter was $\epsilon_{\mathrm{n,rms}} = 9.8\,\mu\mathrm{m}$ at pulse separation of one plasma wavelength if electrons in both buckets are considered and $\epsilon_{\mathrm{n,rms}} = 3.7\,\mu\mathrm{m}$ if only electrons in the first bucket are considered.

The simulations show that higher quantities of charge are captured in the wakefield if the two pulses are closer together. The only single bunch with narrow energy

spread, however, is found at a laser pulse separation of one plasma wavelength. My interpretation of this result is that the pulse overlap is small at a separation of $\lambda_p$ which prevents self-focusing of the injector pulse due to increased local intensity and, therefore, prolonged ionisation injection. If the intensity increases beyond a certain level, electrons can also be trapped in subsequent wakes creating several electron bunches. Furthermore, when the pulse overlap is larger (smaller separation between pulses) the injector can be partially guided in the low-density part of the wakefield further increasing the effect of prolonged injection.

To get a better understanding of how to tune and optimise the electron beam properties, further experiments should be conducted with strong emphasis on a better injector focal spot quality and intensity control, more precise timing measurement between the two pulses and an on-shot jitter diagnostic which measures the pointing fluctuations closer to the actual focal spot than what was achieved in this present experiment.

# Chapter 5

# Reinforcement learning-based laser alignment system

Laser beam alignment is a time-consuming task for many experimental physicists and across many other disciplines which make use of laser beams. While this particularly applies to dedicated laser experiments at high power laser facilities, a myriad of experiments use laser beams as diagnostics rather than as drivers. In all these applications, there is an alignment task performed before each experiment can be initiated which can take up a significant portion of the total duration of the experiment. The alignment also has to be preserved over the duration of the experiment to achieve reliable results. This is difficult due to possible drifts of the laser beam position which may be due to changes in environmental conditions such as pressure, temperature or (unintentional) human interaction.

Experimental parameters can be controlled manually or by a problem-specific pre-programmed optimisation routine. Another possible method that has received increased interest recently is to make use of machine learning (ML) techniques. Examples for ML control in experiments can be found for a broad range of topics such as the creation of Bose-Einstein condensates [233, 234], wakefield acceleration [235, 236], and free-electron lasers [237], just to name a few. Furthermore, in 2021, an article was published that implemented an ML alignment system for coupling a laser beam into an optical fibre using custom-built components [238].

ML techniques have both advantages and disadvantages compared to other methods which have to be carefully considered when choosing the optimal optimisation procedure. For example, they may offer a solution even if the underlying physical model is not well understood. On the other hand, lengthy training processes outweigh the benefits if a solution can be obtained in a different manner.

In this chapter, I investigate a novel approach to beam alignment using reinforcement learning (RL) techniques and present a flexible model that can be applied to various environments. Major advantages of the RL system are that

- it learns to reach the objective even if the beam has left the field of vision,
- it works with motors that do not have an encoder and are prone to hysteresis[1],
- optical components can be moved and the model can be retrained without reprogramming an optimisation routine,
- it enables live online optimisation without human access to the experimental setup.

The idea for this project came during the planning stage of the 2PII experiment (see Chapter 4) when the difficulties of stable off-axis parabola (OAP) alignment were considered. While it would have been useful to implement this system at the HERCULES campaign, COVID-19 related travel restrictions made this part of the experiment infeasible given the limited on-site preparation and set up time available.

This chapter is split into three main parts: a brief introduction to RL and two experimental sections which show the implementation of RL algorithms for the alignment of a Mach-Zehnder interferometer and an OAP.

## 5.1 Introduction to reinforcement learning

Machine learning (ML) allows systems controlled by some form of artificial intelligence to improve in solving a specific task after gaining experience. Typically, ML can be divided into different sub-methods according to the structure of the training data and the way this data is presented.

- **Supervised learning** (SL): learning using data which is labelled by an external agent (supervisor) to detect features and label new data accordingly to what has been learned. This technique is used for tasks such as the detection of features like boundaries in images [239].

[1]This feature makes it difficult to use popular methods such as Bayesian optimisation with Gaussian processes which would require knowledge of the input to the function which is being optimised.

- **Unsupervised learning** (UL): learning to find (hidden) features in unlabelled data. This technique can be used to classify data without the necessity for costly labelling of data by humans. UL has applications in tasks such as detection of anomalies [240] or speech recognition [241].

- **Semi-supervised learning** (SSL): learning from both, labelled and unlabelled data combining the SL and UL approaches to ML.

- **Reinforcement learning** (RL): learning from interacting with an environment and receiving a reward for an action taken by the RL agent. RL has gained much attention through beating humans at games such as Atari computer games [242], real-time strategy computer games [243], or even excelling at chess and go [244, 245].

Often, the above-mentioned methods are performed in the framework of Deep Learning (DL) in which artificial neural networks (ANN) are used to perform certain computational tasks as will be discussed later. ANNs consist of nodes typically arranged in interconnected layers such that a node in layer $i$ is connected to nodes in layers $i-1$ and $i+1$ but not connected to other nodes in layer $i$. The transition from the input layer to the output layer is task-agnostic and the process of "learning" is emulated through iteratively updating the weights associated with the connection between two nodes.

The basic structure of an RL algorithm which describes how an agent (which uses a specific model) interacts with an environment is shown in Fig. 5.1. The interpreter[2] is a method which performs an observation from which it draws the current state of the environment (which is a set of parameters necessary to describe the environment in a task-specific manner). The interpreter also computes the reward associated with the current state and passes them both to the agent. The agent uses this input to update its model[3] from which it then draws a conclusion about which action to take next in order to solve the task set to the agent in a specific manner. Technically speaking, the agent does not "know" what solving the task means and is, therefore, usually programmed to maximise the future cumulative reward, also called "return"[4].

Often, the decision-making process solved in RL is a Markov Decision Process (MDP) which was studied by Bellman [246]. An MDP is an iterative discrete process

[2]The interpreter is often viewed to be part of the environment and not depicted as a separate object.

[3]The terms "agent" and "model" are often used interchangeably.

[4]The return at step $t$ can be defined as $R_t = \sum_{k=1}^{k_{\max}} r_{\mathrm{t+k}}$.

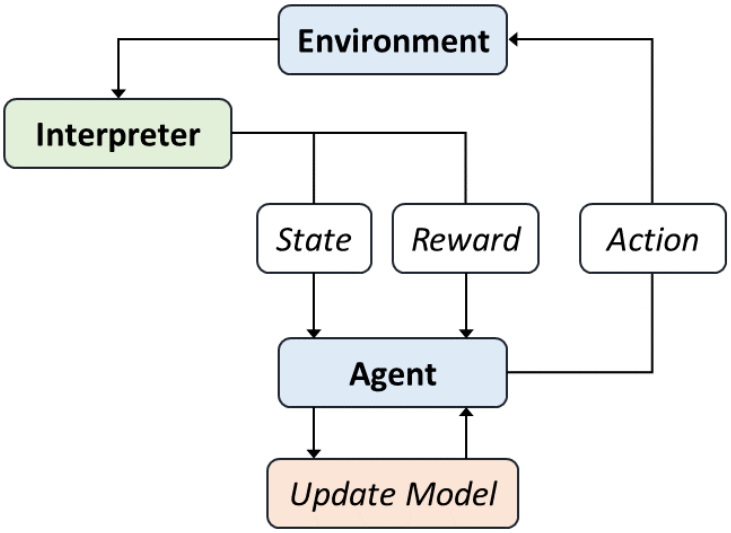



Figure 5.1: This schematic shows the reinforcement learning flowchart in which an agent interacts with an environment through actions which change the state and the associated reward which are passed on from the environment by an interpreter method.

that can be described by a 4-tuple $\{\mathcal{S},\ \mathcal{A},\ \mathcal{P}^a_{s,s'},\ \mathcal{R}^a_{s,s'}\}$ of state space $\mathcal{S}$ (set of all possible states at iteration t), action space $\mathcal{A}$ (set of all possible actions at iteration t), transition probability $\mathcal{P}^a_{s,s'}$ (probability to transition from state $s = s_t$ to state $s' = s_{t+1}$ through taking action $a = a_t$), and expected (mean) reward $\mathcal{R}^a_{s,s'}$ (expected reward acquired from transitioning from state $s = s_t$ to state $s' = s_{t+1}$ through taking action $a = a_t$). An important property of an MDP is that all future quantities are independent of the step $t - 1$ or any steps before that.

One possibility to enable an RL agent to update its decision making process (to "learn") is through *Q-learning* which is a method associated with solving the Bellman equation

$$Q_{t+1}(s,a) = \mathbb{E}_{s'}[r + \gamma \max_{a'} Q_t(s',a')|s,a]\ , \tag{5.1}$$

where r is the immediate reward, $\gamma \in [0,1]$ is the discount factor, and $\mathbb{E}$ is the expected return operator. The action $a'$ is chosen such that $Q_t$ is maximised. The eponymous $Q$ is a state-action value function describing how large the expected return is when taking an action $a$ from state $s$ following policy $\pi$:

$$Q^\pi(s,a) = \mathbb{E}_\pi[R^*_t|s_t = s, a_t = a] = \mathbb{E}_\pi[r_{t+1} + \gamma \sum_{k=1}^{k_{\max}} \gamma^{k-1} r_{t+k+1}|s_t = s, a_t = a]\ . \tag{5.2}$$

Here, $R^*$ is the discounted return. Practically, the state-action space will in many cases become too large for each Q-value to be stored as a matrix entry. A method tackling this problem is the "Deep Q-Network" (DQN) in which a nonlinear function approximator is used to approximate the action-value function. In the first implementation of a DQN which included experience replay and a target network by Mnih *et al.* [247] the optimal Q-values $Q^{opt}(s', a')$ were replaced by the approximations $Q(s', a', \theta_i^-)$ which are extracted from the last neural network layer. Here, $\theta_i^-$ are parameters from previous iterations.

Another approach to select an optimal action can be found in policy gradient (PG) methods in which the action is obtained directly from a (stochastic) map from state space rather than through the maximum Q-value. PG methods utilise an independent function approximator whose parameters are updated according to the gradient of the policy's performance with respect to the policy's parameters (following the gradient of future reward) [248]. However, there exist large plateaus of small gradients making the algorithm inefficient. Building upon this approach, it can be shown that a "natural" gradient method in which a metric based on the policy structure is used represents the optimal descent direction for the PG [249]. PG methods can have superior convergence properties because the problem of errors in the value function propagating to the policy (causing a resonant oscillation feature) is evaded.

In this work, both Q-functions and PGs were used for different problems to show their respective advantages. A DQN was implemented using *Tensorflow*'s sequential model layer API which used experience replay and a target network. Experience replay allows for saving data sets from previous steps from which a "mini-batch" is sampled and used for more efficient training. The target network implementation uses a second network which is updated after a certain amount of episodes which helps the stability of the learning process and prevents divergence of the non-linear function approximator [250]. While describing the equations solved by this network would be beyond the scope of this thesis, it is important to note that the hidden layers used an "relu" (Rectified Linear Unit) activation function which modifies the nodes' values through an operation $f(x) = \max(0, x)$. Furthermore, the network used an "Adam" optimizer [251] which is a stochastic gradient descent method which optimizes the training procedure.

Further to the DQN method, I implemented a Natural Actor-Critic (NAC) PG algorithm which uses the least-squares method to estimate the natural gradient. This NAC method consists of two distinct steps for the evaluation of the policy (performed by the "critic") and the improvement of the policy (performed by the "actor") which

allows efficient use of the memory of past experiences. An NAC agent models probabilities of actions which means it can learn stochastic policies. Therefore, unlike the DQN, the NAC algorithm used is not $\epsilon$-greedy[5]. This property reduces oscillations or divergence from an optimal value function (assuming continuous function approximation) [252].

## 5.2 Alignment of Mach-Zehnder interferometer arms

The Mach-Zehnder interferometer (MZI) uses two beam splitters to separate and recombine a coherent beam to measure a relative phase shift between the two "copies" of the incoming beam. The split parts of the beam have to be aligned such that after recombination at the second beam splitter they overlap and are parallel. This can be verified by two measurements - one after co-propagating over a short distance and the other over a long distance. If the relative position has not changed from one measurement to the other both interferometer arms are well aligned. Perfect alignment leads to perfect superposition of the beams which means that one of the two paths after the second beam splitter has no photons and the other one all photons. However, a slight misalignment leads to interference fringes which are generally sought for when measuring for example plasma-induced phase shifts (as seen in the previous chapters).

In this section, I will describe the experimental setup, the specifics of the RL code that was written to perform the experiment, the training procedure, and the results of testing the trained model.

### 5.2.1 Experimental implementation

In practice, an MZI can be aligned using shutters which block either arm of the interferometer so that no fringes can be detected. The goal is then to move the beam onto a specific position on two camera screens – one in the near field (NF) and one in the far field (FF). Repeating this procedure for the second arm, which was blocked by the shutter, will ultimately lead to a well-aligned interferometer because the two beam "copies" co-propagate on the same path. As the process is equivalent for both interferometer arms, I have only trained one in this chapter. This means that effects

[5]This means that there is an exploration and exploitation involved in the algorithm. The former leads to a random action while the latter uses an action determined by some function which estimates which action will be optimal in a given case.

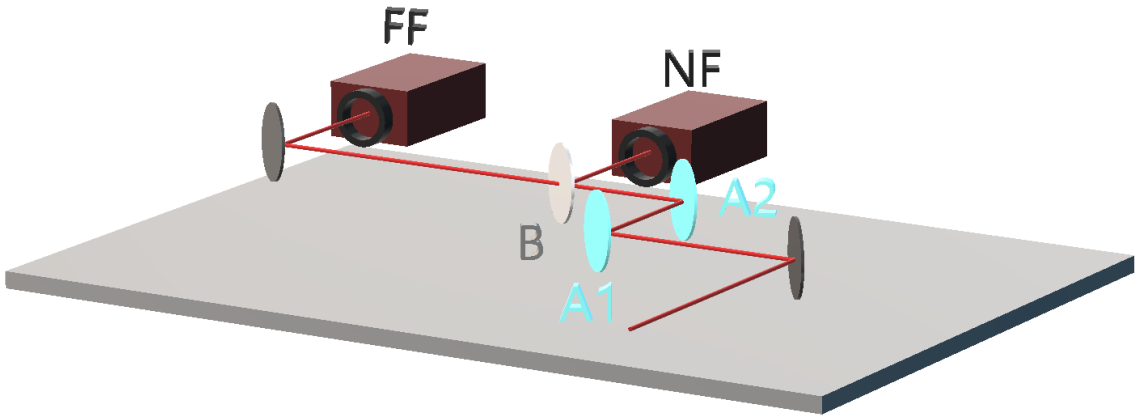



Figure 5.2: This schematic shows a schematic of a set-up of one arm of a Mach-Zehnder interferometer in which component A1 is a beam splitter (in this one-arm set-up acting as a mirror), A2 is a mirror and B is a beam splitter. The yaw and pitch of components A1 and A2 can be remotely controlled using motorised actuators. The laser beam is split at B and is incident onto the near field (NF) and far field (FF) cameras to produce an image from which the laser beam positions (the *observation*) are measured.

such as fringe spacing are not studied. A schematic of the set-up for a single arm is shown in Fig. 5.2.

#### 5.2.1.1 Reward

The reward calculation in RL is very problem-specific and crucial for finding an optimal policy that can solve the task which is set to the agent. In this section, the reward $r$ is calculated from the distance of the beam's centre $[x, y]$ to the centre of the respective screen $[x_0, y_0]$

$$r = -\sum_{k\in\{\mathrm{NF,FF}\}} \sqrt{(x_k - x_{0,k})^2 + (y_k - y_{0,k})^2} \tag{5.3}$$

where the index $k$ runs over the near field (NF) and far field (FF) cameras. In this work, the agent did not learn from raw camera images but rather from processed data (see Section 5.2.1.2) allowing a smooth transition of a simulation-trained model to an experimental implementation.

A cutoff value $L$ was introduced for the reward function. Once $r > L$ was satisfied, the model had reached its objective. Upon successful completion, the training run ("episode") ended and an (optional) extra reward was given to the agent. The reward (eq. 5.3) was chosen to be negative so that the agent had an incentive to successfully accomplish the task before the maximum number of steps per episode was reached.

#### 5.2.1.2 Image processing using computer vision

The algorithm which takes the raw image from the camera and returns the observation as well as a boolean (describing whether the beam is on or off the screen) uses functions from the **cv2** [253] library to process the data. First, the image is converted to grey-scale. Then, a Gaussian blur (using a $5 \times 5$ pixel kernel) is applied to the image using **cv2**.*GaussianBlur()* to flatten noise. The next step is to compute the maximum and minimum intensity (brightness) level using the **cv2**.*minMaxLoc()* function. From the maximum value, the cutoff threshold is calculated using a pre-defined factor between 0 and 1. This threshold is used to determine which pixels to discard (below threshold) and which to keep (above threshold) when determining the shape, size and position of the beam. Using **cv2**.*erode()* and **cv2**.*dilate()*, unwanted isolated pixels are removed from the mask. From this mask a contour is drawn using **cv2**.*findContours()* where the **cv2**.RETR_EXTERNAL and **cv2**.CHAIN_APPROX_SIMPLE flags are used[6]. Next, it is checked whether the beam is on or off-screen. Due to the intensity re-scaling of the camera when the laser hit the boundary a method had to be implemented that did not depend on absolute values to perform the check. Therefore, a set of conditions was introduced that had to be satisfied to distinguish whether the beam was off-screen:

- $$\ln\left(\frac{max + \upsilon}{min + \upsilon}\right) < \Upsilon_1 \ , \tag{5.4}$$

- $$min < \Upsilon_2 \quad . \tag{5.5}$$

In equation 5.4, a small value $\upsilon = 0.1$ was introduced to avoid numerical instabilities. $\Upsilon_1$ was found through trial and error and was set to a value of 2.5. The constant $\Upsilon_2$ was, again, found through experimental trial and set to be 10.0. If the beam was on-screen the observation (centre of the contour) was returned.

#### 5.2.1.3 Equipment

The raw images were detected using Allied Vision Marlin F-033 cameras which were connected to the computer using a PCI Express Firewire card and controlled through a Python wrapper for Allied Vision's Vimba C API [254]. Mirrors A1 and A2 were mounted in Newport 8822-AC piezo actuator driven mirror mounts with a 0.7 µrad angular resolution, connected to the PC via an 8742-4-KIT four-axis controller which

[6]These flags disable the detection of any inner contours which could be encircled by outer contours and avoid storing superfluous data to draw the contour, respectively.

received commands via a Python script. The laser used was a Helium-Neon laser (continuous wave at $\lambda_0 = 633\,\text{nm}$) with 5 mW output power.

### 5.2.2 Training the model

The training routine is shown in Alg. 1 as pseudo-code. There are two nested loops (outer loop over all episodes and inner loop over all steps). The outer loop is stopped when the maximum amount of pre-defined episodes is reached and the inner loop is stopped when either the current episode was successful or the maximum amount of steps per episode was reached. In this work an "$\epsilon$-greedy" routine was used in which the likelihood of random exploration to find the best policy decays exponentially with increasing episode count.

Whenever the beam left the observation screen, the observation value was set to a specific pre-defined value $[x_{\text{OFF}}, y_{\text{OFF}}]$. Fig. 5.3 shows a possible scenario in which the beam is on screen A but off screen B. The red "+" markers show the observation values passed on to the agent while the yellow "+" markers show the screen centres from which the reward is calculated in Eq. 5.3.

In the simulation environment used for training (described in Section 5.2.2.1), a virtual screen threshold was introduced above which the observation was automatically set to the pre-determined off-screen values. This was done to train the model in a manner which can be easily transferred to the laboratory set-up. Therefore, there can be a difference in laser position and observation on screen (B) as shown in Fig. 5.3.

In this work, a target network [247] was used which was updated every $U$ episodes. This means that, even though the learning network is updated every step, the network weights will only be copied to the executing (target) network after $U$ episodes. This method helps with stabilising the learning progress through minimising correlations with the target network values.

#### 5.2.2.1 Simulation environment

The two mirror set-up is trivial to simulate as it only requires trigonometric operations and knowledge of the mirror angles and distances between components. Defining

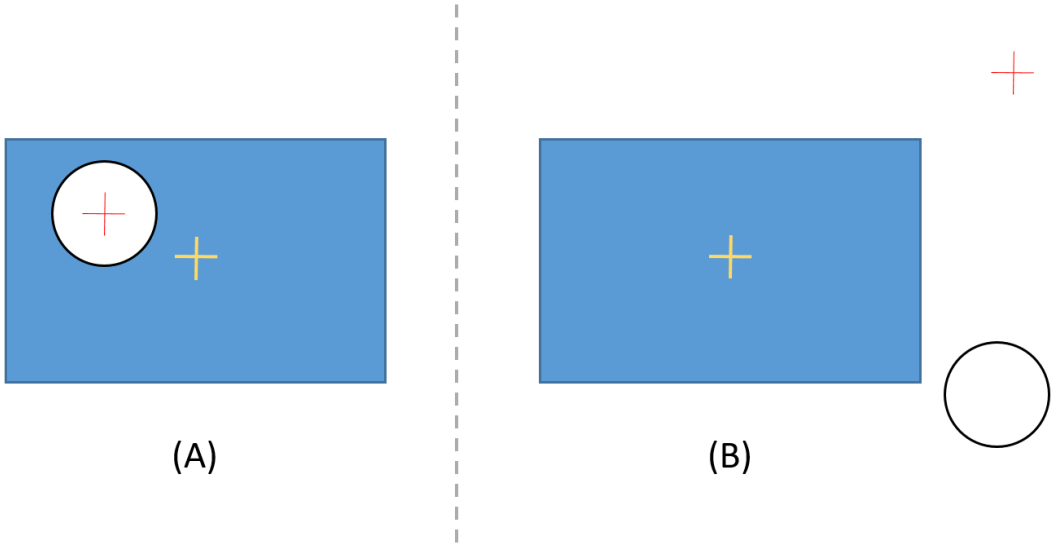



Figure 5.3: Illustration of a possible observation on near field camera (A) and far field camera (B). The yellow "+" marks the centre position of the screen and the red "+" marks the position from which the interpreter takes the observation data values. The black circle symbolises the laser beam position on (or next to) the screen.

**Algorithm 1** Pseudo-code of reinforcement learning procedure.

$\Theta \in ]0, 1[$
**while** (i $\leq$ N_EPISODES) **do**
  state $\leftarrow$ *get_state*()
  **while** (n $\leq$ N_STEPS) **and** (done = **false**) **do**
    **if** *random*$(0, 1) > \Theta^{n}$ **then**
      take action from Q − value approximator [according to observation/state]
    **else**
      take random action
    **end if**
    new_state $\leftarrow$ *get_state*()
    reward $\leftarrow$ *compute_reward*(new_state)
    done $\leftarrow$ *is_done*(new_state)
    memory $\leftarrow$ *append_memory*(state, new_state, action, reward)
    **if** (memory_size > MIN_MEMORY_SIZE) **then**
      *train_network*(random_selection $\subseteq$ memory) using the **tensorflow.keras** library
      **if** (mod(i, UPDATE_EVERY) = 0) **then**
        target_model_weights $\leftarrow$ model_weights
      **end if**
    **end if**
    state $\leftarrow$ new_state
  **end while**
**end while**

$z_1$ ... distance between first mirror (A1) and second mirror (A2) ,
$z_2$ ... distance between A2 and beam splitter (B) ,
$z_3$ ... distance between B and the near field screen (NF) ,
$z_4$ ... distance between B and the far field screen (FF) ,
$t_{i,0}$ ... tilt about the i-axis of the incoming beam ,
$t_{i,1}$ ... additional tilt from misalignment of A1 ,
$t_{i,2}$ ... additional tilt from misalignment of A2 ,

the x and y positions on each screen (set of observations) can be computed using

$$\begin{pmatrix} x_{\mathrm{NF}} \\ y_{\mathrm{NF}} \\ x_{\mathrm{FF}} \\ y_{\mathrm{FF}} \end{pmatrix} = C_1 \begin{pmatrix} z_1 \sin\left(C_2(t_{x,0}+t_{x,1})\right) + (z_2+z_3)\sin\left(C_2(t_{x,0}+t_{x,1}+t_{x,2})\right) \\ z_1 \sin\left(C_2(t_{y,0}+t_{y,1})\right) + (z_2+z_3)\sin\left(C_2(t_{y,0}+t_{y,1}+t_{y,2})\right) \\ z_1 \sin\left(C_2(t_{x,0}+t_{x,1})\right) + (z_2+z_4)\sin\left(C_2(t_{x,0}+t_{x,1}+t_{x,2})\right) \\ z_1 \sin\left(C_2(t_{y,0}+t_{y,1})\right) + (z_2+z_4)\sin\left(C_2(t_{y,0}+t_{y,1}+t_{y,2})\right) \end{pmatrix} . \quad (5.6)$$

$C_1$ and $C_2$ are factors to account for conversion from real distance to pixels on screen or to angle, respectively. The simplicity of this "simulation" approach makes computing the result of the observation very time efficient. This simulation environment is used to train the agent using the methods below.

#### 5.2.2.2 Deep Q-Network (DQN)

The model can be trained using different parameters for the deep neural network structure and the reinforcement learning framework. It is possible to train the model on a standard PC or laptop. The runtime primarily depends on training parameters such as number of episodes $N_{\mathrm{EPISODES}}$, number of steps per episode $N_{\mathrm{STEPS}}$ (and, hence, implicitly success rate which depends on parameters such as decay rate and initial exploration parameter $\epsilon$), memory size, network structure and laser initialisation radius[7]. A model using $2.5 \times 10^4$ episodes with 100 steps per episode took approximately 8 hours to train using the simulation environment.

Fig. 5.4 shows training data for a model trained using parameters shown in Tab. 5.1. The exploration parameter $\epsilon$ decays as $\epsilon_{s+1} = \epsilon_0 \Theta^i$, where $\epsilon_0$ is the starting value of $\epsilon$ at the first episode, $\Theta$ is the decay exponent and $i$ is the episode. With a probability of $\epsilon$ the action taken at each step is random rather than taken from the function approximator. The reward accumulated over each episode increases quickly and starts to converge to an optimal value at around 2500 episodes. One notes that, at this point, still more than half of the actions are random. This is also the point at which training speed increases significantly due to the decreased number of steps needed to reach the success condition after which the episode is terminated. In what follows the trained model is referred to as *DQN2M*.

[7]This is the radius within which the centre of the laser beam can be initialised – not the radius of the laser beam.

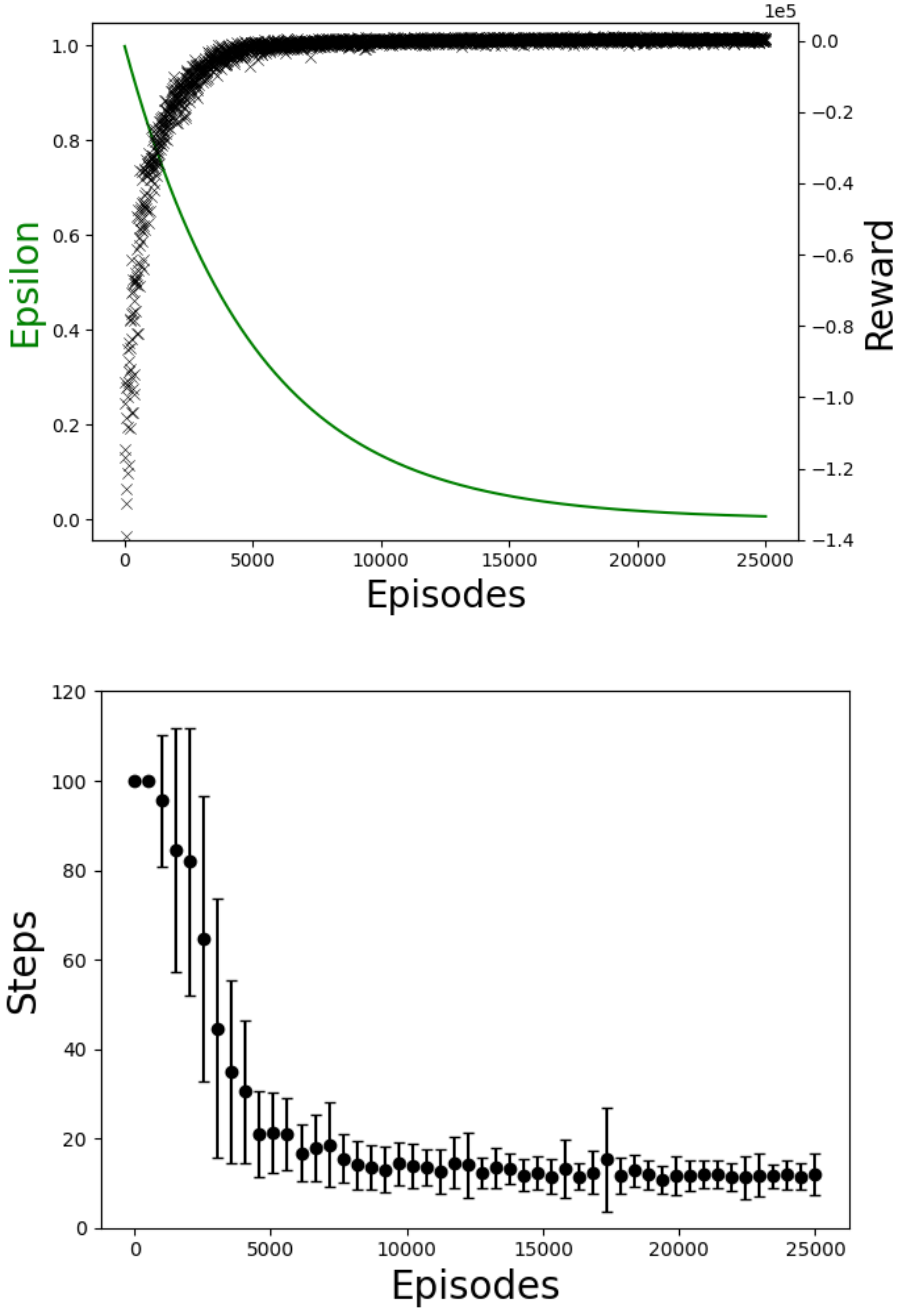



Figure 5.4: This figure shows data from training the *DQN2M* network using a simulation. The top panel shows the $\epsilon$ exploration value and the training reward (summed over all steps of the current episode) plotted against the training episode. The bottom panel shows the number of steps it took the network to finish each episode. The results are averaged over 500 episodes with standard deviation bars shown. The maximum amount of steps per episode was 100 after which the training was stopped.

| Parameter | Description | Value |
|---|---|---|
| $\gamma$ | Discount | 0.97 |
| $\eta$ | Learning Rate | 0.001 |
| S | Replay Memory Size (RMS) | $10^5$ |
| $S_{min}$ | Min RMS to start training | 5000 |
| $n_{MB}$ | Minibatch Size | 64 |
| U | Update target every | 50 |
| $N_{STEPS}$ | Max Steps per Episode | 100 |
| $r_s$ | Success Reward | 2000 |
| $N_{EPISODES}$ | Episodes | 25000 |
| $\Theta$ | Decay Exponent | 0.9998 |
| $\epsilon_{min}$ | Min Epsilon | $10^{-4}$ |
| $\chi$ | Initialisation Limit | 700 |
| $[x_{OFF}, y_{OFF}]$ | Fixed Off-Screen Position | [1000,1000] |
| LAYERS | No. of hidden neural network layers | 2 |
| NODES | Nodes per neural network layer | 25 |

Table 5.1: List of constants used for training the 2 mirror setup.

#### 5.2.2.3 Training from experiment

Training using the experimental setup is more time consuming (e.g. due to duration of motor movement or necessity for manual reset) but can produce more reliable results because every aspect of the physical process is automatically considered in the environment. The piezo actuators did not have an absolute position encoder which meant that, after each failed run, the observation had to be reset manually to $[x_1, y_1, x_2, y_2]$, where $\sqrt{x_i^2 + y_i^2} < 10$ was satisfied. For this purpose, a routine was written which stops the execution loop and jumps to the observation routine which plots the raw and post-processed camera output and prints the current laser positions to a terminal at high frequency. After realignment, the execution loop is entered at the next episode. As this method took much longer than training from the simulation and due to the success and transferability of the *DQN2M* model, the approach was cancelled after 5000 episodes (using $\Theta = 0.999$, a value smaller than what was used in the simulation environment, to see possible convergence earlier). At this point, the model did not yet show indications of solving the task sufficiently well.

### 5.2.3 Testing agent performance

The next step was to test the success of the trained agent on a real set-up. The *DQN2M* model was evaluated for three sets of parameters in which the cutoff value

$L$ and the maximal initialisation position $[x_{\text{init}}, y_{\text{init}}]$ (see equation 5.6 with $t_{i,0} = 0$ and $t_{i,1} = t_{i,2} = \chi$) were varied.

#### 5.2.3.1 Probability distribution and limits of beam initialisation

The probability distribution for the position of initialisation can be computed using a convolution $h$ of the two uniform probability distributions $f$ and $g$ (one for each mirror):

$$f_{i,\sigma}(\iota) = \begin{cases} \frac{1}{2D_{1,\sigma}\chi} & \text{if} \quad -D_{1,\sigma}\chi < \iota < D_{1,\sigma}\chi \\ 0 & \text{otherwise} \end{cases} \tag{5.7}$$

$$g_{i,\sigma}(\iota) = \begin{cases} \frac{1}{2D_{2,\sigma}\chi} & \text{if} \quad -D_{2,\sigma}\chi < \iota < D_{2,\sigma}\chi \\ 0 & \text{otherwise} \end{cases} \tag{5.8}$$

$$h_{i,\sigma}(\iota) = (f_{i,\sigma} * g_{i,\sigma})(\iota) = \int_{-\infty}^{\infty} f_{i,\sigma}(\iota - t) g_{i,\sigma}(t) dt \ . \tag{5.9}$$

Here, it was assumed that the angle $\alpha = C_2(t_{i,1} + t_{i,2})$ is small such that $\sin\alpha = \alpha$ and $\sigma \in \{\text{NF,FF}\}$ and $i \in \{\text{X,Y}\}$. The constants are $D_{1,\text{NF}} = C_3(z_2 + z_3)$, $D_{2,\text{NF}} = C_3(z_1 + z_2 + z_3)$, $D_{1,\text{FF}} = C_3(z_2 + z_4)$, $D_{2,\text{FF}} = C_3(z_1 + z_2 + z_4)$ and $C_3 = C_1C_2$ (see Eq. 5.6). Using $D_{2,\sigma} > D_{1,\sigma}$, $h_{i,\sigma}(\iota)$ can be found (see Appendix A.8) to be

$$h_{i,\sigma}(\iota) = \begin{cases} \frac{\iota + (D_{1,\sigma} + D_{2,\sigma})\chi}{4D_{1,\sigma}D_{2,\sigma}\chi^2} & \text{if} \quad -(D_{1,\sigma} + D_{2,\sigma})\chi \le \iota < (D_{1,\sigma} - D_{2,\sigma})\chi \\ \frac{1}{2D_{2,\sigma}\chi} & \text{if} \quad (D_{1,\sigma} - D_{2,\sigma})\chi \le \iota \le (D_{2,\sigma} - D_{1,\sigma})\chi \\ \frac{-\iota + (D_{1,\sigma} + D_{2,\sigma})\chi}{4D_{1,\sigma}D_{2,\sigma}\chi^2} & \text{if} \quad (D_{2,\sigma} - D_{1,\sigma})\chi < \iota \le (D_{1,\sigma} + D_{2,\sigma})\chi \\ 0 & \text{otherwise} \end{cases} . \tag{5.10}$$

To find the probability distribution on the screen $\sigma$, one can multiply the independent functions $h_{\text{X},\sigma}(x)$ and $h_{\text{Y},\sigma}(y)$ which results in a distribution $p_\sigma(x, y)$ as shown in Fig. 5.5. These limits may shift between NF and FF since $D_{1,\text{NF}}/D_{2,\text{NF}} \neq D_{1,\text{FF}}/D_{2,\text{FF}}$. The distribution can by inference be related to the screen size by setting $(D_{1,\sigma}+D_{2,\sigma})\chi$ equal to the respective initialisation limit $L_\sigma$ which can be measured for any given set-up.

A characterisation run was performed using the picomotors to measure the mapping factor between $\chi$ and the distance in pixels on screen through the change in beam position. To this end, many steps of size $\chi = 550$ were taken using all motors. The results of the travelled beam distance on screen were averaged and are listed in Tab. 5.2.

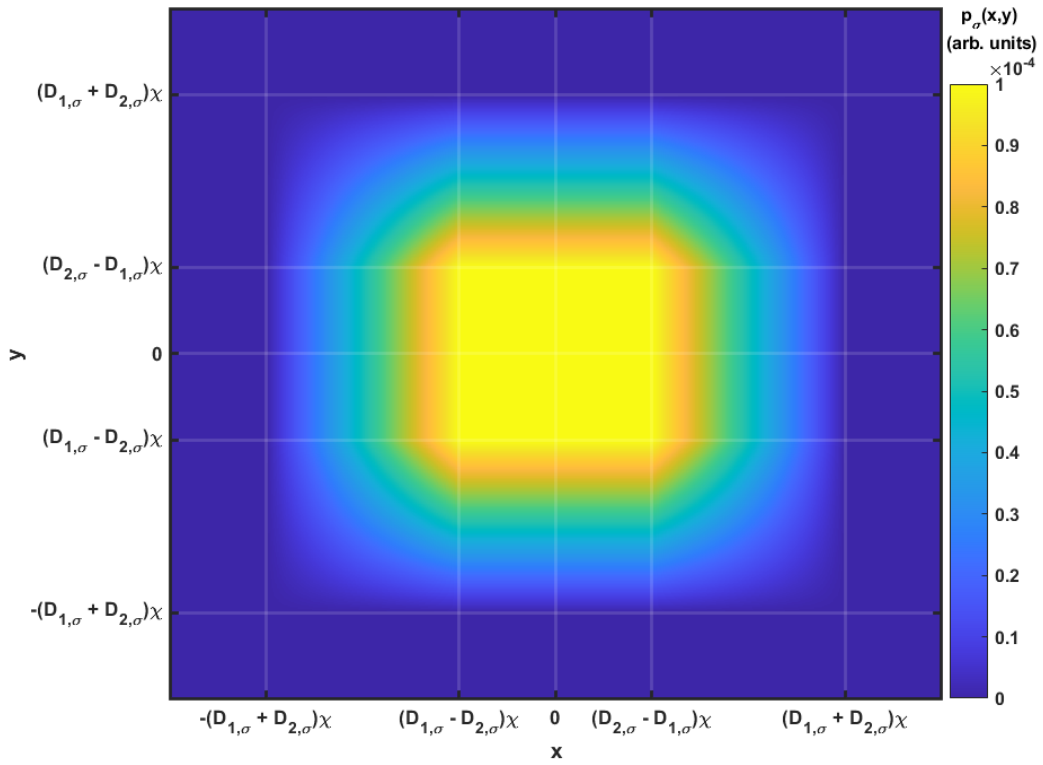



Figure 5.5: Probability density function of random initialisation.

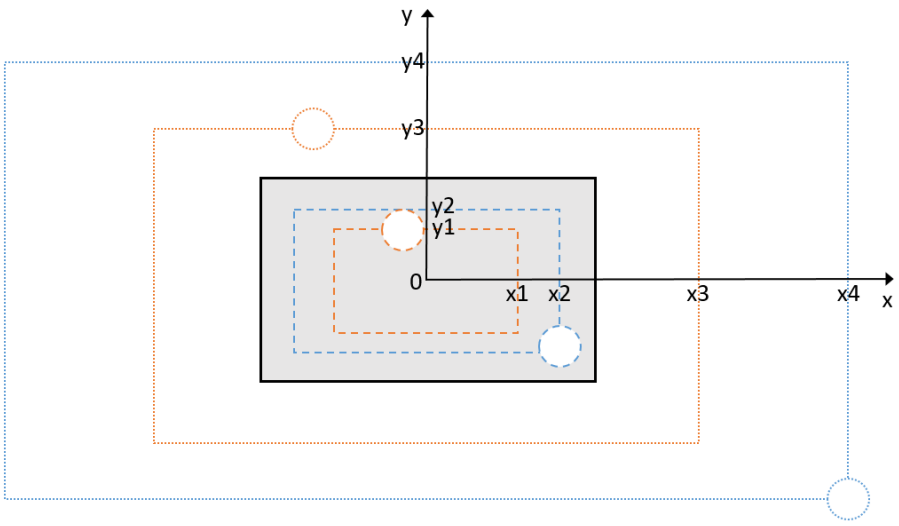



Figure 5.6: Schematic showing beam initialisation limits obtained from calibration measurements. Dotted lines represent the limit on the FF camera, dashed lines represent the limit on the NF camera. The grey area represents the respective screen size. Orange lines correspond to test sets A and B, while blue lines correspond to test set C.

| Motor | Screen | Mean | Standard Deviation |
|---|---|---|---|
| x1 | NF | 7.71 | 1.68 |
| x1 | FF | 32.23 | 6.01 |
| y1 | NF | 7.37 | 0.69 |
| y1 | FF | 34.89 | 4.91 |
| x2 | NF | 22.21 | 1.99 |
| x2 | FF | 56.95 | 4.18 |
| y2 | NF | 8.38 | 1.21 |
| y2 | FF | 22.17 | 3.01 |

Table 5.2: Measurements of mean step sizes for step size parameter $\chi = 550$. The measurements are taken after performing steps starting from the centre and going towards the respective screen boundary. The mean (in units of pixel) was taken over the amount of steps.

Using a motor initialisation parameter of $\chi = 5000$ gives displacement values (L) from the center (in pixels) of $x1 = 190$, $x2 = 272$, $x3 = 567$, $x4 = 811$, $y1 = 100$, $y2 = 143$, $y3 = 363$, and $y4 = 519$. In comparison, the positive screen limits are [320,240]. A schematic illustrating the initialisation limits $[x_{\text{init}}, y_{\text{init}}]$ with respect to the screen dimensions is shown in Fig. 5.6.

#### 5.2.3.2 Results

As mentioned above, three trials were executed where every trial consisted of a set of 100 episodes with 100 possible steps per episode before classifying the test as failed. Test set $A$ had a (reward) cutoff value of $L = -40$ and a randomisation value $\chi$ of 3500. Test set $B$ had an increased cutoff of $L = -25$ making it more difficult to satisfy the success condition and making the final state more precise. Test set $C$ had an increased $\chi = 5000$ changing the probability function and making off-screen beam initialisation even more likely.

The results of the three test runs are shown in Fig. 5.7. The model had a success rate of 100% for all three sets. As expected, the average number of steps per episode was lowest (19.81) in $A$ due to the beam initialisation closer to the centre and less restrictive cutoff condition. There was an increase in the average number of steps in $B$ (25.13) and $C$ (23.60). The ($1\sigma$) standard deviations are 7.58 ($A$), 7.55 ($B$), and 7.41 ($C$). The maximum value of steps over all episodes is 44.

These results show that the model trained in the simulation environment can be used successfully on an imperfect system in which step sizes vary and the incoming angle may be different. It is noticeable, that the agent has learned that there is a

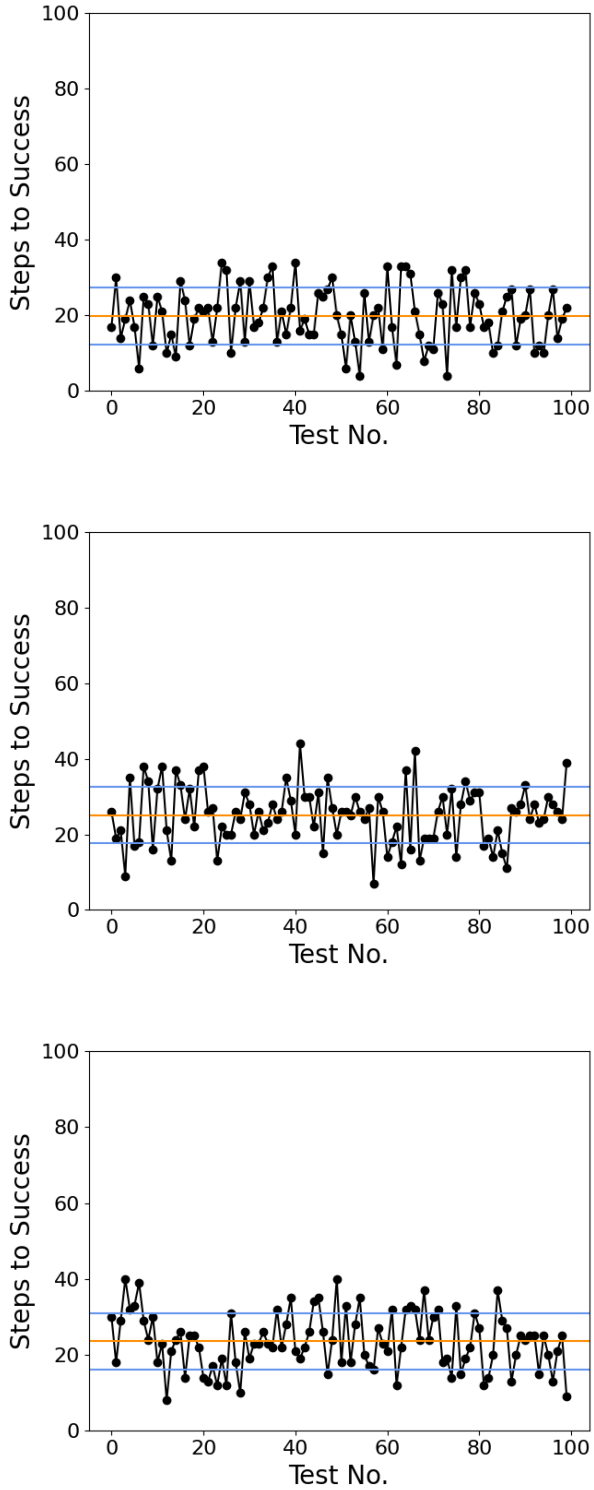



Figure 5.7: Results of the *DQN2M* model trained from a simulation. The randomisation values are 3500 (top), 3500 (middle), and 5000 (bottom). The cutoff values are -40 (top), -25 (middle), and -40 (bottom). The orange lines indicate respective means while the blue lines indicate the standard deviation.

correlation between an on-screen observation on one screen and an off-screen observation on the other screen. In order to bring the second beam onto the screen, it "purposefully" misaligns the first beam to minimise the cumulative reward over 100 or fewer steps.

This is a first step of showing that laser alignment using DQNs can work successfully in a laboratory environment and can be further optimised by improving learning parameters or using more efficient RL algorithms.

## 5.3 Alignment of off-axis parabolic mirror

Off-axis parabolic mirrors (OAP) are frequently used in laser experiments as they can create a diffraction-limited laser spot while having a smaller footprint than full parabolic mirrors and – especially for short focal lengths – allow for greater accessibility to the experimental set-up. However, aligning an OAP is a non-trivial task in an experimental environment as it is made for a specific angle of incoming light. Any deviation from this angle or from perfect collimation of the laser beam will cause optical aberrations such as astigmatism (longitudinal separation of the sagittal and tangential focal planes) or coma (wedge-shaped focal spot due to dependence of the location of the focus on the radial position on the OAP of rays incident at the wrong angle) which broaden the focal spot and reduce the maximum achievable intensity. If the OAP has a sufficiently large diameter translational errors of the beam (at constant angle of incidence) do not change the focal spot quality but only its position.

In order to account for these effects, it is necessary to have full control over the OAP's $x$, $y$, and $z$-position, as well as its pitch and yaw. In addition, control over either the incoming beam direction or the camera screen position onto which the beam is focused is needed.

### 5.3.1 Experimental implementation

It is important to note that the coordinate system (C) of the camera screen on which observations are made and the coordinate system (C') of the delay stage are related through a rotation of $\theta$ about the $z$-axis. This means that a translation of the focal spot along y can only be achieved by using both $x'$ and $y'$ motors in a certain relation according to the rotation matrix

$$\begin{pmatrix} x' \\ y' \end{pmatrix} = \begin{pmatrix} \cos\theta & -\sin\theta \\ \sin\theta & \cos\theta \end{pmatrix} \begin{pmatrix} x \\ y \end{pmatrix} \ . \tag{5.11}$$

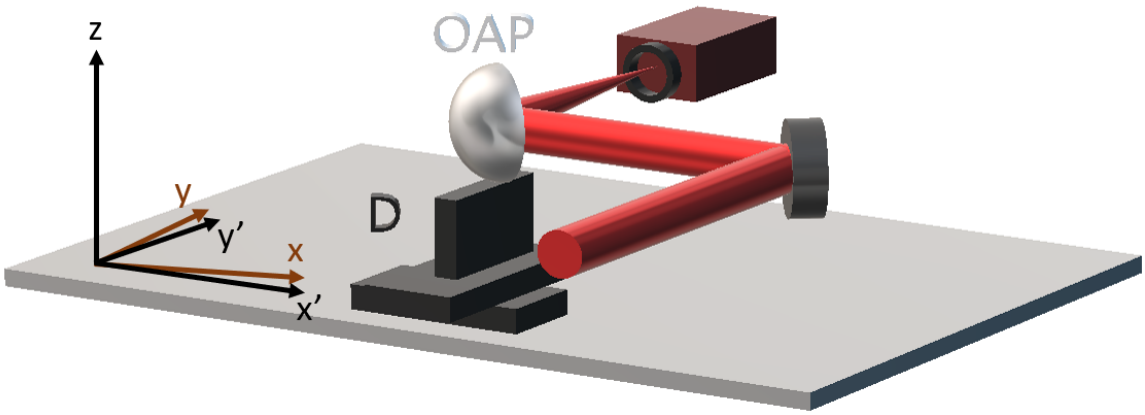



Figure 5.8: This schematic shows the set-up of the experimental training for off-axis parabola alignment. The motorised $x$-$y$-$z$-stage (D) and the pitch and yaw motors attached to the off-axis parabola (OAP) give the required 5-axis control to focus the laser beam (stylised in red) onto the CCD.

A schematic of the laboratory set-up is presented in Fig. 5.8. It shows the focusing of the incoming beam onto the camera. The translation stage can move along $x'$, $y'$ and $z' = z$, while the motors attached to the OAP can change its orientation in the $x'$-$y'$ plane (yaw) as well as the $y'$-$z$ plane (pitch).

#### 5.3.1.1 Equipment

In this set-up I used Thorlabs Z812 motorised actuators mounted in a KM200 2-inch optics mount and an MT3/M-Z8 motorised translator stage. To visualise the beam an Allied Vision Marlin F-033 camera was used. A Thorlabs BE10M-B beam expander was used to increase the beam diameter. A photograph of the components on the optical table in the laboratory can be seen in Appendix D.

### 5.3.2 Training the model

Successful training of a deep neural network depends to a large extent on the choice of training parameters, appropriate observation and action spaces, and the right choice of reward function. The observation and the resulting reward of each observation are the only parts that are linked to the physical problem (optimising the focal spot of a laser beam) and known by the agent. All other manifestations of the problem such as the physics related to beam aberrations are not implemented which makes RL a convenient choice able to even solve unknown problems.

The action space had to include every movement of the OAP necessary to align and focus the laser beam on the camera screen and was chosen to be

$$\begin{aligned}\mathcal{A}_1 = [&+\kappa\Delta x', -\kappa\Delta x', +\kappa\Delta y', -\kappa\Delta y', +\kappa\Delta z,\\ &-\kappa\Delta z, +\kappa\Delta\theta, -\kappa\Delta\theta, +\kappa\Delta\beta, -\kappa\Delta\beta] \ ,\end{aligned} \tag{5.12}$$

where $\kappa$ is a multiplication factor to the motor step size, $\Delta\theta$ is a change in yaw and $\Delta\beta$ is a change in pitch.

A first attempt to build the observation space was made using the position of the centre of the beam on the CCD and the beam size ($\mathcal{S}_p$) measured in number of pixels irradiated above a set intensity threshold. To get these states a similar detection method was used as presented in Section 5.2.1.2.

The observation space obtained from the processed image was therefore

$$\mathcal{O}^* = [x, z, \mathcal{S}_p] \ . \tag{5.13}$$

After several unsuccessful training attempts while scanning through the main training parameters ($\eta, \gamma, \mathrm{n_{MB}}, \Theta$, etc.) it became apparent that the network could not draw all the necessary information from the observation to choose an optimal action to solve the problem. Therefore, the observation space was iterated until the training showed promising results. The observation was updated such that the new spot size $\mathcal{S}_r$ was calculated by fitting a minimum enclosing circle to the pixels above the pre-set intensity threshold and returning the radius of this circle. This made the size parameter less responsive to change but made it possible to prevent focal spots with very strong astigmatism from obtaining scores associated with a small size (e.g. a line focus which covers few pixels but is far from optimised). In addition, I added two further parameters to the observation list which helped to improve the training:

- the eccentricity $e = \sqrt{1 - (b/a)^2}$, where $a$ and $b$ are the respective semi-major and semi-minor axes of an ellipse fitted to the threshold mask,
- the angle corresponding to the orientation of the fitted ellipse $\alpha \in [0, 180]$.

If the angle $\theta$ of the translation stage is small, a further difficulty arises which prevents the algorithm from making an "informed" choice: there is no unique solution for which action to choose when the beam is well-aligned apart from the focal spot's distance from the screen. This will cause a round focal spot of larger diameter than at the exact focal distance. This observation state cannot be linked to a unique action as being "too close" and "too far" will result in the same observation. Therefore, "memory" was added to the state. This was done through expanding the observation space size

| Observation | $x$ | $z$ | $\mathcal{S}_r$ | $e$ | $\alpha$ |
|---|---|---|---|---|---|
| A2 | -228 | 145 | 19.0 | 96.0 | 22.4 |
| B2 | -159 | -144 | 13.5 | 97.2 | 116.5 |

Table 5.3: Observation values for data obtained in Fig. 5.9. $x$ and $z$ are the positions on the CCD (relative to the screen centre) in pixel, $\mathcal{S}_r$ is the size of the spot, $e$ is the eccentricity of the ellipse fitted to the spot (scaled to a range between 0 and 100), and $\alpha$ is the angle in degree between z-axis and major ellipse axis (counted clockwise).

from 5 to 6 appending the size of the previous step $\mathcal{S}_{r,-1}$ to the current observation (see Alg. 2).

**Algorithm 2** Algorithm for new extended observation state.

Define $x_0, z_0, \mathcal{S}_{r,0}, e_0, \alpha_0$
$[x_1, z_1, \mathcal{S}_{r,1}, e_1, \alpha_1] \leftarrow get_state()$
Observation $\leftarrow append([\mathcal{S}_{r,0}], [x_1, z_1, \mathcal{S}_{r,1}, e_1, \alpha_1])$
# COMMENT : Observation is now $[\mathcal{S}_{r,0}, x_1, z_1, \mathcal{S}_{r,1}, e_1, \alpha_1]$
**while** current step $\leq$ final step **do**
  $[x_k, z_k, \mathcal{S}_{r,k}, e_k, \alpha_k] \leftarrow get_state()$
  Observation $\leftarrow$ Observation$[-3 : -2]$
  Observation $\leftarrow append($Observation$, [x_k, z_k, \mathcal{S}_{r,k}, e_k, \alpha_k])$
  # COMMENT : Observation is now $[\mathcal{S}_{r,k-1}, x_k, z_k, \mathcal{S}_{r,k}, e_k, \alpha_k]$
**end while**

Therefore, the new observation space was set to be:

$$\mathcal{O} = [\mathcal{S}_{r,-1}, x, z, \mathcal{S}_r, e, \alpha] \ . \tag{5.14}$$

An example of the beam detection is shown in Fig. 5.9 where the masks computed using the cv2 algorithm are shown on the right-hand side. The observation values obtained from panels (A2) and (B2) are listed in Tab. 5.3.

#### 5.3.2.1 Reward calculation

The performance of the network and the quality of training given a certain amount of steps does not only depend on the initial training parameters and the applicability of the observation state, but also on the reward which is calculated from the observation. As mentioned previously, the reward is connected to a state-action pair and indicates whether an action chosen at a certain observation contributed to solving the (unknown) problem.

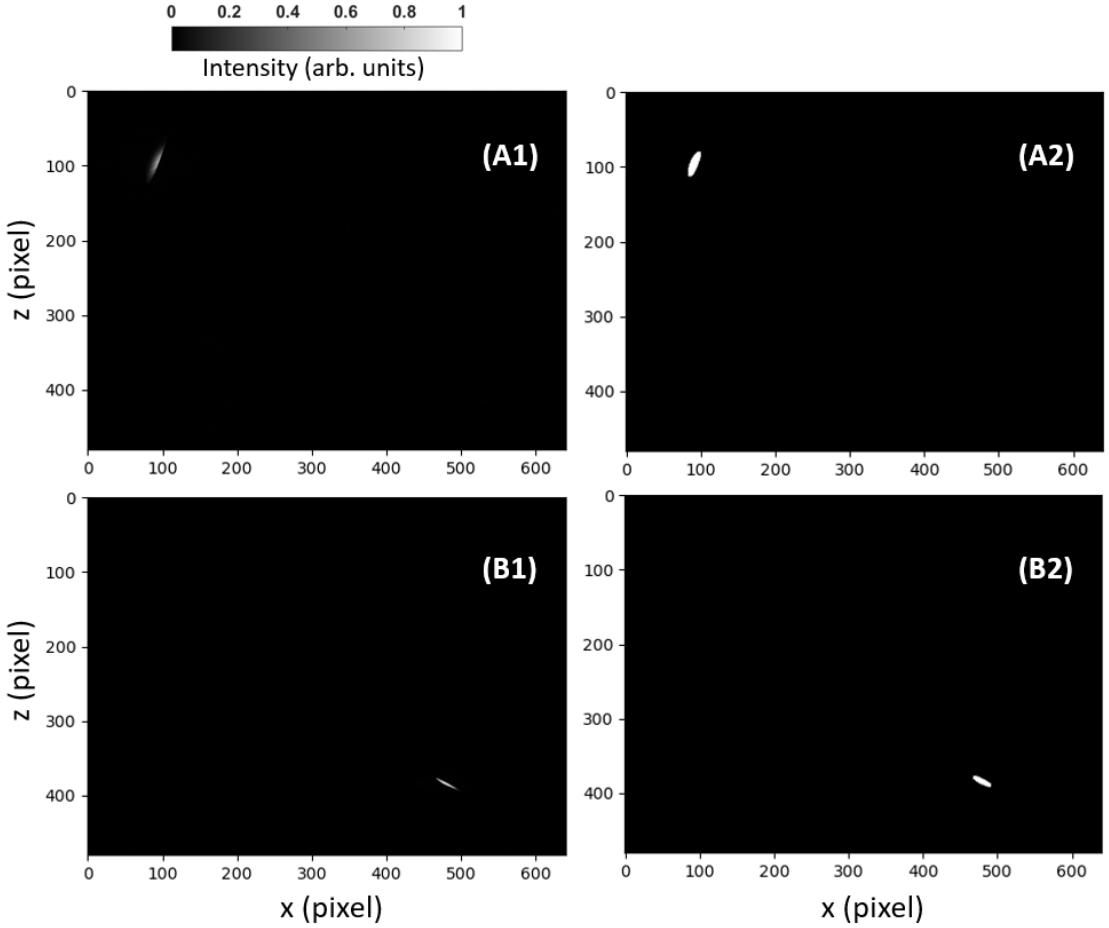



Figure 5.9: This figure shows the raw CCD data (left panels) and the intensity threshold masks from the computer vision data processing routine (right panels) for two motor positions. The top panels have relative motor positions of [$\Theta$(yaw) = +0.7, $\beta$ (pitch) = +0.7, x' = 0, y' = −0.7, z = 0] while the bottom panels have positions of [yaw = −0.4, pitch = −0.4, x' = +0.4, y' = −0.4, z = +0.4]. White pixels are irradiated while black pixels are not.

The first reward function which was used is given by

$$r_1 = -\left((\Delta x^2 + \Delta z^2)^{3/4} + \Gamma \mathcal{S}_r^2\right) \ . \tag{5.15}$$

The variables $\Delta x$ and $\Delta z$ are the distances of the beam centre to the screen centre in pixels. $\Gamma$ is a factor putting a special emphasis on either bringing the beam to the screen centre ($\Gamma < 1$) or minimising its radius ($\Gamma > 1$). The exponents of the distances from the screen centre (3/2) and the spot size (2) were chosen to penalise deviations from the perfect score (zero in both cases) differently for the two tasks. They were found through trial and error and can be further adapted to tailor the reward to the set-up's needs.

At a later stage, to work within a normalised framework and to penalise bad performance more strongly, a different reward function was introduced and trialled which read

$$r_2 = \exp\left\{-\frac{\mathcal{S}_r}{\mathcal{S}_{r,\max}}\right\} \exp\left\{-\left(\frac{\Delta x^2 + \Delta z^2}{\Delta x_{\max}^2 + \Delta z_{\max}^2}\right)^{1/2}\right\} - 1 \ . \tag{5.16}$$

This function returned normalised values between $e^{-2} - 1 \simeq -0.86$ and 0. However, it was found that it could also return a "good" value even if one of the parameters was not optimised well due to the nature of the function's slopes. Throughout the testing procedure, this function was, again, changed to

$$r_3 = \mathcal{A}\left(1 - \frac{\Delta x^2 + \Delta z^2}{\Delta x_{\max}^2 + \Delta z_{\max}^2}\right)^{\gamma_1} \left(1 - \left(\frac{\mathcal{S}_r}{\mathcal{S}_{r,\max}}\right)^2\right)^{\gamma_2} - 1 \ , \tag{5.17}$$

where the exponents $\gamma_1$ and $\gamma_2$ can be used to fine-tune the steepness of each individual learning slope. In this case, they were set to $\gamma_1 = \gamma_2 = 2$. This function is normalised to give a maximum amplitude of $\mathcal{A}$ and incentivises the agent to optimise both sub-tasks at the same time. If, for example, the size is large not even a perfectly centred beam returns a good reward. The three reward functions are plotted in Fig. 5.10. In all cases, a (negative) penalty is added to the return if the beam leaves the CCD.

#### 5.3.2.2 Simulation environment

There are commercial and open-source software packages which allow the beam shape to be simulated at a specific plane after being focused by an OAP using different computational approaches from Fourier optics to ray tracing. However, all methods that I have found take several seconds per step to simulate on a conventional computer. Therefore, there was no advantage of using a simulation environment to train the agent over training from the experimental set-up itself.

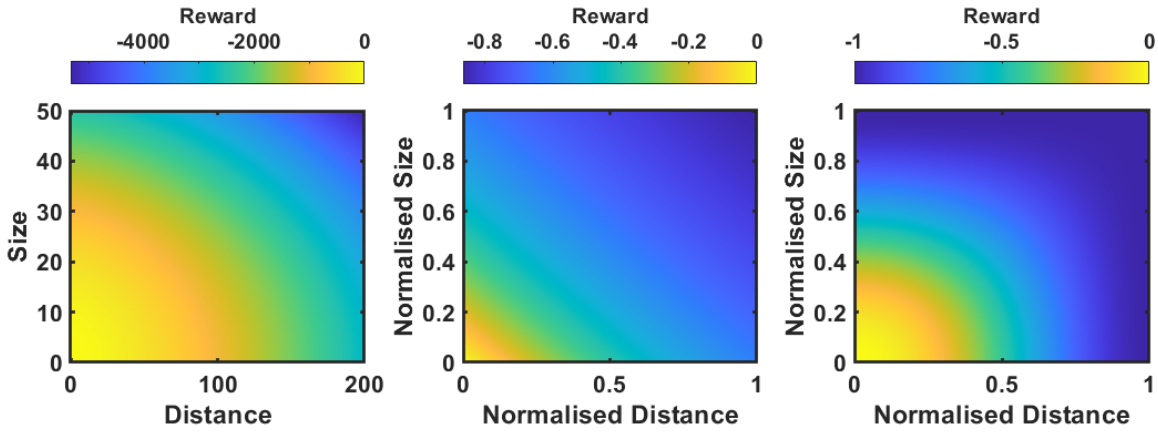



Figure 5.10: This figure shows the reward for functions $r_1$ (left), $r_2$ (middle), and $r_3$ (right) plotted against spot size and distance from centre.

#### 5.3.2.3 Training from experiment

Since the step duration of the actuators is $\sim 1\,\mathrm{s}$, a training set of 20,000 episodes with 100 steps per episode takes over 3 weeks to run. Therefore, the approach taken was to carefully tune the parameters to find a region in which the learning curve starts early on and to optimise the system from there.

The first method used was a DQN agent which I will refer to as *DQNOAP1*. This agent was trained to maximise the cumulative reward $r_1$ over each episode. The episode was labelled "successful" whenever the reward reached a value $r_1 > -100$. For example, this cutoff value is reached for $\mathcal{S}_r = 7.0$, $\Delta x = 10$, and $\Delta y = 10$. As a comparison, the best focal radius that can be achieved by hand is $\mathcal{S}_r = 4.9$ and typical initialisation values during training were around $\mathcal{S}_r = 15$ for a randomisation variable $\chi = 0.7$ (which is not to be compared to the $\chi$ value of the previous section due to different actuator models). The training parameters for *DQNOAP1* are shown in Tab. 5.4.

*DQNOAP1* was trained over 13480 episodes with 70 steps per episode. This training run took 8 days, 6 hours and 25 minutes. The training results are presented in Fig. 5.11. The success rate averaged over the last 500 episodes was 87.4%.

The second method used an NAC agent [255] which I will refer to as *NACOAP1*. This agent was trained to maximise the cumulative reward $r_2$ over each episode. The new episode was successful if $\{(\mathcal{S}_r \leq 5.0) \wedge (\sqrt{\Delta x^2 + \Delta y^2} \leq 15.0)\}$ was true. The

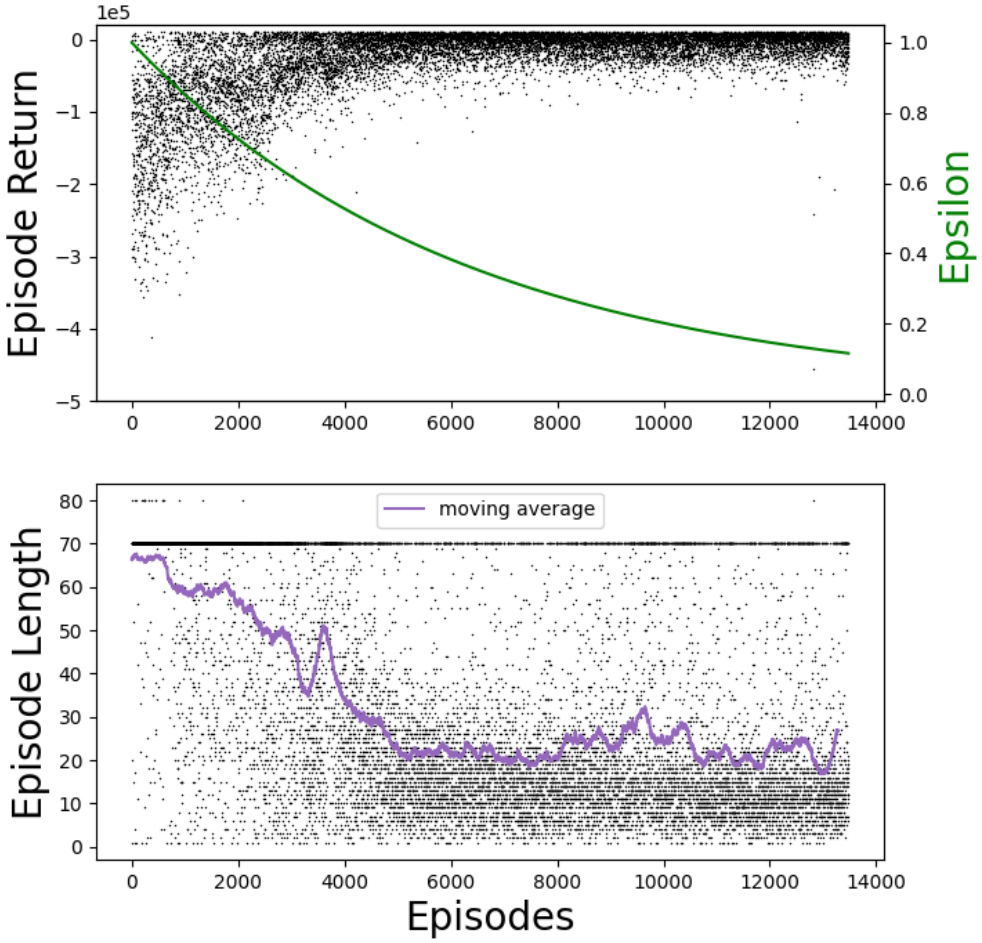



Figure 5.11: This figure shows the results of the training of the *DQNOAP1* agent. The episode length had an upper limit of 70 steps. Occasional values of 80 can be seen in the bottom panel which correspond to the case where one of the actuators ran out of range which automatically aborted the episode. The moving average was taken over 200 data points.

| Parameter | Description | Value |
|---|---|---|
| $\gamma$ | Discount | 0.98 |
| $\eta$ | Learning Rate | 0.0001 |
| S | Replay Memory Size (RMS) | 100000 |
| $S_{min}$ | Min RMS to start training | 1000 |
| $n_{MB}$ | Minibatch Size | 100 |
| U | Update target every | 10 |
| $N_{STEPS}$ | Max Steps per Episode | 70 |
| $r_s$ | Success Reward | 20000 |
| $N_{EPISODES}$ | Episodes | 13840 |
| $\Theta$ | Decay Exponent | 0.9998 |
| $\epsilon_{min}$ | Min Epsilon | 0.001 |
| $\chi$ | Initialisation Limit | 0.7 |
| $[x_{OFF}, y_{OFF}]$ | Fixed Off-Screen Position | [20000,20000] |
| LAYERS | No. of hidden neural network layers | 2 |
| NODES | Nodes per neural network layer | 10 |

Table 5.4: List of constants used for training *DQNOAP1*.

initialisation parameter was set to $\chi = 0.7$. The reward discount factor was set to $\gamma = 0.99$ and the learning rate was $\eta = 0.05$. A linear function approximator using a Fourier basis [256] of orders 5 (to combine different state variables) and 10 (applied to each state independently) was used. The probability with which a specific action was selected (the policy) was based on a linear softmax function (which is in essence a logistic function).

Details of the NAC training run are shown in Fig. 5.12. The episode length had an upper limit of 70 steps up to the point where the training was interrupted (see vertical black dashed line in Fig. 5.12). After the agent was reloaded the maximum episode length was set to 110 steps and the success reward was increased to 100. The first few episodes had a very low return due to the beam wandering off-screen or becoming too faint (out of focus) for the detection algorithm. The positive band in the reward structure is due to the additional success reward.

The data shows a slow but continuous decrease in episode length indicating that training made the agent's performance better. This can also be seen in the bottom panel in which the initial return (obtained after beam initialisation and before taking the first action of each episode) is plotted for each episode. The abundance of successful episodes is higher for low initial returns in the beginning but becomes independent of the initial return later in the training. This shows that *NACOAP1* learns to solve the alignment task for both "easy" and "difficult" scenarios equally well. The success

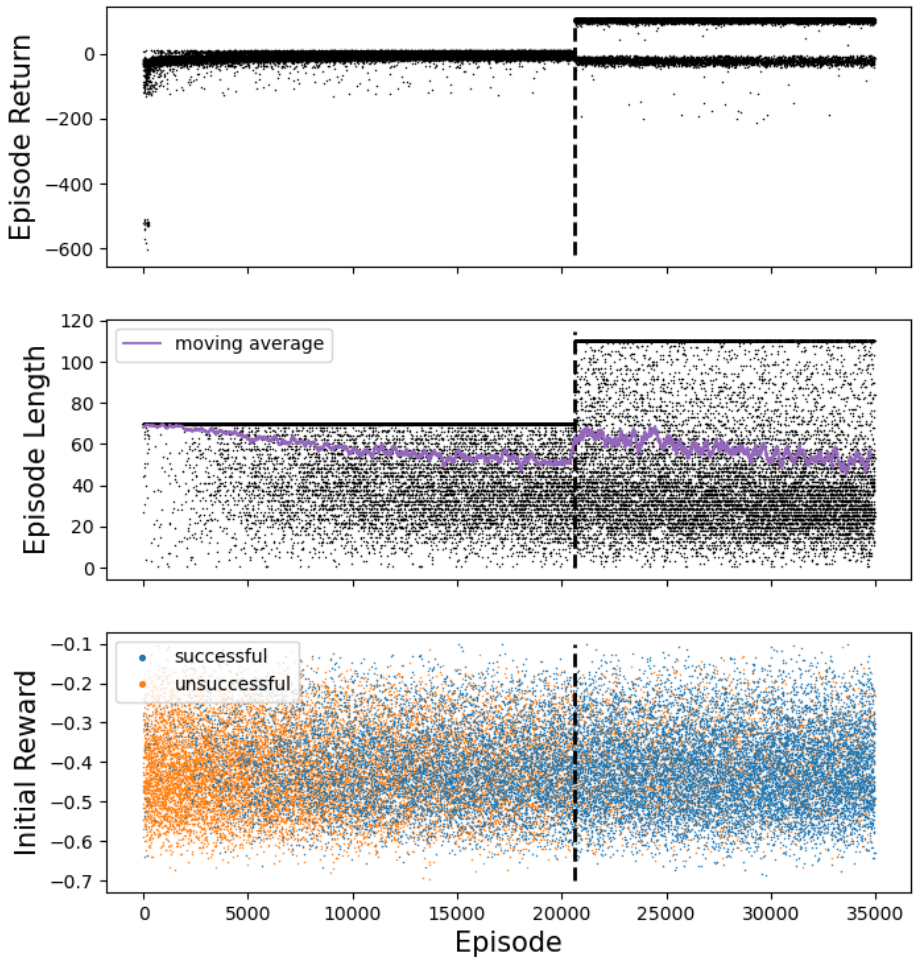



Figure 5.12: This figure shows the results of the training of the *NACOAP1* agent. The vertical black dashed line indicates a break of training after which the agent was reloaded with different training parameters.

rate of the last 500 episodes was 82.8%.

While these results show that training improves the respective agent's performance it is not possible to have a fair direct comparison between the two methods used due to changes in important training parameters such as reward function or episode length. Therefore, two new agents were trained in equal conditions: *DQNOAP2* and *NACOAP2*. Both used the reward function $r_3$ and a maximum episode length of 100 steps. To successfully finish an episode, the agent had to achieve $\{(\mathcal{S}_r \leq 6.0) \wedge (\sqrt{\Delta x^2 + \Delta y^2} \leq 10.0)\}$ which was challenging due to the fixed step size[8]. All other training parameters were unchanged.

The results of *DQNOAP2* which trained for 19840 episodes are shown in Fig. 5.13. As can be seen, there is a region – roughly between steps 8000 and 11000 – where the agent was seemingly stuck in a bad solution approach and the small epsilon value prevented fast recovery. The success rate averaged over the last 500 steps was 44.2%.

The results of *NACOAP2* which trained for 20446 episodes are shown in Fig. 5.14. In comparison to *DQNOAP2*, there are fewer episodes in which the return is very low but the averaged episode length decreases more slowly. The success rate averaged over the last 500 steps was 26.8%. This means that the rate of training improvement is worse for this given set of training parameters.

Although *DQNOAP2* performed better, both success rates were lower than expected. It was found that the step size was chosen too large (or the success range too small) to always give an optimal route to success. Depending on which of the five actuators used, taking one step could lead to a new spot position 19 pixels away from the previous location. In many cases, this would cause an oscillation about the optimal position space returning good rewards but failing to end the episode. As both agents suffered from the same problem, the comparison still holds for the given set of training parameters.

### 5.3.3 Testing agent performance

Due to the fact that the agent was trained on the experimental set-up a dedicated test was not necessary. The last episodes of each training run allow to draw the same conclusions as a dedicated test.

[8] A fixed step size has the advantage of keeping the action state small but prevents optimisation of the problem as a function of the distance from the screen centre.

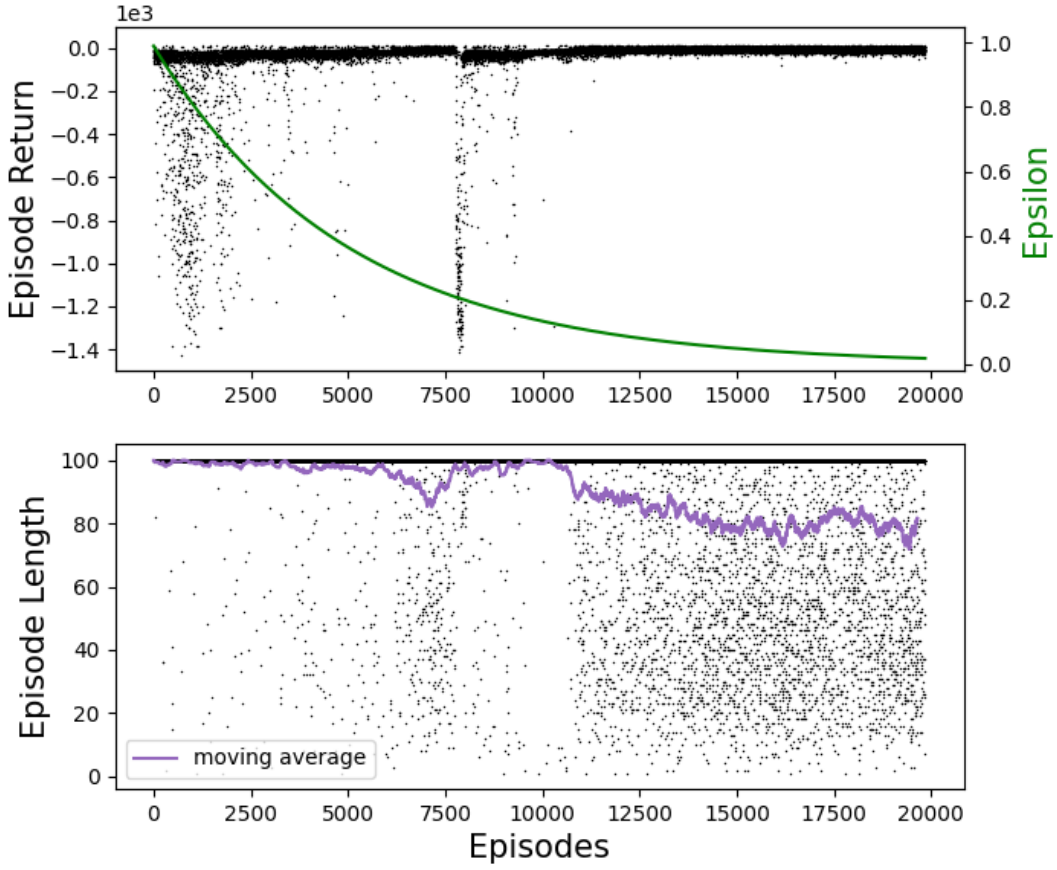



Figure 5.13: This figure shows the episode return (top panel) and episode length (bottom panel) of the training of the *DQNOAP2* agent. The episode length had an upper limit of 100 steps. The maximum number of episodes was 19840.

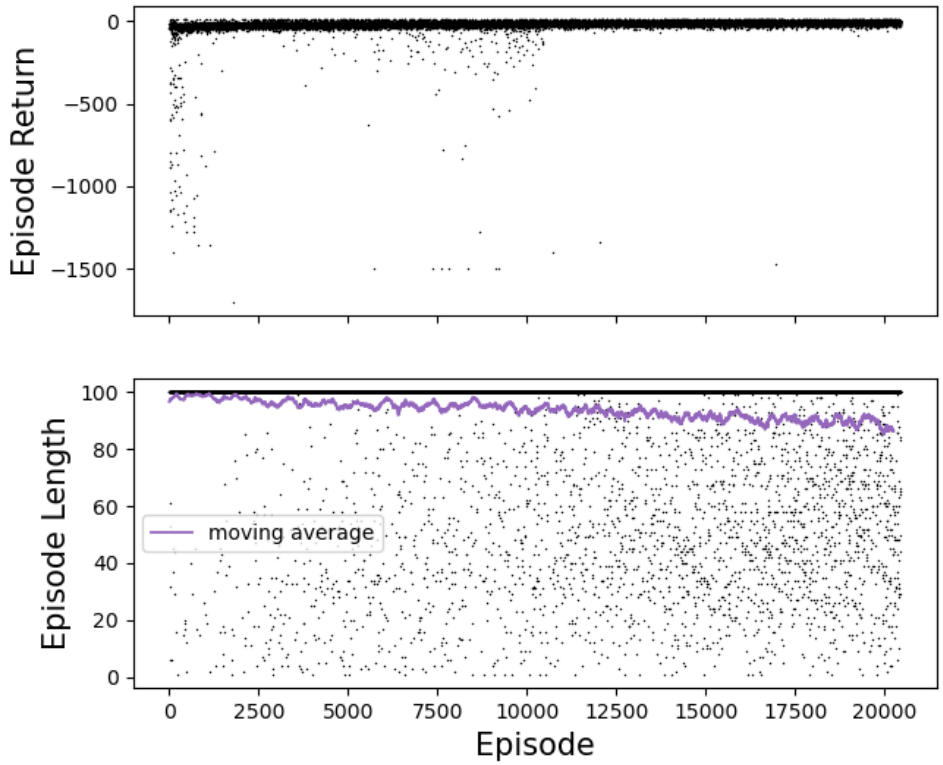



Figure 5.14: This figure shows the episode return (top panel) and episode length (bottom panel) of the training of the *NACOAP2* agent. The episode length had an upper limit of 100 steps. The maximum number of episodes was 20446.

## 5.4 Conclusion

The RL framework that has been built within this project has shown some promising initial results for solving specific alignment tasks in the laboratory. A two-mirror system trained using simple trigonometric functions was successful in learning the simultaneous beam alignment on near and far field cameras even if a beam was lost from the screen. The use of motors that had significant variations in step size did not have an impact on the agent's ability to learn effectively. Further modifications have to be made to allow real-time alignment of an interferometer (such as implementing optimal fringe spacing as an alignment objective).

In addition, an agent learnt the alignment of an OAP which is a considerably more complex task. It solved the problem with a high probability during performance tests in which moderate completion conditions applied. For hard completion conditions (where the step size was large compared to the final target area) the probability decreased. While it was shown that this probability does not depend on the initial conditions of each testing run, it has to be mentioned that this only holds within the limits tested. Therefore, to tackle severe misalignment where the beam is not in located the vicinity of the camera CCD, a different (faster) training framework has to be implemented to train for these eventualities. To this end, I have started a collaboration with other researchers to develop and implement a fast simulation routine for optical set-ups on which an agent can be trained. Furthermore, future training runs should include a variable step size to achieve higher precision when close to the optimal focal spot.

# Chapter 6

# Summary and outlook

Generating highly-relativistic electron bunches with current laser technology is a relatively straightforward task. Considerably more difficult is to improve the beam quality, maximum energy or maximum charge in an effective manner, for which one has to be able to understand the mechanisms which underlie the injection and acceleration processes in a wakefield. Furthermore, very precise control of experimental conditions is required to test and use one's understanding of a process and reliable diagnostics are necessary to measure and verify an experimental result. With the work conducted in this thesis I hope to have contributed to the pursuit of building better electron accelerators.

## 6.1 Summary

The introduction to this thesis gave an overview of the relevance of this research in a general scope and listed past publications and contributions of collaborators to the work described in this thesis. Chapter 2 described theoretical concepts and computational methods used in the field of laser-plasma physics and, more precisely, laser-driven wakefield acceleration. Chapter 3 described a study of the behaviour of quasi-linear and non-linear wakefields driven in plasma of nanometre-sized clusters. The results of two-dimensional particle-in-cell simulations and a numerical WENO model solving a set of differential equations were compared to experimental observations from an oblique-angle single-shot frequency-domain-holography diagnostic. The change in wakefield shape and its implications were discussed. Then, the electron injection mechanism into cluster wakefields using large-amplitude laser pulses was studied. The results of this section were compared to experimental findings from other groups. The high charge beams could be used for X-ray generation. Chapter

4 studied an electron injection process in which the injection and wakefield generation processes are decoupled through the use of two separate laser pulses of equal laser wavelength. Mono-energetic electron bunches were produced in an experiment when the two pulses had a specific temporal separation but injection ceased for values outside of this separation region. Differences were found between using circular and linear polarisation with the latter causing a larger energy spread. Simulations using similar conditions to the experiment were run which showed that in the region of stronger overlap more charge was injected in the case of linear polarisation. This mechanism could be used to enable guided drive pulses of low amplitude to accelerate injected bunches over long distances. Chapter 5 presented work on a reinforcement learning laser alignment system which showed that two motorised mirrors controlled by an agent can be used to align a beam to a certain position in near and far field diagnostics. The training was performed using a simulation environment and successful transition to the laboratory environment was shown. In addition, an off-axis parabolic mirror was aligned from a randomised position using another reinforcement learning agent.

None of the methods studied offers a perfect solution to cover all requirements sought for in modern wakefield accelerators. However, depending on the application, some could be preferred over others. For example, in order to create high X-ray fluxes, one needs to reliably create high beam charges. The cluster injection process allows for both high charge and reproducibility and the results found in this thesis offer an explanation for these observations. The large transverse momenta observed in cluster-injected electrons could potentially lead to efficient sources of polarised betatron radiation. A disadvantage for many applications is the large energy spread of the electrons within the beam due to the continuous injection—a feature observed also by many other research groups. In contrast to the cluster injection scheme, the two-pulse ionisation injection scheme offers a route to low emittance beams with small relative energy spreads (at lower charges). While the results presented in this thesis are the first experimental observation of this scheme, the theoretical predictions of energy spreads around 2% were not met. Thus, at this stage, the results are not competitive with other methods that have achieved sub-percent energy spreads. However, this being a proof-of-principle experiment, many improvements can be made to the set up to achieve better stability and higher electron beam quality. Once these improvements are made, the scheme—in combination with guiding channels—could deliver state of the art electron beams at GeV energies. While there appear to be obvious routes to decreasing the injection volume (thus reducing emittance and energy

spread) by tuning the laser pulse parameters, it is more difficult to decrease the spatial jitter of the laser beams which, at low laser intensities (slightly above the injection threshold), could be even more detrimental to the repeatability than seen in this thesis.

## 6.2 Future work

The reinforcement learning algorithms have shown promising preliminary results but are far from being a universal solution for aligning long beamlines with numerous optics. To this end, a fast and optimised simulation environment shall be investigated allowing for efficient (and possibly even parallelised) training. This could allow the use of such systems in future high-power laser experiments.

Concerning electron injection into wakefields, a high-repetition rate laser system would be advantageous to run parameter scans testing the limits of and finding optimised parameters for a two-pulse injection scheme. In future experiments, special care should be given to relative spatial beam jitter, precise pulse delay control, and the quality of the focal spots and the intensity characterisation.

# Appendix A

# Detailed derivations

## A.1 Solution to Maxwell equations

In vacuum, both the charge density $\rho$ and the current $\mathbf{j}$ are zero. Introducing the scalar potential $\Phi$ and the vector potential $\mathbf{A}$, which are defined via the electric and magnetic fields

$$\mathbf{E} = -\nabla\Phi - \frac{\partial}{\partial t}\mathbf{A} \ , \tag{A.1}$$

$$\mathbf{B} = \nabla \times \mathbf{A} \ , \tag{A.2}$$

equations 2.1-2.4 can be rewritten. Since $\mathbf{A}$ is not uniquely defined (an infinite set of values of $\mathbf{A}$ simultaneously satisfy equations A.1 and A.2, also known as "gauge invariance") a gauge has to be chosen. In Lorenz gauge, where

$$\nabla \cdot \mathbf{A} + \frac{1}{c^2}\frac{\partial \Phi}{\partial t} = 0 \tag{A.3}$$

the potentials are given by

$$\nabla^2\Phi = \frac{1}{c^2}\frac{\partial^2\Phi}{\partial t^2} \ , \tag{A.4}$$

$$\nabla^2\mathbf{A} = \frac{1}{c^2}\frac{\partial^2\mathbf{A}}{\partial t^2} \ . \tag{A.5}$$

In Coulomb gauge, where

$$\nabla \cdot \mathbf{A} = 0 \tag{A.6}$$

the potentials are given by

$$\nabla^2\Phi = 0 \ , \tag{A.7}$$

$$\nabla^2\mathbf{A} - \frac{1}{c^2}\frac{\partial^2\mathbf{A}}{\partial t^2} = \frac{1}{c^2}\nabla\frac{\partial\Phi}{\partial t} \ . \tag{A.8}$$

In Coulomb gauge, possible solutions for the potentials are

$$\Phi(\mathbf{z}, t) = 0 \tag{A.9}$$

and

$$\mathbf{A}(\mathbf{z},t) = A_0 \cos\left(\omega_0 t - \mathbf{k_z}\cdot\mathbf{z} + \phi_0\right) , \tag{A.10}$$

where $A_0$ is the amplitude, $\omega_0$ is the angular frequency of the oscillation, $\mathbf{k_z}$ is the wave vector and $\phi_0$ is a constant phase. This solves equations A.7 and A.8 and gives the dispersion relation of light in vacuum

$$\frac{\omega_0}{|k_z|} = c \ . \tag{A.11}$$

## A.2 Frequency of electron oscillations in a cold plasma

Assuming that oscillations of involved quantities are small any products of the first (or higher) order terms can be neglected. Substituting $n_e = n_{e,0} + n_{e,1}$, $v_e = v_{e,1}$ (no initial currents), $n_{e,0} = n_{i,0}$, and $E = E_1$ (no electric field in equilibrium state) into equations 2.51, 2.52, and 2.53, and assuming that there are no spatial or temporal electron density gradients $\partial_x n_{e,0} = \partial_t n_{e,0} = 0$, one finds:

$$m_e \frac{\partial v_{e,1}}{\partial t} = -eE_1 \ , \tag{A.12}$$

$$\frac{\partial n_{e,1}}{\partial t} + n_{e,0}\frac{\partial v_{e,1}}{\partial x} = 0 \ , \tag{A.13}$$

$$\frac{\partial E_1}{\partial x} = -\frac{e n_{e,1}}{\epsilon_0} \ . \tag{A.14}$$

Using a plane wave *ansatz* for the oscillatory terms:

$$n_{e,1} = \mathcal{N}\exp\{i(k_x x - \omega t)\} \ , \tag{A.15}$$

$$v_{e,1} = \mathcal{V}\exp\{i(k_x x - \omega t)\} \ , \tag{A.16}$$

$$E_{e,1} = \mathcal{E}\exp\{i(k_x x - \omega t)\} \ , \tag{A.17}$$

equations A.12, A.13, A.14 simplify to

$$-i\omega m_e \mathcal{V} = -e\mathcal{E} \ , \tag{A.18}$$

$$-i\omega\mathcal{N} + ik_x n_{e,0}\mathcal{V} = 0 \ , \tag{A.19}$$

$$ik_x\mathcal{E} = -\frac{e\mathcal{N}}{\epsilon_0} \ , \tag{A.20}$$

respectively. When combining equations A.18, A.19, and A.20 the terms $\mathcal{V}$, $\mathcal{N}$, $\mathcal{E}$, and $k_x$ cancel and the frequency $\omega = \sqrt{n_{e,0}e^2/(m_e\epsilon_0)}$ is obtained.

## A.3 Redundancy of Maxwell equations for subsequent iterations in the particle-in-cell method

Given that Gauss's law for magnetism

$$\nabla \cdot \mathbf{B} = 0 \tag{A.21}$$

holds initially, it can be shown using Faraday's law

$$\frac{\partial \boldsymbol{B}}{\partial t} = -\nabla \times \boldsymbol{E} \tag{A.22}$$

that its temporal derivative is also zero

$$\frac{\partial}{\partial t}\left(\nabla \cdot \mathbf{B}\right) = \nabla \cdot \frac{\partial \mathbf{B}}{\partial t} = -\nabla \cdot \left(\nabla \times \boldsymbol{E}\right) = 0 \tag{A.23}$$

since the divergence of the curl of any vector field equals zero. Gauss's law in its differential form

$$\nabla \cdot \mathbf{E} = \frac{\rho}{\epsilon_0} \tag{A.24}$$

can be reproduced from Ampere's law:

$$\frac{\partial \boldsymbol{E}}{\partial t} = c^2(\nabla \times \boldsymbol{B}) - \frac{\boldsymbol{J}}{\epsilon_0}\ . \tag{A.25}$$

This is done by taking the divergence

$$\frac{\partial}{\partial t}(\nabla \cdot \mathbf{E}) = c^2 \nabla \cdot (\nabla \times \boldsymbol{B}) - \frac{\nabla \cdot \boldsymbol{J}}{\epsilon_0} = -\frac{\nabla \cdot \boldsymbol{J}}{\epsilon_0} \tag{A.26}$$

and comparing the equation to the charge conservation law (continuity equation without source/sink)

$$\frac{\partial \rho}{\partial t} + \nabla \cdot \mathbf{J} = 0 \tag{A.27}$$

from which one obtains

$$\nabla \cdot \mathbf{E} = \frac{\rho}{\epsilon_0}\ . \tag{A.28}$$

## A.4 Calculation of pre-factor for density reconstruction

The path difference between a pulse going through vacuum and another pulse going through a symmetric plasma profile along direction z can be given by

$$\Delta s = \int_{-L}^{L} (1-\eta) dz\ = \frac{n_e}{2n_{\mathrm{cr}}} 2L, \tag{A.29}$$

where $\eta \approx 1 - n_e/(2n_{\rm cr})$ is the refractive index at $n_e \ll n_{\rm cr}$, $2L$ is the distance over which the interaction with the plasma occurs, and $n_{\rm cr}$ is the critical density. The phase shift is related to the path difference by

$$\Delta\Phi = \frac{2\pi}{\lambda_0}\Delta s \ = \frac{\pi}{\lambda_0}\frac{n_e}{n_{\rm cr}}2L \ . \tag{A.30}$$

Here, $\lambda_0$ is the laser wavelength. From the above equation the pre-factor of $\lambda_0 n_{\rm cr}/\pi$ can be found through division.

## A.5 Cluster initialisation factor for linear ramp

The normalised space coordinate within the ramp direction is

$$u(x) = \frac{x - x_0}{x_1 - x_0} = \frac{x - x_0}{\Delta x} \ . \tag{A.31}$$

The density within the linear ramp is

$$n(x) = \frac{x - x_0}{\Delta x}(n_1 - n_0) + n_0 = u(x)\Delta n + n_0 \ . \tag{A.32}$$

Integrating over space gives

$$N = \int_{x_0}^{x_1} n(x)dx = \frac{1}{2}(n_0 + n_1)(x_1 - x_0) = \overline{n}\Delta x \ , \tag{A.33}$$

from which the normalised density value can be obtained

$$\frac{n(x)}{N} = \frac{n_0 + u\Delta n}{\overline{n}\Delta x} = \left(\frac{\partial x}{\partial r}\right)^{-1} \ . \tag{A.34}$$

Therefore,

$$\frac{\partial x}{\partial r} = \frac{\overline{n}\Delta x}{n_0 + u\Delta n} \tag{A.35}$$

and using equation A.31

$$\frac{\partial u}{\partial r} = \frac{\overline{n}}{n_0 + u\Delta n} \tag{A.36}$$

follows. Reformulating and integrating yields

$$\int_0^u (n_0 + u'\Delta n)du' = \int_0^r \overline{n}dr' \tag{A.37}$$

$$n_0 u + \frac{1}{2}\Delta n u^2 = \overline{n}r \tag{A.38}$$

$$u^2 + 2\frac{n_0}{\Delta n}u - 2\frac{\overline{n}}{\Delta n}r = 0 \tag{A.39}$$

from which $u$ can be found to be

$$\begin{aligned} u &= -\frac{n_0}{\Delta n} \pm \sqrt{(\frac{n_0}{\Delta n})^2 + 2\frac{\overline{n}}{\Delta n} r} \\ &= \frac{\sqrt{n_0^2 + r(n_1^2 - n_0^2)} - n_0}{n_1 - n_0} \ . \end{aligned} \tag{A.40}$$

From this equation it follows that

$$u = \begin{cases} 0, & \text{for} \quad r = 0 \\ 1, & \text{for} \quad r = 1 \\ \sqrt{r}, & \text{for} \quad n_0 = 0 \end{cases} \tag{A.41}$$

with which the factor $u = \sqrt{r}$ for the ramp region can be found. $u(r)$ is the normalised x position up to which a fraction $r$ of cluster centres is placed. This means that $r$ is a random number $R$ projected onto the new, smaller, volume of interest (the ramp volume). Using this result and equation A.31 it can be determined where the randomised cluster center positions are initialised within the ramp region:

$$x_c = x_0 + \sqrt{\frac{R}{V_n}} \Delta x \ , \tag{A.42}$$

where $x_c$ is the cluster centre position, $R$ is a random number with uniform distribution between 0 and 1, and $V_n$ is the ratio of ramp volume over total volume $V_n = V_r / V_{tot}$.

## A.6 Equation of motion in co-moving frame

The Lorentz force on an electron of charge $e$ in an electromagnetic field can be written as

$$\frac{d\mathbf{p}}{dt} = -e(\mathbf{E} + \mathbf{v} \times \mathbf{B}) \ . \tag{A.43}$$

Assuming that $\mathbf{E} = (0, E_y, 0)$, $\mathbf{B} = (0, 0, B_z)$ and using the relations $\mathbf{E} = -\nabla\Phi - \frac{\partial \mathbf{A}}{\partial t}$ and $\mathbf{B} = \nabla \times \mathbf{A}$ gives

$$\begin{aligned} \frac{dp_y}{dt} &= -e(E_y - v_x B_z) \\ &= e(\frac{\partial A_y}{\partial t} + v_x \frac{\partial A_y}{\partial x}) = e\frac{dA_y}{dt} \ , \end{aligned} \tag{A.44}$$

where $\partial_y \Phi$ was omitted and

$$\begin{aligned}
\frac{dp_x}{dt} &= e\left(\frac{\partial \Phi}{\partial x} - \frac{p_y}{m\gamma}\frac{\partial A_y}{\partial x}\right) \\
&= e\frac{\partial \Phi}{\partial x} - \frac{e^2 A_y}{m\gamma}\frac{\partial A_y}{\partial x} \\
&= mc\left(c\frac{\partial \tilde{\Phi}}{\partial x} - \frac{c}{\gamma}a_y\frac{\partial a_y}{\partial x}\right) \\
&= mc\left(c\frac{\partial \tilde{\Phi}}{\partial x} - \frac{c}{2\gamma}\frac{\partial a_y^2}{\partial x}\right) \ ,
\end{aligned} \tag{A.45}$$

where $A_x = 0$, $\tilde{\Phi} = e\Phi/(mc^2)$, and $a_y = eA_y/(mc)$. The equation of motion now reads

$$\frac{1}{mc}\frac{dp_x}{dt} = \frac{d(\gamma\beta_x)}{dt} = c\frac{\partial \tilde{\Phi}}{\partial x} - \frac{c}{2\gamma}\frac{\partial a_y^2}{\partial x} \ . \tag{A.46}$$

In order to find an expression for the spatial derivative of $a^2$, the relativistic Lorentz factor is introduced [69]

$$\gamma = \gamma_\perp \gamma_\parallel = \frac{\sqrt{1+a^2}}{\sqrt{1-\beta_x^2}} \ , \tag{A.47}$$

which gives

$$\gamma^2(1-\beta_x^2) - 1 = a^2 \ . \tag{A.48}$$

The next step is to introduce new coordinates $\tau = t$ and $\xi = x - v_g t$ describing a frame co-moving with the laser pulse:

$$\frac{\partial}{\partial x} = \frac{\partial \tau}{\partial x}\frac{\partial}{\partial \tau} + \frac{\partial \xi}{\partial x}\frac{\partial}{\partial \xi} = \frac{\partial}{\partial \xi} \tag{A.49}$$

$$\frac{\partial}{\partial t} = \frac{\partial \tau}{\partial t}\frac{\partial}{\partial \tau} + \frac{\partial \xi}{\partial t}\frac{\partial}{\partial \xi} = \frac{\partial}{\partial \tau} - v_g\frac{\partial}{\partial \xi} \ . \tag{A.50}$$

Taking the derivative of equation A.48 with respect to $\xi$ gives

$$\frac{\partial a^2}{\partial \xi} = \frac{\partial}{\partial \xi}[\gamma^2(1-\beta_x^2) - 1] = 2\gamma\left(\frac{\partial \gamma}{\partial \xi} - \beta_x^2\frac{\partial \gamma}{\partial \xi} - \gamma\beta_x\frac{\partial \beta_x}{\partial \xi}\right) \ , \tag{A.51}$$

giving the desired expression.

Expressing the total derivative of the equation of motion in partial terms reads

$$\frac{d}{dt}(\gamma\beta_x) = \left(\frac{\partial}{\partial \tau} - v_g\frac{\partial}{\partial \xi} + v_x\frac{\partial}{\partial \xi}\right)\gamma\beta_x \ , \tag{A.52}$$

where I have used $\frac{\partial \xi}{\partial t} = v_x$. We now equate eqs. A.46 and A.52 to obtain[1] the expression sought for:

$$\frac{1}{c}\frac{\partial}{\partial \tau}(\gamma\beta_x) = \frac{\partial}{\partial \xi}\left[\tilde{\Phi} - \gamma + \beta_g\gamma\beta_x\right] = \frac{\partial}{\partial \xi}\left[\tilde{\Phi} - \gamma(1 - \beta_g\beta_x)\right] \ . \tag{A.55}$$

## A.7 Error Factor for Overlapping Beams

If two Gaussian beams are separated by distance $s$, their electron density can be expressed as

$$\begin{aligned}\int_{-\infty}^{\infty} n_{e,2}dy &= n_0\int_{-\infty}^{\infty}\left(e^{-(y-s/2)^2/w_0^2} + e^{-(y+s/2)^2/w_0^2}\right)dy \\ &= 2n_0\frac{\sqrt{\pi}}{2}w_0[\mathrm{erf}(\infty) - \mathrm{erf}(-\infty)] \\ &= 2n_0\sqrt{\pi}w_0 \ .\end{aligned} \tag{A.56}$$

The integral over the square of the electron density gives

$$\begin{aligned}\int_{-\infty}^{\infty} n_{e,2}^2dy &= n_0^2\int_{-\infty}^{\infty}\left(e^{-(y-s/2)^2/w_0^2} + e^{-(y+s/2)^2/w_0^2}\right)^2dy \\ &= 2n_0^2\sqrt{\frac{\pi}{2}}w_0 + 2\int_{-\infty}^{\infty} e^{-2(y^2+(s/2)^2)/w_0^2}dy \\ &= \sqrt{2\pi}n_0^2w_0\left(1 + e^{-s^2/(2w_0^2)}\right) \ .\end{aligned} \tag{A.57}$$

The ratio of Eq. 3.29 for one and two beams is

$$\left(\frac{(\int n_e dy)^3}{\int n_e^2 dy}\right) / \left(\frac{2(\int n_{e,2}dy)^3}{\int n_{e,2}^2 dy}\right) = \frac{1 + e^{-\frac{1}{2}(s/w_0)^2}}{2} \ . \tag{A.58}$$

## A.8 Probability distribution function for beam initialisation position

The integral

$$\int_{-\infty}^{\infty} f_{i,\sigma}(\iota - t)g_{i,\sigma}(t)dt \tag{A.59}$$

[1] using the result from eq. A.51

$$\left(\frac{\partial}{\partial \tau} - v_g\frac{\partial}{\partial \xi} + v_x\frac{\partial}{\partial \xi}\right)\gamma\beta_x = \frac{\partial \tilde{\Phi}}{\partial \xi} - \frac{c}{2\gamma}\left(2\gamma\frac{\partial \gamma}{\partial \xi} - 2\beta_x^2\gamma\frac{\partial \gamma}{\partial \xi} - 2\gamma^2\beta_x\frac{\partial \beta_x}{\partial \xi}\right) \tag{A.53}$$

$$\frac{1}{c}\frac{\partial}{\partial \tau}(\gamma\beta_x) = \frac{1}{c}\frac{\partial \tilde{\Phi}}{\partial \xi} - \frac{\partial \gamma}{\partial \xi} + \beta_x^2\frac{\partial \gamma}{\partial \xi} + \gamma\beta_x\frac{\partial \beta_x}{\partial \xi} + \frac{v_g}{c}\frac{\partial}{\partial \xi}(\gamma\beta_x) - \beta_x\frac{\partial}{\partial \xi}(\gamma\beta_x) \tag{A.54}$$

can be evaluated in different regions. It is constant if $(D_{1,\sigma\chi} - D_{2,\sigma\chi}) \leq \iota < (D_{2,\sigma\chi} - D_{1,\sigma\chi})$ with

$$\int_{-D_{1,\sigma\chi}}^{D_{1,\sigma\chi}} \frac{1}{2D_{1,\sigma\chi}} \frac{1}{2D_{2,\sigma\chi}} dt = \frac{1}{2D_{2,\sigma\chi}} \ . \tag{A.60}$$

In the regions $\iota \geq (D_{1,\sigma\chi} + D_{2,\sigma\chi})$ and $\iota \leq (-D_{1,\sigma\chi} - D_{2,\sigma\chi})$ the integral equals zero as there is no overlap between $f$ and $g$.

The next case is the region where $(-D_{1,\sigma\chi} - D_{2,\sigma\chi}) < \iota \leq (-D_{1,\sigma\chi} + D_{2,\sigma\chi})$. For any $\iota$, there is only overlap between the two functions in the region $-D_{2,\sigma\chi} \leq t < \iota + D_{1,\sigma\chi}$ which gives the new integration limits

$$\int_{-D_{2,\sigma\chi}}^{\iota + D_{1,\sigma\chi}} \frac{1}{2D_{1,\sigma\chi}} \frac{1}{2D_{2,\sigma\chi}} dt = \frac{\iota + D_{1,\sigma\chi} + D_{2,\sigma\chi}}{4D_{1,\sigma\chi} D_{2,\sigma\chi}} \ . \tag{A.61}$$

The last case can be solved analogously in the region $(-D_{1,\sigma\chi} + D_{2,\sigma\chi}) < \iota \leq (D_{1,\sigma\chi} + D_{2,\sigma\chi})$. The integration limits are found from the overlap region $\iota - D_{1,\sigma\chi} \leq t \leq D_{2,\sigma\chi}$. Therefore, the last part of the convolution is

$$\int_{\iota - D_{1,\sigma\chi}}^{D_{2,\sigma\chi}} \frac{1}{2D_{1,\sigma\chi}} \frac{1}{2D_{2,\sigma\chi}} dt = \frac{-\iota + D_{1,\sigma\chi} + D_{2,\sigma\chi}}{4D_{1,\sigma\chi} D_{2,\sigma\chi}} \ . \tag{A.62}$$

## A.9 Fit of the annular injector beam profile

The initial values passed to the fitting function were obtained using the moments of the respective parameters. For example, the centre of the beam was obtained by calculating the moments of x and y under a probability density function proportional to the intensity. The centre of mass of a function (in this case intensity) is at

$$q_0 = \frac{\int q\rho(q)\,\mathrm{d}q}{\int \rho(q)\,\mathrm{d}q} \ , \tag{A.63}$$

where $q$ is the coordinate and $\rho$ is the density function.

A least squares method was used to fit the model function in Eq. 4.21 to the raw data for 4 images at locations separated by 200 µm each. The fitting uncertainty was obtained by taking the sum of squared residuals $(I_{\mathrm{model}} - I_{\mathrm{data}})^2$ over the entire image. Then, the Hessian matrix with elements

$$\mathcal{H}_{ij} \equiv \frac{\partial^2 f}{\partial p_i \partial p_j} \ , \tag{A.64}$$

where $p \in \{I_0, x_0, y_0, R, r\}$ and $f$ is the model function, was calculated numerically using the second derivatives of the obtained residual value with respect to all fitted

parameters. After normalisation with the optimal sum of squared derivatives the matrix was inverted. The square root of the diagonal values is equal to the standard deviation of the respective parameter.

A significant part of this fit uncertainty comes from the fact that, unlike the model, the "ring" in the data is not continuous but oscillates between high and low intensity values along the circumference (a feature caused by the actuators of the deformable mirror optimising the wave front) which can be seen by applying the fit to a perfect model with similar oscillations.

## A.10 Airy disk spot size

The Airy disk is given by the Fraunhofer diffraction intensity distribution of a beam limited by a circular aperture at focus. The radius of the intensity minimum of the Airy disk can be found using the formula

$$r_A = 1.22\lambda \frac{f}{D} \ , \tag{A.65}$$

where $f$ is the focal length and $D$ is the beam diameter. The intensity profile is

$$I = I_0 \left[ \frac{2J_1(u)}{u} \right]^2 \ , \tag{A.66}$$

where $J_1$ is the Bessel function of order 1 and $u = krD/2f$ ($k$ is the wave vector and $r$ is the radius). The spot size $w_0$ can be calculated as the value at which the function A.66 falls to $I = e^{-2} I_0$ and is

$$w_0 = 0.67 r_A \ . \tag{A.67}$$

The FWHM can be found in similar manner to be $0.84 r_A$. Inserting the parabola focal lengths and beam diameters, the injector's FWHM is 3.12 µm and the driver's it is 32.93 µm.

# Appendix B

# Code

## B.1 Modifications to OSIRIS 4

The relevant parts of the new source code that was incorporated into the OSIRIS development version is shown below. The subroutine "read_input_std" gets information from the input deck and uses this input to compute the amount, size and position of the clusters in the ramp and main region. The subroutine "get_den_value_std" initialises the density distribution (according to the predefined boundaries) which is later filled with macro-particles.

```
subroutine read_input_std( this, input_file, coordinates )
! [...]

case ( "cluster" )
    this%type = p_cluster
        if ( mpi_node() == 0 ) then
                write(0,*) "setting up cluster variables"
        endif
! set sphere variables
    this%cluster_density = cluster_density
    this%cluster_avg_density = cluster_avg_density
    this%cluster_shape = cluster_shape
    this%cluster_xmin = cluster_xmin
    this%cluster_xmax= cluster_xmax
    this%cluster_xmin_ramp = cluster_xmin_ramp
    this%cluster_xmax_ramp = cluster_xmax_ramp
    this%cluster_width = cluster_width

    if(cluster_seed == 0) then
        write(0,*) "warning! cluster_seed = 0"
    endif
! set up random seed
    ! ------ use seed from input deck ------
    ! a random seed using date_and_time is problematic, as it &
    ! will be different for each call. Every node should create &
    ! the same cluster. Furthermore, the electrons should also have the &
    ! same random numbers as any other implemented species.

    call random_seed(size=i_seed)

    allocate(a_seed(1:i_seed))
```

```
    a_seed(1) = cluster_seed


! creates a pseudo-random seed array to feed random_number()
    do i=1, i_seed-1
        dummy = a_seed(i)
        dummy = IEOR(dummy, ISHFT(dummy,13))
        dummy = IEOR(dummy, ISHFT(dummy,-17))
        dummy = IEOR(dummy, ISHFT(dummy,5))
        a_seed(i+1) = dummy
    enddo


    call random_seed(put=a_seed)
    deallocate(a_seed)
! done getting seed

! gets the cluster volume
    d = this%cluster_width
    a = d/2.

    if(this%cluster_shape=="sphere") then
        if(p_x_dim == 1) then
            write(0,*) "sphere not defined in 1D!"
            write(0,*) "aborting..."
            stop
        else if(p_x_dim == 2) then
            cluster_volume = a*a*PI_16
        else if (p_x_dim == 3) then
                cluster_volume = (4./3.)*a*a*a*PI_16
        endif
    else if (this%cluster_shape=="square") then

        if(p_x_dim == 1) then !can be implemented if necessary
            write(0,*) "square not defined in 1D!"
            write(0,*) "aborting..."
            stop
        else if(p_x_dim == 2) then
            cluster_volume = d*d
        else if (p_x_dim == 3) then
                cluster_volume = d*d*d
        endif

    endif

! gets total volume
total_volume = 1.0
total_volume_ramp = 1.0
do i= 1, p_x_dim
        total_volume = total_volume*(this%cluster_xmax(i) &
                        -this%cluster_xmin(i))
    total_volume_ramp = total_volume_ramp*(this%cluster_xmax_ramp(i) &
                    -this%cluster_xmin_ramp(i))
enddo

! gives the number of clusters
! N_clusters = avg_density * total_volume / (cluster density * cluster volume)
!            = total mass / mass per cluster
N_clusters = int(this%cluster_avg_density*(total_volume + 0.5*total_volume_ramp) &
            /(this%cluster_density*cluster_volume))

allocate(this%cluster_center(p_x_dim,N_clusters), stat=ierr)

boundary_rando = total_volume_ramp/(2*total_volume+total_volume_ramp)

do cl = 1, N_clusters
    call random_number(rando)
```

```
    if(rando < boundary_rando) then
        this%cluster_center(1, cl) = cluster_xmin_ramp(1) &
                                   + sqrt(rando/boundary_rando) &
                                   * (cluster_xmax_ramp(1)-cluster_xmin_ramp(1))
    else
        this%cluster_center(1, cl) = cluster_xmin(1) &
                                   + (rando-boundary_rando)/(1-boundary_rando) &
                                   * (cluster_xmax(1)-cluster_xmin(1))
    endif
    do n = 2, p_x_dim
        call random_number(rando)
        !creates an array with the cluster center positions
            this%cluster_center(n, cl) = cluster_xmin(n) + rando &
                                       * (cluster_xmax(n)-cluster_xmin(n))
    enddo
enddo

!this sorts the clusters in x direction to save computational time later on.
do n= 1, N_clusters
    do cl = 1, N_clusters-n
        if (this%cluster_center(1,cl+1) < this%cluster_center(1,cl)) then
            q = this%cluster_center(1,cl)
            this%cluster_center(1,cl) = this%cluster_center(1,cl+1)
            this%cluster_center(1,cl+1) = q
        endif
    enddo
enddo


if ( mpi_node() == 0 ) then
                print *, "cluster number total:", N_clusters
endif

this%N_clusters = N_clusters

![...]
end subroutine read_input_std



subroutine get_den_value_std( this, pxx, npxx, den_value )
![...]
case (p_cluster)  ! cluster

den_value = 0.0
max_index = size(this%cluster_center,2)
!code speed-up by looping through only relevant clusters, not all of them
t = 1

do while (this%cluster_center(1,t)  .LT. (pxx(1,1) - this%cluster_width) &
                  .AND. t .LT. max_index)
        t = t+1
enddo

s = t

do while (this%cluster_center(1,s) .LE. (pxx(1,npxx) + this%cluster_width) &
                  .AND. s .LT. max_index)
    s = s+1
enddo


! Density is evaluated from cluster centers and widths
if (this%cluster_shape == "sphere") then

do k = 1, npxx !loop over all cells

    do p = t, s !loop over all relevant clusters
```

```
        r = ( pxx(1,k) - this%cluster_center(1,p) )**2
        do i = 2, p_x_dim
                r = r + ( pxx(i,k) - this%cluster_center(i,p) )**2
        enddo
        r = sqrt(r)

        if (r <= 0.5*this%cluster_width) then
        den_value(k) = 1.0_p_k_part*this%cluster_density
        endif

    enddo
enddo

else if (this%cluster_shape == "square") then

do k = 1, npxx !loop over all cells

    do p = t, s!loop over all relevant clusters

        r = abs( pxx(1,k) - this%cluster_center(1,p) )
        do i = 2, p_x_dim
            r = max( abs(pxx(i,k) - this%cluster_center(i,p)), r)
        enddo

        if (r <= this%cluster_width*0.5) then
            den_value(k) = 1.0_p_k_part*this%cluster_density
        endif

    enddo
enddo

else
    write(0,*) "cluster_shape must be square or sphere!"
    write(0,*) "aborting..."
    stop

endif

![...]
end subroutine get_den_value_std
```

# Appendix C

# Further simulation results

## C.1 Error of phase shift measurement using oblique angle probe pulse

The wakefield propagates along $\hat{x}$ with velocity $\mathbf{v}_{w,x} = c$ and the probe pulse propagates along $\sin\alpha\hat{z} + \cos\alpha\hat{x}$ with relative velocity $\mathbf{v}_{p,x} = c(\cos\alpha - 1) = c\sin\alpha(-\tan\alpha/2)$ and $\mathbf{v}_{p,z} = c\sin\alpha$. In the coordinates of the probe pulse this frame shift can be written as

$$x = (\partial_\xi x)\xi + (\partial_t x)t \tag{C.1}$$

and

$$z = (\partial_\xi z)\xi + (\partial_t z)t\ . \tag{C.2}$$

The phase picked up by the probe pulse can be written using these coordinates as

$$\Phi(y,\xi) = \int \Phi'(x(t,\xi), y, z(t,\xi))dt = \int \Phi'(x(z,\xi), y, z)\frac{\partial t}{\partial z}dz\ . \tag{C.3}$$

The factor $\partial z/\partial t = c\sin\alpha$ (velocity projection onto $z$) gives the change in phase magnitude due to the blurring effect. The variable $x(z,\xi)$ can be expressed as

$$x(z,\xi) = \xi - \tan(\alpha/2)z \tag{C.4}$$

where $t$ was obtained from Eq. C.2 and inserted into Eq. C.1. Therefore, the blur picked up in the $\xi$ coordinate, which can be related to the wavelength of the probe given a specific chirp factor, is proportional to the radial extent $r$ of the structure and is given by $r\tan(\alpha/2)$. Fig. C.1 shows the temporal evolution of the phase shift caused by the interaction of the probe pulse (propagating at an angle of 8°) with the wakefield's density perturbation. The blur is caused by the probed structures being

shifted towards larger frequencies with increasing time. However, this effect is small (relative error of up to 7% for an angle of incidence of 8° where the largest errors are in regions where the signal is weakest reducing the impact to the measured phase).

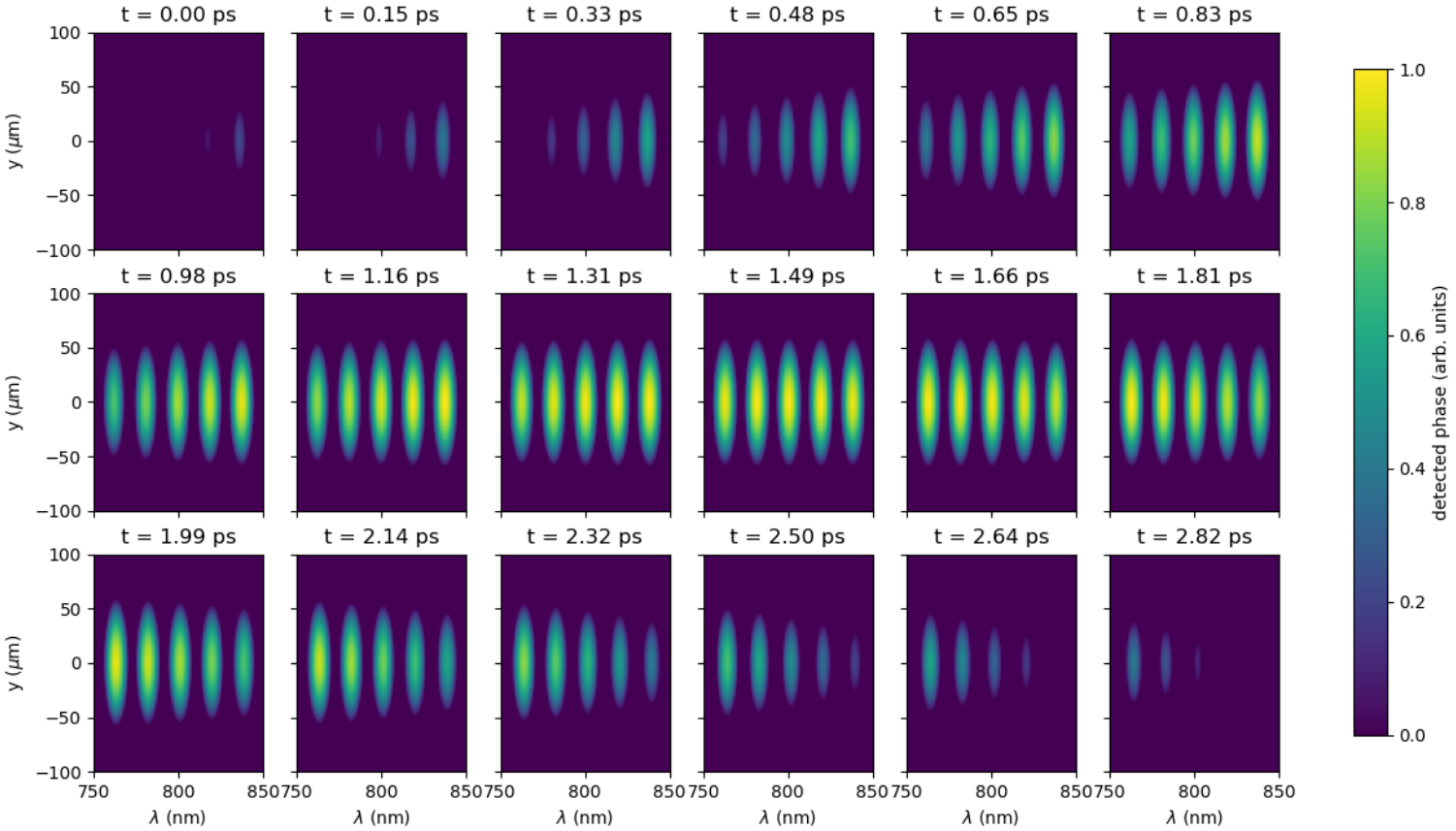



Figure C.1: Phase picked up by linearly chirped probe pulse propagating at an angle of 8° with respect to the synthetic wakefield. The wakefield is radially symmetric along its propagation axis.

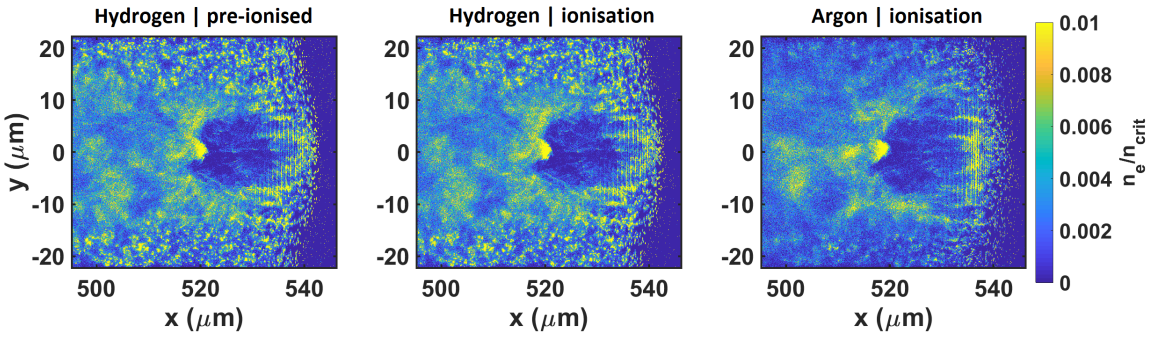



Figure C.2: Electron density for three different simulations. The left panel uses hydrogen clusters which are pre-ionised and initialised with 10eV. The middle panel also uses hydrogen cluster but computes the ionisation from the laser interaction. The right panel uses argon clusters which are also being ionised by the laser pulse. All snapshots are taken at the same simulation time step.

## C.2 Impact of ionisation on cluster wakefield behaviour

Here, further simulation results using OSIRIS are presented justifying the use of pre-ionised clusters of 10 eV. Figure C.2 shows that the charge trapping process in the cluster wakefield bubble is similar comparing pre-ionised results with those in which an ionisation module was used. This is also reflected in the momentum phase space plots in Fig. C.3. The maximum momentum is identical between all three simulations presented.

It can be observed that the cluster peak density on the top and bottom corner of the argon simulation is lower compared to the hydrogen cases. This is due to the fact that cluster initialisation density was computed such that the total electron density in the simulation box is equal across all simulations if 16 of the 18 available electrons are ionised from the argon atom.

While this is true for the inner region of the simulation box where the bubble is located and where the trapping process occurs, less electrons are ionised on the outside as can be seen in Fig. C.4 where the argon ionisation states for each ion cluster are shown. There is a broad band of 16 times positively charged ions in the central location where the wakefield is driven. In the outside regions where the laser has lower intensity this value drops down to 8.

The impact of collisions on the cluster ionsiation rate was also studied with a

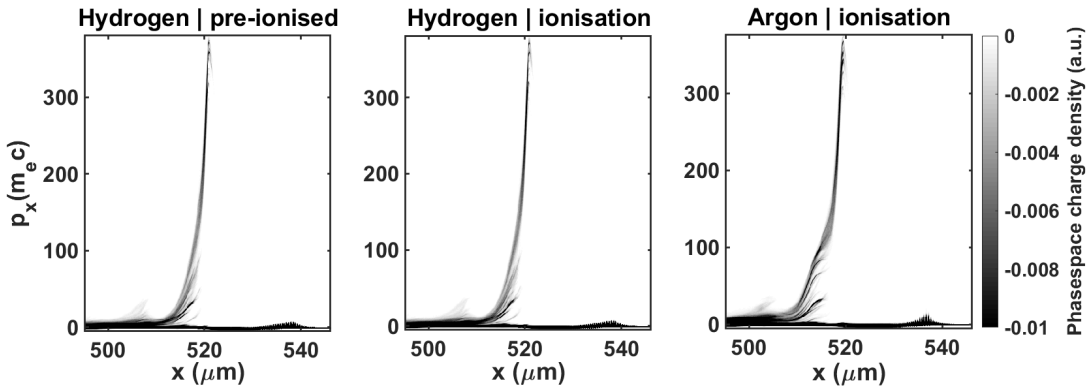



Figure C.3: Longitudinal momentum phase space for three different simulations. The left panel uses hydrogen clusters which are pre-ionised and initialised with 10eV. The middle panel also uses hydrogen cluster but computes the ionisation from the laser interaction. The right panel uses argon clusters which are also being ionised by the laser pulse. All snapshots are taken at the same simulation time step.

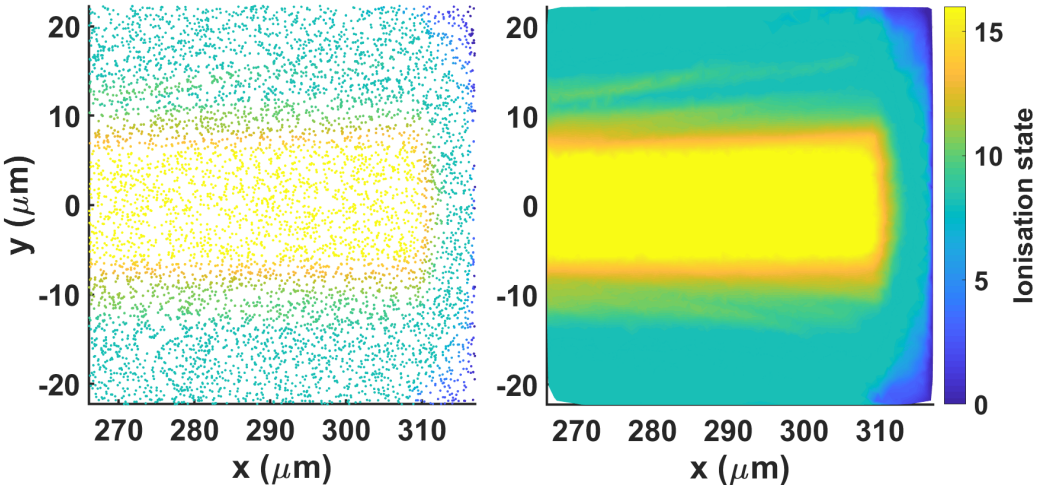



Figure C.4: This figure shows the ionisation states of argon clusters. The left panel shows the ionisation state of the ions of each cluster. The right panel shows a Delaunay triangulation surface for the same data for better visualisation.

different code (Smilei). To this end, a high-resolution simulation of a single cluster was conducted which interacted with a pulsed plane[1] wave. Figure C.5 plots the ionisation states at different time steps for simulations including and excluding collisional effects in the ionisation process. Again, the cluster is homogeneously ionised with 16 electrons removed after less than 15 fs. There are found to be only marginal differences when including the collisional module.

[1]The transverse intensity profile can be assumed to be constant over the extent of a cluster separation distance.

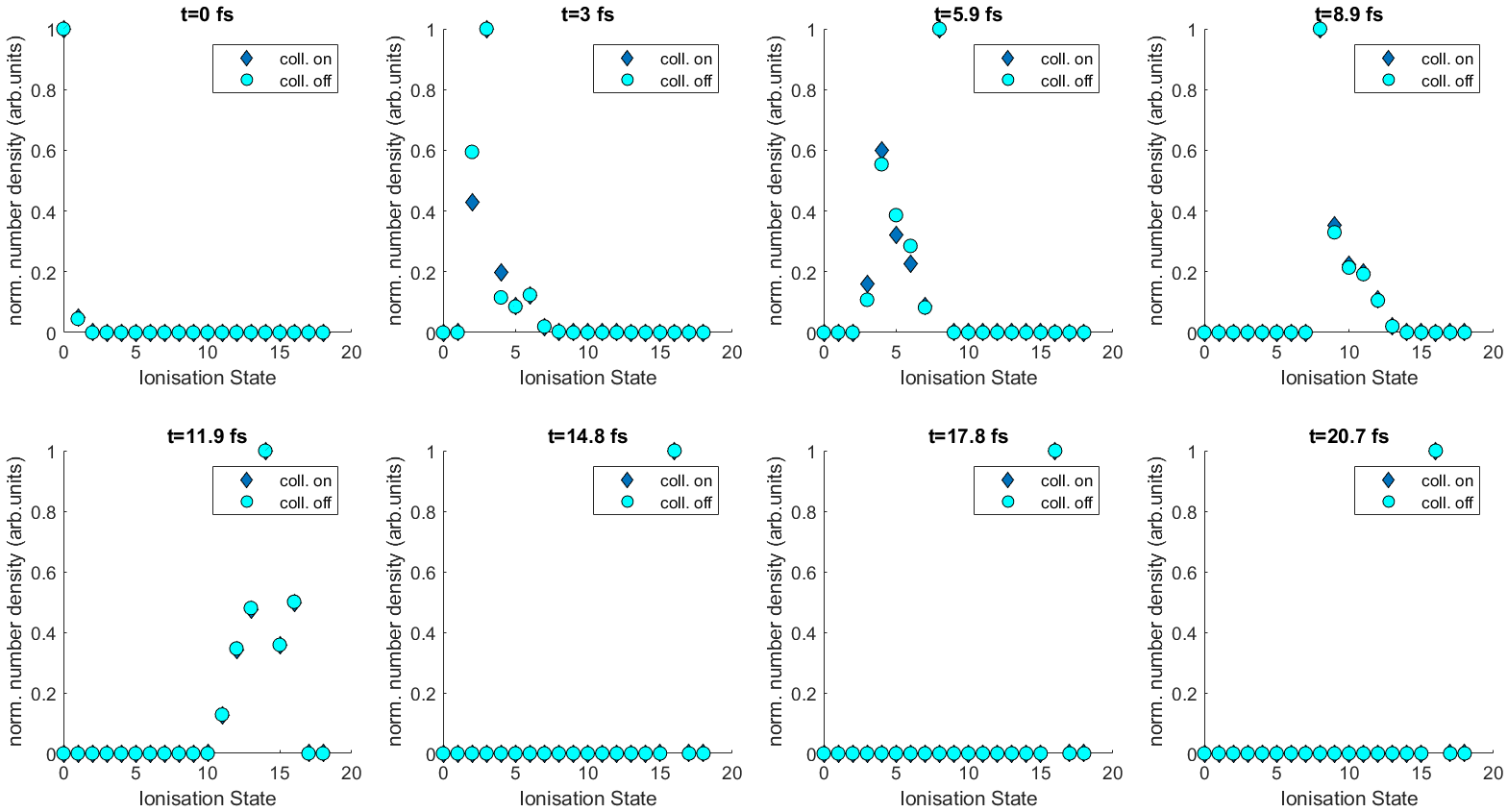



Figure C.5: This figure presents the abundance of different ionisation states in a single cluster interacting with a plane wave at different time steps. Diamonds markers represent the use of collisions in the ionisation process while circles represent field ionisation only.

Another point to discuss is why collisions seem to have a negligible impact and can be turned off in simulations to save computational time (approximately 50%). Ishikawa and Blenski [257] show that collisional ionisation plays no role in rare gas clusters when the mean free path is larger than the cluster diameter. Bauer [175] finds that (at a laser wavelength of $\lambda_0 = 800\,\mathrm{nm}$) the collisional frequency is much lower in clusters than its usual value in plasma and argues that energy is absorbed through "electron-cluster collisions" (which would be treated automatically in PIC simulations). Kundu and Bauer [172] argue that for short and intense laser pulses interaction with rare gas clusters collisional ionisation and absorption are of minor importance at $\lambda_0 \geq 800\,\mathrm{nm}$ in strong contrast to the nonlinear resonant absorption process. They state that the electron cloud excursion amplitude is time-dependent meaning that the "modified eigenfrequency" will dynamically pass through nonlinear resonance.

# Appendix D

# Photograph of laboratory setup

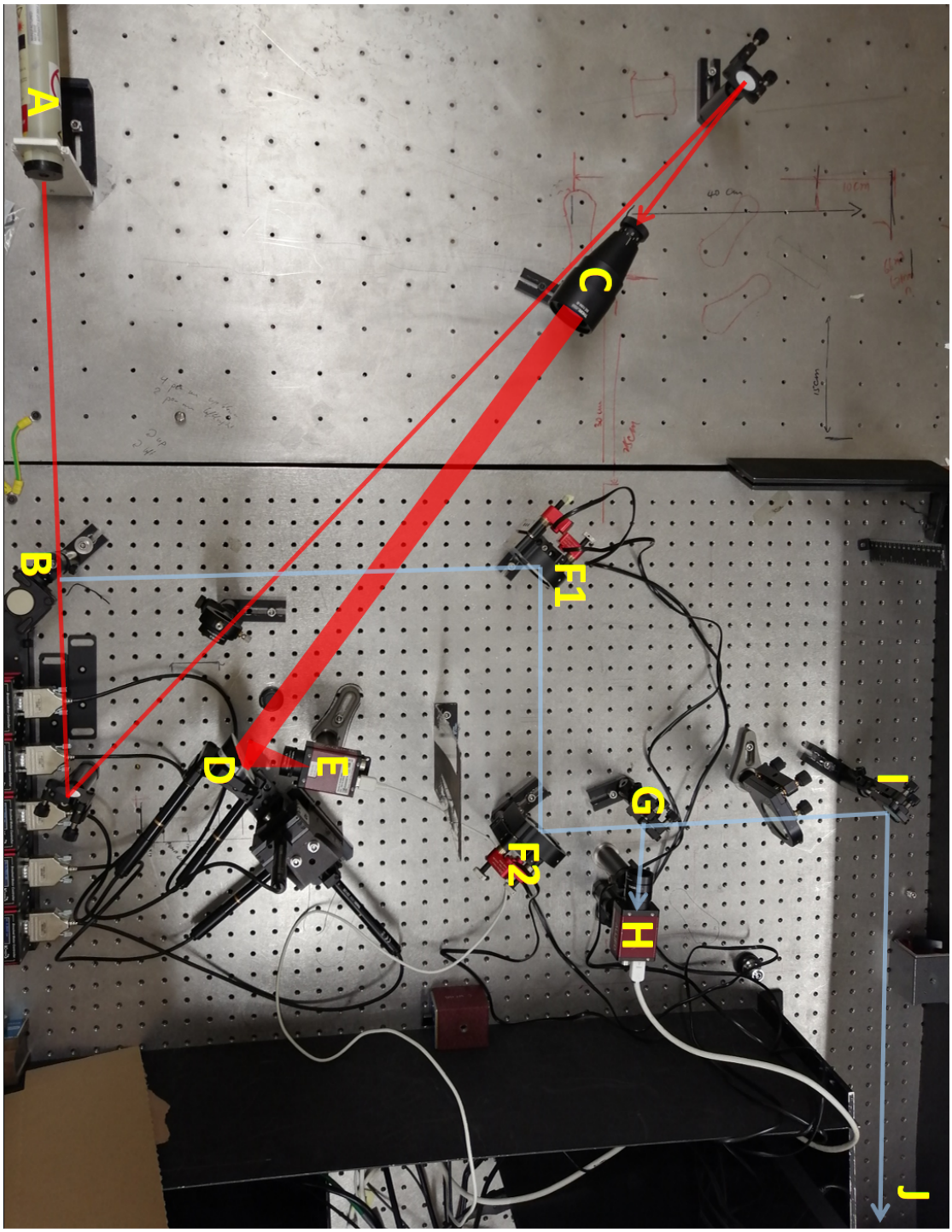



Figure D.1: Photograph of reinforcement learning alignment setup. A: 5 mW, Helium-Neon CW laser source; B: Flip mirror to quickly divert beam between both setups; C: Beam expander; D: Off-axis parabolic mirror mounted on motorised x-y-z stage; E: Camera for focal spot measurement; F1: Motorised mirror; F2: Motorised mirror; G: 50/50 beam splitter; H: Near-field camera; I: mirror sending the beam to far-field camera (J).

# Bibliography


[1] ATLAS Collaboration. Observation of a new particle in the search for the standard model higgs boson with the ATLAS detector at the LHC. *Physics Letters B*, 716(1):1–29, 2012.

[2] CMS Collaboration. Observation of a new boson at a mass of 125 GeV with the CMS experiment at the LHC. *Physics Letters B*, 716(1):30–61, 2012.

[3] S. Hooker and C. Webb. *Laser physics*. Oxford master series physics. Oxford University Press, Oxford, 2010.

[4] U. Amaldi. Cancer therapy with particle accelerators. *Nuclear Physics A*, 654(1):C375–C399, 1999.

[5] A. J. Antolak. Overview of accelerator applications for security and defense. *Reviews of Accelerator Science and Technology*, 08:27–36, 2015.

[6] J. D. Cockcroft, E. T. S. Walton, and E. Rutherford. Experiments with high velocity positive ions. - (i) further developments in the method of obtaining high velocity positive ions. *Proceedings of the Royal Society of London. Series A, Containing Papers of a Mathematical and Physical Character*, 136(830):619–630, 1932.

[7] CERN. Facts and figures about LHC. https://home.cern/resources/faqs/facts-and-figures-about-lhc, accessed 09 July 2021.

[8] S. A. Barengolts, V. G. Mesyats, V. I. Oreshkin, E. V. Oreshkin, K. V. Khishchenko, I. V. Uimanov, and M. M. Tsventoukh. Mechanism of vacuum breakdown in radio-frequency accelerating structures. *Phys. Rev. Accel. Beams*, 21:061004, Jun 2018.

[9] V. I. Veksler. Coherent principle of acceleration of charged particles. *CERN Symposium on High Energy Accelerators and Pion Physics*, pages 80–83, 1956.

[10] Ya. B. Faĭnberg. Acceleration of charged particles in a plasma. *Soviet Physics Uspekhi*, 10(6):750–758, Jun 1968.

[11] T. Tajima and J. M. Dawson. Laser electron accelerator. *Phys. Rev. Lett.*, 43:267–270, Jul 1979.

[12] J. Nishizawa. Extension of frequencies from maser to laser. *Proceedings of the Japan Academy, Series B*, 85(10):454–465, 2009.

[13] T. H. Maiman. Stimulated optical radiation in ruby. *Nature*, 187(4736):493–494, Aug 1960.

[14] S. Borneis, T. Laštovička, M. Sokol, T.-M. Jeong, F. Condamine, O. Renner, V. Tikhonchuk, H. Bohlin, A. Fajstavr, J.-C. Hernandez, and et al. Design, installation and commissioning of the eli-beamlines high-power, high-repetition rate hapls laser beam transport system to p3. *High Power Laser Science and Engineering*, 9:e30, 2021.

[15] C. N. Danson, C. Haefner, J. Bromage, T. Butcher, J.-C. F. Chanteloup, E. A. Chowdhury, A. Galvanauskas, L. A. Gizzi, J. Hein, D. I. Hillier, and et al. Petawatt and exawatt class lasers worldwide. *High Power Laser Science and Engineering*, 7:e54, 2019.

[16] D. Strickland and G. Mourou. Compression of amplified chirped optical pulses. *Optics Communications*, 56(3):219–221, 1985.

[17] A. Dubietis, G. Jonušauskas, and A. Piskarskas. Powerful femtosecond pulse generation by chirped and stretched pulse parametric amplification in bbo crystal. *Optics Communications*, 88(4):437–440, 1992.

[18] I. N. Ross, P. Matousek, M. Towrie, A. J. Langley, and J. L. Collier. The prospects for ultrashort pulse duration and ultrahigh intensity using optical parametric chirped pulse amplifiers. *Optics Communications*, 144(1):125–133, 1997.

[19] C. E. Clayton, K. A. Marsh, A. Dyson, M. Everett, A. Lal, W. P. Leemans, R. Williams, and C. Joshi. Ultrahigh-gradient acceleration of injected electrons by laser-excited relativistic electron plasma waves. *Phys. Rev. Lett.*, 70:37–40, Jan 1993.

[20] N. E. Andreev, L. M. Gorbunov, V. I. Kirsanov, A. A. Pogosova, and R. R. Ramazashvili. Resonant excitation of wakefields by a laser pulse in a plasma. *Soviet Journal of Experimental and Theoretical Physics Letters*, 55:571, May 1992.

[21] J. Krall, A. Ting, E. Esarey, and P. Sprangle. Enhanced acceleration in a self-modulated-laser wake-field accelerator. *Phys. Rev. E*, 48:2157–2161, Sep 1993.

[22] A. Pukhov and J. Meyer-ter Vehn. Laser wake field acceleration: the highly non-linear broken-wave regime. *Applied Physics B*, 74(4):355–361, Apr 2002.

[23] A Pukhov, S Gordienko, S Kiselev, and I Kostyukov. The bubble regime of laser–plasma acceleration: monoenergetic electrons and the scalability. *Plasma Physics and Controlled Fusion*, 46(12B):B179–B186, Nov 2004.

[24] I. Kostyukov, A. Pukhov, and S. Kiselev. Phenomenological theory of laser-plasma interaction in "bubble" regime. *Physics of Plasmas*, 11(11):5256–5264, 2004.

[25] W. Lu, C. Huang, M. Zhou, M. Tzoufras, F. S. Tsung, W. B. Mori, and T. Katsouleas. A nonlinear theory for multidimensional relativistic plasma wave wakefields. *Physics of Plasmas*, 13(5):056709, 2006.

[26] S. P. D. Mangles, C. D. Murphy, Z. Najmudin, A. G. R. Thomas, J. L. Collier, A. E. Dangor, E. J. Divall, P. S. Foster, J. G. Gallacher, C. J. Hooker, D. A. Jaroszynski, A. J. Langley, W. B. Mori, P. A. Norreys, F. S. Tsung, R. Viskup, B. R. Walton, and K. Krushelnick. Monoenergetic beams of relativistic electrons from intense laser-plasma interactions. *Nature*, 431:535 –, Sep 2004.

[27] C. G. R. Geddes, Cs Toth, J. van Tilborg, E. Esarey, C. B. Schroeder, D. Bruhwiler, C. Nieter, J. Cary, and W. P. Leemans. High-quality electron beams from a laser wakefield accelerator using plasma-channel guiding. *Nature*, 431:538 –, Sep 2004.

[28] J. Faure, Y. Glinec, A. Pukhov, S. Kiselev, S. Gordienko, E. Lefebvre, J.-P. Rousseau, F. Burgy, and V. Malka. A laser-plasma accelerator producing monoenergetic electron beams. *Nature*, 431:541 –, Sep 2004.

[29] R. J. Shalloo, C. Arran, A. Picksley, A. von Boetticher, L. Corner, J. Holloway, G. Hine, J. Jonnerby, H. M. Milchberg, C. Thornton, R. Walczak, and S. M. Hooker. Low-density hydrodynamic optical-field-ionized plasma channels generated with an axicon lens. *Phys. Rev. Accel. Beams*, 22:041302, Apr 2019.

[30] B. Miao, L. Feder, J. E. Shrock, A. Goffin, and H. M. Milchberg. Optical guiding in meter-scale plasma waveguides. *Phys. Rev. Lett.*, 125:074801, Aug 2020.

[31] A. Alejo, J. Cowley, A. Picksley, R. Walczak, and S. M. Hooker. Demonstration of kilohertz operation of hydrodynamic optical-field-ionized plasma channels. *Phys. Rev. Accel. Beams*, 25:011301, Jan 2022.

[32] W. P. Leemans, B. Nagler, A. J. Gonsalves, Cs Tóth, K. Nakamura, C. G. R. Geddes, E. Esarey, C. B. Schroeder, and S. M. Hooker. GeV electron beams from a centimetre-scale accelerator. *Nature Physics*, 2:696, Sep 2006.

[33] S. Karsch, J. Osterhoff, A. Popp, T. P. Rowlands-Rees, Zs. Major, M. Fuchs, B. Marx, R. Hörlein, K. Schmid, L. Veisz, S. Becker, U. Schramm, B. Hidding, G. Pretzler, D. Habs, F. Grüner, F. Krausz, and S. M. Hooker. GeV-scale electron acceleration in a gas-filled capillary discharge waveguide. *New Journal of Physics*, 9(11):415–415, Nov 2007.

[34] S. Kneip, S. R. Nagel, S. F. Martins, S. P. D. Mangles, C. Bellei, O. Chekhlov, R. J. Clarke, N. Delerue, E. J. Divall, G. Doucas, K. Ertel, F. Fiuza, R. Fonseca, P. Foster, S. J. Hawkes, C. J. Hooker, K. Krushelnick, W. B. Mori, C. A. J. Palmer, K. Ta Phuoc, P. P. Rajeev, J. Schreiber, M. J. V. Streeter, D. Urner, J. Vieira, L. O. Silva, and Z. Najmudin. Near-GeV acceleration of electrons by a nonlinear plasma wave driven by a self-guided laser pulse. *Phys. Rev. Lett.*, 103:035002, Jul 2009.

[35] X. Wang, R. Zgadzaj, N. Fazel, Z. Li, S. A. Yi, Xi Zhang, W. Henderson, Y.-Y. Chang, R. Korzekwa, H.-E. Tsai, C.-H. Pai, H. Quevedo, G. Dyer, E. Gaul, M. Martinez, A. C. Bernstein, T. Borger, M. Spinks, M. Donovan, V. Khudik, G. Shvets, T. Ditmire, and M. C. Downer. Quasi-monoenergetic laser-plasma acceleration of electrons to 2GeV. *Nature Communications*, 4:1988, Jun 2013.

[36] W. P. Leemans, A. J. Gonsalves, H.-S. Mao, K. Nakamura, C. Benedetti, C. B. Schroeder, Cs. Tóth, J. Daniels, D. E. Mittelberger, S. S. Bulanov, J.-L. Vay,

C. G. R. Geddes, and E. Esarey. Multi-GeV electron beams from capillary-discharge-guided subpetawatt laser pulses in the self-trapping regime. *Phys. Rev. Lett.*, 113:245002, Dec 2014.

[37] A. J. Gonsalves, K. Nakamura, J. Daniels, C. Benedetti, C. Pieronek, T. C. H. de Raadt, S. Steinke, J. H. Bin, S. S. Bulanov, J. van Tilborg, C. G. R. Geddes, C. B. Schroeder, Cs. Tóth, E. Esarey, K. Swanson, L. Fan-Chiang, G. Bagdasarov, N. Bobrova, V. Gasilov, G. Korn, P. Sasorov, and W. P. Leemans. Petawatt laser guiding and electron beam acceleration to 8 GeV in a laser-heated capillary discharge waveguide. *Phys. Rev. Lett.*, 122:084801, Feb 2019.

[38] C. Caizergues, S. Smartsev, V. Malka, and C. Thaury. Phase-locked laser-wakefield electron acceleration. *Nature Photonics*, 14(8):475–479, Aug 2020.

[39] D McGloin and K Dholakia. Bessel beams: Diffraction in a new light. *Contemporary Physics*, 46(1):15–28, 2005.

[40] K. Oubrerie, I. A. Andriyash, R. Lahaye, S. Smartsev, V. Malka, and C. Thaury. Axiparabola: a new tool for high-intensity optics. *Journal of Optics*, 24(4):045503, Mar 2022.

[41] Dustin H. Froula, David Turnbull, Andrew S. Davies, Terrance J. Kessler, Dan Haberberger, John P. Palastro, Seung-Whan Bahk, Ildar A. Begishev, Robert Boni, Sara Bucht, Joseph Katz, and Jessica L. Shaw. Spatiotemporal control of laser intensity. *Nature Photonics*, 12(5):262–265, May 2018.

[42] J. P. Palastro, J. L. Shaw, P. Franke, D. Ramsey, T. T. Simpson, and D. H. Froula. Dephasingless laser wakefield acceleration. *Phys. Rev. Lett.*, 124:134802, Mar 2020.

[43] S. Steinke, J. van Tilborg, C. Benedetti, C. G. R. Geddes, C. B. Schroeder, J. Daniels, K. K. Swanson, A. J. Gonsalves, K. Nakamura, N. H. Matlis, B. H. Shaw, E. Esarey, and W. P. Leemans. Multistage coupling of independent laser-plasma accelerators. *Nature*, 530(7589):190–193, Feb 2016.

[44] B. Hidding, S. Hooker, S. Jamison, B. Muratori, C. Murphy, Z. Najmudin, R. Pattathil, G. Sarri, M. Streeter, C. Welsch, M. Wing, and G. Xia. Plasma wakefield accelerator research 2019 - 2040: A community-driven uk roadmap compiled by the plasma wakefield accelerator steering committee (pwasc), 2019.

[45] A. Adelmann et al. Low Emittance X-FEL Development. *eConf*, C0508213:THPP016, 2005.

[46] E. Brunetti, R. P. Shanks, G. G. Manahan, M. R. Islam, B. Ersfeld, M. P. Anania, S. Cipiccia, R. C. Issac, G. Raj, G. Vieux, G. H. Welsh, S. M. Wiggins, and D. A. Jaroszynski. Low emittance, high brilliance relativistic electron beams from a laser-plasma accelerator. *Phys. Rev. Lett.*, 105:215007, Nov 2010.

[47] F. Albert, B. B. Pollock, J. L. Shaw, K. A. Marsh, J. E. Ralph, Y.-H. Chen, D. Alessi, A. Pak, C. E. Clayton, S. H. Glenzer, and C. Joshi. Angular dependence of betatron x-ray spectra from a laser-wakefield accelerator. *Phys. Rev. Lett.*, 111:235004, Dec 2013.

[48] S. K. Barber, J. van Tilborg, C. B. Schroeder, R. Lehe, H.-E. Tsai, K. K. Swanson, S. Steinke, K. Nakamura, C. G. R. Geddes, C. Benedetti, E. Esarey, and W. P. Leemans. Measured emittance dependence on the injection method in laser plasma accelerators. *Phys. Rev. Lett.*, 119:104801, Sep 2017.

[49] S. Di Mitri. On the importance of electron beam brightness in high gain free electron lasers. *Photonics*, 2(2):317–341, 2015.

[50] J. P. Couperus, R. Pausch, A. Köhler, O. Zarini, J. M. Krämer, M. Garten, A. Huebl, R. Gebhardt, U. Helbig, S. Bock, K. Zeil, A. Debus, M. Bussmann, U. Schramm, and A. Irman. Demonstration of a beam loaded nanocoulomb-class laser wakefield accelerator. *Nature Communications*, 8(1):487, Sep 2017.

[51] S M Hooker, R Bartolini, S P D Mangles, A Tünnermann, L Corner, J Limpert, A Seryi, and R Walczak. Multi-pulse laser wakefield acceleration: a new route to efficient, high-repetition-rate plasma accelerators and high flux radiation sources. *Journal of Physics B: Atomic, Molecular and Optical Physics*, 47(23):234003, nov 2014.

[52] O. Jakobsson, S. M. Hooker, and R. Walczak. Gev-scale accelerators driven by plasma-modulated pulses from kilohertz lasers. *Phys. Rev. Lett.*, 127:184801, Oct 2021.

[53] W. P. Leemans, A. J. Gonsalves, H.-S. Mao, K. Nakamura, C. Benedetti, C. B. Schroeder, Cs. Tóth, J. Daniels, D. E. Mittelberger, S. S. Bulanov, J.-L. Vay,

C. G. R. Geddes, and E. Esarey. Multi-gev electron beams from capillary-discharge-guided subpetawatt laser pulses in the self-trapping regime. *Phys. Rev. Lett.*, 113:245002, Dec 2014.

[54] M. Litos, E. Adli, W. An, C. I. Clarke, C. E. Clayton, S. Corde, J. P. Delahaye, R. J. England, A. S. Fisher, J. Frederico, S. Gessner, S. Z. Green, M. J. Hogan, C. Joshi, W. Lu, K. A. Marsh, W. B. Mori, P. Muggli, N. Vafaei-Najafabadi, D. Walz, G. White, Z. Wu, V. Yakimenko, and G. Yocky. High-efficiency acceleration of an electron beam in a plasma wakefield accelerator. *Nature*, 515(7525):92–95, Nov 2014.

[55] C. Benedetti, S. S. Bulanov, E. Esarey, C. G. R. Geddes, A. J. Gonsalves, A. Huebl, R. Lehe, K. Nakamura, C. B. Schroeder, D. Terzani, J. van Tilborg, M. Turner, J. L. Vay, T. Zhou, F. Albert, J. Bromage, E. M. Campbell, D. H. Froula, J. P. Palastro, J. Zuegel, D. Bruhwiler, N. M. Cook, B. Cros, M. C. Downer, M. Fuchs, B. A. Shadwick, S. J. Gessner, M. J. Hogan, S. M. Hooker, C. Jing, K. Krushelnick, A. G. R. Thomas, W. P. Leemans, A. R. Maier, J. Osterhoff, K. Poder, M. Thevenet, W. B. Mori, M. Palmer, J. G. Power, and N. Vafaei-Najafabadi. Linear collider based on laser-plasma accelerators, 2022.

[56] A. Ghaith, M.-E. Couprie, D. Oumbarek-Espinos, I.A. Andriyash, F. Massimo, J.A. Clarke, M. Courthold, V. Bayliss, A. Bernhard, M. Trunk, M. Valléau, O. Marcouillé, A. Chancé, S. Licciardi, V. Malka, F. Nguyen, and G. Dattoli. Undulator design for a laser-plasma-based free-electron-laser. *Physics Reports*, 937:1–73, 2021. Undulator design for a laser-plasma-based free-electron-laser.

[57] N. Bourgeois, J. Cowley, and S. M. Hooker. Two-pulse ionization injection into quasilinear laser wakefields. *Phys. Rev. Lett.*, 111:155004, Oct 2013.

[58] F. Albert and A. G. R. Thomas. Applications of laser wakefield accelerator-based light sources. *Plasma Physics and Controlled Fusion*, 58(10):103001, Sep 2016.

[59] S. Kneip, C. McGuffey, F. Dollar, M. S. Bloom, V. Chvykov, G. Kalintchenko, K. Krushelnick, A. Maksimchuk, S. P. D. Mangles, T. Matsuoka, Z. Najmudin, C. A. J. Palmer, J. Schreiber, W. Schumaker, A. G. R. Thomas, and V. Yanovsky. X-ray phase contrast imaging of biological specimens with femtosecond pulses of betatron radiation from a compact laser plasma wakefield accelerator. *Applied Physics Letters*, 99(9):093701, 2011.

[60] J. M. Cole, D. R. Symes, N. C. Lopes, J. C. Wood, K. Poder, S. Alatabi, S. W. Botchway, P. S. Foster, S. Gratton, S. Johnson, C. Kamperidis, O. Kononenko, M. De Lazzari, C. A. J. Palmer, D. Rusby, J. Sanderson, M. Sandholzer, G. Sarri, Z. Szoke-Kovacs, L. Teboul, J. M. Thompson, J. R. Warwick, H. Westerberg, M. A. Hill, D. P. Norris, S. P. D. Mangles, and Z. Najmudin. High-resolution $\mu$ct of a mouse embryo using a compact laser-driven x-ray betatron source. *Proceedings of the National Academy of Sciences*, 115(25):6335–6340, 2018.

[61] A. Döpp, L. Hehn, J. Götzfried, J. Wenz, M. Gilljohann, H. Ding, S. Schindler, F. Pfeiffer, and S. Karsch. Quick x-ray microtomography using a laser-driven betatron source. *Optica*, 5(2):199–203, Feb 2018.

[62] M. Fuchs, R. Weingartner, A. Popp, Z. Major, S. Becker, J. Osterhoff, I. Cortrie, B. Zeitler, R. Hörlein, G. D. Tsakiris, U. Schramm, T. P. Rowlands-Rees, S. M. Hooker, D. Habs, F. Krausz, S. Karsch, and F. Grüner. Laser-driven soft-x-ray undulator source. *Nature Physics*, 5(11):826–829, Nov 2009.

[63] K. N. Kim, Y. Hwangbo, S.-g. Jeon, J. Kim, S. Han, and K. B. Kim. Characteristics of a very high energy electron beam in a laser wakefield accelerator for cancer therapy. *Journal of the Korean Physical Society*, 77(5):399–403, Sep 2020.

[64] L. Labate, D. Palla, D. Panetta, F. Avella, F. Baffigi, F. Brandi, F. Di Martino, L. Fulgentini, A. Giulietti, P. Köster, D. Terzani, P. Tomassini, C. Traino, and L. A. Gizzi. Toward an effective use of laser-driven very high energy electrons for radiotherapy: Feasibility assessment of multi-field and intensity modulation irradiation schemes. *Scientific Reports*, 10(1):17307, Oct 2020.

[65] T. Kurz, T. Heinemann, M. F. Gilljohann, Y. Y. Chang, J. P. Couperus Cabadağ, A. Debus, O. Kononenko, R. Pausch, S. Schöbel, R. W. Assmann, M. Bussmann, H. Ding, J. Götzfried, A. Köhler, G. Raj, S. Schindler, K. Steiniger, O. Zarini, S. Corde, A. Döpp, B. Hidding, S. Karsch, U. Schramm, A. Martinez de la Ossa, and A. Irman. Demonstration of a compact plasma accelerator powered by laser-accelerated electron beams. *Nature Communications*, 12(1):2895, May 2021.

[66] P. Varga and P. Török. The Gaussian wave solution of Maxwell's equations and the validity of scalar wave approximation. *Optics Communications*, 152(1):108 – 118, 1998.

[67] B. Saleh and M. Teich. *Fundamentals of Photonics, 3rd Edition*. Feb 2019.

[68] S. Feng and H. G. Winful. Physical origin of the Gouy phase shift. *Opt. Lett.*, 26(8):485–487, Apr 2001.

[69] P. Gibbon. *Short Pulse Laser Interactions with Matter*. Published by Imperial College Press and distributed by World Scientific Publishing Co., 2005.

[70] J. D. Lawson. Lasers and accelerators. *IEEE Transactions on Nuclear Science*, 26(3):4217–4219, 1979.

[71] P. M. Woodward. A method of calculating the field over a plane aperture required to produce a given polar diagram. *Journal of the Institution of Electrical Engineers-Part IIIA: Radiolocation*, 93(10):1554–1558, 1946.

[72] R. B. Palmer. *A laser driven grating Linac*. Birkhaeuser Verlag, Switzerland, 1980.

[73] E. Esarey, C. B. Schroeder, and W. P. Leemans. Physics of laser-driven plasma-based electron accelerators. *Rev. Mod. Phys.*, 81:1229–1285, Aug 2009.

[74] W. L. Kruer. *The Physics of Laser Plasma Interactions*. CRC Press, 2003.

[75] F. Chen. *Introduction to Plasma Physics and Controlled Fusion*. Third edition. Springer International Publishing AG Switzerland, 2016.

[76] P. Lambropoulos. Topics on multiphoton processes in atoms**work supported by a grant from the national science foundation no. mps74-17553. volume 12 of *Advances in Atomic and Molecular Physics*, pages 87–164. Academic Press, 1976.

[77] G. S. Voronov and N. B. Delone. Ionization of the xenon atom by the electric field of ruby laser emission. *Soviet Journal of Experimental and Theoretical Physics Letters*, 1:66, Apr 1965.

[78] P. Agostini, F. Fabre, G. Mainfray, G. Petite, and N. K. Rahman. Free-free transitions following six-photon ionization of xenon atoms. *Phys. Rev. Lett.*, 42:1127–1130, Apr 1979.

[79] T Auguste, P Monot, L A Lompre, G Mainfray, and C Manus. Multiply charged ions produced in noble gases by a 1 ps laser pulse at lambda =1053 nm. *Journal of Physics B: Atomic, Molecular and Optical Physics*, 25(20):4181–4194, oct 1992.

[80] M. V. Ammosov, N. B. Delone, and V. P. Krainov. Tunnel Ionization Of Complex Atoms And Atomic Ions In Electromagnetic Field. In John A. Alcock, editor, *High Intensity Laser Processes*, volume 0664, pages 138 – 141. International Society for Optics and Photonics, SPIE, 1986.

[81] G. L. Yudin and M. Y. Ivanov. Nonadiabatic tunnel ionization: Looking inside a laser cycle. *Phys. Rev. A*, 64:013409, Jun 2001.

[82] Y. Ma, D. Seipt, A. E. Hussein, S. Hakimi, N. F. Beier, S. B. Hansen, J. Hinojosa, A. Maksimchuk, J. Nees, K. Krushelnick, A. G. R. Thomas, and F. Dollar. Polarization-dependent self-injection by above threshold ionization heating in a laser wakefield accelerator. *Phys. Rev. Lett.*, 124:114801, Mar 2020.

[83] P. Sprangle, C. Tang, and E. Esarey. Relativistic self-focusing of short-pulse radiation beams in plasmas. *IEEE Transactions on Plasma Science*, 15(2):145–153, 1987.

[84] R. Wagner, S.-Y. Chen, A. Maksimchuk, and D. Umstadter. Electron acceleration by a laser wakefield in a relativistically self-guided channel. *Phys. Rev. Lett.*, 78:3125–3128, Apr 1997.

[85] A. G. R. Thomas, Z. Najmudin, S. P. D. Mangles, C. D. Murphy, A. E. Dangor, C. Kamperidis, K. L. Lancaster, W. B. Mori, P. A. Norreys, W. Rozmus, and K. Krushelnick. Effect of laser-focusing conditions on propagation and monoenergetic electron production in laser-wakefield accelerators. *Phys. Rev. Lett.*, 98:095004, Mar 2007.

[86] C. Ren, B. J. Duda, R. G. Hemker, W. B. Mori, T. Katsouleas, T. M. Antonsen, and P. Mora. Compressing and focusing a short laser pulse by a thin plasma lens. *Phys. Rev. E*, 63:026411, Jan 2001.

[87] J. Faure, Y. Glinec, J. J. Santos, F. Ewald, J.-P. Rousseau, S. Kiselev, A. Pukhov, T. Hosokai, and V. Malka. Observation of laser-pulse shortening in nonlinear plasma waves. *Phys. Rev. Lett.*, 95:205003, Nov 2005.

[88] E. Esarey, P. Sprangle, J. Krall, and A. Ting. Overview of plasma-based accelerator concepts. *IEEE Transactions on Plasma Science*, 24(2):252–288, 1996.

[89] W. Lu, M. Tzoufras, C. Joshi, F. S. Tsung, W. B. Mori, J. Vieira, R. A. Fonseca, and L. O. Silva. Generating multi-GeV electron bunches using single stage laser wakefield acceleration in a 3d nonlinear regime. *Phys. Rev. ST Accel. Beams*, 10:061301, Jun 2007.

[90] E. Esarey and M. Pilloff. Trapping and acceleration in nonlinear plasma waves. *Physics of Plasmas*, 2(5):1432–1436, 1995.

[91] S. V. Bulanov, F. Pegoraro, A. M. Pukhov, and A. S. Sakharov. Transverse-wake wave breaking. *Phys. Rev. Lett.*, 78:4205–4208, Jun 1997.

[92] S. M. Hooker. Developments in laser-driven plasma accelerators. *Nat. Photonics*, 7:775 –, Sep 2013.

[93] B. A. Shadwick, C. B. Schroeder, and E. Esarey. Nonlinear laser energy depletion in laser-plasma accelerators. *Physics of Plasmas*, 16(5):056704, 2009.

[94] C. G. Durfee and H. M. Milchberg. Light pipe for high intensity laser pulses. *Phys. Rev. Lett.*, 71:2409–2412, Oct 1993.

[95] Y. Ehrlich, C. Cohen, A. Zigler, J. Krall, P. Sprangle, and E. Esarey. Guiding of high intensity laser pulses in straight and curved plasma channel experiments. *Phys. Rev. Lett.*, 77:4186–4189, Nov 1996.

[96] D. J. Spence and S. M. Hooker. Investigation of a hydrogen plasma waveguide. *Phys. Rev. E*, 63:015401, Dec 2000.

[97] R. J. Shalloo, C. Arran, L. Corner, J. Holloway, J. Jonnerby, R. Walczak, H. M. Milchberg, and S. M. Hooker. Hydrodynamic optical-field-ionized plasma channels. *Phys. Rev. E*, 97:053203, May 2018.

[98] A. Picksley, A. Alejo, J. Cowley, N. Bourgeois, L. Corner, L. Feder, J. Holloway, H. Jones, J. Jonnerby, H. M. Milchberg, L. R. Reid, A. J. Ross, R. Walczak, and S. M. Hooker. Guiding of high-intensity laser pulses in 100-mm-long hydrodynamic optical-field-ionized plasma channels. *Phys. Rev. Accel. Beams*, 23:081303, Aug 2020.

[99] C. B. Schroeder, E. Esarey, B. A. Shadwick, and W. P. Leemans. Trapping, dark current, and wave breaking in nonlinear plasma waves. *Physics of Plasmas*, 13(3):033103, 2006.

[100] S. Kalmykov, S. A. Yi, V. Khudik, and G. Shvets. Electron self-injection and trapping into an evolving plasma bubble. *Phys. Rev. Lett.*, 103:135004, Sep 2009.

[101] S. P. D. Mangles, G. Genoud, M. S. Bloom, M. Burza, Z. Najmudin, A. Persson, K. Svensson, A. G. R. Thomas, and C.-G. Wahlström. Self-injection threshold in self-guided laser wakefield accelerators. *Phys. Rev. ST Accel. Beams*, 15:011302, Jan 2012.

[102] S. Kuschel, M. B. Schwab, M. Yeung, D. Hollatz, A. Seidel, W. Ziegler, A. Sävert, M. C. Kaluza, and M. Zepf. Controlling the self-injection threshold in laser wakefield accelerators. *Phys. Rev. Lett.*, 121:154801, Oct 2018.

[103] C. McGuffey, A. G. R. Thomas, W. Schumaker, T. Matsuoka, V. Chvykov, F. J. Dollar, G. Kalintchenko, V. Yanovsky, A. Maksimchuk, K. Krushelnick, V. Yu. Bychenkov, I. V. Glazyrin, and A. V. Karpeev. Ionization induced trapping in a laser wakefield accelerator. *Phys. Rev. Lett.*, 104:025004, Jan 2010.

[104] C. E. Clayton, J. E. Ralph, F. Albert, R. A. Fonseca, S. H. Glenzer, C. Joshi, W. Lu, K. A. Marsh, S. F. Martins, W. B. Mori, A. Pak, F. S. Tsung, B. B. Pollock, J. S. Ross, L. O. Silva, and D. H. Froula. Self-guided laser wakefield acceleration beyond 1 GeV using ionization-induced injection. *Phys. Rev. Lett.*, 105:105003, Sep 2010.

[105] M. Z. Mo, A. Ali, S. Fourmaux, P. Lassonde, J. C. Kieffer, and R. Fedosejevs. Quasimonoenergetic electron beams from laser wakefield acceleration in pure nitrogen. *Applied Physics Letters*, 100(7):074101, 2012.

[106] B. B. Pollock, C. E. Clayton, J. E. Ralph, F. Albert, A. Davidson, L. Divol, C. Filip, S. H. Glenzer, K. Herpoldt, W. Lu, K. A. Marsh, J. Meinecke, W. B. Mori, A. Pak, T. C. Rensink, J. S. Ross, J. Shaw, G. R. Tynan, C. Joshi, and D. H. Froula. Demonstration of a narrow energy spread, $\sim 0.5$ GeV electron beam from a two-stage laser wakefield accelerator. *Phys. Rev. Lett.*, 107:045001, Jul 2011.

[107] C. G. R. Geddes, K. Nakamura, G. R. Plateau, Cs. Toth, E. Cormier-Michel, E. Esarey, C. B. Schroeder, J. R. Cary, and W. P. Leemans. Plasma-density-gradient injection of low absolute-momentum-spread electron bunches. *Phys. Rev. Lett.*, 100:215004, May 2008.

[108] A. J. Gonsalves, K. Nakamura, C. Lin, D. Panasenko, S. Shiraishi, T. Sokollik, C. Benedetti, C. B. Schroeder, C. G. R. Geddes, J. van Tilborg, J. Osterhoff, E. Esarey, C. Toth, and W. P. Leemans. Tunable laser plasma accelerator based on longitudinal density tailoring. *Nature Physics*, 7(11):862–866, Nov 2011.

[109] H. Ekerfelt, M. Hansson, I. Gallardo González, X. Davoine, and O. Lundh. A tunable electron beam source using trapping of electrons in a density down-ramp in laser wakefield acceleration. *Scientific Reports*, 7(1):12229, Sep 2017.

[110] K. Schmid, A. Buck, C. M. S. Sears, J. M. Mikhailova, R. Tautz, D. Herrmann, M. Geissler, F. Krausz, and L. Veisz. Density-transition based electron injector for laser driven wakefield accelerators. *Phys. Rev. ST Accel. Beams*, 13:091301, Sep 2010.

[111] A. Buck, J. Wenz, J. Xu, K. Khrennikov, K. Schmid, M. Heigoldt, J. M. Mikhailova, M. Geissler, B. Shen, F. Krausz, S. Karsch, and L. Veisz. Shock-front injector for high-quality laser-plasma acceleration. *Phys. Rev. Lett.*, 110:185006, May 2013.

[112] L. T. Ke, K. Feng, W. T. Wang, Z. Y. Qin, C. H. Yu, Y. Wu, Y. Chen, R. Qi, Z. J. Zhang, Y. Xu, X. J. Yang, Y. X. Leng, J. S. Liu, R. X. Li, and Z. Z. Xu. Near-GeV electron beams at a few per-mille level from a laser wakefield accelerator via density-tailored plasma. *Phys. Rev. Lett.*, 126:214801, May 2021.

[113] E. Esarey, R. F. Hubbard, W. P. Leemans, A. Ting, and P. Sprangle. Electron injection into plasma wakefields by colliding laser pulses. *Phys. Rev. Lett.*, 79:2682–2685, Oct 1997.

[114] C. B. Schroeder, P. B. Lee, J. S. Wurtele, E. Esarey, and W. P. Leemans. Generation of ultrashort electron bunches by colliding laser pulses. *Phys. Rev. E*, 59:6037–6047, May 1999.

[115] H. Kotaki, S. Masuda, M. Kando, J. K. Koga, and K. Nakajima. Head-on injection of a high quality electron beam by the interaction of two laser pulses. *Physics of Plasmas*, 11(6):3296–3302, 2004.

[116] G. Fubiani, E. Esarey, C. B. Schroeder, and W. P. Leemans. Beat wave injection of electrons into plasma waves using two interfering laser pulses. *Phys. Rev. E*, 70:016402, Jul 2004.

[117] J. Faure, C. Rechatin, A. Norlin, A. Lifschitz, Y. Glinec, and V. Malka. Controlled injection and acceleration of electrons in plasma wakefields by colliding laser pulses. *Nature*, 444(7120):737–739, Dec 2006.

[118] H. Kotaki, I. Daito, M. Kando, Y. Hayashi, K. Kawase, T. Kameshima, Y. Fukuda, T. Homma, J. Ma, L.-M. Chen, T. Zh. Esirkepov, A. S. Pirozhkov, J. K. Koga, A. Faenov, T. Pikuz, H. Kiriyama, H. Okada, T. Shimomura, Y. Nakai, M. Tanoue, H. Sasao, D. Wakai, H. Matsuura, S. Kondo, S. Kanazawa, A. Sugiyama, H. Daido, and S. V. Bulanov. Electron optical injection with head-on and countercrossing colliding laser pulses. *Phys. Rev. Lett.*, 103:194803, Nov 2009.

[119] O. Lundh, J. Lim, C. Rechatin, L. Ammoura, A. Ben-Ismaïl, X. Davoine, G. Gallot, J.-P. Goddet, E. Lefebvre, V. Malka, and J. Faure. Few femtosecond, few kiloampere electron bunch produced by a laser-plasma accelerator. *Nature Physics*, 7:219, Jan 2011.

[120] F. Li, J. F. Hua, X. L. Xu, C. J. Zhang, L. X. Yan, Y. C. Du, W. H. Huang, H. B. Chen, C. X. Tang, W. Lu, C. Joshi, W. B. Mori, and Y. Q. Gu. Generating high-brightness electron beams via ionization injection by transverse colliding lasers in a plasma-wakefield accelerator. *Phys. Rev. Lett.*, 111:015003, Jul 2013.

[121] B. Hidding, G. Pretzler, J. B. Rosenzweig, T. Königstein, D. Schiller, and D. L. Bruhwiler. Ultracold electron bunch generation via plasma photocathode emission and acceleration in a beam-driven plasma blowout. *Phys. Rev. Lett.*, 108:035001, Jan 2012.

[122] E. Cormier-Michel, B. A. Shadwick, C. G. R. Geddes, E. Esarey, C. B. Schroeder, and W. P. Leemans. Unphysical kinetic effects in particle-in-cell modeling of laser wakefield accelerators. *Phys. Rev. E*, 78:016404, Jul 2008.

[123] R. Courant, K. Friedrichs, and H. Lewy. Über die partiellen differenzengleichungen der mathematischen physik. *Mathematische Annalen*, 100(1):32–74, Dec 1928.

[124] K. Yee. Numerical solution of initial boundary value problems involving maxwell's equations in isotropic media. *IEEE Transactions on Antennas and Propagation*, 14(3):302–307, 1966.

[125] R. A. Fonseca, L. O. Silva, F. S. Tsung, V. K. Decyk, W. Lu, C. Ren, W. B. Mori, S. Deng, S. Lee, T. Katsouleas, and J. C. Adam. Osiris: A three-dimensional, fully relativistic particle in cell code for modeling plasma based accelerators. In P. M. A. Sloot, A. G. Hoekstra, C. J. K. Tan, and J. J. Dongarra, editors, *Computational Science — ICCS 2002*, pages 342–351, Berlin, Heidelberg, 2002. Springer Berlin Heidelberg.

[126] T. D. Arber, K. Bennett, C. S. Brady, A. Lawrence-Douglas, M. G. Ramsay, N. J. Sircombe, P. Gillies, R. G Evans, H. Schmitz, A. R. Bell, and C. P. Ridgers. Contemporary particle-in-cell approach to laser-plasma modelling. *Plasma Physics and Controlled Fusion*, 57(11):113001, sep 2015.

[127] J. Derouillat, A. Beck, F. Pérez, T. Vinci, M. Chiaramello, A. Grassi, M. Flé, G. Bouchard, I. Plotnikov, N. Aunai, and et al. Smilei: A collaborative, open-source, multi-purpose particle-in-cell code for plasma simulation. *Computer Physics Communications*, 222:351–373, Jan 2018.

[128] O. F. Hagena and W. Obert. Cluster formation in expanding supersonic jets: Effect of pressure, temperature, nozzle size, and test gas. *The Journal of Chemical Physics*, 56(5):1793–1802, 1972.

[129] T. Ditmire, T. Donnelly, A. M. Rubenchik, R. W. Falcone, and M. D. Perry. Interaction of intense laser pulses with atomic clusters. *Phys. Rev. A*, 53:3379–3402, May 1996.

[130] O. F. Hagena. Cluster ion sources (invited),. *Rev Sci. Instrum.*, 63(4):2374, 1992.

[131] R. A. Smith, T. Ditmire, and J. W. G. Tisch. Characterization of a cryogenically cooled high-pressure gas jet for laser/cluster interaction experiments. *Review of Scientific Instruments*, 69(11):3798–3804, 1998.

[132] A. Murakami, J. Miyazawa, H. Tsuchiya, T. Murase, N. Ashikawa, T. Morisaki, R. Sakamoto, and H. Yamada. Characteristics of hydrogen supersonic cluster beam generated by a laval nozzle. *J. Plasma Fusion Res. SERIES*, 9:79–83, Feb 2010.

[133] H. Lu, G. Chen, G. Ni, R. Li, and Z. Xu. Impact of gas backing pressure and geometry of conical nozzle on the formation of methane clusters in supersonic jets. *J. Phys. Chem. A*, 114(1):2–9, Jan 2010.

[134] Y. Tao, R. Hagmeijer, E. T. A. van der Weide, H. M. J. Bastiaens, and K.-J. Boller. Revisiting argon cluster formation in a planar gas jet for high-intensity laser matter interaction. *Journal of Applied Physics*, 119(16):164901, 2016.

[135] M. Aladi, R. Bolla, D.E. Cardenas, L. Veisz, and I.B. Földes. Cluster size distributions in gas jets for different nozzle geometries. *Journal of Instrumentation*, 12(06):C06020–C06020, jun 2017.

[136] S. Grieser, B. Aurand, E. Aktan, D. Bonaventura, M. Büscher, M. Cerchez, I. Engin, L. Leßmann, C. Mannweiler, R. Prasad, O. Willi, and A. Khoukaz. Nm-sized cryogenic hydrogen clusters for a laser-driven proton source. *Review of Scientific Instruments*, 90(4):043301, 2019.

[137] B. R. Lee, P. K. Singh, Y. J. Rhee, and C. H. Nam. Spatiotemporal characteristics of high-density gas jet and absolute determination of size and density of gas clusters. *Scientific Reports*, 10(1):12973, Jul 2020.

[138] T. Ditmire, T. Donnelly, A. M. Rubenchik, R. W. Falcone, and M. D. Perry. Interaction of intense laser pulses with atomic clusters. *Phys. Rev. A*, 53:3379–3402, May 1996.

[139] H. M. Milchberg, S. J. McNaught, and E. Parra. Plasma hydrodynamics of the intense laser-cluster interaction. *Phys. Rev. E*, 64:056402, Oct 2001.

[140] A. Gupta, T. M. Antonsen, and H. M. Milchberg. Propagation of intense short laser pulses in a gas of atomic clusters. *Phys. Rev. E*, 70:046410, Oct 2004.

[141] I. Yu. Skobelev, A. Ya. Faenov, A. I. Magunov, T. A. Pikuz, A. S. Boldarev, V. A. Gasilov, J. Abdallach, G. C. Junkel-Vives, T. Auguste, S. Dobosz, P. d'Oliveira, S. Hulin, P. Monot, F. Blasco, F. Dorchies, T. Caillaud, C. Bonte, C. Stenz, F. Salin, P. A. Loboda, I. A. Litvinenko, V. V. Popova, G. V. Baidin, and B. Yu. Sharkov. X-ray spectroscopy diagnostic of a plasma produced by femtosecond laser pulses irradiating a cluster target. *Journal of Experimental and Theoretical Physics*, 94(5):966–976, May 2002.

[142] B. N. Breizman, A. V. Arefiev, and M. V. Fomyts'kyi. Nonlinear physics of laser-irradiated microclusters. *Phys. Plasmas*, 12(5):056706, 2005.

[143] T. M. Antonsen, T. Taguchi, A. Gupta, J. Palastro, and H. M. Milchberg. Resonant heating of a cluster plasma by intense laser light. *Phys. Plasmas*, 12(5):056703, 2005.

[144] D. R. Symes, M. Hohenberger, A. Henig, and T. Ditmire. Anisotropic explosions of hydrogen clusters under intense femtosecond laser irradiation. *Phys. Rev. Lett.*, 98:123401, Mar 2007.

[145] Y. Fukuda, Y. Akahane, M. Aoyama, Y. Hayashi, T. Homma, N. Inoue, M. Kando, S. Kanazawa, H. Kiriyama, S. Kondo, H. Kotaki, S. Masuda, M. Mori, A. Yamazaki, K. Yamakawa, E.Yu. Echkina, I.N. Inovenkov, J. Koga, and S.V. Bulanov. Ultrarelativistic electron generation during the intense, ultrashort laser pulse interaction with clusters. *Phys. Lett A*, 363(1):130 – 135, 2007.

[146] Th. Fennel, K.-H. Meiwes-Broer, J. Tiggesbäumker, P.-G. Reinhard, P. M. Dinh, and E. Suraud. Laser-driven nonlinear cluster dynamics. *Rev. Mod. Phys.*, 82:1793–1842, Jun 2010.

[147] A. McPherson, B. D. Thompson, A. B. Borisov, K. Boyer, and C. K. Rhodes. Multiphoton-induced x-ray emission at 4-5 kev from xe atoms with multiple core vacancies. *Nature*, 370(6491):631–634, 1994.

[148] Y. Fukuda, A. Ya. Faenov, T. Pikuz, M. Kando, H. Kotaki, I. Daito, J. Ma, L. M. Chen, T. Homma, K. Kawase, T. Kameshima, T. Kawachi, H. Daido, T. Kimura, T. Tajima, Y. Kato, and S. V. Bulanov. Soft x-ray source for nanostructure imaging using femtosecond-laser-irradiated clusters. *Applied Physics Letters*, 92(12):121110, 2008.

[149] T. D. Donnelly, T. Ditmire, K. Neuman, M. D. Perry, and R. W. Falcone. High-order harmonic generation in atom clusters. *Phys. Rev. Lett.*, 76:2472–2475, Apr 1996.

[150] J. W. G. Tisch, T. Ditmire, D. J. Fraser, N. Hay, M. B. Mason, E. Springate, J. P. Marangos, and M. H. R. Hutchinson. Investigation of high-harmonic generation from xenon atom clusters. *Journal of Physics B: Atomic, Molecular and Optical Physics*, 30(20):L709–L714, oct 1997.

[151] M. Aladi et al. High harmonic generation and ionization effects in cluster targets. *High Power Laser Sci. Eng.*, 2:e32, 2014.

[152] Y. Tao, R. Hagmeijer, H. M. J. Bastiaens, S. J. Goh, P. J. M. van der Slot, S. G. Biedron, S. V. Milton, and K.-J. Boller. Cluster size dependence of high-order harmonic generation. *New Journal of Physics*, 19(8):083017, aug 2017.

[153] T. Ditmire, J. Zweiback, V. P. Yanovsky, T. E. Cowan, G. Hays, and K. B. Wharton. Nuclear fusion from explosions of femtosecond laser-heated deuterium clusters. *Nature*, 398(6727):489–492, Apr 1999.

[154] T. Tajima, Y. Kishimoto, and M. C. Downer. Optical properties of cluster plasma. *Phys. Plasmas*, 6(10):3759–3764, 1999.

[155] L. Zhang, L.-M. Chen, W.-M. Wang, W.-C. Yan, D.-W. Yuan, J.-Y. Mao, Z.-H. Wang, C. Liu, Z.-W. Shen, A. Faenov, T. Pikuz, D.-Z. Li, Y.-T. Li, Q.-L. Dong, X. Lu, J.-L. Ma, Z.-Y. Wei, Z.-M. Sheng, and J. Zhang. Electron acceleration via high contrast laser interacting with submicron clusters. *Applied Physics Letters*, 100(1):014104, 2012.

[156] M. Mirzaie, N. A M Hafz, S. Li, K. Gao, G. Li, Q. Ul-Ain, and J. Zhang. Laser acceleration in argon clusters and gas media. *Plasma Physics and Controlled Fusion*, 58(3):034014, Mar 2016.

[157] J. Wood. *Betatron radiation from laser wakefield accelerators and its applications*. PhD thesis, Imperial College London, 2017.

[158] S. Dobosz, M. Lezius, M. Schmidt, P. Meynadier, M. Perdrix, D. Normand, J.-P. Rozet, and D. Vernhet. Absolute kev photon yields from ultrashort laser-field-induced hot nanoplasmas. *Phys. Rev. A*, 56:R2526–R2529, Oct 1997.

[159] T. Ditmire, R. A. Smith, J. W. G. Tisch, and M. H. R. Hutchinson. High intensity laser absorption by gases of atomic clusters. *Phys. Rev. Lett.*, 78:3121–3124, Apr 1997.

[160] Lin Jing-Quan, Zhang Jie, Li Ying-Jun, Chen Li-Ming, Lü Tie-Zheng, Teng Hao, Man Bao-Yuan, and Zhao Li-Zeng. Measurements of laser absorption and ion energy in femtosecond laser-cluster interaction. *Chinese Physics Letters*, 18(2):211–213, Feb 2001.

[161] A. Mikaberidze, U. Saalmann, and J. M. Rost. Energy absorption of xenon clusters in helium nanodroplets under strong laser pulses. *Phys. Rev. A*, 77:041201, Apr 2008.

[162] I. Last and J. Jortner. Quasiresonance ionization of large multicharged clusters in a strong laser field. *Phys. Rev. A*, 60:2215–2221, Sep 1999.

[163] C. Siedschlag and J. M. Rost. Enhanced ionization in small rare-gas clusters. *Phys. Rev. A*, 67:013404, Jan 2003.

[164] C. Deiss. *Simulation of the dynamics of laser-cluster interaction.* PhD thesis, TU Wien, 2009.

[165] I. Last and J. Jortner. Electron and nuclear dynamics of molecular clusters in ultraintense laser fields. ii. electron dynamics and outer ionization of the nanoplasma. *The Journal of Chemical Physics*, 120(3):1348–1360, 2004.

[166] T. Döppner, J. P. Müller, A. Przystawik, S. Göde, J. Tiggesbäumker, K.-H. Meiwes-Broer, C. Varin, L. Ramunno, T. Brabec, and T. Fennel. Steplike intensity threshold behavior of extreme ionization in laser-driven xenon clusters. *Phys. Rev. Lett.*, 105:053401, Jul 2010.

[167] J. Zweiback, T. Ditmire, and M. D. Perry. Femtosecond time-resolved studies of the dynamics of noble-gas cluster explosions. *Phys. Rev. A*, 59:R3166–R3169, May 1999.

[168] Gustav Mie. Beiträge zur optik trüber medien, speziell kolloidaler metallösungen. *Annalen der Physik*, 330(3):377–445, 1908.

[169] D. Komar. *Dynamics of laser-induced cluster Coulomb explosion studied by charge-state and energy resolving ion spectroscopy.* PhD thesis, University of Rostock, 2018.

[170] J. W. G. Tisch, N. Hay, K. J. Mendham, E. Springate, D. R. Symes, A. J. Comley, M. B. Mason, E. T. Gumbrell, T. Ditmire, R. A. Smith, J. P. Marangos, and M. H. R. Hutchinson. Interaction of intense laser pulses with atomic clusters: Measurements of ion emission, simulations and applications. *Nuclear Instruments and Methods in Physics Research Section B, Beam Interactions with Materials and Atoms*, 205(1-4):310–323, 2003. ATOMIC AND MOLECULAR PHYSICS.

[171] H. M. Milchberg, S. J. McNaught, and E. Parra. Plasma hydrodynamics of the intense laser-cluster interaction. *Phys. Rev. E*, 64:056402, Oct 2001.

[172] M. Kundu and D. Bauer. Nonlinear resonance absorption in the laser-cluster interaction. *Phys. Rev. Lett.*, 96:123401, Mar 2006.

[173] C. Rose-Petruck, K. J. Schafer, K. R. Wilson, and C. P. J. Barty. Ultrafast electron dynamics and inner-shell ionization in laser driven clusters. *Phys. Rev. A*, 55:1182–1190, Feb 1997.

[174] I. Last and J. Jortner. Dynamics of the coulomb explosion of large clusters in a strong laser field. *Phys. Rev. A*, 62:013201, Jun 2000.

[175] D. Bauer. Small rare gas clusters in laser fields: ionization and absorption at long and short laser wavelengths. *Journal of Physics B: Atomic, Molecular and Optical Physics*, 37(15):3085–3101, Jul 2004.

[176] C. Jungreuthmayer, M. Geissler, J. Zanghellini, and T. Brabec. Microscopic analysis of large-cluster explosion in intense laser fields. *Phys. Rev. Lett.*, 92:133401, Mar 2004.

[177] S. Sarkar, R. Gopal, M. Anand, M. P. Kumar, and M. Krishnamurthy. On the importance of field driven single particle processes in short pulse absorption of clusters. *Scientific Reports*, 9(1):15135, Oct 2019.

[178] M. W. Mayr, L. Ceurvorst, M. F. Kasim, J. D. Sadler, B. Spiers, K. Glize, A. F. Savin, N. Bourgeois, F. Keeble, A. J. Ross, D. R. Symes, R. Aboushelbaya, R. A. Fonseca, J. Holloway, N. Ratan, R. M. G. M. Trines, R. H. W. Wang, R. Bingham, L. O. Silva, P. N. Burrows, M. Wing, P. P. Rajeev, and P. A. Norreys. Wakefields in a cluster plasma. *Phys. Rev. Accel. Beams*, 22:113501, Nov 2019.

[179] M. W. Mayr, B. Spiers, R. Aboushelbaya, R. W. Paddock, J. D. Sadler, C. Sillett, R. H. W. Wang, K. Krushelnick, and P. A. Norreys. Nonlinear wakefields and electron injection in cluster plasma. *Phys. Rev. Accel. Beams*, 23:093501, Sep 2020.

[180] C. J. Hooker, J. L. Collier, O. Chekhlov, R. Clarke, E. Divall, K. Ertel, B. Fell, P. Foster, S. Hancock, A. Langley, D. Neely, J. Smith, and B. Wyborn. The astra gemini project - a dual-beam petawatt ti:sapphire laser system. *J. Phys. IV France*, 133:673–677, 2006.

[181] M. F. Kasim, J. Holloway, L. Ceurvorst, M. C. Levy, N. Ratan, J. Sadler, R. Bingham, P. N. Burrows, R. Trines, M. Wing, and P. Norreys. Quantitative single shot and spatially resolved plasma wakefield diagnostics. *Phys. Rev. ST Accel. Beams*, 18:081302, Aug 2015.

[182] A. Sävert, S. P. D. Mangles, M. Schnell, E. Siminos, J. M. Cole, M. Leier, M. Reuter, M. B. Schwab, M. Möller, K. Poder, O. Jäckel, G. G. Paulus, C. Spielmann, S. Skupin, Z. Najmudin, and M. C. Kaluza. Direct observation of the injection dynamics of a laser wakefield accelerator using few-femtosecond shadowgraphy. *Phys. Rev. Lett.*, 115:055002, Jul 2015.

[183] N. H. Matlis, S. Reed, S. S. Bulanov, V. Chvykov, G. Kalintchenko, T. Matsuoka, P. Rousseau, V. Yanovsky, A. Maksimchuk, S. Kalmykov, G. Shvets, and M. C. Downer. Snapshots of laser wakefields. *Nature Physics*, 2(11):749–753, Nov 2006.

[184] M. F. Kasim. *Quantitative optical probing of plasma accelerators*. PhD thesis, University of Oxford, 2017.

[185] K. C. Gupta, N. Jha, P. Deb, D. R. Mishra, and J. K. Fuloria. Determining the mean size and density of clusters, formed in super sonic jets, by rayleigh scattering and mach-zehnder interferometer. *Journal of Applied Physics*, 118(11):114308, 2015.

[186] G. Pretzier, H. Jager, and T. Neger. High-accuracy differential interferometry for the investigation of phase objects. *Measurement Science and Technology*, 4(6):649–658, Jun 1993.

[187] M. Takeda, H. Ina, and S. Kobayashi. Fourier-transform method of fringe-pattern analysis for computer-based topography and interferometry. *J. Opt. Soc. Am.*, 72(1):156–160, Jan 1982.

[188] N. H. Abel. Auflösung einer mechanischen aufgabe. *Journal für die reine und angewandte Mathematik*, 1:153–157, 1826.

[189] L. Montgomery Smith, D. R. Keefer, and S. I. Sudharsanan. Abel inversion using transform techniques. *Journal of Quantitative Spectroscopy and Radiative Transfer*, 39(5):367–373, 1988.

[190] C. Siders, S. Le Blanc, A. Babine, A. Stepanov, A. Sergeev, T. Tajima, and M. Downer. Plasma-based accelerator diagnostics based upon longitudinal interferometry with ultrashort optical pulses. *IEEE Transactions on Plasma Science*, 24(2):301–315, Apr 1996.

[191] S. P. Le Blanc, E. W. Gaul, N. H. Matlis, A. Rundquist, and M. C. Downer. Single-shot measurement of temporal phase shifts by frequency-domain holography. *Opt. Lett.*, 25(10):764–766, May 2000.

[192] P. Dong, S. A. Reed, S. A. Yi, S. Kalmykov, Z. Y. Li, G. Shvets, N. H. Matlis, C. McGuffey, S. S. Bulanov, V. Chvykov, G. Kalintchenko, K. Krushelnick, A. Maksimchuk, T. Matsuoka, A. G. R. Thomas, V. Yanovsky, and M. C. Downer. Holographic visualization of laser wakefields. *New Journal of Physics*, 12(4):045016, Apr 2010.

[193] E. L. Lindman. "Free-space" boundary conditions for the time dependent wave equation. *J. Comput. Phys*, 18(1):66 – 78, 1975.

[194] E. Esarey, A. Ting, P. Sprangle, D. Umstadter, and X. Liu. Nonlinear analysis of relativistic harmonic generation by intense lasers in plasmas. *IEEE Transactions on Plasma Science*, 21(1):95–104, Feb 1993.

[195] D. Teychenné, G. Bonnaud, and J.-L. Bobin. Wave-breaking limit to the wakefield effect in an underdense plasma. *Phys. Rev. E*, 48:R3248–R3251, Nov 1993.

[196] P. Sprangle, E. Esarey, and A. Ting. Nonlinear interaction of intense laser pulses in plasmas. *Phys. Rev. A*, 41:4463–4469, Apr 1990.

[197] P. Sprangle, E. Esarey, and A. Ting. Nonlinear theory of intense laser-plasma interactions. *Phys. Rev. Lett.*, 64:2011–2014, Apr 1990.

[198] C. Shu. High order weighted essentially nonoscillatory schemes for convection dominated problems. *SIAM Review*, 51(1):82–126, 2009.

[199] Y.-T. Zhang and C.-W. Shu. Chapter 5 - ENO and WENO schemes. In R. Abgrall and C.-W. Shu, editors, *Handbook of Numerical Methods for Hyperbolic Problems*, volume 17 of *Handbook of Numerical Analysis*, pages 103 – 122. Elsevier, 2016.

[200] E. Hewitt and R. E. Hewitt. The Gibbs-Wilbraham phenomenon: An episode in fourier analysis. *Archive for History of Exact Sciences*, 21(2):129–160, Jun 1979.

[201] K. Hain, G. Hain, K. V. Roberts, S. J. Roberts, and W. Köppendörfer. Fully ionized pinch collapse. *Zeitschrift für Naturforschung A*, 15(12):1039 – 1050, 1960.

[202] I. R. Lindemuth. A boundary condition for computational magnetohydrodynamics. *Journal of Computational Physics*, 25(2):104 – 117, 1977.

[203] M. Diaz (user "wme7"). Weno. https://github.com/wme7/WENO/blob/master/Non-lineard1/WENO5resAdv1d.m, accessed 09 July 2021.

[204] P. K. Tiwari and V. K. Tripathi. Stimulated raman scattering of a laser in a plasma with clusters. *Physics of Plasmas*, 11(4):1674–1679, 2004.

[205] L. M. Chen, W. C. Yan, D. Z. Li, Z. D. Hu, L. Zhang, W. M. Wang, N. Hafz, J. Y. Mao, K. Huang, Y. Ma, J. R. Zhao, J. L. Ma, Y. T. Li, X. Lu, Z. M. Sheng, Z. Y. Wei, J. Gao, and J. Zhang. Bright betatron x-ray radiation from a laser-driven-clustering gas target. *Scientific Reports*, 3(1):1912, 2013.

[206] S. J. D. Dann, C. D. Baird, N. Bourgeois, O. Chekhlov, S. Eardley, C. D. Gregory, J.-N. Gruse, J. Hah, D. Hazra, S. J. Hawkes, C. J. Hooker, K. Krushelnick, S. P. D. Mangles, V. A. Marshall, C. D. Murphy, Z. Najmudin, J. A. Nees, J. Osterhoff, B. Parry, P. Pourmoussavi, S. V. Rahul, P. P. Rajeev, S. Rozario, J. D. E. Scott, R. A. Smith, E. Springate, Y. Tang, S. Tata, A. G. R. Thomas, C. Thornton, D. R. Symes, and M. J. V. Streeter. Laser wakefield acceleration with active feedback at 5 hz. *Phys. Rev. Accel. Beams*, 22:041303, Apr 2019.

[207] I. A. Andriyash, R. Lehe, and A. Lifschitz. Laser-plasma interactions with a fourier-bessel particle-in-cell method. *Physics of Plasmas*, 23(3):033110, 2016.

[208] M. Aladi, R. Bolla, D.E. Cardenas, L. Veisz, and I.B. Földes. Cluster size distributions in gas jets for different nozzle geometries. *Journal of Instrumentation*, 12(06):C06020–C06020, Jun 2017.

[209] E. Esarey, B. A. Shadwick, P. Catravas, and W. P. Leemans. Synchrotron radiation from electron beams in plasma-focusing channels. *Phys. Rev. E*, 65:056505, May 2002.

[210] A. Pak, K. A. Marsh, S. F. Martins, W. Lu, W. B. Mori, and C. Joshi. Injection and trapping of tunnel-ionized electrons into laser-produced wakes. *Phys. Rev. Lett.*, 104:025003, Jan 2010.

[211] M. H. Cho, V. B. Pathak, H. T. Kim, and C. H. Nam. Controlled electron injection facilitated by nanoparticles for laser wakefield acceleration. *Scientific Reports*, 8(1):16924, Nov 2018.

[212] S. C. Wilks, J. M. Dawson, W. B. Mori, T. Katsouleas, and M. E. Jones. Photon accelerator. *Phys. Rev. Lett.*, 62:2600–2603, May 1989.

[213] C. D. Murphy, R. Trines, J. Vieira, A. J. W. Reitsma, R. Bingham, J. L. Collier, E. J. Divall, P. S. Foster, C. J. Hooker, A. J. Langley, P. A. Norreys, R. A. Fonseca, F. Fiuza, L. O. Silva, J. T. Mendonca, W. B. Mori, J. G. Gallacher, R. Viskup, D. A. Jaroszynski, S. P. D. Mangles, A. G. R. Thomas, K. Krushelnick, and Z. Najmudin. Evidence of photon acceleration by laser wake fields. *Physics of Plasmas*, 13(3):033108, 2006.

[214] P. Chen and A. Spitkovsky. Optimal laser pulse shaping in laser wakefield accelerators. *AIP Conference Proceedings*, 472(1):321–332, 1999.

[215] A. Spitkovsky and P. Chen. Laser shaping and optimization of the laser-plasma interaction. *AIP Conference Proceedings*, 569(1):183–194, 2001.

[216] C. D. Decker, W. B. Mori, K.-C. Tzeng, and T. Katsouleas. The evolution of ultra-intense, short-pulse lasers in underdense plasmas. *Physics of Plasmas*, 3(5):2047–2056, 1996.

[217] D. Umstadter, J. K. Kim, and E. Dodd. Laser injection of ultrashort electron pulses into wakefield plasma waves. *Phys. Rev. Lett.*, 76:2073–2076, Mar 1996.

[218] E. Esarey, R. F. Hubbard, W. P. Leemans, A. Ting, and P. Sprangle. Electron injection into plasma wakefields by colliding laser pulses. *Phys. Rev. Lett.*, 79:2682–2685, Oct 1997.

[219] L.-L. Yu, E. Esarey, C. B. Schroeder, J.-L. Vay, C. Benedetti, C. G. R. Geddes, M. Chen, and W. P. Leemans. Two-color laser-ionization injection. *Phys. Rev. Lett.*, 112:125001, Mar 2014.

[220] X. L. Xu, Y. P. Wu, C. J. Zhang, F. Li, Y. Wan, J. F. Hua, C.-H. Pai, W. Lu, P. Yu, C. Joshi, and W. B. Mori. Low emittance electron beam generation from a laser wakefield accelerator using two laser pulses with different wavelengths. *Phys. Rev. ST Accel. Beams*, 17:061301, Jun 2014.

[221] S. Li, G. Li, Q. Ain, M. S. Hur, A. C. Ting, V. V. Kulagin, C. Kamperidis, and N. A. M. Hafz. A laser-plasma accelerator driven by two-color relativistic femtosecond laser pulses. *Science Advances*, 5(11), 2019.

[222] P. Tomassini and A. Giulietti. A generalization of abel inversion to non-axisymmetric density distribution. *Optics Communications*, 199(1):143–148, 2001.

[223] G. B. Airy. On the Diffraction of an Object-glass with Circular Aperture. *Transactions of the Cambridge Philosophical Society*, 5:283–291, Jan 1835.

[224] B. Spiers (user "unpairedbracket"). Envelope focusing code. https://github.com/unpairedbracket/envelope_focusing/, accessed 09 July 2021.

[225] B. Spiers. *Laser-accelerated ion beams and their applications*. PhD thesis, University of Oxford, 2021 (to be published, private communication).

[226] C. Sheppard and T. Wilson. Gaussian-beam theory of lenses with annular aperture. *Microwaves, Optics and Acoustics, IEE Journal on*, 2:105 – 112, 08 1978.

[227] J. Cardarelli (user "jcardar"). MagnetSpec_ParticleTracker. https://github.com/jcardar/MagnetSpec_ParticleTracker, accessed 20 August 2021.

[228] J. Boris. Relativistic plasma simulation-optimization of a hybrid code. In *Proceedings, Fourth Conference on Numerical Simulation of Plasmas*. United States Naval Research Office, 1970.

[229] L. Brieda. Particle push in magnetic field (boris method). https://www.particleincell.com/2011/vxb-rotation/, accessed 22 May 2022.

[230] M. J. Mead, D. Neely, J. Gauoin, R. Heathcote, and P. Patel. Electromagnetic pulse generation within a petawatt laser target chamber. *Review of Scientific Instruments*, 75(10):4225–4227, 2004.

[231] A. Poyé, S. Hulin, M. Bailly-Grandvaux, J.-L. Dubois, J. Ribolzi, D. Raffestin, M. Bardon, F. Lubrano-Lavaderci, E. D'Humières, J. J. Santos, Ph. Nicolaï, and V. Tikhonchuk. Physics of giant electromagnetic pulse generation in short-pulse laser experiments. *Phys. Rev. E*, 91:043106, Apr 2015.

[232] S. M. Stigler. Francis Galton's Account of the Invention of Correlation. *Statistical Science*, 4(2):73 – 79, 1989.

[233] P. B. Wigley, P. J. Everitt, A. van den Hengel, J. W. Bastian, M. A. Sooriyabandara, G. D. McDonald, K. S. Hardman, C. D. Quinlivan, P. Manju, C. C. N. Kuhn, I. R. Petersen, A. N. Luiten, J. J. Hope, N. P. Robins, and M. R. Hush. Fast machine-learning online optimization of ultra-cold-atom experiments. *Scientific Reports*, 6(1):25890, May 2016.

[234] A. J. Barker, H. Style, K. Luksch, S. Sunami, D. Garrick, F. Hill, C. J. Foot, and E. Bentine. Applying machine learning optimization methods to the production of a quantum gas. *Machine Learning: Science and Technology*, 1(1):015007, Feb 2020.

[235] R. J. Shalloo, S. J. D. Dann, J.-N. Gruse, C. I. D. Underwood, A. F. Antoine, C. Arran, M. Backhouse, C. D. Baird, M. D. Balcazar, N. Bourgeois, J. A. Cardarelli, P. Hatfield, J. Kang, K. Krushelnick, S. P. D. Mangles, C. D. Murphy, N. Lu, J. Osterhoff, K. Põder, P. P. Rajeev, C. P. Ridgers, S. Rozario, M. P. Selwood, A. J. Shahani, D. R. Symes, A. G. R. Thomas, C. Thornton, Z. Najmudin, and M. J. V. Streeter. Automation and control of laser wakefield accelerators using bayesian optimization. *Nature Communications*, 11(1):6355, Dec 2020.

[236] S. Jalas, M. Kirchen, P. Messner, P. Winkler, L. Hübner, J. Dirkwinkel, M. Schnepp, R. Lehe, and A. R. Maier. Bayesian optimization of a laser-plasma accelerator. *Phys. Rev. Lett.*, 126:104801, Mar 2021.

[237] N. Bruchon, G. Fenu, G. Gaio, M. Lonza, F. H. O'Shea, F. A. Pellegrino, and E. Salvato. Basic reinforcement learning techniques to control the intensity of a seeded free-electron laser. *Electronics*, 9(5), 2020.

[238] R. S. Mathew, R. O'Donnell, D. Pizzey, and I. G. Hughes. The raspberry pi auto-aligner: Machine learning for automated alignment of laser beams. *Review of Scientific Instruments*, 92(1):015117, 2021.

[239] P. Dollar, Z. Tu, and S. Belongie. Supervised learning of edges and object boundaries. In *2006 IEEE Computer Society Conference on Computer Vision and Pattern Recognition (CVPR'06)*, volume 2, pages 1964–1971, 2006.

[240] T. Schlegl, P. Seeböck, S. M. Waldstein, U. Schmidt-Erfurth, and G. Langs. Unsupervised anomaly detection with generative adversarial networks to guide marker discovery. In M. Niethammer, M. Styner, S. Aylward, H. Zhu, I. Oguz, P.-T. Yap, and D. Shen, editors, *Information Processing in Medical Imaging*, pages 146–157, Cham, 2017. Springer International Publishing.

[241] T. Kemp and A. Waibel. Unsupervised training of a speech recognizer using tv broadcasts. In *Proceedings of the International Conference on Spoken Language Processing (ICSLP-98)*, pages 2207–2210, 1999.

[242] V. Mnih, K. Kavukcuoglu, D. Silver, A. Graves, I. Antonoglou, D. Wierstra, and M. Riedmiller. Playing atari with deep reinforcement learning, 2013.

[243] K. Shao, Z. Tang, Y. Zhu, N. Li, and D. Zhao. A survey of deep reinforcement learning in video games, 2019.

[244] D. Silver, T. Hubert, J. Schrittwieser, I. Antonoglou, M. Lai, A. Guez, M. Lanctot, L. Sifre, D. Kumaran, T. Graepel, T. Lillicrap, K. Simonyan, and D. Hassabis. A general reinforcement learning algorithm that masters chess, shogi, and Go through self-play. *Science*, 362(6419):1140–1144, 2018.

[245] D. Silver, J. Schrittwieser, K. Simonyan, I. Antonoglou, A. Huang, A. Guez, T. Hubert, L. Baker, M. Lai, A. Bolton, Y. Chen, T. Lillicrap, F. Hui, L. Sifre, G. van den Driessche, T. Graepel, and D. Hassabis. Mastering the game of go without human knowledge. *Nature*, 550(7676):354–359, Oct 2017.

[246] R. Bellman. A markovian decision process. *Indiana Univ. Math. J.*, 6:679–684, 1957.

[247] V. Mnih, K. Kavukcuoglu, D. Silver, A. A. Rusu, J. Veness, M. G. Bellemare, A. Graves, M. Riedmiller, A. K. Fidjeland, G. Ostrovski, S. Petersen, C. Beattie, A. Sadik, I. Antonoglou, H. King, D. Kumaran, D. Wierstra, S. Legg, and D. Hassabis. Human-level control through deep reinforcement learning. *Nature*, 518(7540):529–533, Feb 2015.

[248] R. S. Sutton, D. McAllester, S. Singh, and Y. Mansour. Policy gradient methods for reinforcement learning with function approximation. In *Proceedings of the 12th International Conference on Neural Information Processing Systems*, NIPS'99, page 1057–1063, Cambridge, MA, USA, 1999. MIT Press.

[249] S. M Kakade. A natural policy gradient. In T. Dietterich, S. Becker, and Z. Ghahramani, editors, *Advances in Neural Information Processing Systems*, volume 14. MIT Press, 2002.

[250] J. N. Tsitsiklis and B. Van Roy. An analysis of temporal-difference learning with function approximation. *IEEE Transactions on Automatic Control*, 42(5):674–690, 1997.

[251] D. P. Kingma and J. Ba. Adam: A method for stochastic optimization, 2017.

[252] J. Peters, S. Vijayakumar, and S. Schaal. Natural actor-critic. In J. Gama, R. Camacho, P. B. Brazdil, A. M. Jorge, and L. Torgo, editors, *Machine Learning: ECML 2005*, pages 280–291, Berlin, Heidelberg, 2005. Springer Berlin Heidelberg.

[253] User "opencv". opencv-python 3.4.15.55. https://github.com/opencv/opencv-python/, accessed 09 July 2021.

[254] User "morefigs". Pymba. https://github.com/morefigs/pymba, accessed 09 July 2021.

[255] S. Jordan (User "ScottJordan"). python-rllib. https://github.com/ScottJordan/python-rllib, accessed 09 July 2021.

[256] G. Konidaris, S. Osentoski, and P. Thomas. Value function approximation in reinforcement learning using the fourier basis. *Proceedings of the AAAI Conference on Artificial Intelligence*, 25(1), Aug 2011.

[257] K. Ishikawa and T. Blenski. Explosion dynamics of rare-gas clusters in an intense laser field. *Phys. Rev. A*, 62:063204, Nov 2000.